# University of Glasgow

Liu, Peng (2012) *InSAR observations and modeling of Earth surface displacements in the Yellow River Delta (China).* PhD thesis.

http://theses.gla.ac.uk/3787/

# InSAR observations and modeling

# of Earth surface displacements in the

# Yellow River Delta (China)

Peng Liu

BEng Surveying and Mapping, Central South University, China

Submitted in fulfillment of the requirements for the Degree of
Doctor of Philosophy

School of Geographical and Earth Sciences
College of Science and Engineering
University of Glasgow

September 2012

# Abstract

Subsidence in river deltas is a complex process that has both natural and human causes (Boesch et al., 1994). The Yellow River delta is used for farming, contains an important nature reserve for wild animals especially for waterfowl, has a population of 1.64 million, and is the location of significant oil fields (Chen et al., 2012). Increasing human activities like farming and petroleum extraction are affecting the Yellow River delta, and one consequence is subsidence. This subsidence may have social, economic and environmental impacts (Syvitski et al., 2009). The purpose of this thesis is to measure the surface displacement in Yellow River delta and to investigate the causes of measured displacement.

The use of Interferometric Synthetic Aperture Radar (InSAR) for Earth surface displacement mapping has increased since the 1990s when a lot of radar images become available. InSAR time series techniques identify displacement of an area between different image acquisition times. In this study, StaMPS package was employed to process Envisat ASAR images collected between 2007 and 2010. StaMPS selects only the stable pixels from interferograms to maintain the coherence signals over a long time interval. Consistent results between two descending tracks show subsidence with a mean velocity of up to 30 mm/yr in the radar line of sight direction in Gudao Town (oilfield), Gudong oilfield and Xianhe Town of the delta, and also show that subsidence is not uniform across the delta. Field investigation shows an association between areas of subsidence and of petroleum extraction.

In a 9 $km^2$ area of the Gu-Dao Oilfield in the delta, InSAR derived surface deformation is used to model the geometry, volume or pressure change of the deformation source, namely the extraction of fluids, using three different models: the spherical source Mogi type model, the finite prolate spheroid model and the poroelastic disk reservoir model. In general, good fits between InSAR observations and modelled displacements are seen. The source depths estimated in the three models agree well with the published oilfield depth. The subsidence observed in the vicinity of the oilfield is thus suggested to be caused by fluid extraction.

For Mogi type model, a uniform subsidence rate of about 7 mm/yr is co-estimated. InSAR observations in Xianhe Town in the delta, which is not affected by oil extraction, also

shows 8~12 mm/yr uniform subsidence. It is suggested this uniform subsidence is caused by other sources e.g. loading and sediment compaction. Since InSAR only measures relative displacement, accurate determination of small uniform rate need the reference phase provided by other observations e.g. GPS and levelling.

Mogi model provides the volume change in Gudao oilfield. The ellipsoidal source and the disk reservoir model the pressure changes. Additional reservoir information e.g. material parameter will help better confine the model parameters. Although no production data is available for comparison, the volume and pressure changes obtained from the models, together with InSAR observed displacement might be of interest for oil industry, to predict future subsidence in Gudao oilfield.

# Table of Contents

# List of Tables

# List of Figures

# Acknowledgement

First and foremost I would like to thank my supervisors Dr. Zhenhong Li and Prof. Trevor Hoey for their guidance, patience and support. I would like to thank them for the many hours they spend with me in discussion about various aspects of this research. I am indebted to Zhenhong for countless times taking advantage of his lunch time. Their comments and suggestions for my posters, PPT slides, abstracts, my first Journal paper and this thesis are invaluable. I thank Prof. Noel Gourmelen and Dr. Cristina Persano for reviewing my thesis and providing useful comments, corrections and discussions in my viva.

I owe thanks to Prof. Yanxiong Liu for all his assistance during my fieldtrip to Yellow River delta and also Linjun Zhu for his filed guidance. Thanks to Callum Dowds and Kenny Roberts for carrying out the Laser Diffraction analysis. Thanks to Callum Dowds and Peter Chung for carrying out SEM analysis and providing SEM images. Thanks to Gary for maintaining the server in a good condition. Thanks to Les for printing the conference posters. Thanks to Dr. Jane Drummond and Andy Singleton for improving my writing. Thanks to Zhiwei Zhou for recovering my fragile laptop and the lost data.

I would like to thank Dr. Yangmao Wen for solving my endless InSAR software problems at the beginning of my PhD. Thanks to Wanpeng Feng for his instant help with InSAR and modeling problems. I would like to thank Dr. Zhong Lu, Prof. Yuri Fialko, and Prof. Paul Segall for answering my questions.

I would like to acknowledge China Scholarship Council and University of Glasgow for funding my PhD programme.

Finally, I am grateful to my parents for their selfless support, to my wife Dujiao for her love, and my little boy Dingchen for his nappies.

# Declaration of originality

I confirm that the work described in this thesis is my own work unless otherwise cited or acknowledged. The thesis is of my own composition and has not been submitted for any other degree at the University of Glasgow or any other institution.

Peng Liu

September 2012

# Abbreviations

| | |
|---|---|
| 2D FFT | Two-Dimensional discrete Fast Fourier Transform |
| AOE | Atmospheric effects and Orbital Error |
| ALOS | Advanced Land Observing Satellite |
| APS | Atmospheric Phase Screen |
| ASAR | Advanced Synthetic Aperture Radar |
| CITES | Convention on International Trade in Endangered Species |
| COSMO-SkyMed | COnstellation of small Satellites for the Mediterranean basin Observation |
| DDG | Detectable Deformation Gradient |
| DEM | Digital Elevation Model |
| DEOS | Delft Institute of Earth Observation and Space Systems |
| Doris | Delft object-oriented radar interferometric software |
| Envisat | Environmental Satellite |
| ERS | European Remote sensing Satellite |
| Es | Eogene (Palaeogene) Shahejie formation |
| Ed | Eogene (Palaeogene) Dongying formation |
| FEM | Finite Element numerical Model |
| GPS | Global Positioning System |
| InSAR | Interferometric Synthetic Aperture Radar |
| JPL | Jet Propulsion Laboratory |
| NCP | Northern China Plain |
| Ng | Neogene Guantao formation |
| Nm | Neogene Minghuazhen formation |

| | |
|---|---|
| PRF | Pulse Repetition Frequency |
| PS | Persistent scatterers |
| ROI_PAC | Repeat Orbit Interferometry PACkage |
| RXO | Flushed zone resistivity |
| SAR | Synthetic Aperture Radar |
| SBAS | Small BAseline Subset |
| SDFP | Slowly Decorrelating Filtered Phase |
| SEM | Scanning Electron Microscopy |
| SLC | Single Look Complex |
| SMX | SanMenXia |
| SNAPHU | Statistical-Cost, Network-Flow Algorithm for Phase Unwrapping |
| SNR | Signal Noise Ratio |
| SP | Spontaneous potential |
| SRTM | Shuttle Radar Topography Mission |
| StaMPS | Stanford Method for Persistent Scatterers |
| TIN | Triangular Irregular Network |
| XLD | XiaoLangDi |
| YRDNNR | Yellow River Delta National Nature Reserve |

# Chapter 1 Introduction

Nearly half a billion people live on or near deltas (Wang et al., 2012). Many of the world's deltas are subsiding and causing public concern for subsequent relative sea level rise (Syvitski et al., 2009). The Yellow River delta is formed where the Yellow River enters the Bohai Sea. Although the delta is still prograding, subsidence risk is increasing by trapping of sediment in 3147 reservoirs in the catchment (Jia and Wang, 2011), sea level rise induced by ongoing climate change, and hydrocarbon extraction from underlying sediments. However, the pattern of current surface displacement in the Yellow River delta has not been mapped. Repeat pass Interferometric synthetic Aperture Radar (InSAR) is able to map the Earth surface displacement with sub centimetre accuracy over a wide area (e.g. $100 \times 100 \ km$). In this thesis, InSAR techniques are employed to investigate displacement in the Yellow River delta from 2007 to 2010.

## 1.1 The Yellow River Delta
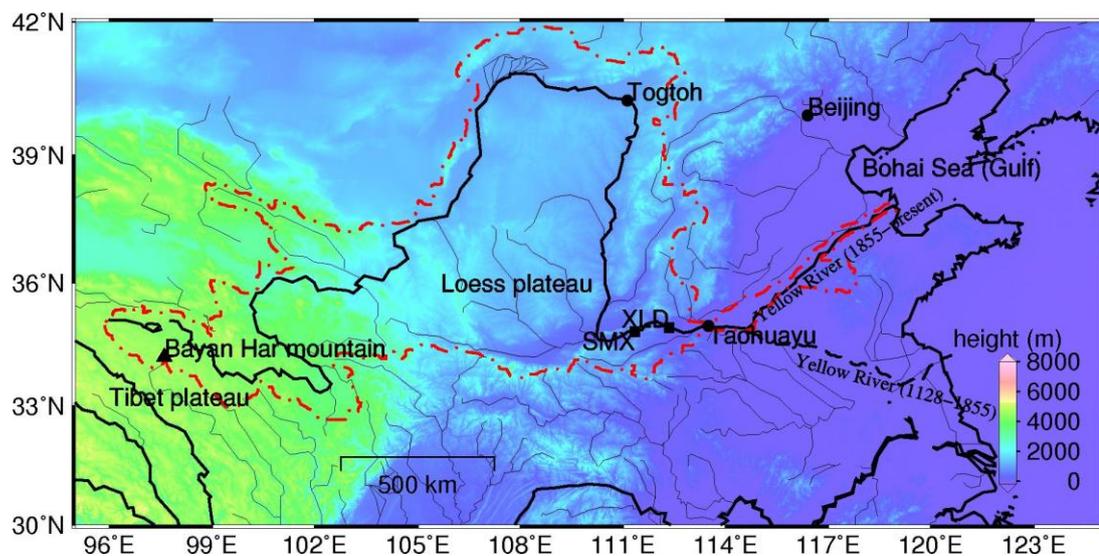


**Figure 1.1 The Yellow River and its drainage basin after (Wang et al., 2010, Saito et al., 2000). The red dotted line outlines the drainage basin. The Yellow River is the black solid line. The river course near the mouth between 1128 and 1855 is the black dashed line. Togtoh County and Taohuayu Town divide the Yellow River to upper, middle and lower reaches. SMX (Sanmenxia) and XLD (Xiaolangdi) are the major reservoirs in middle reaches of the river. Background is ETOPO1, a 1 arc-minute global relief model of Earth's surface. ETOPO1 by NOAA of NGDC integrates land topography and ocean bathymetry (http://www.ngdc.noaa.gov/mgg/global/global.html).**

The Yellow River originates from Bayan Har Mountain in the Qinghai-Tibet Plateau and flows for 5464 km through nine provinces before it discharges into Bohai Sea (Fig. 1.1). The Yellow River, which is the cradle of Chinese culture, gets its water colour and name from the silt it acquires from the Loess plateau. The annual sediment discharge to the sea is

1100 million tonnes 1950-99, comparable to the load of the Amazon River (Milliman and Syvitski, 1992, Ren and Shi, 1986). However, the annual amount has reduced to only 150 million tonnes from 2000 to 2006, due to sediment trapping by large reservoirs (e.g. XLD reservoir in Figure 1.1), soil conservation practise in Loess Plateau, and regional climate change (Wang et al., 2010).
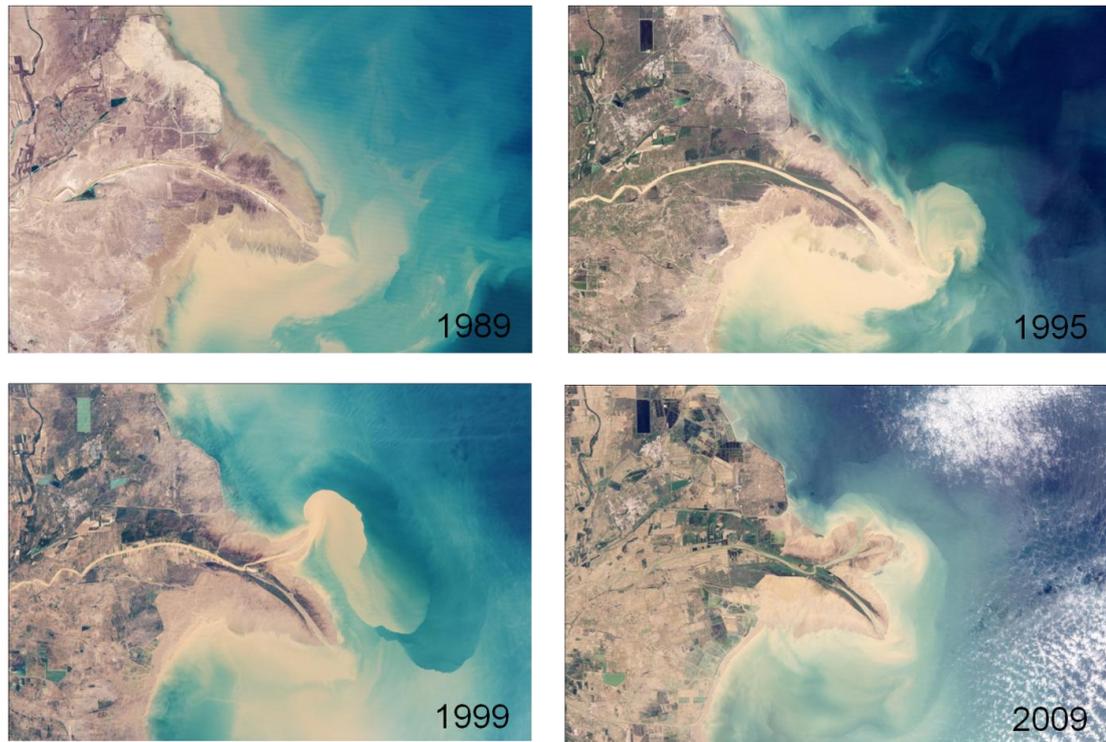


**Figure 1.2 Landsat images (60 km × 90 km) showing progradation of the Yellow River delta over 20 years. Images are from NASA observatory.**
**(http://earthobservatory.nasa.gov/Features/WorldOfChange/yellow_river.php)**

After a major shift in channel course in 1855, the Yellow River re-entered Bohai Sea (Fig. 1.1). There have been ten major channel adjustments from 1855 to present (Shi and Zhang, 2003, Chu et al., 2006), shaping a new mega delta of 5000 km$^2$ (Wang et al., 2010). Xu (2003) estimated the river mouth extension rate to have been 1.1~1.2 km/yr between 1981~1995. The cuspate delta formed after the recent channel shift in 1976 is now a young coastal wetland ecosystem called Yellow River Delta National Nature Reserve (YRDNNR) which was established in 1992 (Fang and Xu, 2000). YRDNNR is an excellent habitat for 500, 000 to 1 million birds and other animals, of which about 40 bird species, several species of marine mammals, reptiles and fishes are listed in CITES appendices (Chen et al., 2012).

Coastal subsidence has caused wetland loss in many delta regions. Public concern over wetland loss in Louisiana in the 1980s led to extensive studies to understand the underlying

reasons for this loss (Boesch et al., 1994). Hydrocarbon production in Louisiana (Morton et al., 2006), Holocene sediment compaction in the Mississippi delta (Tornqvist et al., 2008), and many other reasons (Boesch et al., 1994) are thought to be related to this complex process.

Similarly to the Louisiana Gulf coast, extensive hydrocarbon production exists in the Yellow River delta. Located in the Yellow River delta and Bohai Gulf, Shengli oilfield is the second largest oilfield in China with annual production of 27 million tonnes. Shengli oilfield has many production units and facilities distributed in the Yellow River delta, including within the nature reserve (Chen et al., 2012).

Until now, studies have focused on the ecological risks of droughts, floods, storms, and petroleum pollution in wetlands of Yellow River delta (Cui et al., 2009, Xu et al., 2004, Yue et al., 2003). Beyond these ecological risk assessments, relatively little is known about the magnitude and rate of subsidence in the wetlands. Subsidence associated with relative sea level rise will also alter the coastal environment of the Yellow River delta, and affect the local residents and oil production. The social, ecological and economical reasons highlight the necessity of understanding subsidence in the Yellow River delta.

## 1.2   InSAR

The idea of radar interferometry dates back to the 1970s (Graham, 1974), but it was in the 1980s that applications of InSAR for topography mapping were published (Gabriel and Goldstein, 1988, Goldstein et al., 1988, Zebker and Goldstein, 1986). Implementation of airborne system interferometry (e.g. JPL/NASA TOPSAR) produced InSAR derived DEMs with an accuracy of 1-3 m (Madsen et al., 1995). Shuttle Radar Topography Mission (SRTM) is a key product of simultaneous interferometry for near global ($56°S\sim60°N$) topography mapping, using a space borne system (Farr, 2007, Rabus et al., 2003). A three year global topography mapping mission has being undertaken since October 2010 by TanDEM-X (Krieger et al., 2007, Moreira et al., 2004) and its twin satellite TerraSAR-X, when they moved into close formation to acquire radar images of the same area simultaneously.

The capability of repeat-pass InSAR for displacement mapping was first demonstrated by *Gabriel et al.* (1989). Its development accelerated only after the launch of ERS-1 in 1991; since then a large amount of data is available for repeat-pass radar interferometry. The

potential of the technique was shown by the remarkable discovery that the radar interferometry was capable of detecting the displacement field of the 1992 Landers earthquake (Massonnet et al., 1993). Moreover it has been proved that InSAR is able to detect deformation with sub-centimetre accuracy. InSAR is now widely used in measuring the Earth's surface dynamics, e.g. land subsidence due to human activities (Osmanoglu et al., 2011, Buckley et al., 2003, Fielding et al., 1998, Massonnet et al., 1997) and natural phenomenon, such as earthquakes(Li et al., 2011, Wright et al., 2004, Massonnet et al., 1994) and volcano eruptions (Ofeigsson et al., 2011, Lu and Dzurisin, 2010, Amelung et al., 2000, Massonnet et al., 1995).

Specifically for subsidence in delta regions, InSAR has been used to measure subsidence rates of 8 *mm/yr* in youngest deposition centres and 2~6 mm/yr in slightly older deposition centres in the Nile delta Egypt (Becker and Sultan, 2009), due to sediment compaction (Stanley and Hait, 2000, Stanley, 1988). *Mazzotti et al* (2009) used InSAR, GPS and levelling to map the vertical movements in the Fraser River delta, Canada, suggesting that areas with 1-2 *mm/yr* subsidence are due to primary consolidation of shallow Holocene sediment, and those with 3-8 *mm/yr* subsidence are affected by recent artificial loading.

However, repeat-pass space borne InSAR is limited by decorrelation (Zebker and Villasenor, 1992) and atmospheric heterogeneities (Zebker et al., 1997), e.g. thermal noise in radar systems, change of reflectivity characteristics of backscatters and signal propagation delay differences due to different atmospheric conditions. To maximise the potential of InSAR, a lot of recent and current work is aimed at developing time series algorithms (e.g. Permanent scattering or Persistent scattering (PS) InSAR (Ferretti et al., 2001, Hooper et al., 2007), Small baseline InSAR (Berardino et al., 2002, Hooper, 2008) and SqueeSAR (Ferretti et al., 2011)) to statistically minimize the interferometric noise and mitigate atmospheric disturbance. Other work includes correction of atmospheric effects using independent atmospheric water vapour data e.g. MERIS (Li et al., 2012), MODIS (Li et al., 2006b), GPS (Li et al., 2006a, Webley et al., 2002), and Numerical weather models (Foster et al., 2006, Wadge et al., 2002), where techniques allow 50~60% reduction of atmospheric effect.

## 1.3  Surface displacement modelling

Magnitudes and rates of surface displacement from geodetic observations can be used to quantitatively model subsurface processes. Mogi (1958) found a surprising agreement

between the modelled displacement using a spherical source and the actual deformation measured by precise survey. With the development of geodetic techniques, GPS observations are used to model crustal deformation (Feigl et al., 1993, Sagiya et al., 2000). InSAR observations of displacement due to the Landers earthquake agree extremely well with the dislocation model in the intermediate and far field (Massonnet et al., 1993). GPS and InSAR have also been combined to model interseismic strain accumulation(Chlieh et al., 2004, Gourmelen et al., 2010, Cavalié et al., 2008, Elliott et al., 2008), coseismic slip distribution (Jonsson et al., 2002, Simons et al., 2002, Feng et al., 2012),  and postseismic deformation (Peltzer et al., 1998, Pollitz et al., 2000, Fialko, 2004, Shen et al., 1994). InSAR or GPS measurements have also been used to model other displacements including volcano dynamics (Manconi and Casu, 2012, Biggs et al., 2010), subsidence (Hoffmann et al., 2001, Fialko and Simons, 2000) and landslides (Fruneau et al., 1996).

From InSAR observations, fluid loss induced displacements usually show non-uniform subsidence patterns e.g. volcanic eruption, underground water extraction, hydrocarbon production. Dilatation centres are used to model the subsidence displacement.

Delta subsidence can also be modelled using dilatation models if it is caused by fluid extraction. Modelling subsidence using a continuous elastic medium assumes that the fluid exists within a cavity in homogenous isotropic elastic half space (Davis, 1986) e.g. a magma chamber. Analytical solutions that have been developed include spherical point source (Mogi, 1958, Anderson, 1936), finite spherical source (McTigue, 1987), ellipsoidal point source (Davis, 1986), finite ellipsoidal source (Yang et al., 1988), point and finite rectangular dislocation source (Okada, 1985, Okada, 1992), and circular crack source (Fialko et al., 2001).

Assuming the fluid e.g. magma to be confined within a cavity can be sound for a volcano chamber. However, for an elastic medium that is not completely continuous, such as fluid exists in more distributed way (e.g. ground water in a shallow aquifer system, hydrocarbons in reservoir rocks). Terzaghi (1943) developed the principle of effective stress to incorporate the mechanical effect of water on the behaviour of soil. Biot (1941) introduced a general poroelastic theory in three dimensions. The theory was developed by Nur and Byerlee (1971) into an exact effective stress law for deformation of rocks with fluid. Segall (1992) gave the analytical solution of the effective stress equation in an axisymmetric space and applied the solution to model subsidence in a hydrocarbon reservoir (Segall et al., 1994).

## 1.4   Aims of the thesis

This thesis focuses on surface displacement mapping, using time series InSAR technique and the modelling of surface displacement in the Yellow River delta.

The questions need to be addressed for InSAR in this study are as follows:

*Question 1: Is it feasible to use InSAR to monitor surface movements in the Yellow River Delta region? How accurate can the InSAR results be?*

*Questions 2: What is the major cause of surface displacement in the Yellow River delta region?*

*Question 3: Is the major cause the sole reason for subsidence?*

*Questions 4: What are the limitations for applying InSAR to the Yellow River delta?*

The questions that need to be addressed for modelling in this study are as follows:

*Question 1: Which mechanisms have been used to model the surface movements caused by oil extraction? Why are different models used? What are the differences between them?*

*Question 2: Can the most appropriate models match the observed displacements? Is there any reason for the residuals? How close are the models to the reality?*

*Question 3: What is the limitation of modelling application in the Yellow River delta?*

*Question 4: Is subsidence a major problem? Can it be predicted?*

## 1.5 Outline of the thesis

Chapter 2 reviews the SAR theory, InSAR phase component.

Chapter 3 reviews time series InSAR technique. The data processing steps are given with examples from the Badong landslide in the Three Gorges region, China.

Chapter 4 reviews the geomorphology and geology of the Yellow River delta, and the Geology of the Gudao oilfield which is the model area. Sediment properties of samples collected from the Yellow River delta are also presented.

In Chapter 5, time series InSAR technique is used to map surface displacement in the Yellow River delta. Two adjacent InSAR tracks are used to validate the InSAR rates and time series. Association between subsidence and oil extraction is shown.

In Chapter 6, a hydrocarbon production induced subsidence is simulated based on the Lacq gas field of France (Segall et al., 1994). The simulated subsidence is modelled using spherical source and poroelastic disk reservoir. The InSAR observed displacement in Gudao oilfield are also modelled using spherical source, finite ellipsoidal source and poroelastic disk reservoir.

The conclusions and recommendations for future research are given in Chapter 7.

# Chapter 2 Principles of InSAR

In this chapter, some basic concepts of InSAR and the phase component of radar interferometry are introduced.  Some images are from Badong in Three Gorges area of China.

## 2.1 SAR

The side-looking radar works when it flies along the orbit in the azimuth direction over areas of interest, with the antenna transmitting electromagnetic waves and receiving the pulse backscattered from the Earth surface in the range direction (Fig. 2.1). The SAR image is constructed using the amplitude and time delay of the return signal (Brown and Porcello, 1969, Chan and Koo, 2008).
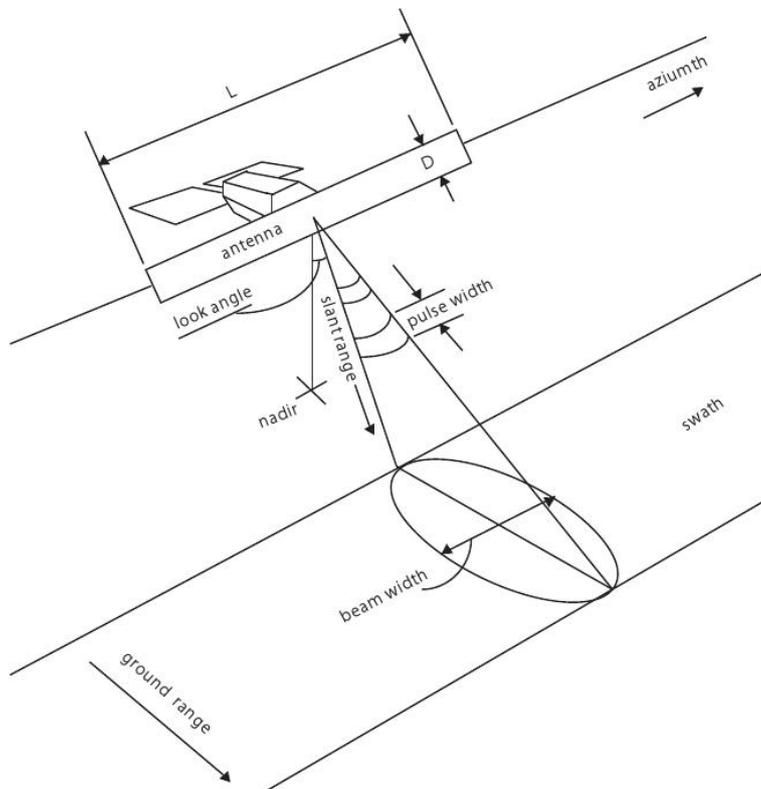


**Figure 2.1 Side looking radar antenna illuminates terrain strip, after Bamler and Hartlz (1998).**

Each pixel of the SAR image is actually a complex number. Hence these images are also called Single Look Complex (SLC) SAR images. The complex number contains both amplitude (Fig. 2.2a) and phase (Fig. 2.2b) information. Each pixel of SAR images represents a certain area on the Earth's surface in which there are hundreds of elementary targets. The complex value of a pixel is a combination of such elementary target reflection

results, when the corresponding area is illuminated by radar pulses.

(a)



(b)



(radians)
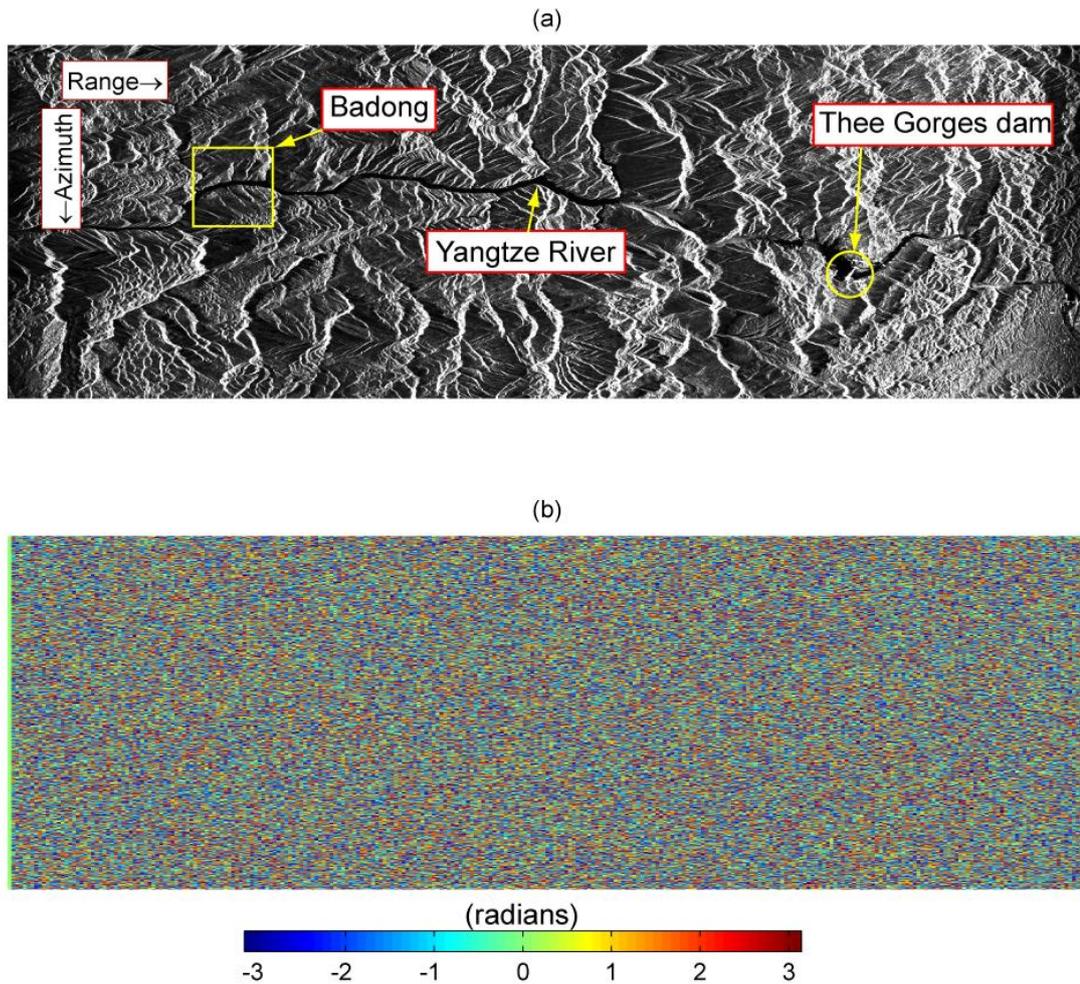
**Figure 2.2 An example of a SLC image from Envisat Track 075 covering the Three Gorges area, China. (a). SLC amplitude image. (b). SLC phase image. It is a descending image. The area is illuminated from east by the travel of satellite from north to south with radar wave incidence angle of 23°. Some terrain behind the mountain ridges are in shadow, as a result of the fact that no return signal from that area reaches the antenna. Water surfaces show mirror reflection with no back scattering signal to the radar. Hence the Yangtze River and Three Gorges reservoir area are also in black.**

SAR images usually show a distribution of bright pixels surrounded by dark pixels. This is the result of different reflectivity functions of each pixel under illumination (Ferretti et al., 2007). A bright pixel means that there are strong reflection targets existing in the area, such as exposed rocks in the field, buildings or roads, or artificial corner reflectors that can be installed to strengthen the amplitude of signal returned from small areas. The size of a pixel is called the range resolution and the azimuth resolution.

The range resolution is the minimum distance between two objects that can be identified. In radar engineering, $\Delta R_r$ is given as

$$\Delta R_r = \frac{c\tau}{2} \qquad\qquad (2.1)$$

where $c$ is the speed of light and $\tau$ is the radar pulse length which is the time that the radar transmits microwaves, while the coefficient $1/2$ here is because of the round-trip of the pulse wave (Brown and Porcello, 1969).

In order to achieve a higher resolution in range direction, we need to reduce the pulse length $\tau$, which also means an increase in radar power if we cannot accept the trade off between radar backscatter signal noise ratio (SNR) and pulse length. In practice, a technique called range compression has been adopted to improve range resolution.

$$\Delta R_r = \frac{c}{2W} \qquad\qquad (2.2)$$

where $W$ is the bandwidth of both transmitter and receiver. The problem is solved by transmitting a long duration pulse which is power efficient and using matched filtering on the received pulse to collect pulse energy to the peak value. It is a process as if a narrow pulse were transmitted. The bandwidth of Envisat ASAR is $16\ MHz$ (Fornaro et al., 2005), corresponding to $9.4\ m$ slant range resolution (Rosich, 2003) from image mode swath IS1 to IS7. Thus the ground range resolution can be given as:

$$\Delta R_g = \frac{\Delta R_r}{sin\theta} \qquad\qquad (2.3)$$

where $\theta$ is the radar beam incidence angle to the normal direction of the Earth surface. The typical incidence angle of Envisat ASAR is $23°$, thus the ground range resolution of ASAR images is about $24\ m$.

The azimuth resolution of a radar system is a function of the antenna length (Brown and Porcello, 1969):

$$\Delta L = \frac{\lambda}{L}\rho \qquad\qquad (2.4)$$

where $\rho$ is the slant range between the radar and the earth surface, $L$ is the antenna length, $\lambda$ is radar wavelength and $\lambda/L$ is thus the beam width. The equation unveils that, a high azimuth resolution requires a very long antenna. For instance, for Envisat satellite altitude of $790 \pm 10\ km$, an azimuth resolution of $5m$ needs an antenna $9\ km$ long, which is

unrealistic. The problem of the limited antenna dimension can be circumvented by synthesizing a small antenna along the azimuth direction (Fig. 2.3).
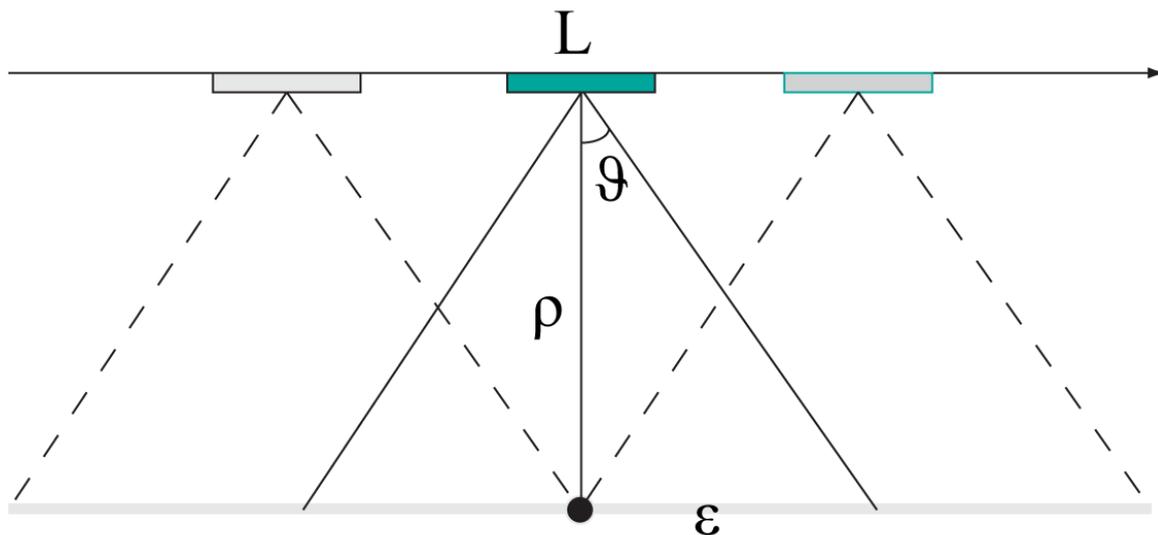


**Figure 2.3 Schematic map of radar antenna synthesis (top view). $\vartheta$ is the half illumination angle, $\rho$ is the distance between antenna and target, $\varepsilon$ is the half length of ground illumination, and $L$ is antenna length.**

According to diffraction resolution:

$$sin\vartheta = \frac{\lambda}{L} \tag{2.5}$$

It can be seen from Figure 2. 3 that

$$\varepsilon = \rho tan\vartheta \tag{2.6}$$

As $\varepsilon \ll \rho$, $tan\vartheta \approx sin\vartheta$, substituting (2.5) into (2.6):

$$\varepsilon = \rho sin\vartheta = \rho \frac{\lambda}{L} \tag{2.7}$$

The synthetic aperture has a length of $L' = 2\varepsilon$. Using Equations (2.4) and (2.7), the azimuth resolution for synthetic aperture radar is:

$$\Delta L' = \frac{\lambda}{L'}\rho = \frac{\lambda\rho}{2\varepsilon} = \frac{L}{2} \tag{2.8}$$

Along track resolution, $\Delta L'$ is thus independent of range and of wavelength. It looks as if azimuth resolution can be improved by reducing the dimension of the antenna, $L$.

However, for a moving satellite, the maximum Doppler shift (Gordon, 1996) occurs at the maximum angle $\vartheta$ (Fig. 2.3) is

$$\Delta f = 2f_0 \frac{V}{c} sin\vartheta = 2\frac{c}{\lambda}\frac{V}{c}\frac{\lambda}{L} = \frac{2V}{L} \qquad (2.9)$$

where $f_0$ is the carrier frequency, $V$ is the satellite speed relative to ground, and $\Delta f$ is the Doppler shift. With identical orbital speed, shorter antenna corresponds to higher Doppler shift. In order not to alias the radar signals, the pulse repetition frequency must be greater than the Doppler shift. The antenna length of Envisat ASAR is $10\ m$ (Zink, 2002), so the azimuth resolution is $5m$. Its orbital velocity of $7.5\ km/s$ require a minimum Pulse Repetition Frequency (PRF) of $1500\ Hz$, while the PRF range of ASAR is $1686{\sim}2123\ Hz$ (Miranda, 2010). Due to different resolutions in azimuth and range, a multi look ratio is necessary for a near square pixel look. For instance, 4 and 20 looks in range and azimuth directions respectively are necessary for ASAR to get a square pixel of about $100 \times 100\ m$.

## 2.2 InSAR

InSAR is the interferometry of SAR images. Repeat-pass Synthetic Aperture Radar Interferometry (InSAR) is a microwave radar system for measuring the Earth's surface movements or topography when there is no displacement. Since radar generates microwave itself, it does not depend on any external sources, which means its all-day working capability. Compared with optical remote sensing systems, InSAR has the advantage to be able to work nearly all weather conditions because microwave can penetrate clouds (Rosen et al., 2000).

Although SAR images carry both amplitude and phase information (Fig. 2.2), InSAR mainly uses the phase information of the SAR images. Amplitude images are used for offset tracking of large scale movements (Strozzi et al., 2002, Michel et al., 1999) and SLC image co-registration (Nitti et al., 2011, Moreira and Scheiber, 2000, Lin et al., 1992). In InSAR time series, bright pixels that remain stable over a long time are more likely to be selected as stable pixels.

Two SLC SAR images collected over the same area with a similar geometry can be used to generate an interferogram, which is the phase difference between the two SAR images. The first phase value of a pixel in an SAR image can be given as:

$$\phi_1 = 2\frac{2\pi}{\lambda}\rho_1 + \omega_1 \qquad\qquad (2.10)$$

where $\rho_1$ is the distance between satellite antenna and the pixel, $\lambda$ is the electromagnetic wavelength, e.g. 5.6 cm for ERS-1/2. $\omega_1$ is unknown phase due to the interaction of the wave and the ground. The phase value of each pixel on the SAR image is the sum of signal propagation delay and the backscattering phase change. Similarly, the second value of the same pixel in a different time is kept in another SAR image.

$$\phi_2 = 2\frac{2\pi}{\lambda}\rho_2 + \omega_2 \qquad\qquad (2.11)$$

The interferometric phase for this pixel is the difference of these two phase values.

$$\delta\phi = \phi_1 - \phi_2 = 2\frac{2\pi}{\lambda}(\rho_1 - \rho_2) + (\omega_1 - \omega_2) \qquad\qquad (2.12)$$

An interferogram is composed of the interferometric phases of all pixels. If the interactions between radar waves and the targets are the same during the two acquisitions, the interference of the two SAR image would then eliminate the scattering part and the resultant phase value is:

$$\delta\phi = 2\frac{2\pi}{\lambda}\delta\rho \qquad\qquad (2.13)$$

The phase difference of the two SAR images corresponds to the range changes between the satellite antenna and the targets on the earth. In practice, the phase from SAR interferometry is wrapped. It is biased from the real value by $k \cdot 2\pi$, which is called the phase integer cycle ambiguity, and needs to be recovered by adding its integer cycles (Fig. 2.4). This process is called phase unwrapping.

$$\delta\phi' = W\left\{2\frac{2\pi}{\lambda}\delta\rho\right\} + k \cdot 2\pi \qquad (k \in Z) \qquad\qquad (2.14)$$

where W is the wrapping operator, Z is the set of integers. In practice, phase unwrapping is implemented by calculating the phase difference between neighboring pixels. The unwrapped phase is built pixel by pixel across the interferogram. However, the reconstructed phase surface is still relative in space. An offset might exist with the real value. That is why InSAR is a double difference of phase in space and time. The measured phase changes are relative in three dimensions, two dimensions in space, and one

dimension in time.
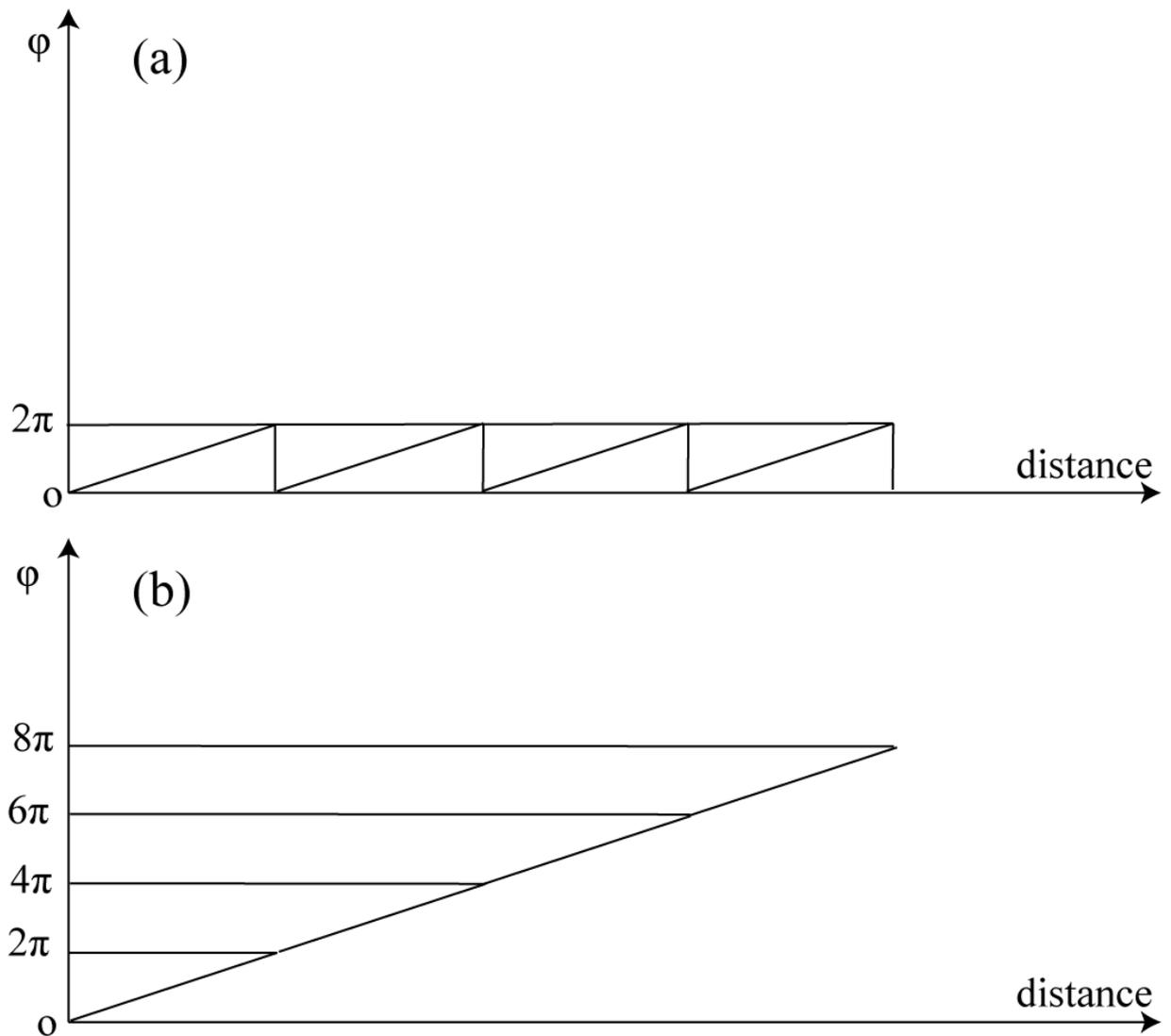


**Figure 2.4 Schematic map of phase unwrapping. (a) Wrapped phase; (b) Unwrapped phase**

After phase unwrapping, the phase changes on the interferogram can be converted into range changes, $\delta\rho$, as follows

$$\delta\rho = \frac{1}{2}\frac{\lambda}{2\pi}\delta\phi' \qquad (2.15)$$

The range change is the component of the Earth surface displacement in the radar line of sight direction and is the measure that InSAR users are interested in. InSAR time series is the combination of time series range change of the same pixels to investigate surface displacements with high temporal resolution. Since the interferometric phases are double differences, the range changes are also double differences. The assumption of a stable area or absolute displacement from independent observations e.g. GPS and leveling can be used to calibrate range changes from InSAR measurements.

The phase of the interferogram are the sum of five terms:

$$\phi_{ifg} = \phi_{def} + \phi_{topo} + \phi_{orb} + \phi_{aps} + \phi_n \qquad (2.16)$$

where $\phi_{ifg}$ is the phase of the interferogram; $\phi_{def}$ is the deformation phase due to earth surface movement; $\phi_{topo}$ is the topography phase by different satellite positions when different SAR images are acquired; $\phi_{orb}$ is the orbit error due to inaccurate orbit information; $\phi_{aps}$ is the atmospheric phase screen generated by different atmospheric condition when SAR images are acquired and $\phi_n$ is the noise phase from radar system or image processing.

In practice, to extract the displacement phase that we are interested in, other phase contributions should be isolated. Each of these phase components is discussed below.

## 2.2.1 Topography phase

When a DEM is unavailable, a different interferogram of the same area is used to remove the topographic contribution (Zebker et al., 1994). Nowadays, topography removal mainly uses a DEM and InSAR geometry to synthesize an interferogram of no displacement that is then subtracted from the measured interferogram (Massonnet and Feigl, 1998).
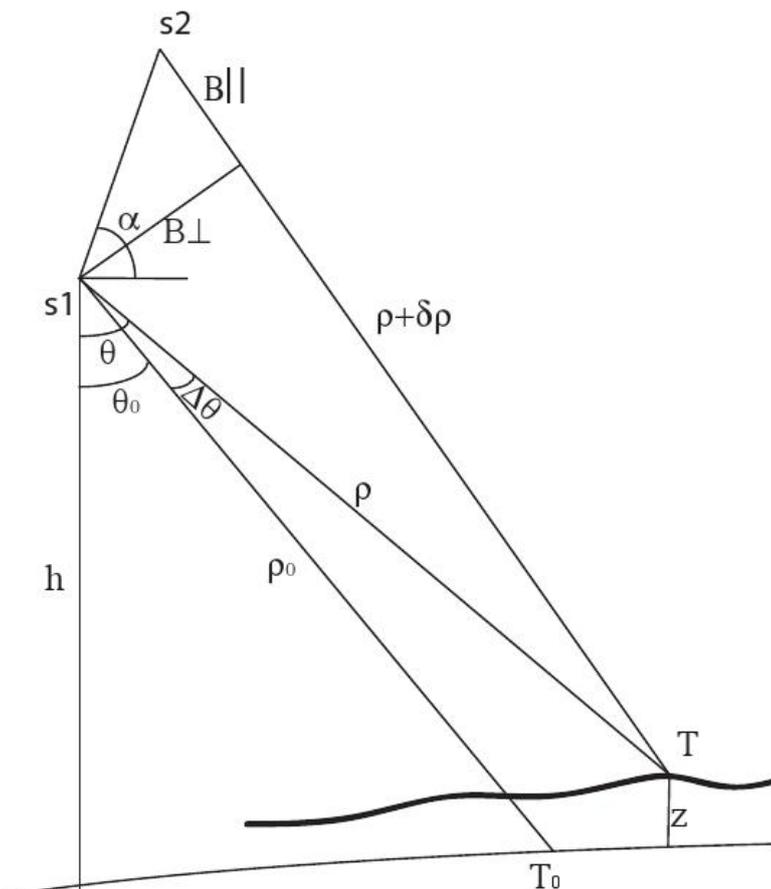
**Figure 2.5 InSAR geometry.** $s1$ **and** $s2$ **are the positions of satellites during image acquisition times.** $h$ **is the satellite height.** $T_0$ **is zero elevation surface.** $\rho$ **is the distance between the satellite and the target.** $\theta$ **is the off nadir radar look angle.** $s1s2$ **is the spatial baseline between the satellites.** $\alpha$ **is the horizontal baseline angle. The baseline between two sensors can be divided into the perpendicular baseline** $B_\perp$ **and parallel baseline** $B_\parallel$ **to the radar looking direction.**

### 2.2.1.1 Range change due to spatial baseline

Even if there is no surface displacement, there is still range change related to InSAR geometry and topography so long as the two satellite positions are not identical. An equation of range change, $\delta\rho$, without displacement can be given using the cosine rule (Fig. 2.5)

$$(\rho + \delta\rho)^2 = \rho^2 + B^2 - 2\rho B sin(\theta - \alpha) \qquad (2.17)$$

As $\delta\rho \ll \rho$, $\delta\rho^2$ can be neglected, and the approximate expression of $\delta\rho$ is:

$$\delta\rho \approx -Bsin(\theta - \alpha) + \frac{B^2}{2\rho} \qquad (2.18)$$

In the Envisat ASAR case with $\rho = 790$ km, the second term on the right side of the expression is:

$$\frac{B^2}{2\rho} = \frac{B^2}{1580000} \qquad\qquad (2.19)$$

For example, with 1100 meter baseline, the second order baseline term corresponds to a range change of 0.7658 meters. Even for a very short 100 meter spatial baseline, the second order baseline term corresponds to a range change of 0.0063 meters. With $\lambda = 5.6$ cm,

$$\frac{0.0063 \text{ m}}{0.056 \text{ m}} \cong \frac{1}{8.89} > \frac{1}{10} \text{ cycle} \qquad\qquad (2.20)$$

The second order term cannot be ignored until the phase cutting becomes meaningless. A typical noise level of one-sixteenth of a fringe has been observed for natural targets of ERS. Furthermore, resolving phase differences smaller than one tenth of a cycle is difficult (Massonnet and Feigl, 1998), so the second order term can be ignored but only when the spatial baseline is shorter than 100 meters (Li, 2005).

$$\delta\rho = -B\sin(\theta - \alpha) = -B_{\parallel} \qquad \left(\frac{B^2}{2\rho} < \frac{1}{10} \text{cycle}\right) \qquad (2.21)$$

Equation (2.20) is approximately the parallel component of the baseline (Zebker et al., 1994, Zebker and Goldstein, 1986). Equation (2.18) shows that $\delta\rho$ is a function of $\theta$, which is related to the position of the pixel. The radar incidence angle of a pixel can be calculated using a DEM and satellite geometry in order to remove $\delta\rho$ from the interferogram.

## 2.2.2.2 Curved Earth effect

Even when the Earth surface is flat, interferometric phase caused by the surface still exists. This component of phase should be removed from the total interferometric phase too (Fig. 2.6).
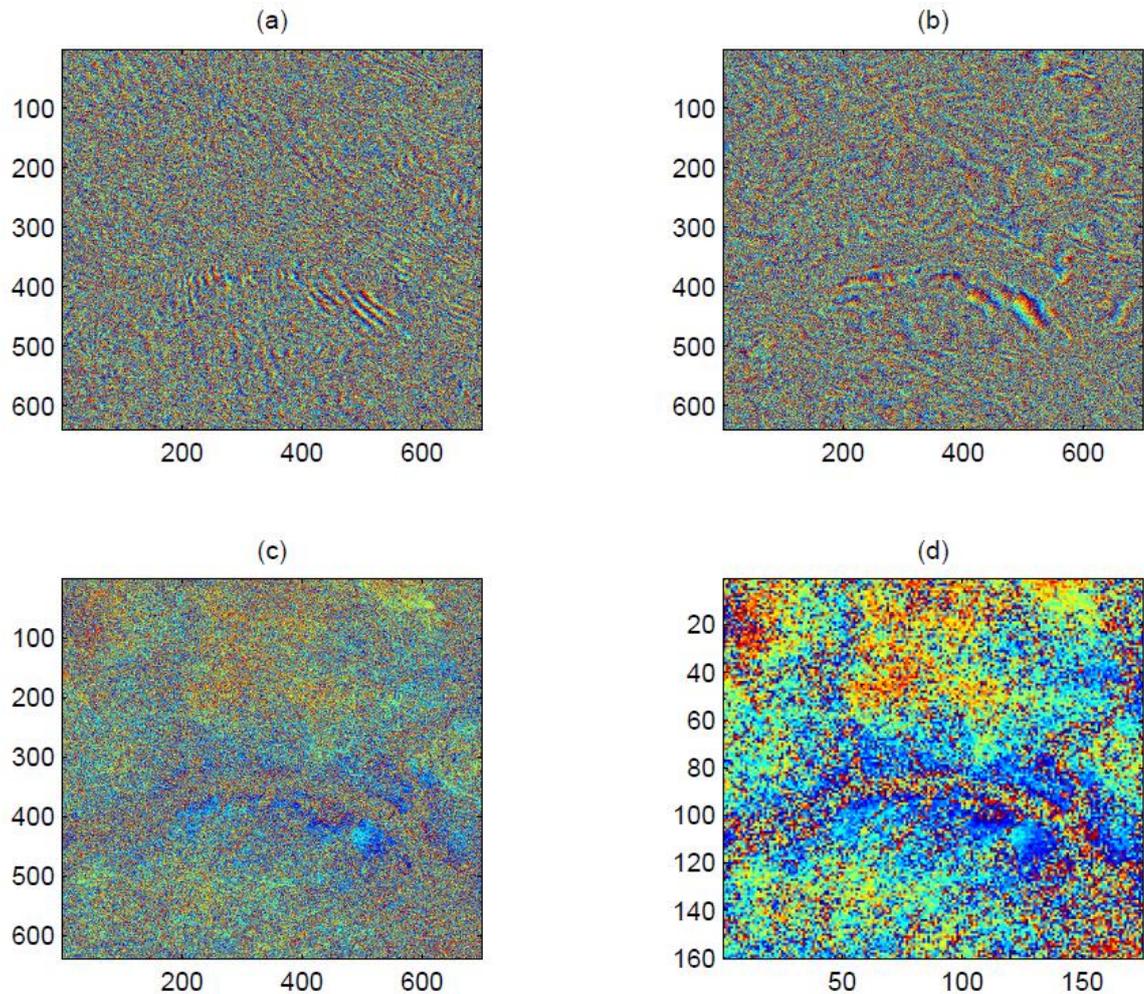
**Figure 2.6 An example of Topography removal in Badong, Three Gorges area, China. (a) Envisat ASAR Interferogram multi-looked by a factor of 5 in azimuth direction; (b) Interferogram from (a) after removal of reference phase using the WGS-84 ellipsoid; (c) Interferogram from (b) after removal of reference topography by SRTM; (d) Interferogram from (c) multi-looked by 4 in both range and azimuth directions. The axes represent the number of pixels.**

From Equation (2.21), the phase component due to the Earth surface curvature is:

$$\delta\phi = \frac{4\pi}{\lambda}\,\mathrm{B}\sin(\theta - \alpha) - \frac{4\pi}{\lambda}\,\mathrm{B}\sin(\theta_0 - \alpha) \qquad (2.22)$$

where $\theta_0$ is the look angle if the pixel is on the zero height reference surface (Fig. 2.5).

Substituting $\Delta\theta = (\theta - \theta_0)$ into Equation (2.22),

$$\delta\phi = \frac{4\pi}{\lambda}\mathrm{B}\big(\sin(\theta_0 - \alpha + \Delta\theta) - \sin(\theta_0 - \alpha)\big) \qquad (2.23)$$

Since $\Delta\theta = (\theta - \theta_0)$ is small, $cos\Delta\theta \approx 1$, this further reduces to:

$$\delta\phi = \frac{4\pi}{\lambda} B cos(\theta_0 - \alpha) sin\Delta\theta \qquad (2.24)$$

Since $\Delta\theta = (\theta - \theta_0)$ is small, $sin\Delta\theta \approx \Delta\theta$. Using $B_\perp = Bcos(\theta_0 - \alpha)$, Equation (2.24) can be given as:

$$\delta\phi = \frac{4\pi}{\lambda} \Delta\theta B_\perp \qquad (2.25)$$

Equation (2.24) is Equation (12) in (Zebker et al., 1994). The Earth curvature phase to be removed from the interferometric phase is thus estimated by the product of the look angle change and the perpendicular baseline.

### 2.2.2.3 Altitude ambiguity

From satellite geometry (Fig 2.5), the elevation of the target is:

$$z = h - \rho cos\theta \qquad (2.26)$$

Differentiating gives,

$$dz = \rho sin\theta d\theta \qquad (2.27)$$

Substituting $d\theta$ Equation (2.27) into Equation (2.25) at the limit $\Delta\theta = d\theta$, gives

$$dz = -\frac{\lambda}{4\pi} \frac{\rho sin\theta}{B_\perp} d\phi \qquad (2.28)$$

Equation (2.28) represents the sensitivity of the height to flattened phase without curved Earth effect. In practice, we use the altitude of ambiguity $h_a = \left| \frac{dz}{d\phi} . 2\pi \right|$ to describe this sensitivity. $h_a$ is the elevation change of one fringe on the interferogram, given by

$$h_a = \frac{\lambda}{2} \frac{\rho sin\theta}{B_\perp} \qquad (2.29)$$

Equation (2.28) shows that altitude ambiguity is dominated by $B_\perp$. The longer the perpendicular baseline, the more sensitive the phase is to topography. It can be seen from Equation (2.13) that in displacement cases:

$$d\rho = \frac{\lambda}{4\pi}d\phi \qquad\qquad\qquad (2.30)$$

Comparing Equation (2.28) with Equation (2.30), for the same amount of phase change, $d\phi$, the topography variation, $dz$, is $\frac{\rho sin\theta}{B_\perp}$ times of range change d$\rho$. Inversely, since $\frac{\rho sin\theta}{B_\perp} \gg 1$, the interferometric phase is much more sensitive to range change than to topography variation (Zebker et al., 1994). This explains why the accuracy of InSAR is higher in displacement mapping than topography mapping.

## 2.2.2 Orbit ramp

Because the spatial baseline of the interferogram is used to remove the topography phase during displacement mapping, inaccurate knowledge of the spatial baseline will result in poor determination of the interferometric phase from the reference ellipsoid and topography, leaving residual fringes in the interferogram (Fig. 2.7).
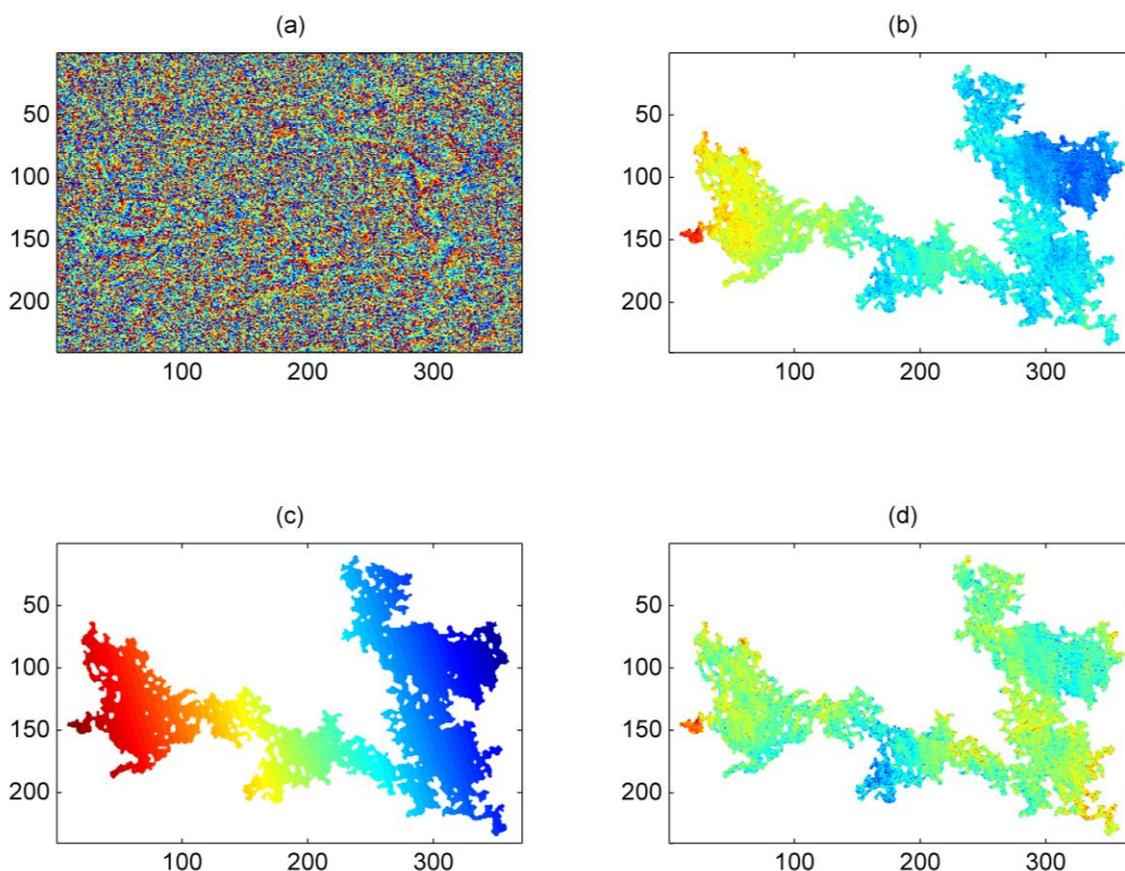


**Figure 2.7 An example of orbit ramp in Three Gorges area, China. (a) flattened interferogram; (b) unwrapped filtered interferogram; (c) phase ramp; (d) de-ramped & unwrapped interferogram. The scales are the number of pixels. White area suffers decorrelation, which is explained in Section 2.2.5.**

The most precise ERS orbits calculation have 5~8 cm error in radial and cross-track positioning (Scharroo and Visser, 1998), making orbital error unavoidable. The orbital error should be less than one fringe across a $100 \times 100\ km$ frame with 95% confidence, and can be well approximated by a linear phase ramp in range and azimuth (Hanssen, 2001, Kampes, 2006). Quadratic functions are better able to estimate the orbit error over 1000 km length scales (Pritchard et al., 2002, Fournier et al., 2011). *Biggs et al.* (2007) developed a network orbital correction method attempting to keep the long-wavelength displacement signal when removing orbital contribution. Their method may have combined ionospheric and long wavelength tropospheric signals with the orbit errors, because 1.5 fringes rather than 1 fringe are seen across a $100 \times 100\ km$ frame. Orbit error estimation in point-wise InSAR time series is introduced later in this chapter.

## 2.2.3 Atmospheric phase screen

When radar waves propagate through the layers of the atmosphere, phase changes compared to when the waves pass the same distance through a vacuum are inevitably generated. As the two SAR images are acquired at different times, atmospheric conditions are not identical for both, corresponding to different phase changes in time. Even for a single SAR image, the atmospheric state varies between pixels. Hence the propagation of the effects of atmospheric heterogeneity in time and space will result in a variable atmospheric phase screen (APS) across the interferogram. Phase distortion presumed to be generated in the ionosphere has been noticed over Mount Etna from interferograms of the same event (Massonnet et al., 1995). *Zebker et al.* (1997) suggested that temporal and spatial atmospheric water vapor variations induce greater atmospheric effects than other troposphere effects, particularly pressure and temperature, in terms of both absolute magnitude and variation in time and space. *Zebker et al.* (1997) estimated that 20% changes in relative humidity lead to 10 cm deformation errors. Hanssen (2001) observed that RMS (root mean square) of atmospheric effects reach from 2-16 mm in $40 \times 40\ km$ area with extreme changes of 120 mm delay in the case of thunderstorms during SAR acquisitions.

In the ionosphere, the free electrons interact with electromagnetic waves. *Hanssen* (2001) pointed out that an increase in the ionosphere's electron content results in a decrease of the observed range for a SAR image, or a phase advance, while an area with increased partial water vapour pressure will have an increased observed range, or a phase delay. The ionosphere phase advance is also related with the carrier frequency and the incidence angle

of radar waves. Subsequently, the phase advance or delay in a SAR image will cause APS in interferogram.

APS can be estimated using several methods including: numerical weather models such as MM5 (Foster et al., 2006, Wadge et al., 2002); GPS (Li et al., 2006a, Webley et al., 2002); spectrometer data (Li et al., 2006b); integration of spectrometer with GPS (Li et al., 2005); and, combination of spectrometer data with a weather model (Puysségur et al., 2007). Each of these methods has been successfully applied. In reality, the performance of weather models depends on the initial conditions, the choice of model physics and the model resolution (Foster et al., 2006). The poor temporal and spatial resolutions of global weather models may fail to provide reliable results (Fournier et al., 2011). A sufficiently dense GPS network is not often available. Coincident spectrometer observations associated with SAR images are only available for images from the Envisat satellite. Spectrometer data can only be collected during cloud free weather conditions and in day time.

## 2.2.4 Deformation phase

Since the radar wavelength is much smaller than a pixel, a single pixel in a radar image represents hundreds of elementary back scatterers within the pixel area (e.g. for typical ERS pixel size of 4 m along track and 20 m across, the ratios of the pixel size to the wavelength are 71 and 357 respectively). As a result, the phase value of a pixel is the ensemble contribution from all the elementary backscatters through the reflection coefficient function. For one SAR image, the phase value containing these multiple contributions of individual values is unknown. However, as shown in Equation (2.12), interferometry of two SAR images will eliminate these unknown contributions and isolate the phase contributions to its changes, only if the elementary targets contribute the same way to both images.

The phase changes measured are modulo $(-\pi, \pi)$, which corresponds to the range change being a fraction of one wavelength, leaving ambiguity of integer cycles. It is possible to unwrap the interferogram and resolve the ambiguity by numbering the fringes in succession only if the changes between neighboring pixels do not exceed one integer cycle.

Therefore, the feasibility of radar interferometry for displacement surveying applications depends on the displacement rates (Hanssen, 2001). The theoretical maximum detectable deformation gradient (DDG) is one fringe per pixel (i.e. half wavelength per pixel)

(Massonnet and Feigl, 1998). However, decorrelation and atmospheric effects can also blur the fringes, adding difficulty to continuous displacement mapping. Decorrelation can be partly circumvented by using a point-wise InSAR method (e.g. Small baseline InSAR technique). For Large scale deformation exceeding DDG, a speckle tracking (offset) technique can be used by co-registration of amplitude images.

## 2.2.5 Coherence and decorrelation

Coherence is the correlation between the two SAR images which are used to form the interferogram. It is a measurement for the quality of the interferogram. Low coherence is usually referred as decorrelation. How much deformation can be retrieved from the interferogram depends on how serious the decorrelation is. No coherence, there will be no useful information. Several factors can decrease the coherence. Changes in the scattering properties of the Earth surface, often caused by changes in vegetation or dielectric properties of soil, are referred to as temporal decorrelation effects (Zebker and Villasenor, 1992). The longer the time interval (also known as temporal baseline) between radar images, the greater the temporal decorrelation can be. Spatial decorrelation occurs due to different incidence angles of radar beams during radar scanning (Zebker and Villasenor, 1992). The longer the perpendicular baseline (i.e. satellite separation) between the radar images, the higher the likelihood of spatial decorrelation.
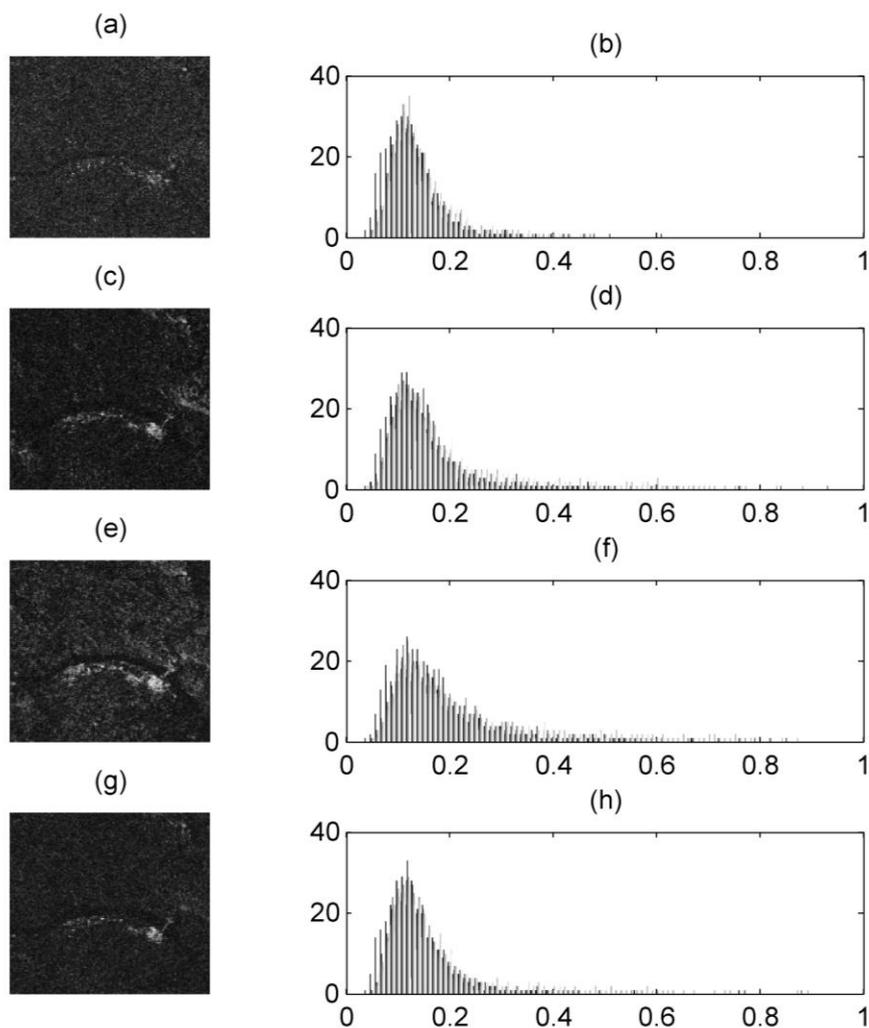
**Figure 2.8 (a) Coherence map of interferogram 20040523-20060423 from descending Track 075 of Envisat/ASAR in Badong in the Three Gorges area, and its corresponding histogram counts for each pixel with a step of 0.01 from 0 to 1. The two SAR acquisitions are 700 days apart. Perpendicular baseline ($B_\perp$) is 250.8 m; (b) Coherence of 20060423-20080323 (700 days, 43.7 m $B_\perp$) and its histogram counts; (c) Coherence of 20060319-20060423 (35 days, 121.7 m $B_\perp$) and its histogram counts; (d) Coherence of 20060423-20081019 (910 days, 73.7 m $B_\perp$) and its histogram counts. Interferograms (a) and (b) have identical temporal baseline but different perpendicular baseline lengths to show spatial decorrelation. Interferograms (c) and (d) have different temporal baselines but similar perpendicular baseline lengths to show temporal decorrelation.**

The complex coherence between two images is defined as:

$$\gamma_c = \frac{E\{S_1 \cdot S_2^*\}}{\sqrt{E\{S_1 \cdot S_1^*\} \cdot E\{S_2 \cdot S_2^*\}}} \qquad (2.31)$$

where:

$E\{.\}$ is the expectation; $*$ is the complex conjugate; $\gamma_c$ is the complex coherence; $S_1$ is the first radar signal; $S_2$ is the second radar signal.

In practice, the coherence is defined by $|\gamma_c|$ and its estimator is:

$$\hat{\gamma} = \left| \frac{\frac{1}{N}\sum_{i=1}^{N} E\{S_{1,i} \cdot S_{2,i}^*\}}{\sqrt{\frac{1}{N}\sum_{i=1}^{N} E\{S_{1,i} \cdot S_{1,i}^*\} \cdot \frac{1}{N}\sum_{i=1}^{N} E\{S_{2,i} \cdot S_{2,i}^*\}}} \right| \qquad (2.32)$$

Multilooking is performed in Equation (2.32) to reduce noise. If multi-looking is performed, a factor of 5, which is the aspect ratio of the pixel, is usually chosen to obtain square like pixels.

In Figure 2.8, the multi-looked mean coherences are 0.129 and 0.145 for 20040523-20060423 (Fig. 2.8a) and 20060423-20080323 (Fig. 2.8b). If the temporal decorrelations for the two interferograms are similar for the same time span of 700 days, the higher mean coherence for 20060423-20080323 (Fig. 2.8b) may due to a shorter spatial baseline of 43.7m than 250.8 m for 20040523-20060423. This is an example of how sensor geometries alter the coherence of interferograms. The coherence decreases when the perpendicular baseline increases.

For 20060319-20060423 (Fig. 2.8c) and 20060423-20081019 (Fig. 2.8d) with similar spatial baselines of 121.7 m and 73.7 m, their mean coherences are 0.168 and 0.135, respectively, which may be caused by different temporal baselines of 35 days and 910 days. The coherence decreases when the temporal baseline increases.

The point-wise InSAR technique to be introduced in Chapter 3 identifies stable (coherent) pixels in the interferograms, weeding out unstable (uncorrelated) pixels in time. If enough PS/SDFP pixels are kept, the identification of deformation can be easier without the interference from decorrelated pixels.

# Chapter 3 Time series InSAR algorithm

In this chapter, the time series point wise InSAR technique used in this thesis is shown through a case study in Badong County in the Three Gorges area of China because the water level changes in Three Gorges reservoir can be independent observations to validate InSAR time series in Badong. This validation exercise is also published as (Liu *et al.*, 2013), which is included in the thesis as Appendix C.

## 3.1 Point wise InSAR technique

Point wise InSAR technique differs from traditional InSAR by only using pixels that exhibit some phase stability over a time series of interferograms. Such pixels are described as persistent/permanent scatterers (PS) or SDFP (slowly decorrelating filtered phase) pixels. Radar echoes from SDFP pixels have Gaussian circular statistics and are independent from noise, remaining detectable over a long time period (Hooper, 2008).

Different approaches have been developed for identifying stable pixels in a series of interferograms. The amplitude dispersion index was proposed by (Ferretti et al., 2001) as a good proxy for phase standard deviation in high signal to noise ratio urban areas.

In addition, many point wise algorithms require not only that a PS pixel exhibits phase stability over time, but also that its phase history must be consistent with an assumed model of how displacement varies with time (Kampes, 2006, Colesanti et al., 2003).

In this study, the Stanford Method for Persistent Scatterers (StaMPS) method is employed (Hooper, 2008, Hooper et al., 2007). In contrast to most other PS methods, StaMPS uses phase spatial correlation to identify PS pixels instead of amplitude analysis (Ferretti et al., 2001, Colesanti and Wasowski, 2006, Kampes, 2006, Ketelaar, 2009). The advantage of this strategy is the capability to detect PS/SDFP pixels with low amplitude, which is often the case in natural terrains. The probability for a pixel to be PS/SDFP is estimated through phase analysis, which is successively refined in a series of iterations. Without any prior assumption about the temporal nature of ground deformation, StaMPS (Fig. 3.1) relies on the spatial correlation of deformation rather than any assumption of the temporal dependence of deformation. In StaMPS, the algorithms for PS and SDFP pixels are basically identical. However, different interferograms are used. Single master

interferograms are used for PS pixel selection, while multiple master interferograms with small baselines are used for SDFP pixels selection.
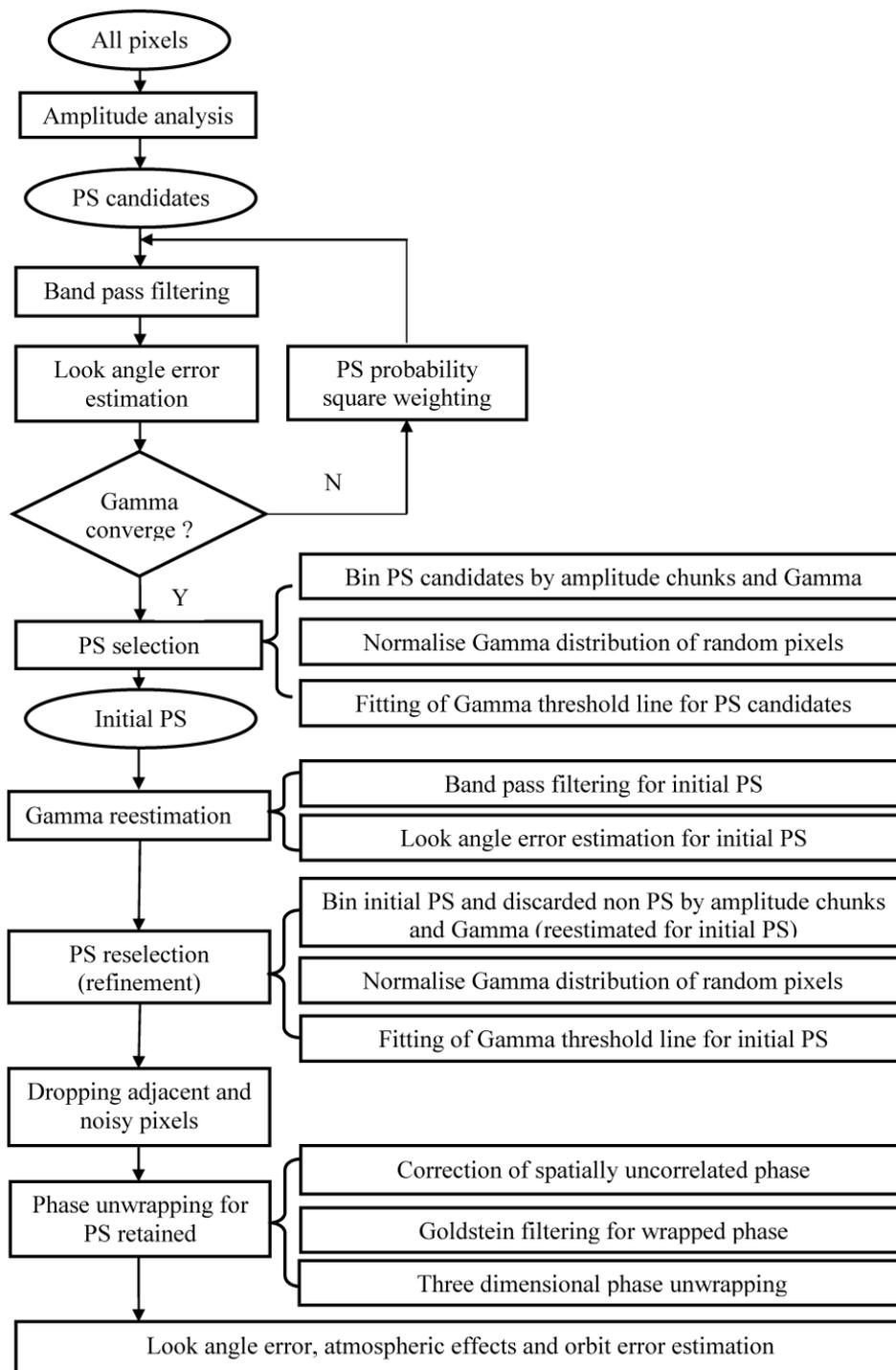


**Figure 3.1 Flow chart of PS processing in StaMPS (Hooper et al., 2007).**

## 3.2 Amplitude dispersion index

For SDFP pixels dominated by Gaussian scattering mechanisms, amplitude dispersion (Ferretti et al., 2001), $D_A$ , is used as a good indication of phase stability to reduce the

number of SDFP candidates (Hooper et al., 2007). Lower $D_A$ indicates higher phase stability.

$$D_A = \frac{\sigma}{\mu},$$ (3.1)

where $\sigma$ and $\mu$ is the standard deviation and mean value of a series of pixel amplitudes. The pixels selected as PS candidates have amplitude dispersion smaller than 0.4 (Hooper et al., 2007). They are refined using the spatial phase correlation (Hooper, 2008).

## 3.3 PS/SDFP pixels selection with phase analysis

The processes in this section are summarized from the Matlab codes of StaMPS (Hooper et al., 2007). The phase model for PS/SDFP candidates' refinement can be written as:

$$\psi = W\{\phi_D + \phi_A + \phi_O + \phi_\theta + \phi_N\}$$ (3.2)

The phase value of a single pixel after topography removal is the sum of contributions from deformation $\phi_D$, atmospheric effects $\phi_A$, orbit errors $\phi_O$, look angle error $\phi_\theta$ and random noises $\phi_N$ due to variability in scattering, thermal noise, and data processing errors such as co-registration errors. $W$ is the wrapping operator, as the interferometric phases we get are all modulo $2\pi$, which makes phase unwrapping compulsory after PS identification.

One phase character of PS/SDFP pixels is that the phase noise $\phi_N$ is small enough that it does not obscure the signal. In this case, $\phi_N$ is dominated by the first four terms $\phi_D$, $\phi_A$, $\phi_O$ and $\phi_\theta$. In StaMPS, $\phi_N$ is estimated by subtracting the four dominant terms $W\{\phi_D + \phi_A + \phi_O + \phi_\theta\}$ from the initial phase value $\psi$. The first estimation of $\phi_N$ is used to weight the contribution of each pixel to re-estimate $W\{\phi_D + \phi_A + \phi_O + \phi_\theta\}$ and to subtract the re-estimation of $W\{\phi_D + \phi_A + \phi_O + \phi_\theta\}$ to calculate a new estimation of $\phi_N$. In StaMPS, this loop is iterated until the values of $\phi_N$ converge (Hooper et al., 2007).

### 3.3.1 Phase spatial correlation with adjacent pixels

The estimation of $W\{\phi_D + \phi_A + \phi_O + \phi_\theta\}$ is implemented using their correlation with adjacent pixels. The spatially correlated phase $\tilde{\psi}$ for $W\{\phi_D + \phi_A + \phi_O + \phi_\theta + \phi_N\}$ is estimated through band pass filtering (Fig. 3.2).

$$G(u,v) = L(u,v) + \beta \left( \frac{H(u,v)}{\overline{H}(u,v)} - 1 \right)^{\alpha} \qquad\qquad (3.3)$$

$$H(u,v) = |Z(u,v)| \qquad\qquad (3.4)$$

Where $L(u,v)$ is a fifth-order Butterworth filter, with a typical cut-off wavelength of 800 m, $\alpha$ (typically 1) and $\beta$ (typically 0.3) are adjustable weighting parameters, and $Z(u,v)$ is the smoothed intensity of 2-D fast Fourier transform (FFT) (Goldstein and Werner, 1998).



**Figure 3.2 An example of spatial low pass band filtering of wrapped phase for phase correlation analysis in Badong using interferogram 23 April 2006 – 11 July 2010 in one loop of its phase analysis. (a) Wrapped phase of PS candidates corresponding to $\psi$ in Equation (3.5). (b) Weighted wrapped phase for filtering in one loop of phase analysis. (c) Filtered phase from combined low pass filtering in one loop of phase analysis corresponding to $\tilde{\psi}$ in Equation (3.5). (d) Residual phase after filtering in the first round of phase analysis corresponding to $\delta + \phi_{\theta}^{u} + \phi_{N}^{u}$ in Equation (3.5).**

Equation (3.2) can thus be rewritten after the estimation of the spatially correlated component as

$$\psi = W\{\tilde{\psi} + \delta + \phi_\theta^u + \phi_N^u\} \qquad (3.5)$$

where $\tilde{\psi}$ are the estimated spatially correlated components, and $\delta$ is the spatially uncorrelated part of $W\{\phi_D + \phi_A + \phi_O\}$. For the spatially correlated length set in phase analysis, $\delta$ is expected to be small (Hooper et al., 2007). $\phi_\theta^u$ is the spatially uncorrelated look angle error. $\phi_N^u$ is the spatially uncorrelated noise.

## 3.3.2 Look angle error

Spatially correlated look angle error (e.g. inaccurate DEM mapping) can be estimated by band pass filtering of surrounding pixels, and spatially uncorrelated look angle error $\phi_\theta^u$ due to phase centre deviation can be estimated through its correlation with the perpendicular baseline. Specifically, the spatially uncorrelated look angle error is caused by the difference between the assumed geometric centre and the actual phase centre for a pixel (Hooper et al., 2007). Look angle error, $\Delta\theta$, can be given in terms of horizontal and vertical components of the distance between geometric and phase centres:

$$\Delta\theta = \frac{\Delta h \sin(\theta_{inc}) + \Delta\xi \cos(\theta_{inc})}{\rho} \qquad (3.6),$$

where $\Delta h$ is the vertical component of the distance between the geometric and phase centres, $\Delta\xi$ is the horizontal component of the distance, $\theta_{inc}$ is the radar incidence angle at the Earth surface and $\rho$ is the distance between the satellite and the pixel. Even if the DEM is 100% accurate, as long as the two centres do not overlap, the offsets $\Delta h$ and $\Delta\xi$ will be non-zero and project a tangential component (with respect to the direction of radar beam). As $\rho$ is much greater than pixel size (800 km >> 100 m), the straight tangential component of the distance between the geometric and phase centers is approximated as an arc segment of $\rho$, which corresponds to a radian angle difference $\Delta\theta$ in the radar looking direction. Unlike deformation and other spatially correlated phase components that show similarities among neighboring pixels, $\Delta\theta$ is limited to the spatial extent of the pixel itself and is thus referred to as the spatially uncorrelated look angle error. Because the look angle error is spatially uncorrelated, it can be estimated after the spatial low pass band filtering.

The reference phase due to curved earth effect also results in a look angle change (Fig. 2.5 in Section 2.2.1 of Chapter 2). Hence the look error can be estimated in a similar way as Equation (2.25) in Section 2.2.2.2 of Chapter 2 for earth flattening:

$$\widehat{\phi_\theta^u} = \frac{4\pi}{\lambda} B_\perp \widehat{\Delta\theta}, \qquad\qquad (3.7),$$

where $\phi_\theta^u$ is the interferometric phase error related with the perpendicular baseline $B_\perp$ and the spatially uncorrelated look angle error $\Delta\theta$. Because of satellite orbit control and large $\rho$ between the satellite and the pixel, the look angle error $\Delta\theta$ is stable for the pixel through all satellite acquisitions of the same track. However the perpendicular spatial baselines $B_\perp$ between image acquisitions are variable from hundreds to over a thousand meters within the critical baseline scope, which makes the phase error $\phi_\theta^u$ also variable through interferograms. It may appear that $\Delta\theta$ can be easily estimated by least squares using its redundant values in different interferograms. However, in reality the residual interferometric phase after low pass band filtering includes not only the phase due to spatially uncorrelated look angle error, but also phases due to inaccurate estimation of the spatially correlated part and spatially uncorrelated phase noise $\phi_N^u$. Since phase noise level is an important criterion for the selection of PS/SDFP pixels, $\phi_N^u$ is also what needs to be addressed through phase analysis. Hence the spatially uncorrelated look angle error is estimated together with the phase noise using least squares inversion, which is described as parameter space search by Hooper et al. (2007). This estimation is a nonlinear process because the phase is still wrapped. The derivations below are from the Matlab codes of StaMPS (Hooper et al., 2007).

The parameter search is implemented by trials of $\phi_\theta^u$ within the limitation equivalent to a typical DEM error of 10 m (Farr, 2007) and in increments of $\pi/4$, in order to see which $\phi_\theta^u$ achieves the maximum gamma statistics for the pixel. Gamma is a measure of phase noise level and serves as an indicator if a pixel belongs to PS.

The relationship between height change and phase change is given in Equation (2.28) in Section 2.2.2.3 of Chapter 2, so the trial limitation for $\phi_\theta^u$ equivalent to 10 m height error can be written as:

$$\phi_{\theta,lim}^u = H_{error,max} \frac{4\pi}{\lambda} \frac{B_{\perp,range}}{\rho sin\theta} \qquad (H_{error,max} = 10 \text{ m}) \qquad\qquad (3.8)$$

where $\phi_{\theta,lim}^{u}$ is the search limitation of $\phi_{\theta}^{u}$, $H_{error,max}$ is the maximum height error of 10 m and $B_{\perp,range}$ is the perpendicular spatial baseline range for all interferograms. In other words, $B_{\perp,range}$ is the maximum perpendicular spatial baseline that can be formed with any available combination of SAR images. In the PS case study of Badong, a total number of 29 interferograms were formed with a common master image using 30 SAR images. Of the 29 interferograms, the maximum positive spatial perpendicular baseline with the master image is 249.7 m, and maximum negative spatial perpendicular baseline is -645.7 m. Hence the perpendicular baseline range $B_{\perp,range}$ is 895.4 m for the dataset.

**Table 3.1. Trial phase by spatially uncorrelated look angle error. The search is over $N$ interferograms and in $(2S+1)$ separate trials for each PS candidate. Each row of the table represents the same interferogram with trials increments of $\pi/4$ multiplied by factors from $-S$ to $S$. Each column of the table represents different interferograms with the same trial increment. The phase error due to spatially uncorrelated look angle error is proportional to the length of perpendicular baseline for one PS candidate. That is why the parameter search is scaled by the factor $B_{\perp,i}/B_{\perp,range}$ in each cell.**

| $\frac{B_{\perp,1}}{B_{\perp,range}}\frac{\pi}{4}(-S)$ | $\frac{B_{\perp,1}}{B_{\perp,range}}\frac{\pi}{4}(-S+1)$ | $\cdots$ | $\frac{B_{\perp,1}}{B_{\perp,range}}\frac{\pi}{4}j$ | $\cdots$ | $\frac{B_{\perp,1}}{B_{\perp,range}}\frac{\pi}{4}(S-1)$ | $\frac{B_{\perp,1}}{B_{\perp,range}}\frac{\pi}{4}S$ |
|---|---|---|---|---|---|---|
| $\frac{B_{\perp,2}}{B_{\perp,range}}\frac{\pi}{4}(-S)$ | $\frac{B_{\perp,2}}{B_{\perp,range}}\frac{\pi}{4}(-S+1)$ | $\cdots$ | $\frac{B_{\perp,2}}{B_{\perp,range}}\frac{\pi}{4}j$ | $\cdots$ | $\frac{B_{\perp,2}}{B_{\perp,range}}\frac{\pi}{4}(S-1)$ | $\frac{B_{\perp,2}}{B_{\perp,range}}\frac{\pi}{4}S$ |
| $\cdots$ | $\cdots$ | $\cdots$ | $\cdots$ | $\cdots$ | $\cdots$ | $\cdots$ |
| $\frac{B_{\perp,i}}{B_{\perp,range}}\frac{\pi}{4}(-S)$ | $\frac{B_{\perp,i}}{B_{\perp,range}}\frac{\pi}{4}(-S+1)$ | $\cdots$ | $\frac{B_{\perp,i}}{B_{\perp,range}}\frac{\pi}{4}j$ | $\cdots$ | $\frac{B_{\perp,i}}{B_{\perp,range}}\frac{\pi}{4}(S-1)$ | $\frac{B_{\perp,i}}{B_{\perp,range}}\frac{\pi}{4}S$ |
| $\cdots$ | $\cdots$ | $\cdots$ | $\cdots$ | $\cdots$ | $\cdots$ | $\cdots$ |
| $\frac{B_{\perp,N-1}}{B_{\perp,range}}\frac{\pi}{4}(-S)$ | $\frac{B_{\perp,N-1}}{B_{\perp,range}}\frac{\pi}{4}(-S+1)$ | $\cdots$ | $\frac{B_{\perp,N-1}}{B_{\perp,range}}\frac{\pi}{4}j$ | $\cdots$ | $\frac{B_{\perp,N-1}}{B_{\perp,range}}\frac{\pi}{4}(S-1)$ | $\frac{B_{\perp,N-1}}{B_{\perp,range}}\frac{\pi}{4}S$ |
| $\frac{B_{\perp,N}}{B_{\perp,range}}\frac{\pi}{4}(-S)$ | $\frac{B_{\perp,N}}{B_{\perp,range}}\frac{\pi}{4}(-S+1)$ | $\cdots$ | $\frac{B_{\perp,N}}{B_{\perp,range}}\frac{\pi}{4}j$ | $\cdots$ | $\frac{B_{\perp,N}}{B_{\perp,range}}\frac{\pi}{4}(S-1)$ | $\frac{B_{\perp,N}}{B_{\perp,range}}\frac{\pi}{4}S$ |

For a single pixel of the $i_{th}$ interferogram, the trial phase can be given as a matrix (Table 3.1). Because the parameter search is limited to $\phi_{\theta,lim}^{u}$ (Equation 3.8), the trial phase should satisfy:

$$\left|\widehat{\phi_{\theta,i,trial}^{u}}\right| = \left|\frac{B_{\perp,i}}{B_{\perp,range}}\frac{\pi}{4}j\right| \leq \phi_{\theta,lim}^{u} \qquad i \in (1,2,\cdots,m). \qquad (3.9)$$

Since any perpendicular baseline $B_{\perp,i}$ is in the range of $B_{\perp,range}$

$$\left|\frac{B_{\perp,i}}{B_{\perp,range}}\right| \leq 1 \qquad (3.10)$$

and any trial increments of $\pi/4$ are in the range of the maximum increment

$$\left| \frac{\pi}{4} j \right| \leq \frac{\pi}{4} S \tag{3.11}$$

Equation (3.9) can be assured by

$$\frac{\pi}{4} S \leq \phi_{\theta,lim}^u \tag{3.12}$$

that is

$$S \leq 8 \frac{\phi_{\theta,lim}^u}{2\pi}, \tag{3.13}$$

So $S$ is related with $\phi_{\theta,lim}^u$ and further related with $B_{\perp,range}$. If the Perpendicular baseline range for the dataset is relatively longer, $S$ is likely to be larger, making parameter search in a greater space. This also applies to the maximum height error $H_{error,max}$. Alternatively the increment of $\pi/4$ can be reduced to make denser parameter search. Take the PS case in Badong for example, the factor $\phi_{\theta,lim}^u/2\pi$ in Equation (3.13) is 0.4523, so $S$ is nearly 4 for Badong dataset and the parameter space is

$$\widehat{\phi_{\theta,i,trial}^u} = \frac{B_{\perp,i}}{B_{\perp,range}} \frac{\pi}{4} j \quad (j \in \{-4,-3,-2,-1,0,1,2,3,4\}) \tag{3.14}.$$

**Table. 3.2. Trial phase by spatially uncorrelated look angle error in Badong. Each cell is the intersection of a trial increment on the top and its scaling Perpendicular baseline to the left.**

| Trial phase (radian) | | $-\pi$ | $-\frac{3}{4}\pi$ | $-\frac{1}{2}\pi$ | $-\frac{1}{4}\pi$ | $0$ | $\frac{1}{4}\pi$ | $\frac{1}{2}\pi$ | $\frac{3}{4}\pi$ | $\pi$ |
|---|---|---|---|---|---|---|---|---|---|---|
| $B_{\perp,i}$ | 100.3 | -0.3520 | -0.2640 | -0.1760 | -0.0880 | 0.0000 | 0.0880 | 0.1760 | 0.2640 | 0.3520 |
| (meter) | -29.2 | 0.1024 | 0.0768 | 0.0512 | 0.0256 | 0.0000 | -0.0256 | -0.0512 | -0.0768 | -0.1024 |
| | -108.5 | 0.3810 | 0.2857 | 0.1905 | 0.0952 | 0.0000 | -0.0952 | -0.1905 | -0.2857 | -0.3810 |
| | 171.5 | -0.6020 | -0.4515 | -0.3010 | -0.1505 | 0.0000 | 0.1505 | 0.3010 | 0.4515 | 0.6020 |
| | 249.6 | -0.8760 | -0.6570 | -0.4380 | -0.2190 | 0.0000 | 0.2190 | 0.4380 | 0.6570 | 0.8760 |
| | 64.1 | -0.2252 | -0.1689 | -0.1126 | -0.0563 | 0.0000 | 0.0563 | 0.1126 | 0.1689 | 0.2252 |
| | -327.6 | 1.1494 | 0.8620 | 0.5747 | 0.2873 | 0.0000 | -0.2873 | -0.5747 | -0.8620 | -1.1494 |
| | -239.9 | 0.8417 | 0.6313 | 0.4208 | 0.2104 | 0.0000 | -0.2104 | -0.4208 | -0.6313 | -0.8417 |
| | -645.7 | 2.2656 | 1.6992 | 1.1328 | 0.5664 | 0.0000 | -0.5664 | -1.1328 | -1.6992 | -2.2656 |
| | 141.8 | -0.4978 | -0.3733 | -0.2489 | -0.1244 | 0.0000 | 0.1244 | 0.2489 | 0.3733 | 0.4978 |
| | 121.2 | -0.4253 | -0.3190 | -0.2127 | -0.1063 | 0.0000 | 0.1063 | 0.2127 | 0.3190 | 0.4253 |
| | 196.4 | -0.6894 | -0.5170 | -0.3447 | -0.1723 | 0.0000 | 0.1723 | 0.3447 | 0.5170 | 0.6894 |
| | 165.0 | -0.5789 | -0.4342 | -0.2895 | -0.1447 | 0.0000 | 0.1447 | 0.2895 | 0.4342 | 0.5789 |
| | -340.9 | 1.1960 | 0.8970 | 0.5980 | 0.2990 | 0.0000 | -0.2990 | -0.5980 | -0.8970 | -1.1960 |
| | -306.1 | 1.0742 | 0.8056 | 0.5371 | 0.2685 | 0.0000 | -0.2685 | -0.5371 | -0.8056 | -1.0742 |
| | -173.8 | 0.6098 | 0.4573 | 0.3049 | 0.1524 | 0.0000 | -0.1524 | -0.3049 | -0.4573 | -0.6098 |
| | -193.3 | 0.6782 | 0.5087 | 0.3391 | 0.1696 | 0.0000 | -0.1696 | -0.3391 | -0.5087 | -0.6782 |
| | -61.4 | 0.2157 | 0.1618 | 0.1079 | 0.0539 | 0.0000 | -0.0539 | -0.1079 | -0.1618 | -0.2157 |
| | 43.9 | -0.1542 | -0.1156 | -0.0771 | -0.0385 | 0.0000 | 0.0385 | 0.0771 | 0.1156 | 0.1542 |
| | -317.1 | 1.1128 | 0.8346 | 0.5564 | 0.2782 | 0.0000 | -0.2782 | -0.5564 | -0.8346 | -1.1128 |
| | -170.2 | 0.5974 | 0.4481 | 0.2987 | 0.1494 | 0.0000 | -0.1494 | -0.2987 | -0.4481 | -0.5974 |
| | 72.0 | -0.2529 | -0.1897 | -0.1265 | -0.0632 | 0.0000 | 0.0632 | 0.1265 | 0.1897 | 0.2529 |
| | 73.8 | -0.2591 | -0.1943 | -0.1295 | -0.0648 | 0.0000 | 0.0648 | 0.1295 | 0.1943 | 0.2591 |
| | -368.0 | 1.2914 | 0.9686 | 0.6457 | 0.3229 | 0.0000 | -0.3229 | -0.6457 | -0.9686 | -1.2914 |
| | -408.0 | 1.4317 | 1.0738 | 0.7159 | 0.3579 | 0.0000 | -0.3579 | -0.7159 | -1.0738 | -1.4317 |
| | 163.5 | -0.5737 | -0.4303 | -0.2869 | -0.1434 | 0.0000 | 0.1434 | 0.2869 | 0.4303 | 0.5737 |
| | -152.8 | 0.5362 | 0.4022 | 0.2681 | 0.1341 | 0.0000 | -0.1341 | -0.2681 | -0.4022 | -0.5362 |
| | 65.6 | -0.2304 | -0.1728 | -0.1152 | -0.0576 | 0.0000 | 0.0576 | 0.1152 | 0.1728 | 0.2304 |
| | -233.1 | 0.8182 | 0.6136 | 0.4091 | 0.2045 | 0.0000 | -0.2045 | -0.4091 | -0.6136 | -0.8182 |

The trial phases for all the PS candidates in Badong are given in Table 3.2. For each trial (a column in Table 3.2), the trial phases are subtracted from the phase after low pass band filtering in each corresponding interferogram

$$\psi_{Residual,i} = \psi_i - \tilde{\psi}_i - \widehat{\phi^u_{\theta,i,trial}}$$
(3.15)

In each trial, after removal of trail phase, the residual phases $\psi_{Residual,i}$ are then added up to obtain a gamma value. The trial that returns the maximum gamma is identified. The residual phase is converted to a complex number in exponential form for Gamma statistics as

$$\gamma = \frac{\left|\sum_{i=1}^{N} e^{\sqrt{-1}\psi_{Residual,i}}\right|}{\sum_{i=1}^{N}\left|e^{\sqrt{-1}\psi_{Residual,i}}\right|}$$
(3.16)

The residual phase includes inaccurate estimation of spatially correlated terms, inaccurate estimation of $\phi^u_\theta$ and phase noise. The noise level of PS/SDFP pixels within all the candidates are relatively lower, and all $N$ residual phases are less affected by phase noise.

Hence the inner consistency of residual phases for PS/SDFP pixels is better than other pixels, which is reflected through relatively higher gamma value. Figure 3.3a shows the gamma statistics of all 9 trials for one of the PS candidates in Badong. It can be seen from Equation (3.14) that:

$$\frac{\widehat{\phi_{\theta,i,trial}^{u}}}{B_{\perp,i}} = \frac{1}{B_{\perp,range}} \frac{\pi}{4} j \qquad (3.17)$$

Inside each trial column, the ratios (Equation 3.17) of trial phase errors to their corresponding perpendicular baselines are constant because the baseline range and trial increments are the same. In other words, the phase error due to spatially uncorrelated look angle error for the same pixel in different interferograms will only depend on perpendicular baselines for those interferograms. The same conclusion can be derived from Equation (3.7) where the ratio between phase error and baseline is a constant $K$ ($K = \frac{4\pi}{\lambda} \Delta\theta$). For the trial column with the maximum gamma value, the ratio is:

$$K_{\max\_\gamma} = \frac{1}{B_{\perp,range}} \frac{\pi}{4} j_{\max\_\gamma} \qquad (3.18)$$

The trial column of which the residual phases show the maximum gamma is very likely the one closest to the real phase error. However, the trial phase that showing the maximum gamma value is still not accurate enough. It is further improved in the parameter search. Substituting Equations (3.17) and (3.18) into Equation (3.15), residual phase in the maximum gamma trail can be given in terms of $K_{\max\_\gamma}$:

$$\psi_{Residual,i} = \psi_i - \tilde{\psi}_i - K_{\max\_\gamma} B_{\perp,i} \qquad (3.19)$$

An offset is estimated from the sum of all residual phases and subtracted from the residual phases themselves.

$$e^{\sqrt{-1}\psi'_{Residual,i}} = e^{\sqrt{-1}\psi_{Residual,i}} \cdot \left(\sum_{i=1}^{N} e^{\sqrt{-1}\psi_{Residual,i}}\right)^* \qquad (3.20)$$

where $*$ denotes complex conjugate.

An adjustment for $K_{\max\_\gamma}$ is derived using a least squares inversion of adjusted residual phase.

$$K' = K_{\max\_\gamma} + B_{\perp,i} \backslash \psi'_{Residual,i} \qquad\qquad (3.21)$$

where "\" denotes the least squares inversion.

$K'$ (Fig. 3.3b) is thereafter used to calculate new estimations of phase error by spatially uncorrelated look angle error, residual phases and gamma.

$$\psi''_{Residual,i} = \psi_i - \tilde{\psi}_i - K'B_{\perp,i} \qquad\qquad (3.22)$$

$$\gamma' = \frac{\left| \Sigma_{i=1}^{N} e^{\sqrt{-1}\psi''_{Residual,i}} \right|}{\Sigma_{i=1}^{N} \left| e^{\sqrt{-1}\psi''_{Residual,i}} \right|} \qquad\qquad (3.23)$$

Until now, the parameter search for $\phi_\theta^u$ and $\gamma$ is finished in loop 1 of the iteration. The interferometric phase is then weighted, filtered and searched again in loop 2 of the iteration.
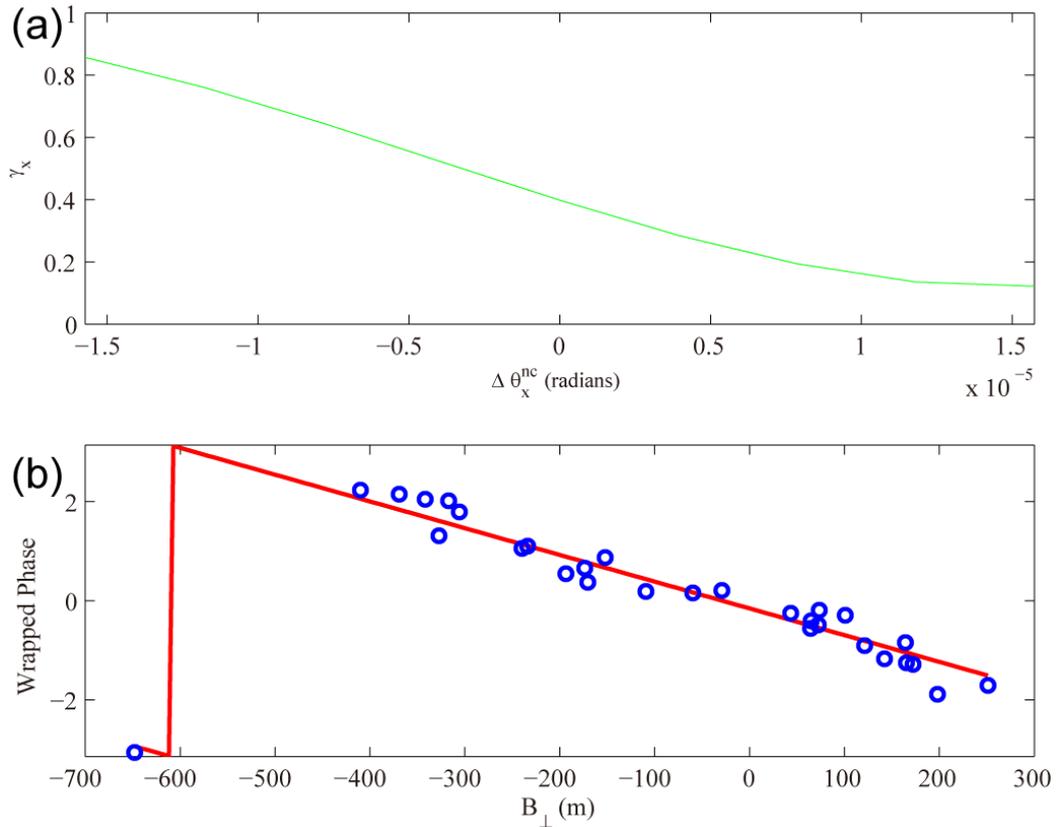


**Figure 3.3. An example parameter space search for look angle error for a PS pixel in Badong. (a) Trial values of look angle error and corresponding gamma value. Horizontal axis is look angle error calculated by** $\Delta\theta = \frac{\phi_\theta^u}{B_\perp}\frac{\lambda}{4\pi} = \frac{\pi/4}{B_{\perp,range}}j\frac{\lambda}{4\pi}$ **(b) A comparison between the residual phase value after low-pass band filtering (blue circles) and phase values predicted by the value of** $K'$ **with maximum** $\gamma$ **(red line).**

The method for interferometric phase weighting is the PS probability square after $\gamma$ is estimated for all the candidates in each loop, as there is a correlation between $\gamma$ and the probability that it is a PS/SDFP. The $\gamma$ values are binned and normalized to get a probability density. The derivations below are from the Matlab codes of StaMPS (Hooper et al., 2007). All PS candidates can be divided into two sets: PS pixels and non-PS pixels, denoted by A and B respectively hereafter. The PS set is $A_i$ and the non-PS set is $B_i$ in the $i_{th}$ $\gamma$ bin of the candidates. The probability density of candidates in this bin can be given in terms of the PS set A and non-PS set B:

$$\frac{A_i+B_i}{A+B} = \left(\frac{A}{A+B}\right)\frac{A_i}{A} + \left(1 - \frac{A}{A+B}\right)\frac{B_i}{B} \tag{3.24}$$

where

$$P(\gamma) = \frac{A_i+B_i}{A+B} \tag{3.25}$$

$P(\gamma)$ is the probability of candidates in the $i_{th}$ bin.

$$\alpha = \frac{A}{A+B} \tag{3.26}$$

$\alpha$ is the PS proportion of all candidates and $0 < \alpha < 1$.

$$P_A(\gamma) = \frac{A_i}{A} \tag{3.27}$$

$P_A(\gamma)$ is the probability of PS pixels in the $i_{th}$ bin.

$$P_B(\gamma) = \frac{B_i}{B} \tag{3.28}$$

$P_B(\gamma)$ is the probability of non-PS pixels in the $i_{th}$ bin.

Using Equations (3.25)-(3.28), Equation (3.24) can be given in the form of probability density when $\gamma$ bins are infinitely small

$$P(\gamma) = \alpha P_A(\gamma) + (1 - \alpha)P_B(\gamma). \tag{3.29}$$

This is the form given in (Hooper et al., 2007). Equation (3.29) includes the distributions of the PS candidates, PS only and non-PS only. $P_A(\gamma)$ is the probability density of PS. $P(\gamma)$ is the probability density of PS candidates based on statistics of gamma after the loop. The probability for non-PS are simulated using the random phase between $[-\pi, \pi]$, considering that the residual phase value after low pass band filtering is random.

$$W\{\psi - \tilde{\psi}\} = e^{\sqrt{-1}\,\psi_{Rand,i}} \tag{3.30}$$

The random phase is also searched for $\phi_\theta^u$ and $\phi_N^u$ following the steps above to get the probability distribution of non-PS $P_B(\gamma)$. $P_B(\gamma)$ is then normalized by assuming that low $\gamma$ between 0 and $\gamma_{low\_threshold}$ (e.g. 0.3) contain no PS pixels.

$$P_A\big(0 \leq \gamma \leq \gamma_{low\_threshold}\big) \approx 0 \tag{3.31}$$

Substituting (3.31) into (3.29) and integrating leads to:

$$\int_0^{\gamma_{low\_threshold}} P(\gamma) = (1-\alpha) \int_0^{\gamma_{low\_threshold}} P_B(\gamma) \tag{3.32}$$

The normalized distribution of non-PS is:

$$P_B'(\gamma) = P_B(\gamma) \frac{\int_0^{\gamma_{low\,threshold}} P(\gamma)}{\int_0^{\gamma_{low\,threshold}} P_B(\gamma)} = (1-\alpha) P_B(\gamma) \tag{3.33}$$

Therefore, the probability to be a PS/SDFP is:

$$P(x \in A) = \frac{A_i}{A_i + B_i} = 1 - \frac{B_i}{A_i + B_i} = 1 - \frac{\left(\frac{B}{A+B}\right) \frac{B_i}{B}}{\frac{A_i + B_i}{A+B}} = 1 - \frac{(1-\alpha) P_B(\gamma)}{P(\gamma)} = 1 - \frac{P_B'(\gamma)}{P(\gamma)} \tag{3.34}$$

Hence the PS probability square weighting is:

$$W = P^2(x \in A) = \big(1 - P(x \in B)\big)^2 = \left(1 - \frac{(1-\alpha) P_B(\gamma)}{P(\gamma)}\right)^2 \tag{3.35}$$
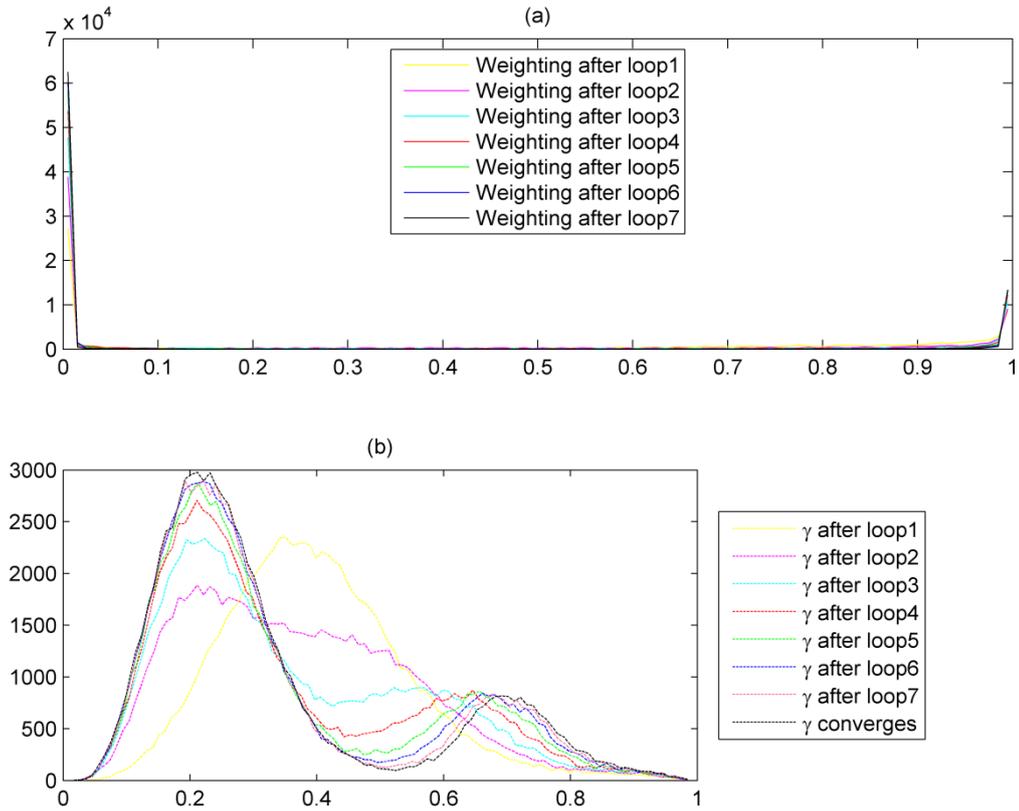
**Figure 3.4 (a) The weighting distribution for all 80752 PS candidates after each loop of this iteration. The weightings are calculated after this loop for the candidates themselves in the next loop. (b) The distribution of $\gamma$ for all PS candidates after each loop of this iteration until $\gamma$ converges. There are 100 bins for both distributions with bin width equally set at 0.01.**

The weighting (Fig. 3.4a) is set for the PS candidates in the next loop of this iteration before filtering, to obtain a new round of the gamma distribution until gamma converges (Fig. 3.4b).

## 3.3.3 Phase noise estimation

According to Euler's formula ($e^{\sqrt{-1}x} = cosx + \sqrt{-1} \cdot sinx$), the denominator of $\gamma$ can be given as:

$$\sum_{i=1}^{N}\left|e^{\sqrt{-1}\psi_{Residual,i}}\right| = \sum_{i=1}^{N}\left|cos\left(\psi_{Residual,i}\right) + \sqrt{-1}\sin\left(\psi_{Residual,i}\right)\right| =$$

$$\sum_{i=1}^{N}\sqrt{cos^2\left(\psi_{Residual,i}\right) + sin^2\left(\psi_{Residual,i}\right)} = \sum_{i=1}^{N}1 = N \tag{3.36}$$

Such that,

$$\gamma = \frac{\left|\sum_{i=1}^{N}e^{\sqrt{-1}\psi_{Residual,i}}\right|}{\sum_{i=1}^{N}\left|e^{\sqrt{-1}\psi_{Residual,i}}\right|} = \frac{1}{N}\left|\sum_{i=1}^{N}e^{\sqrt{-1}\psi_{Residual,i}}\right| \tag{3.37}$$

This is the form of $\gamma$ given in (Hooper et al., 2007).

For a PS/SDFP candidate in one interferogram, subtracting the estimation for spatially correlated parts $\tilde{\psi}$ and the estimation of spatially uncorrelated look angle error $\widehat{\phi_{\theta}^{u}}$ from the wrapped phase will result in:

$$W\{\psi - \tilde{\psi} - \widehat{\phi_{\theta}^{u}}\} = W\{\delta' + \phi_{N}^{u}\}, \qquad\qquad (3.38)$$

where

$$\delta' = \delta + \phi_{\theta}^{u} - \widehat{\phi_{\theta}^{u}}, \qquad\qquad (3.39)$$

where $\delta$ is the spatially uncorrelated part of $W\{\phi_D + \phi_A + \phi_O\}$ as mentioned above, and $\phi_{\theta}^{u} - \widehat{\phi_{\theta}^{u}}$ is the inaccurate estimation for $\phi_{\theta}^{u}$.

For one interferogram, coherence is a good proxy for phase stability, while for a series of interferograms, $\gamma$ represents the phase stability in time (Fig. 3.5). The accuracy of $\gamma$ also depends on the estimation of spatially correlated phase $\tilde{\psi}$. If the surrounding phases of a PS/SDFP candidate are uncorrelated, its spatially correlated phase $\tilde{\psi}$ from band pass filtering will be random. The resulting $\gamma$ will not be a true representation of phase noise, and the pixel will be discarded from PS candidates (Hooper et al., 2007).
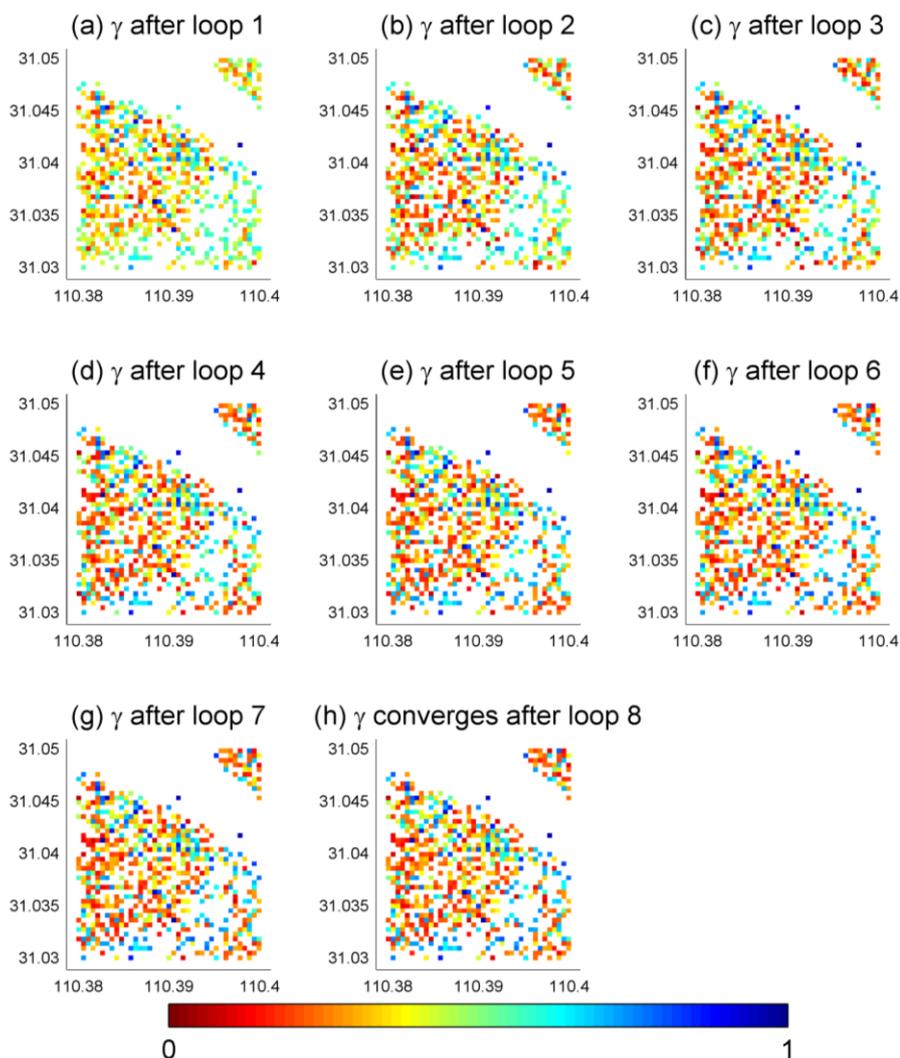
**Figure 3.5 The values of $\gamma$ from loops 1-9 in iteration for an area of $0.02° \times 0.02°$ in Badong.**

## 3.2 PS selection

The processes in this section are summarized from the Matlab codes of StaMPS (Hooper et al., 2007). After each new loop, the new $\gamma$ is compared with its old value after last loop to see the changes of $\gamma$. The RMS of the changes for all $\gamma$ is calculated. If the RMS is bigger than the RMS threshold e.g. 0.005, $\gamma$ has not converged and the interferometric phase are weighted (Equation 3.35) for next loop. If the RMS is smaller than the RMS threshold, the solution should have converged and the iteration stops. The selection of PS pixels is based on the converged probability distribution of $\gamma$ (Hooper et al., 2007). The correlation between $\gamma$ and the probability of a pixel to be PS is already introduced when PS probability square were used for weighting. The selection strategy for PS selection is finding the selection threshold of $\gamma$ for each PS candidate. If the converged $\gamma$ is greater than the selection threshold, the candidate will be initially selected as a PS pixel; otherwise it will be a non-PS pixel.

## 3.2.1 Initial selection using gamma bins and amplitude dispersion chunks

Since amplitude dispersion $D_A$ is a good proxy for phase stability, it is used together with $\gamma$ to calculate the selection thresholds for the candidates. The pixels are firstly binned by $D_A$. Secondly for each $D_A$ chunk, the candidates are binned by $\gamma$ following the steps above for probability square weighting. In each $D_A$ chunk, the proportion of PS, $\alpha_{D_A}$, is also estimated similarly to Equation (3.32).

$$\int_0^{\gamma_{low\_threshold}} P(\gamma) = (1 - \alpha_{D_A}) \int_0^{\gamma_{low\_threshold}} P_B(\gamma) \tag{3.40}$$

The normalized distribution of non-PS for this $D_A$ chunk is like Equation (3.33):

$$P(x \in B) = \frac{P_B'(\gamma)}{P(\gamma)} = \frac{(1 - \alpha_{D_A}) P_B(\gamma)}{P(\gamma)} . \tag{3.41}$$

The maximum fraction of non-PS is:

$$\frac{(1 - \alpha_{D_A}) \int_{\gamma^{low\_thresh}}^1 P_B(\gamma) d\gamma}{\int_{\gamma^{low\_thresh}}^1 P(\gamma) d\gamma} = q , \tag{3.42}$$

which is the form given in (Hooper et al., 2007). The acceptable non-PS fraction $q$ depends on the particular requirements of the application. (Hooper et al., 2007) suggested that when amplitude dispersion $D_A$ increases, $P(\gamma)$ will skew to lower values of $\gamma$, and $\gamma^{low\_thresh}$ will then increase for the same value of $q$ (Fig. 3.6). Hooper et al. [2007] also suggested that the relationship is approximately linear empirically. With a series of $D_A$ chunks and their corresponding $\gamma^{low\_thresh}$, a least square inversion is employed to fit the slope $\kappa$ and select those with $\gamma > \kappa \alpha_{D_A}$ as initial PS pixels. In practice, setting the maximum non-PS pixel density is an alternative way to find $\gamma^{low\_thresh}$ of each $D_A$ chunk by setting the non-PS fraction $q$. The maximum non-PS pixel density approach is to find the lowest $\gamma$ above which the absolute number of non-PS pixels is just below the theoretical maximum non-PS number in this chunk.
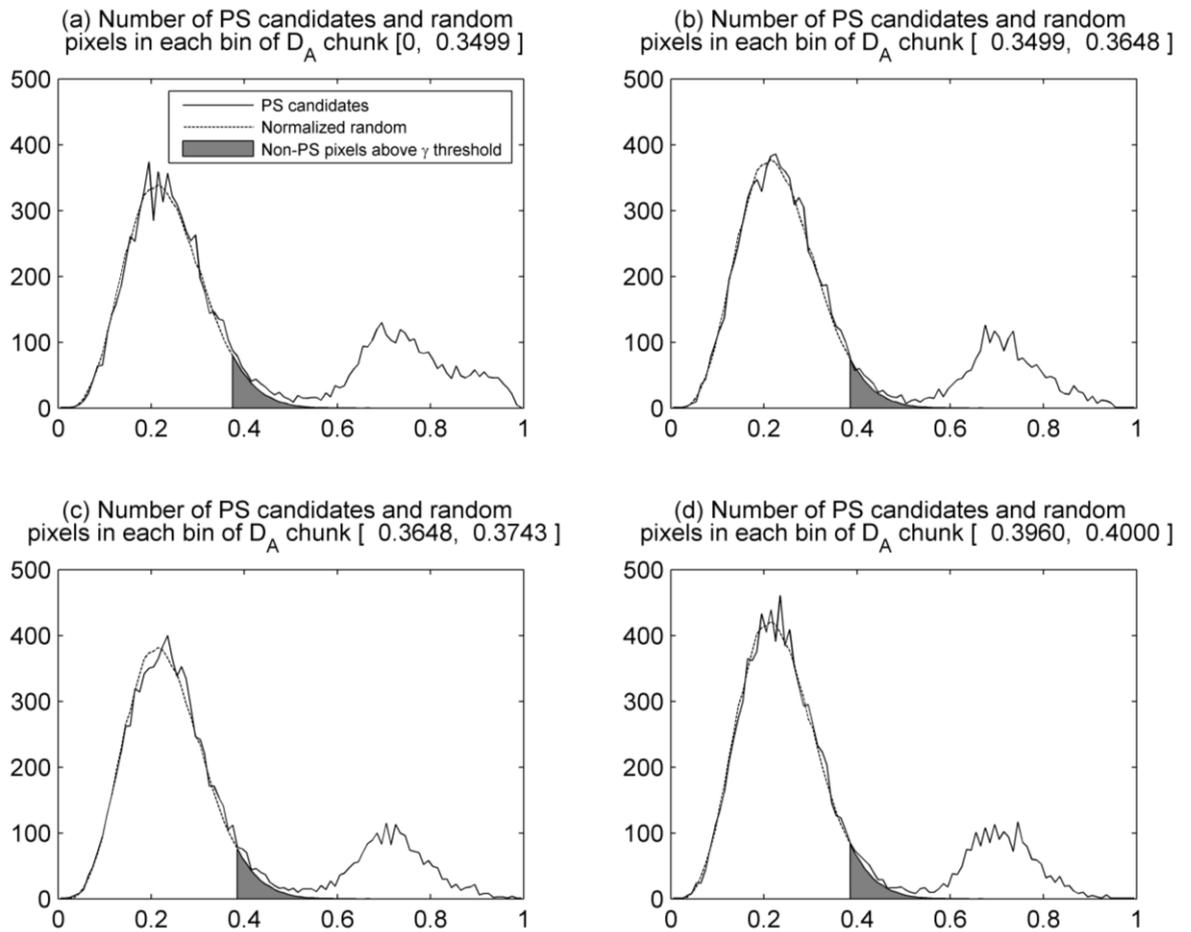
**Figure 3.6 Four examples of distributions of PS candidates and normalised random phases (non-PS pixels) in 8 $D_A$ chunks. The horizontal axis is the 100 $\gamma$ bins equally set between 0 and 1. The vertical axis is the number of pixels in each bin. The random distribution is normalized using the total number of pixels in $\gamma$ bins from 0 to 0.31 of both distributions. A good fit is seen between the normalized random distribution for non-PS (dashed line) and the distribution for PS candidates (solid line) in the lower $\gamma$ bins. The grey area is the distribution of non-PS pixels above the $\gamma^{low\_thresh}$ of this $D_A$ chunk.**

Take the PS case of Badong for example. The study area is about 194 km$^2$ with a theoretical maximum non-PS pixel density of 20 km$^{-2}$ (equivalent to maximum non-PS fraction $q$ of 20%). With 8 $D_A$ chunks, each has about 10000 of the total 80752 PS candidates; the theoretical maximum non-PS pixel number is $20 \times 194/8 = 485$ per $D_A$ chunk. In the first chunk $0 \leq D_A \leq 0.3499$ (Fig. 3.6a), the total number of non-PS pixels that obey normalized random distribution is 627 above the bin $\gamma = 0.36$, 521 above the bin $\gamma = 0.37$, and 430 above the bin $\gamma = 0.38$ The fitted $\gamma$ for 485 non-PS pixels is 0.3738 in this chunk. So $\gamma^{low\_thresh}(0 \leq D_A \leq 0.3499) = 0.3738$. The $\gamma^{low\_thresh}$ for the four $D_A$ chunks in Figure 3.6b, Figure 3.6c, and Figure 3.6d are 0.3794, 0.3799 and 0.3848 respectively. The $\gamma^{low\_thresh}$ of other $D_A$ chunks are also calculated to estimate their slope $\kappa$ using least squares inversion (Fig. 3.7).
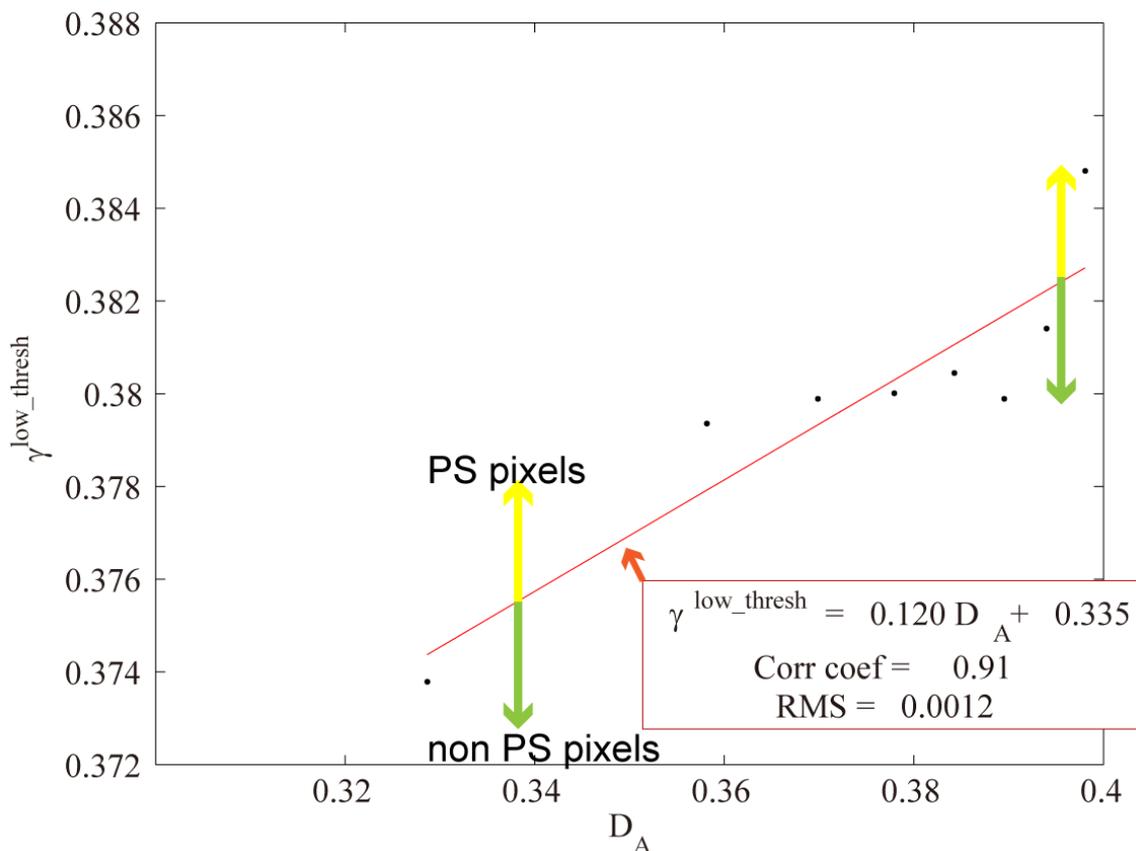
**Figure 3.7 Determination of the PS selection threshold using all 8 $D_A$ chunks in Badong. Black dots represent the 8 $D_A$ chunks in Badong. Each dot has the mean amplitude dispersion of the chunk as its horizontal coordinate and the low gamma threshold of the chunk as its vertical coordinate. A linear function (straight line) is used to fit the data. The red line is the selection threshold used to select PS pixels in the StaMPS Package. Each PS candidate has its $D_A$ from a series of amplitude images and its $\gamma$ from phase analysis. The $D_A$ value corresponds to its $\gamma^{low\_thresh} = 0.120 D_A + 0.335$ on the red line. If its $\gamma$ is greater than $\gamma^{low\_thresh}$, the candidate is initially selected as a PS pixel, otherwise it is a non-PS pixel (Fig. 3.8).**

It can be observed that $\gamma^{low\_thresh}$ increases as $D_A$ increases as suggested by Hooper (Fig. 3.7). Specifically, this can be explained by the distribution of PS candidates in $D_A$ chunks (Fig. 3.6). In lower chunks of $D_A$, the overall phase stability of candidates is likely to be higher, so that the distribution of PS candidates will skew to higher bins of $\gamma$ (Fig. 3.6a). Providing that the total number of candidates is similar in every chunk, there will be fewer PS candidates in lower $\gamma$ bins of lower chunks of $D_A$ (e.g. there are 239 PS candidates in the bin of $\gamma = 0.3$ in the lower chunk of $0.3499 \leq D_A \leq 0.3648$ (Fig. 3.6b) compared with 295 PS candidates in the bin of $\gamma = 0.3$ in the higher chunk of $0.3960 \leq D_A \leq 0.4$ (Fig. 3.6d)). Hence the total number of PS candidates in $\gamma$ bins from 0 to 0.31 that is used to normalize random distribution of non-PS pixels is smaller for lower $D_A$ chunks, which brings down the number of non-PS pixels in every bin of those chunks after normalization (e.g. there are 245 non-PS pixels in the bin of $\gamma = 0.3$ in the lower chunk of $0.3499 \leq$

$D_A \leq 0.3648$ (Fig. 3.6b) compared with about 274 non-PS pixels in the bin of $\gamma = 0.3$ in the higher chunk of $0.3960 \leq D_A \leq 0.4$ (Fig. 3.6d)). As a result, the integration bounds from $\gamma^{low\_thresh}$ to 1 need expanding to get also 485 random pixels in a relatively shrinking random distribution of a lower $D_A$ chunk, which results in a smaller $\gamma^{low\_thresh}$ in a lower $D_A$ chunk.
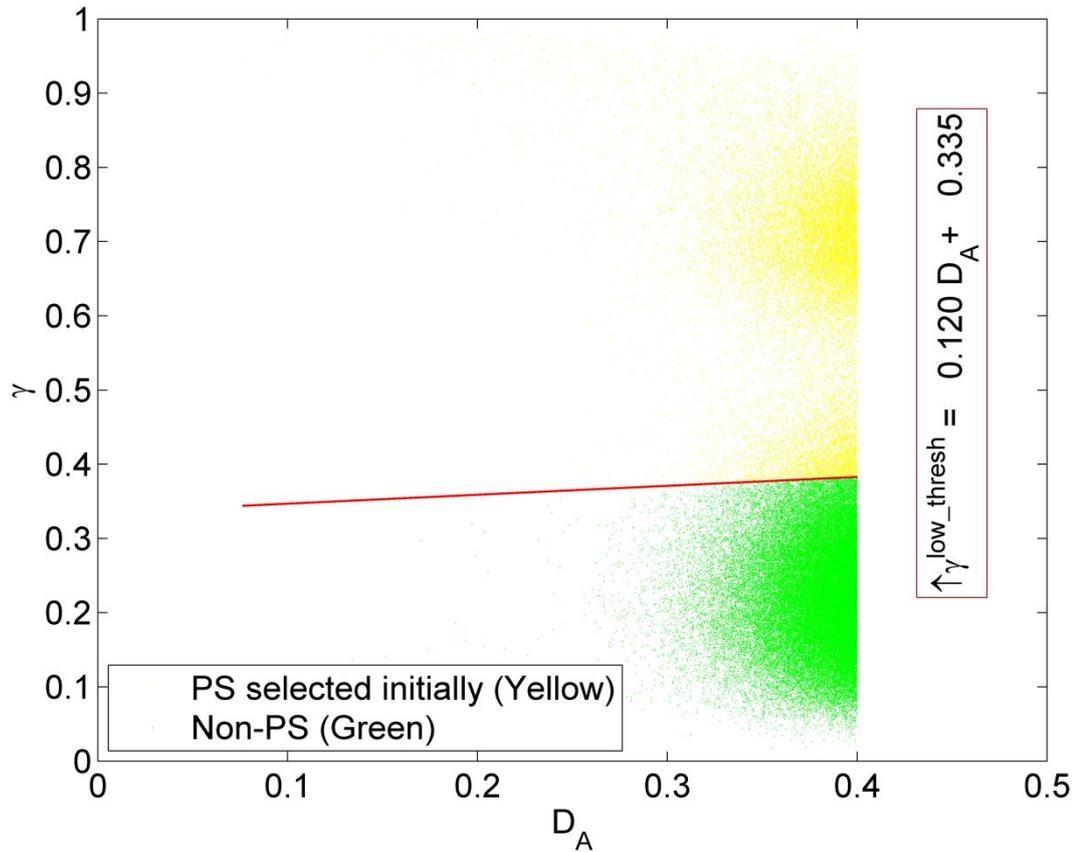


**Figure 3.8 PS pixels selected initially and non-PS pixels left using $\gamma$ and the fitted $\gamma^{low\_thresh}$.** **(a) A linear threshold function is used for distinguish PS and non-PS in Badong. Of all 80572 PS candidates, 20145 (Yellow dots) are selected initially. Theoretically, the Yellow dots still contain $485 \times 8 = 3880$ non-PS pixels, so they are refined in the next gamma re-estimation. Green dots are discarded. Pixels with $D_A > 0.4$ are discarded in the candidate selection step.**

## 3.2.2 Gamma re-estimation for initial PS and PS refinement

When Equation (3.42) is applied, the PS pixels initially selected include a fraction $q$ of non-PS pixels above $\gamma^{low\_thresh}$. So after initial selection of PS pixels a second round of selection is applied, using a method that is quite similar to the first round. In this round, the initial PS pixels are re-filtered for their spatial correlation phase, but the phases are not weighted before filtering and no iteration is used in Gamma re-estimation process (Fig. 3.9).

**Figure 3.9 An example of spatial low pass band filtering of wrapped phase for spatial correlation of PS selected initially in Badong using interferogram 26 July 2007- 21 January 2010. (a) Wrapped phase of PS selected initially corresponding to $\psi$ in Equation (3.5). (b) Filtered phase from combined low pass filtering corresponding to $\tilde{\psi}$ in Equation (3.5). (c) Residual phase after filtering corresponding to $\delta + \phi_\theta^u + \phi_N^u$ in Equation (3.5).**

The residual phases of initial PS after filtering are searched for phase error by spatially uncorrelated look angle errors. The parameter search follows the above mentioned procedure, leaving new residual phases for gamma value re-estimation. It can be seen that the new gamma values are lower than the initial ones for the pixels in the southeast part of the image (Fig. 3.10a and 3.10b). For the whole dataset of Badong, the pattern of the distribution changes with gamma values below the selection threshold appear again (Fig. 3.10c and 3.10d). There are many fewer high gamma values between [0.6, 1] than before. The number of pixels lying between [0.4, 0.6] are increased and the number of gamma values between [0, 0.4] are substantially increased. The change in distribution of gamma means that the PS pixels need to be re-selected using the re-estimated gamma values.

**Figure 3.10 The effect of re-estimating gamma values from the initial PS. (a) gamma values for part of the Badong area before gamma re-estimation. (b) re-estimated gamma values for the same area as (a). (c) distribution of gamma values from (a). (d) Distribution of re-estimated gamma values from (b). In (c) and (d), 1000 bins of equal width are used.**

The re-estimated gamma values are used to reselect PS from initial PS following above mentioned procedure. The re-estimated gamma values of the initially selected PS pixels together with the gamma values of discarded non-PS pixels in the previous session are binned firstly by amplitude dispersion and then by gamma. Low gamma bins are used to normalize the random distribution in each chunk. The normalized random distributions are used to find the gamma threshold in each chunk for the maximum allowable number of non-PS pixels that are mis-classified in the PS set. The discarded non-PS pixels have same gamma values for Figure 3.11 and Figure 3.6. The only difference between Figure 3.11 and Figure 3.6 is whether or not the gamma values of initial PS pixels are re-estimated. The re-estimated initial PS pixels show lower gamma values than before (Fig. 3.10c and Fig. 3.10d) which is why the distribution is lowered in $[0.6, 1]$ and raised in $[0, 0.4]$ when Figure 3.11 and Figure 3.6 are compared.
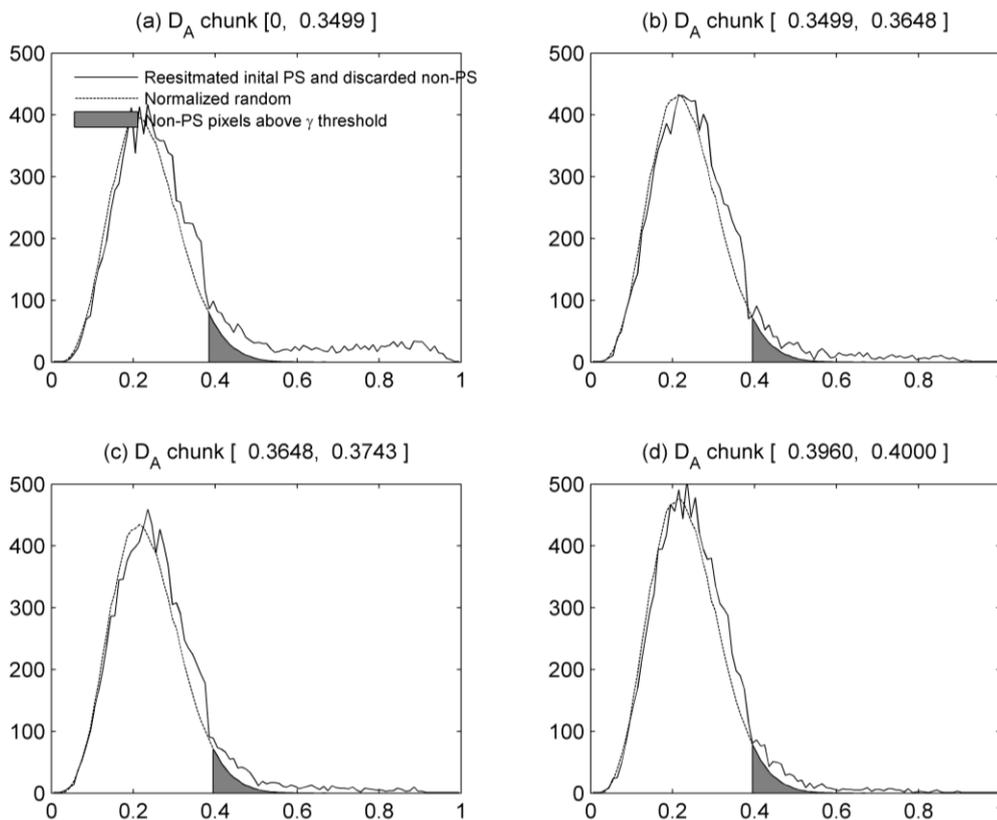
**Figure 3.11 Four examples of distributions of re-estimated initial PS added with discarded non-PS, and normalised random phases (non-PS pixels) in 8 $D_A$ chunks. The horizontal axis is normalised and divided into 100 equal $\gamma$ bins. The vertical axis is the number of pixels in each bin. The random distribution is normalized using the total number of pixels in $\gamma$ bins from 0 to 0.31 of both distributions. The normalized random distributions for non-PS pixels are shown by dashed lines and the distributions for re-estimated initial PS added with discarded non-PS pixels are the solid lines. The grey area is the distribution of non-PS pixels above the $\gamma^{low\_thresh}$ of this $D_A$ chunk.**

The new gamma thresholds from all the chunks are used to estimate the relationship between their $D_A$ and $\gamma^{low\_thresh}$ (Fig. 3.12).
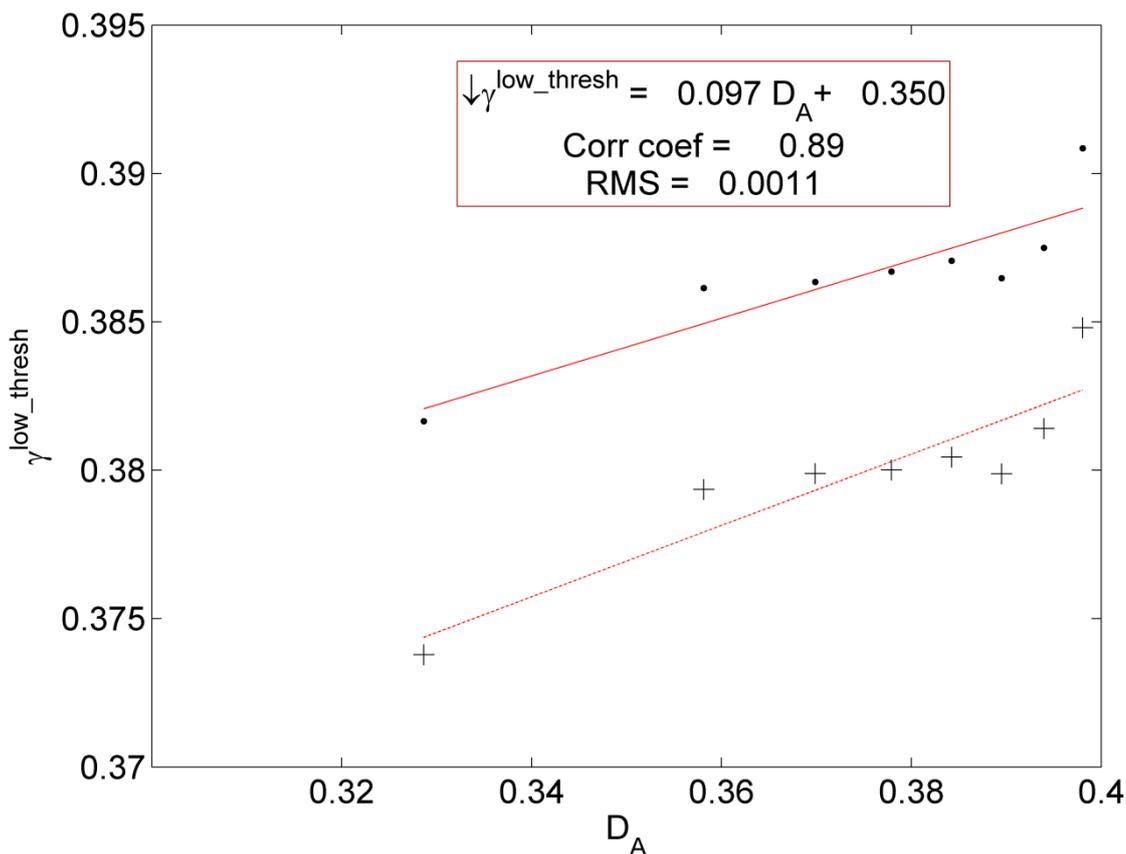
**Figure 3.12 Determination of PS refinement threshold using all 8 $D_A$ chunks in Badong. Black dots represent the 8 $D_A$ chunks in Badong. Each dot has the mean amplitude dispersion of the chunk as its horizontal coordinate and the low gamma threshold of the chunk as its vertical coordinate. A linear function (red straight line) is fitted to the data. The red solid line is the selection threshold used to refine intial PS pixels in the StaMPS Package. Each initial PS has its $D_A$ from a series of amplitude images and its restimated $\gamma$. The $D_A$ value corresponds to a $\gamma^{low\_thresh} = 0.097 D_A + 0.350$ on the red line. If its $\gamma$ is greater than $\gamma^{low\_thresh}$, the initial PS is selected as refined PS, otherwise to the non-PS pixel category (Fig. 3.13). The dashed red line and the black are the previously estimated threshold line and points from Fig. 3.7.**

Although the discarded non-PS pixels from the previous session are also included in the estimation of $\gamma^{low\_thresh}$, they are not included in the step of refining the initial PS pixel estimates. Only the initially selected PS pixels are refined using the approximated threshold line (Fig. 3.13).
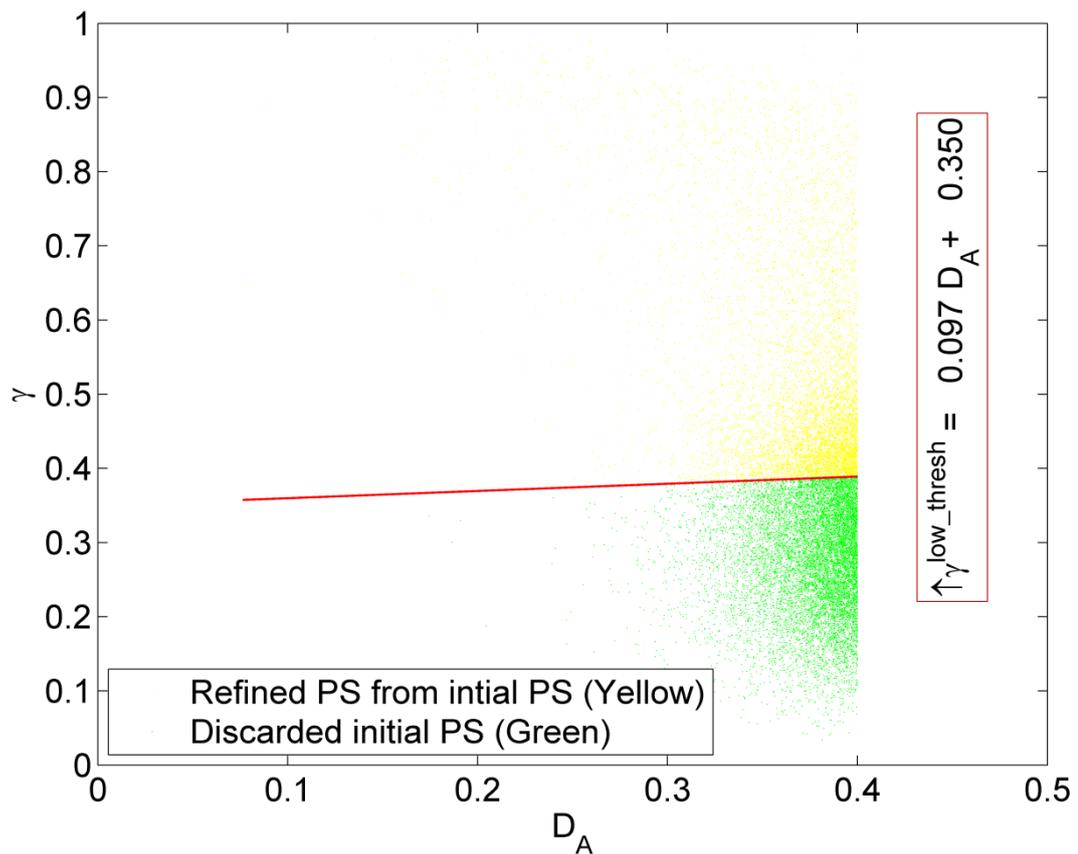
**Figure 3.13 Refined PS pixels and discarded initial PS pixels in Badong PS case. A linear threshold function (red solid line) is used for the refinement. Of all 20145 initial PS, 8097 (Yellow dots) are selected. Pixels with $D_A > 0.4$ are discarded in the candidates selection step.**

## 3.2.3 Dropping adjacent pixels and noisy pixels

A bright scatterer can dominate the pixel which contain itself and even other nearby pixels. The resulting look angle error will prevent those adjacent pixels from being selected as PS if the distance between the bright scatter and the geometric centre of adjacent pixel is great enough (Hooper et al., 2007). However, the look angle error maybe sufficiently small that the adjacent pixel look stable. In order to avoid identifying these as PS pixels, it is assumed in StaMPS that adjacent pixels selected are due to the same scatterer (Hooper et al., 2007). Where adjacent pixels are selected, the pixel containing the scatterer will exhibit the highest gamma value because of the shortest distance between the phase centre and the geometric centre. The pixel with the highest gamma is retained. This removal of adjacent pixels can be shown from an area with denser PS (Fig. 3.14c and 3.14d). This assumption however will mean some loss of information if there are two bright scatterers in adjacent pixels e.g. urban area. The chance of information loss is lower in natural terrains where bright scatter are usually less present.
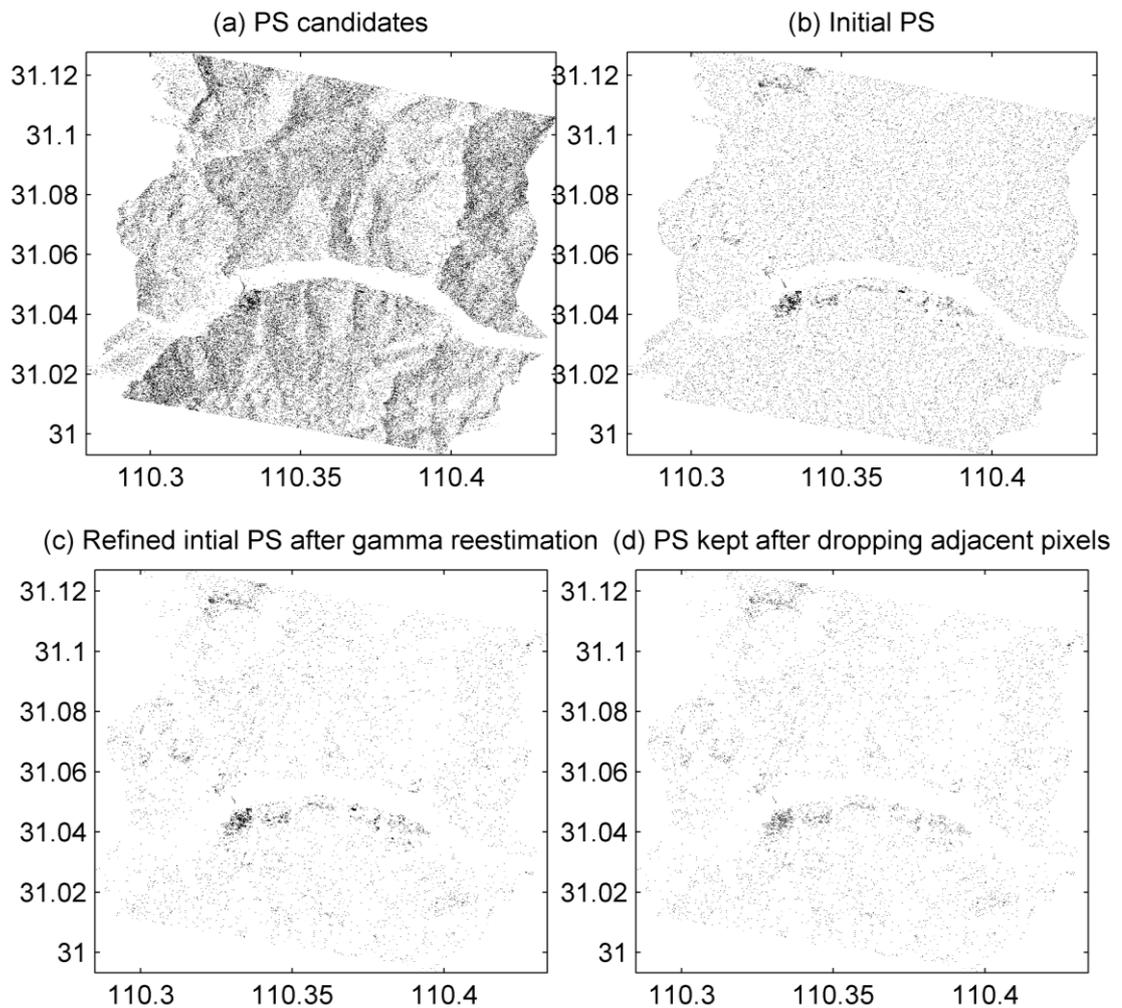
**Figure 3.14 An example of PS points retained after dropping adjacent pixels in the Badong case. (a) PS candidates under amplitude dispersion threshold. (b) Initial PS above gamma threshold. (c) PS points retained after gamma re-estimation. (d) PS retained after dropping adjacent pixels. Of all 80752 PS candidates in Badong, 20145 were selected initially, 8097 refined after gamma re-estimation, and 6678 are kept after dropping adjacent pixels.**

After dropping adjacent pixels, the remaining PS pixels are evaluated by the standard deviation and maximum noise. If the noise standard deviation is smaller than one and the maximum noise is not infinity, the PS point is kept with all others removed as noisy pixels (Hooper et al., 2007).
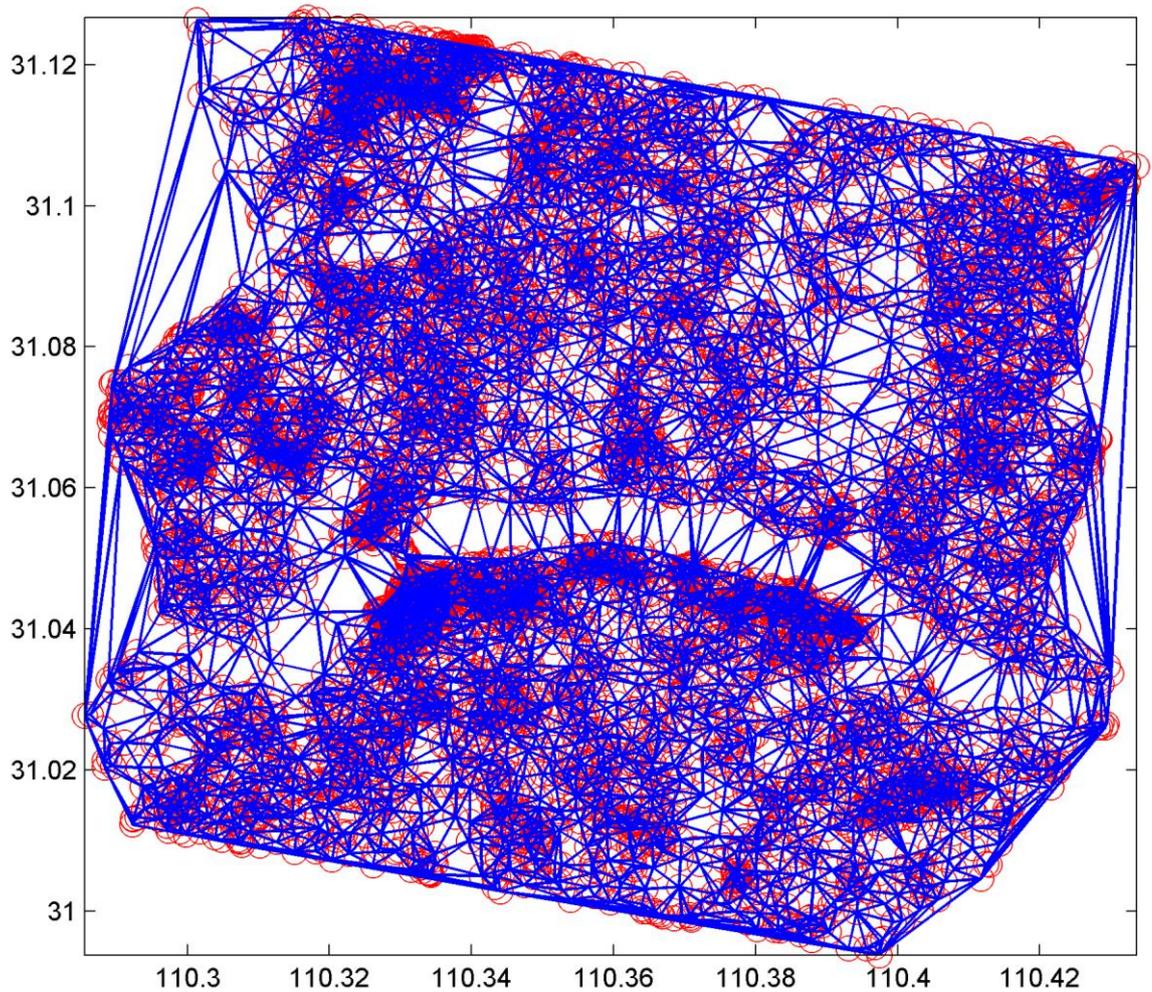
**Figure 3.15 The Delaunay network used to drop noisy pixels. Each PS is marked with a circle. The edges of the triangles are lines.**

The derivations below are from the Matlab codes of StaMPS (Hooper et al., 2007). After dropping adjacent pixels, the remaining pixels can then be used to form a Delaunay triangle network (Fig. 3.15). The triangles in the network are formed of edges. Each edge has two pixels as its nodes. In the example, the 6678 retained PS pixels form 20013 edges. The spatial phase differences on each edge are the angles of the complex multiplications of the two nodes in time series.

$$d_{phc} = C_1 \cdot C_2^* \qquad\qquad (3.43)$$

Where $C_1$ and $C_2$ are two complex nodes of the edge, " $\cdot$ " denotes complex multiplication and " $*$ " denotes a complex conjugate. $d_{phc}$ is the complex multiplication of the nodes. The phase differences of the two nodes on the edge are the phase angles of $d_{phc}$ in time. (e.g. 30 SAR images are used in Badong PS case; each $d_{phc}$ has 30 values, corresponding to 30 spatial phase differences of this edge). The complex multiplications in $d_{phc}$ are:

$$d_{phc} = \{d_{phc,1}, d_{phc,2}, d_{phc,3}, \dots, d_{phc,i}, \dots, d_{phc,N}, d_{phc,(N+1)}\}, \tag{3.44}$$

where $d_{phc,i}$ is the $i_{th}$ complex multiplication of this edge. Because $N$ was used to denote the number of interferograms, the number of spatial complex multiplications for each edge is $N + 1$. The weighted mean complex multiplication for $i_{th}$ complex multiplication $d_{phc,i}$ is calculated using all the values in $d_{phc}$:

$$d_{phc,i,mean} = \sum_{j=1}^{j=N+1} d_{phc,j} \cdot w_j, \tag{3.45}$$

$$w_j = e^{-\frac{1}{2}\frac{t_j^2}{t_w^2}} \Big/ \sum_{j=1}^{j=N+1} e^{-\frac{1}{2}\frac{t_j^2}{t_w^2}}, \tag{3.46}$$

$$t_j = T_j - T_i, \tag{3.47}$$

where $w_j$ is the normalized weighting factor for $d_{phc,j}$, $t_j$ is the time difference between the $j_{th}$ and $i_{th}$ images, $t_w$ is the timing window for exponential weighting (e. g. $t_w$ is set as 180 days in Badong PS case). $T_i$ and $T_j$ are the image acquisition times of the $i_{th}$ and $j_{th}$ images respectively.

The greater the time interval between $T_j$ and $T_i$, the smaller $w_j$ is. The weighting is a normalized symmetric exponential distribution centred with $T_i$. Hence the images far away from $d_{phc,i}$ will have less impact on the weighted mean $d_{phc,i,mean}$ for $d_{phc,i}$ (Fig. 3.16).
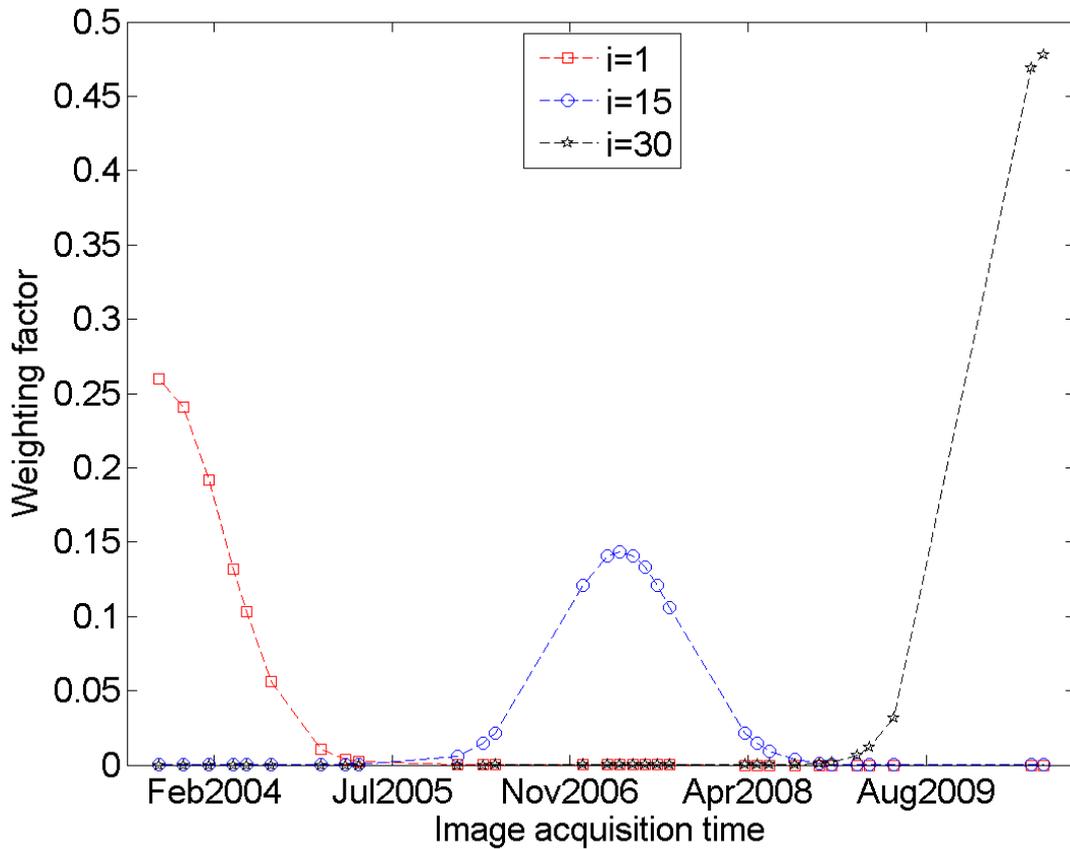
**Figure 3.16 Three examples of weighting factors for complex multiplications in the mean calculation. Each marker is a weighting factor. Horizontal axis is the imagery acquisition time $T_j$. Vertical axis is the weight value $w_j$. The weightings are symmetric with $i_{th}$ complex multiplication. When $i$ moves, $w_j$ changes.**

The derivations below are from the Matlab codes of StaMPS (Hooper et al., 2007).

Subtracting the weighted mean from each complex multiplication is:

$$d'_{phc} = d_{phc} \cdot (d_{phc,i,mean})^* = \{d_{phc,1}, d_{phc,2}, d_{phc,3}, \dots, d_{phc,i}, \dots, d_{phc,N}, d_{phc,(N+1)}\} \cdot$$
$$(d_{phc,i,mean})^* = \{d_{phc,1} \cdot (d_{phc,i,mean})^*, \dots, d_{phc,i} \cdot (d_{phc,i,mean})^*, \dots, d_{phc,(N+1)} \cdot$$
$$(d_{phc,i,mean})^*\} \tag{3.48}$$

A fitting for phase angles of complex set $d'_{phc}$ using a weighted least square is:

$$m = G \backslash d'_{ph} , \tag{3.49}$$

where $d'_{ph}$ are the phase angles of a complex set $d'_{phc}$,

$$G = \{t_1, \dots, t_j, \dots, t_{N+1}\} \tag{3.50}$$

and $m$ minimizes the following

$$(d'_{ph} - G \cdot m)^T \cdot diag(w) \cdot (d'_{ph} - G \cdot m) \,, \qquad (3.51)$$

where $= \{w_1, .., w_j, ..., w_{N+1}\}$, "\" denotes least square inversion and "$T$" denotes matrix transpose.

Subtracting the first estimation, the left residual component is:

$$d''_{ph} = d'_{ph} - G \cdot m \qquad (3.52)$$

The residual phase component is also fitted using weighted least squares:

$$m' = G \backslash d''_{ph} \qquad (3.53)$$

and $m'$ minimizes

$$(d''_{ph} - G \cdot m')^T \cdot diag(w) \cdot (d''_{ph} - G \cdot m') \qquad (3.54)$$

Hence the fitted $i_{th}$ complex multiplication of an edge can be given in terms of the weighted mean and the other two estimations:

$$d_{phc,i,smooth} = d_{phc,i,mean} \cdot e^{\sqrt{-1}(G \cdot m + G \cdot m')} \qquad (3.55)$$

With $N + 1$ complex multiplications, the fitted values of the edge form a line in time:

$$d_{phc,smooth} = \{d_{phc,1,smooth}, ..., d_{phc,i,smooth}, ..., d_{phc,N+1,smooth}\} \qquad (3.56)$$

Hence the complex noises that correspond to the misfits of the smooth line for the edge in time are:

$$d_{phc,noise} = d_{phc} \cdot \left(d_{phc,smooth}\right)^* \qquad (3.57)$$

Another kind of smooth method is the stacking of all $N + 1$ values of this edge except current $i_{th}$ complex multiplication:

$$d_{phc,i,smooth2} = \sum_{j=1}^{j=N+1} d_{phc,j} \cdot w'_j \qquad (3.58)$$

where $\begin{cases} w_j' = w_j & (j \neq i) \\ w_j' = 0 & (j = i) \end{cases}$

It is the same approach as the weighted mean complex multiplication in (3.45) with only the difference in weighting for $i_{th}$ multiplication. Combining all the fitted values, the line in time using the second kind of smoothing is:

$$d_{phc,smooth2} = \{d_{phc,1,smooth2}, \dots, d_{phc,i,smooth2}, \dots, d_{phc,N+1,smooth2}\} \qquad (3.59)$$

Hence the complex noise that corresponds to the misfits of the second smooth line for the edge in time are:

$$d_{phc,noise2} = d_{phc} \cdot (d_{phc,smooth2})^* \qquad (3.60)$$

A relationship between the phase angles of complex noises and the perpendicular baselines is estimated using weighted least squares:

$$K_{ph} = B_\perp \backslash d_{ph,noise} \qquad (3.61)$$

where $K_{ph}$ minimise

$$(d_{ph,noise} - K_{ph} \cdot B_\perp)^T \cdot diag(w'') \cdot (d_{ph,noise} - K_{ph} \cdot B_\perp), \qquad (3.62)$$

where $d_{ph,noise}$ are the phase angles of complex noises $d_{phc,noise}$, $B_\perp$ are the perpendicular baselines. $w''$ is given by

$$w'' = var(d_{ph,noise2}) \qquad (3.63)$$

Where $var$ is variance operator, and $d_{ph,noise2}$ are the phase angles of complex noises $d_{phc,noise2}$.

Finally, the noises of the edge are given as:

$$d'_{ph,noise} = d_{ph,noise} - K \cdot B_\perp \qquad (3.64)$$

The standard deviation of the noise of the edge is:

$$edge\_std = std(d'_{ph,noise}) \ . \hspace{3cm} (3.65)$$

The maximum noise of the edge is:

$$edge_{max} = max\left|d'_{ph,noise}\right| \hspace{3cm} (3.66)$$
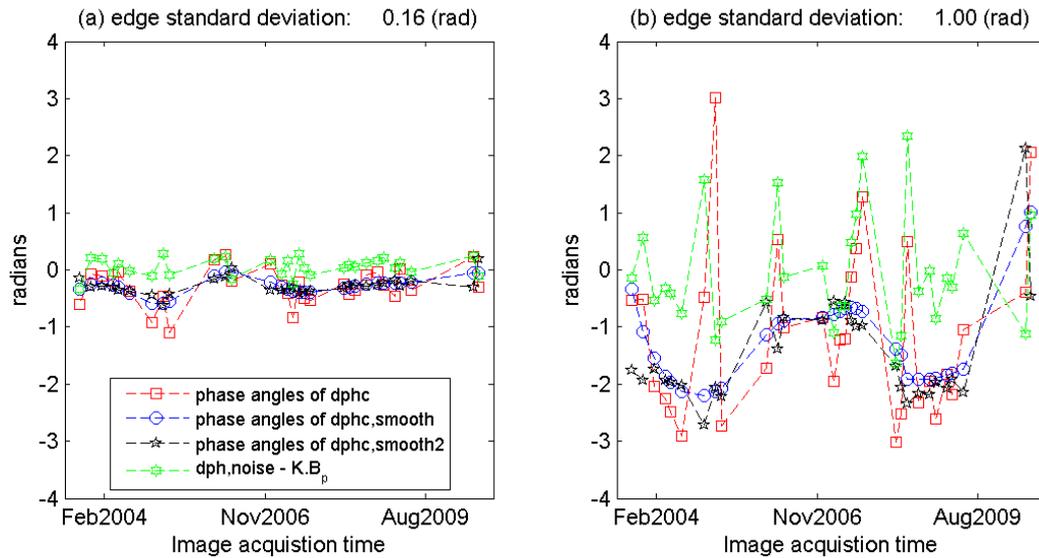


**Figure 3.17 Two examples of edge standard deviations in the Badong PS case. (a) One edge with a standard deviation of 0.16 radians. (b) Another edge with a standard deviation of 1 radians. Red squares are the phase angles of complex multiplications of the two nodes on the edge. Blue circles are the smooth phases of red squares based on weighted mean phases, and least square inversions of residual phases.The black pentagrams are the second kind of smooth phases of red squares based on stacking of weighted phases. The green hexagrams are the noises of the edges after removal of estimated DEM error.**

The $edge\_std$ (Fig. 3.17) and $edge_{max}$ will be given to the two nodes of the edge as the standard deviation and maximum noise of the nodes. If the nodes are connected with more than one edge, the relatively smaller value is chosen for the pair of nodes. If both the standard deviation of the noise and the maximum noise of the node are smaller than their corresponding thresholds, the node is kept as a PS pixel; otherwise it is a noisy pixel and is discarded. In the Badong PS case, 5304 PS pixels are kept after dropping noisy pixels from the 6678 pixels which were left after dropping adjacent pixels.

## 3.3 Phase unwrapping

For selected PS points, the two dimensional phases are still modulo $2\pi$. Phase unwrapping is therefore implemented in order to derive continuous displacement fields. The processes in this section are summarized from the Matlab codes of StaMPS (Hooper et al., 2007).

## 3.3.1 Correction of spatially uncorrelated phase

In StaMPS, the non-spatially correlated part in wrapped interferograms is corrected before unwrapping, including the spatially uncorrelated part of the look angle error $\phi_\theta^u$ and the contribution of the master to the spatially uncorrelated part of the signal (Hooper et al., 2007).
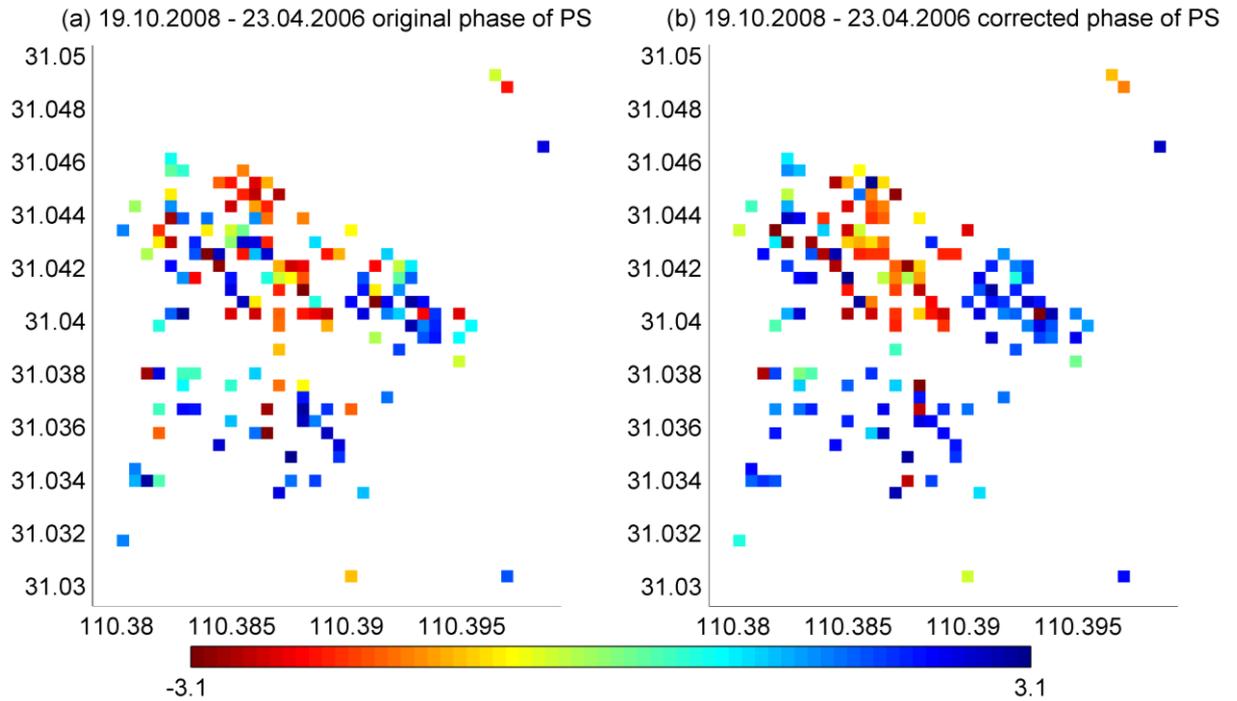


**Figure 3.18 An example of spatially uncorrelated phase correction before phase unwrapping in the Badong PS case. (a) Original phase of PS pixels. (b) Corrected phase of PS pixels.**

As mentioned earlier, the phase error due to spatially uncorrelated look angle error for the same pixel in different interferograms will only depend on perpendicular baselines for those interferograms. The linear relationship $K$ ($K = \frac{4\pi}{\lambda}\Delta\theta$) between the phase error due to spatially uncorrelated look angle error and the perpendicular baseline is estimated in Gamma estimation and estimated again in the Gamma re-estimation during PS refinement. The phase error by look angle error below is given in exponential form of complex number because later the master contribution is retrieved by complex summation.

$$\phi_{\theta,i}^u = e^{\sqrt{-1}K\cdot B_{\perp,i}} \tag{3.67}$$

The master contribution, $\phi^M$, is the sum of complex phase residuals. It was already estimated during Gamma re-estimation after low-pass band filtering and removal of spatially uncorrelated phase error, and is

$$\phi^M = \sum_{i=1}^{N} e^{\sqrt{-1}\psi_{Residual,i}} \qquad\qquad (3.68)$$

where $\psi_{Residual,i}$ is given in Equation (3.19).

The corrected phase of PS (Fig. 3.18b) is:

$$e^{\sqrt{-1}\psi_{corrected,i}} = e^{\sqrt{-1}\psi_i} \cdot \left(e^{\sqrt{-1}K \cdot B_{\perp,i}}\right)^* \cdot \left(\sum_{i=1}^{N} e^{\sqrt{-1}\psi_{Residual,i}}\right)^* \qquad (3.69)$$

where " $*$ " denotes complex conjugate. It can be seen from Equation (3.19) that the corrected phase $\psi_{corrected,i}$ is actually quite similar to the low pass filtered phase $\tilde{\psi}_i$. The difference is $\psi_{corrected,i}$ used stacking of residuals from a series of interferograms but $\tilde{\psi}_i$ only deals with one interferogram and therefore one residual. The corrected phase $\psi_{corrected,i}$ for phase unwrapping will thus contain spatially correlated part of $\{\phi_D + \phi_A + \phi_O + \phi_\theta\}$, which is deformation, spatially correlated atmospheric, orbit and look angle errors. The correction for spatially uncorrelated phase and the later Goldstein filtering will reduce the noise in wrapped phase because noises can be propagated and accumulated through phase unwrapping.

## 3.3.2 PS resample and Goldstein filtering before phase unwrapping
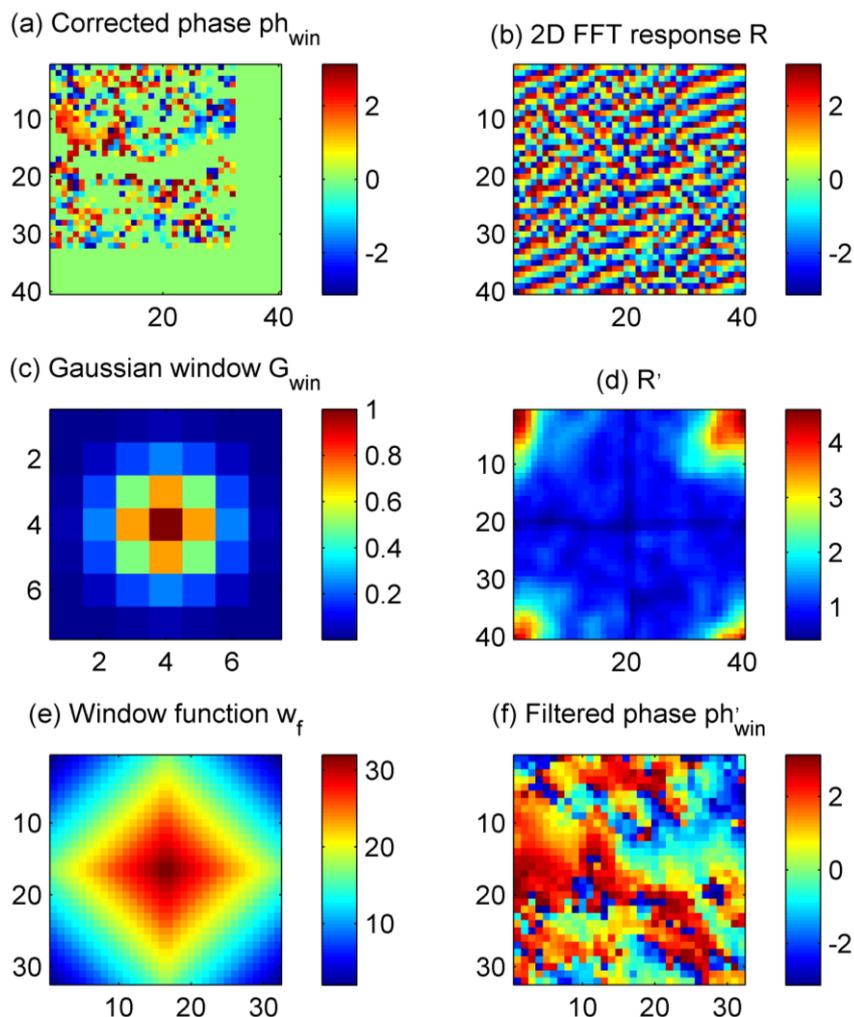


**Figure 3.19 Goldstein filtering for corrected phase of PS. (a) Corrected phase in a 32 x 32 grid window, the bottom and right are eight grids filtering pad with zero. (b) Two-dimensional discrete fast Fourier transformation response. (c) Gaussian window used for convolution. Colour bar is window value (d) New response $R'$ in Equation (3.72). (e) Window function multiplied by filtered phase. (f) Filtered phase after Goldstein filtering. Colour bars are for wrapped phase in (a) and (f), for response in (b) and (d), and for window values in (c) and (e).**

The corrected phases are filtered to reduce phase noise before unwrapping (Goldstein and Werner, 1998). The deduction below are summarized from the Matlab codes of StaMPS (Hooper et al., 2007). The complex phases of PS pixels are sampled to grids of 200 x 200 m $200 \times 200\ m$ size for the use of two-dimensional discrete fast Fourier transform (2D FFT). For the 5304 PS, only 2111 grids are filled. Multiple pixels may fall in the same grid cell, of which the grid value is their complex sum. It is a resample process of the PS, resulting in fewer PS for phase unwrapping. 2D FFT is applied to each window of $32 \times 32$ grid cells and generate the corresponding response $R$ (Fig. 3.19b). $R$ is given by

$$R = fft2(ph_{win}) \,. \tag{3.70}$$

The zero-frequency component of $R$ intensity is shifted to the centre of the spectrum. Shifted $R$ is filtered by a $7 \times 7$ pixel Gaussian window $G_{win}$ (Fig. 3.27c) and shifted back.

$$H = ifftshift(filter2(G_{win}, fftshift(|R|))) \tag{3.71}$$

Where $fftshift$ is zero frequency shift, $filter2$ is convolution and $ifftshift$ is the inverse of the zero frequency shift.

The new response $R'$ is

$$R' = \left(\frac{H}{\bar{H}}\right)^{\alpha} \tag{3.72}$$

where $\bar{H}$ is the median value of $H$, $\alpha$ is the weighting parameter with $\alpha = 0.8$ used in the Badong PS case.

The 2-D inverse discrete Fourier transform is applied to the new response $R'$ (Fig. 3.19d)

$$ph'_{win} = \left(ifft2(fft2(ph_{win}) \cdot R')\right) \cdot w_f \tag{3.73}$$

Where $ifft2$ is the inverse of Fourier transform, $w_f$ (Fig. 3.19e) is a window function, and $ph'_{win}$ (Fig. 3.19f) is the filtered phase in the window.

### 3.3.3 Phase unwrapping network and cost
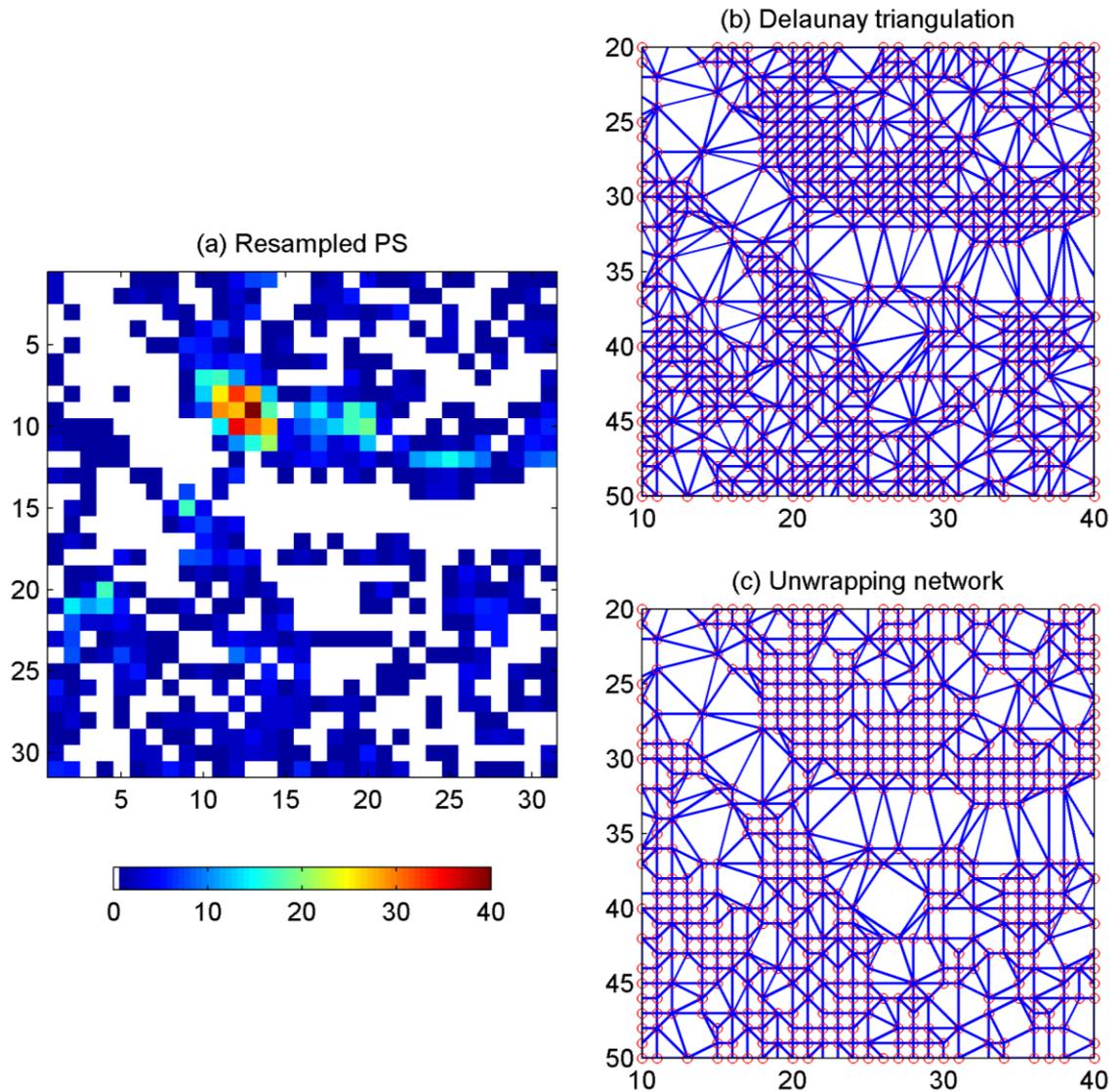


**Figure 3.20 Phase unwrapping network construction. (a) Resample of PS before Goldstein filtering. Each square is a $200 \times 200\ m$ grid. The value of a colour square is the number of PS pixels that fall in this grid. A grid is a new PS pixel with a greater size. White areas contain no PS pixels. (b) Delaunay triangulation built on PS pixels. Each circle represents a pixel. Each line represents an edge of a triangle. (c) Unwrapping network for the PS pixels. X and Y scales are pixel numbers.**

After Goldstein filtering, the PS pixels (Fig. 3.20a) are used to form a Delaunay network (Fig. 3.20b). The Delaunay triangle elements are used to find the nearest PS of each grid. The nearest PS pixels of all grids are used to form an unwrapping network (Fig. 3.20c). The unwrapping network has 4967 edges for the 2111 grid PS.
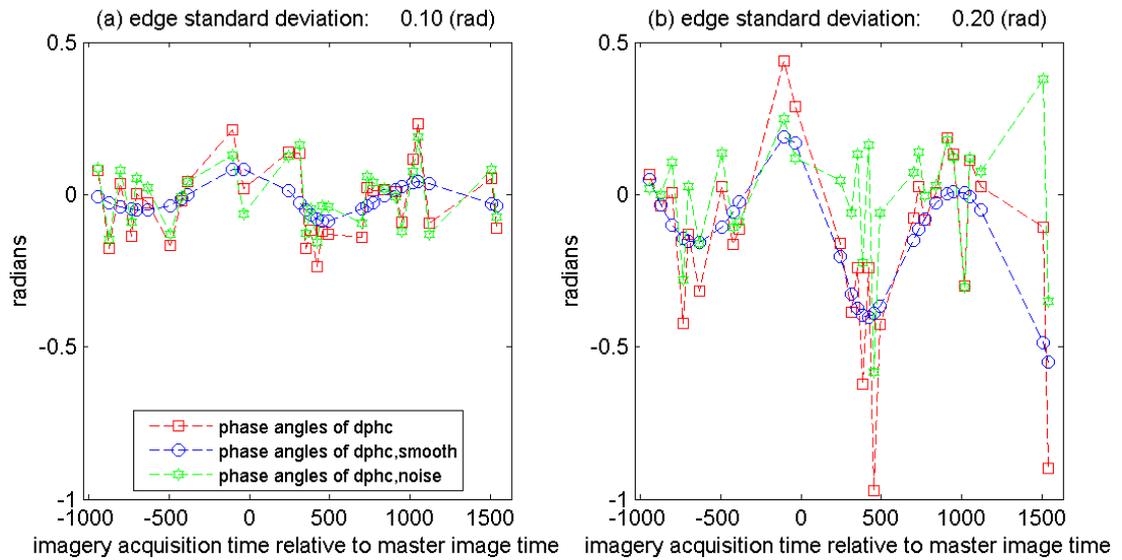
**Figure 3.21 Two examples of PS edge phase. (a) Standard deviation = 0.1. (b) Standard deviation = 0.2. Horizontal axis is the imagery acquisition time relative to master image time. Vertical axis is the phase angle. Red squares are the phase angles of complex multiplications of the two nodes on the edge. Blue circles are the smooth phases of red squares based on weighted mean phases, and least square inversions of residual phases. The green hexagrams are the noises of the edges. The noises are used in phase unwrapping.**

The complex multiplications for each edge (Fig. 3.20c) are smoothed following the steps above (Fig. 3.21). The complex multiplications represent the phase difference between the two nodes of an edge in different times. For each interferogram, the offsets between the original complex multiplications and smoothed multiplications of all edges are used to estimate the costs of phase unwrapping. On each interferogram, phase unwrapping is implemented using the SNAPHU algorithm (Chen and Zebker, 2001) for the 2111 wrapped phase grid. SNAPHU is a statistical-cost, network flow algorithm. The algorithm aims to compute the most likely unwrapped solution with maximum posterior probability estimation given the observable input data. The processes below are summarized from the Matlab codes of StaMPS (Hooper et al., 2007).

The grid offset cost $c_{go}$ between original and smoothed is the noise level of an edge in one interferogram

$$c_{go} = \frac{d_{ph,i,noise}}{2\pi} N_c ,\qquad\qquad\qquad (3.74)$$

Where $N_c$ is the number of short cycles (e.g. 200). $d_{ph,i,noise}$ is the angle of $d_{phc,i,noise}$, which is the complex noise of re-sampled PS in one interferogram. $c_{go}$ is the first input of

each grid in all interferograms for the SNAPHU algorithm an indicator of noise level in spatial dimensions (Fig. 3.22).
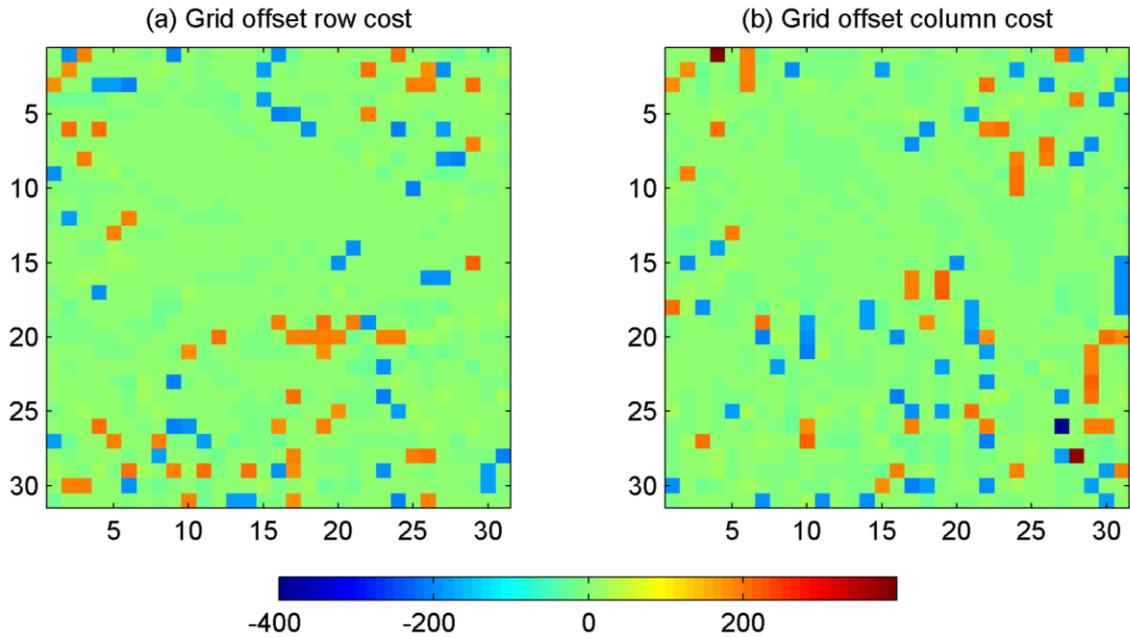


**Figure 3.22 An example of space dimension cost for phase unwrapping from interferogram $21.01.2010 - 26.07.2007$ in Badong PS case. (a) Grid offset row cost. (b) Grid offset column cost. Grids taken by re-sampled PS are given their corresponding offset cost. Empty grids are assigned with zeros for SNAPHU. The figure is the same area as Fig. 3.20**

The signal sequential noise $n_{ss}$ level of an edge can be given as:

$$n_{ss} = \left(\frac{std(d_{ph,noise})}{2\pi}\right)^2 ,$$
(3.75)

Where $d_{ph,noise}$ is the angle of $d_{phc,noise}$, which is the complex noise of re-sampled PS in time and its related steps. "$std$" denotes the standard deviation.

The signal sequential cost $c_{ss}$ of this edge will be:

$$c_{ss} = \frac{n_{ss} \cdot N_c}{c_s} N_e ,$$
(3.76)

Where $N_c$ is the number of short cycles (e.g. 200), $c_s$ is the cost scale (e.g. 100), and $N_e$ is the number of edge occurrences. $c_{ss}$ is the second input of each grid in one interferogram for the SNAPHU algorithm as an indicator of noise level in time dimension (Fig. 3.23).
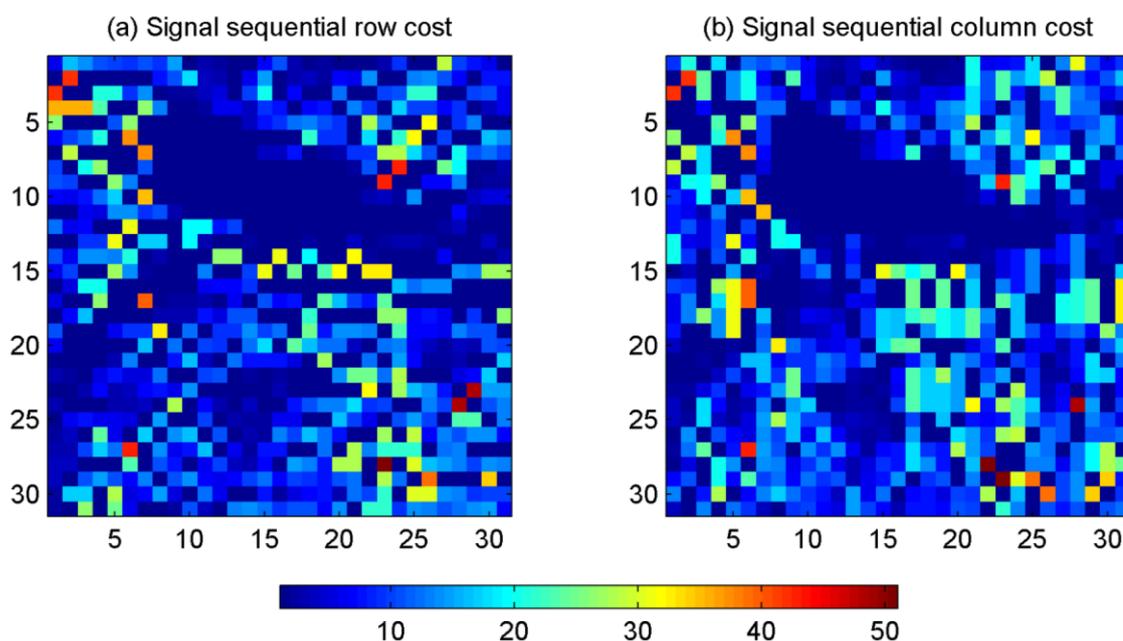
**Figure 3.23 An example of time dimension cost for phase unwrapping in Badong PS case. (a) Signal sequential row cost. (b) Signal sequential column cost. Grids taken by re-sampled PS are given their corresponding signal sequential cost. Empty grid cells are assigned a value one for SNAPHU.**

As mentioned before, the re-sampled PS is sum of multiple PS. Hence the unwrapped phases of the 2111 re-sampled PS are returned to the 5304 PS. That is how interferograms with 5304 PS are unwrapped (Fig. 3.24). Note that although the wrapped phases are corrected by spatially uncorrelated phases before phase unwrapping, the unwrapped phases are wrapped again to find their differences with the wrapped phase. Theses phase differences are added back to the unwrapped phases.
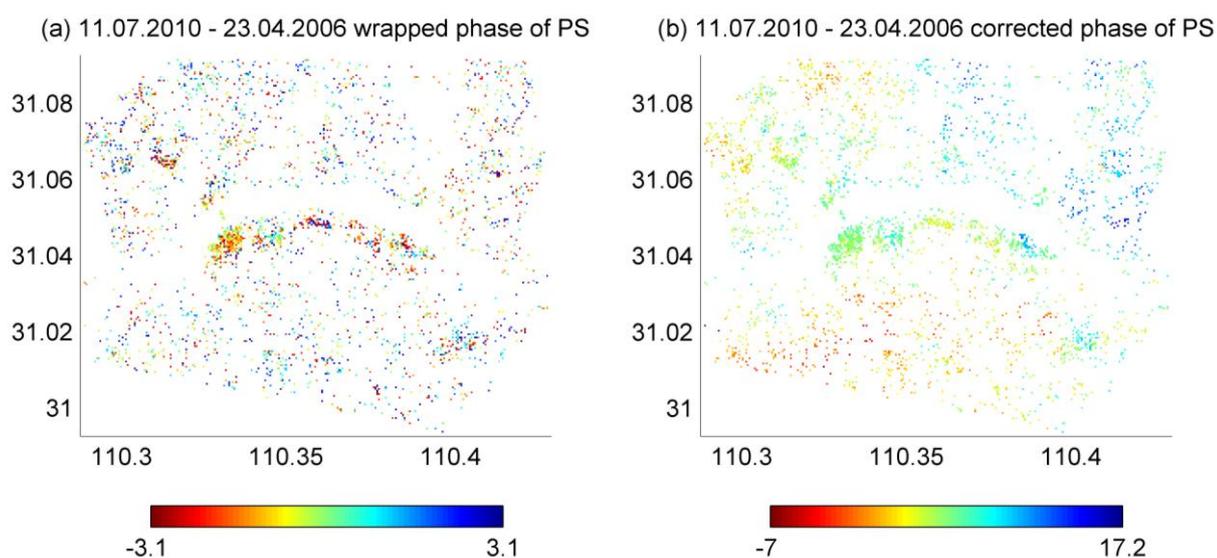


**Figure 3.24 An example of phase unwrapping in Badong PS case. (a) Original phase of PS pixels. (b) Unwrapped phase of PS pixels.**

65

# 3.4 Small baseline network

After phase unwrapping, the phases of PS pixels are already in time series because a common master image is referred for all interferograms. However, for small baseline approach (Berardino et al., 2002), an inversion of deformation increments from the unwrapped interferograms is necessary as multiple master images are used and the phases are not referenced to the same time (Schmidt and Bürgmann, 2003) (Fig. 3.25). The inversion is implemented using linear equations.
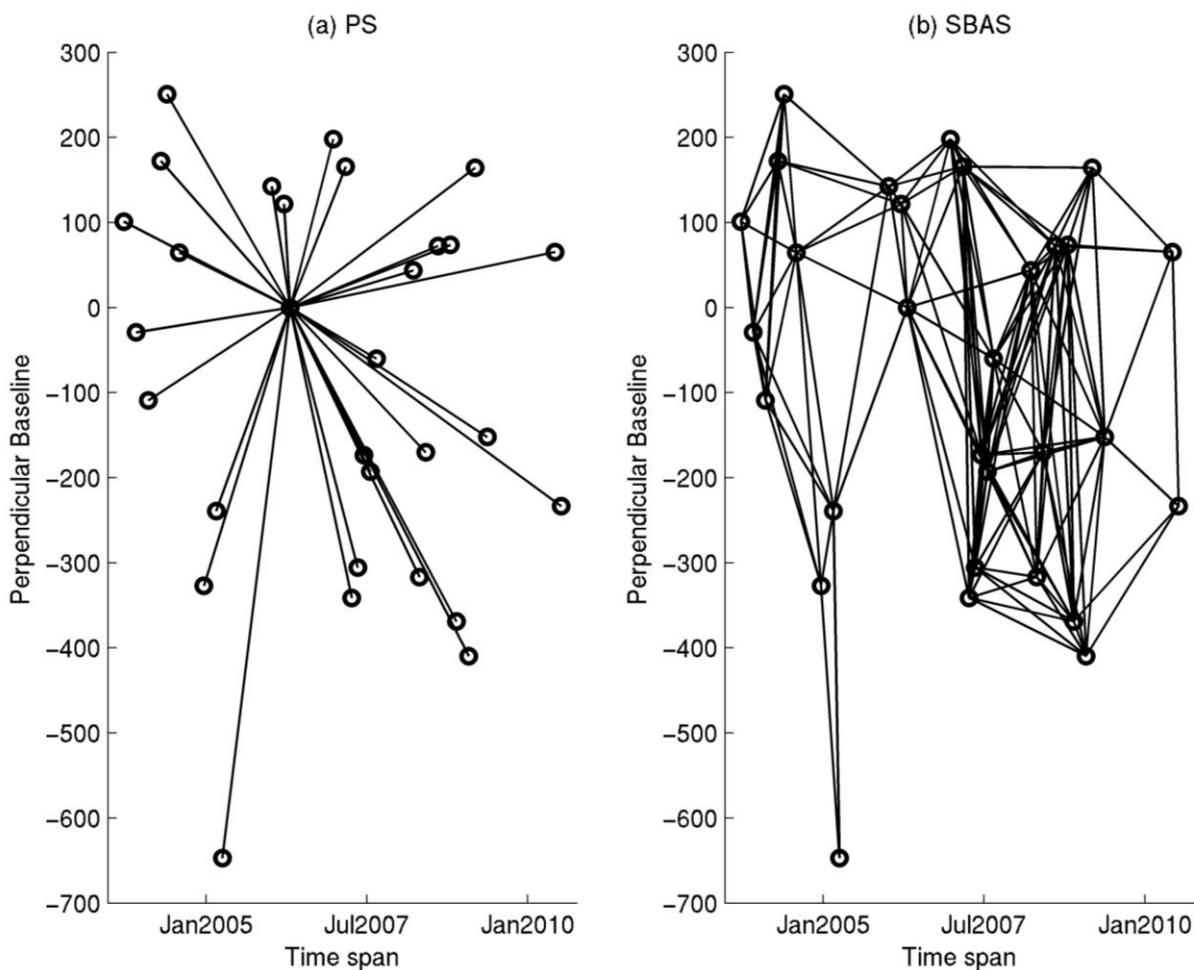


**Figure 3.25 Examples of baseline network in Badong. (a) PS network. (b) (Small baseline) SBAS network. Each circle is a SAR image, each edge is a SAR interferogram. PS interferograms are all connected with a single master scene, while multiple master scenes are used in SBAS interferograms.**

$$Gm = d \tag{3.77}$$

$$m = \{m_1, m_2, \ldots, m_i, \ldots, m_S\} \tag{3.78}$$

$$d = \{d_1, d_2, \ldots, d_j, \ldots, d_N\} \tag{3.79}$$

Where $m$ is a vector of the $S$ range increments in time steps divided by $S + 1$ SAR scenes. $d$ is a vector of the range changes of each interferogram. The length of $d$ depends on how many small baseline interferograms you have. $d$ can be decomposed into linear combinations of $m$. That is how $G$ is formed. Typically, $N$ is significantly greater than $S$, which makes the inversion stable. The inverted phases and displacements are also known as modelled phase and displacement, which are in time series.

## 3.5. Estimation of look angle error, orbit errors and atmospheric effects

The processes in this section are summarized from the Matlab codes of StaMPS (Hooper et al., 2007). As the phase differences between wrapped and rewrapped phase are added back to the unwrapped phase, the unwrapped phases should be estimated again for phase error by spatially uncorrelated look angle error. This estimation differs from the parameter search for look angle errors in gamma estimation. For unwrapped phase, estimating look angle error is a linear inversion whilst for wrapped phase the parameter search is a nonlinear process. The unwrapped phases of a single pixel are used to estimate a linear relationship with its spatial perpendicular baselines using least square (Hooper, 2008):

$$\begin{pmatrix} 1 & B_{\perp,1} & t_1 \\ \vdots & \vdots & \vdots \\ 1 & B_{\perp,i} & t_i \\ \vdots & \vdots & \vdots \\ 1 & B_{\perp,N} & t_N \end{pmatrix} \begin{pmatrix} m \\ K \\ v \end{pmatrix} = \begin{pmatrix} \psi_1 \\ \vdots \\ \psi_i \\ \vdots \\ \psi_N \end{pmatrix} \qquad (3.80).$$

Where $\{\psi_1, \cdots, \psi_i, \cdots \psi_N\}$ are the unwrapped phases of PS pixels or the modelled unwrapped phases of SDFPs, $m$ is the offset for the linear relationship, $K$ is the estimated factor between unwrapped phases and spatial baselines perpendicular, $v$ is the co-estimated velocity, which however is not the final rates produced, and $t_i$ is the time interval between current scene relative to the master scene for PS or modelled SBAS.

The phase error by look angle error is $K \cdot B_{\perp,i}$ for a pixel in each interferogram. The look angle error is $\Delta\theta = \frac{\lambda}{4\pi} K$ for a pixel in all interferograms. Because $m$ presents in every interferogram, it is the master image atmospheric effects and orbital error (AOE).

After estimating look angle error and master AOE, the slave AOE is estimated by triangulation of PS pixels or SDFPs. The phase on an edge is the difference between the

unwrapped phases of two nodes. For time series phases of PS pixels or modelled time series phases of SDFPs, the edge phases are also in time series. The edge phase time series are smoothed using the second kind of smooth for dropping noisy pixels. The smooth edge phases are the low-pass phases, which are thought as the displacement phases when there are no abrupt changes. Subtracting the low-pass phase from the edge phase will leave the high-pass phases, which are thought as the atmospheric effects since the atmospheric phases are not correlated in time. Using the triangulation, the high-pass edge phase are converted back to the pixels using least square since one pixel maybe on several edges. Hence the slave atmospheric phases of each pixel are already estimated in time now. Because the atmospheric effects are also correlated in space, for each interferogram, the slave atmospheric phases are low-pass filtered in space. This is implemented by sum of neighbouring atmospheric phases that are weighted by inverse distances.

However the performance of atmospheric filtering varies from case to case, as it can easily lead to misestimating of deformation signals if both deformation and atmospheric noise represent similar patterns and temporal behaviours (Peltier et al., 2010).
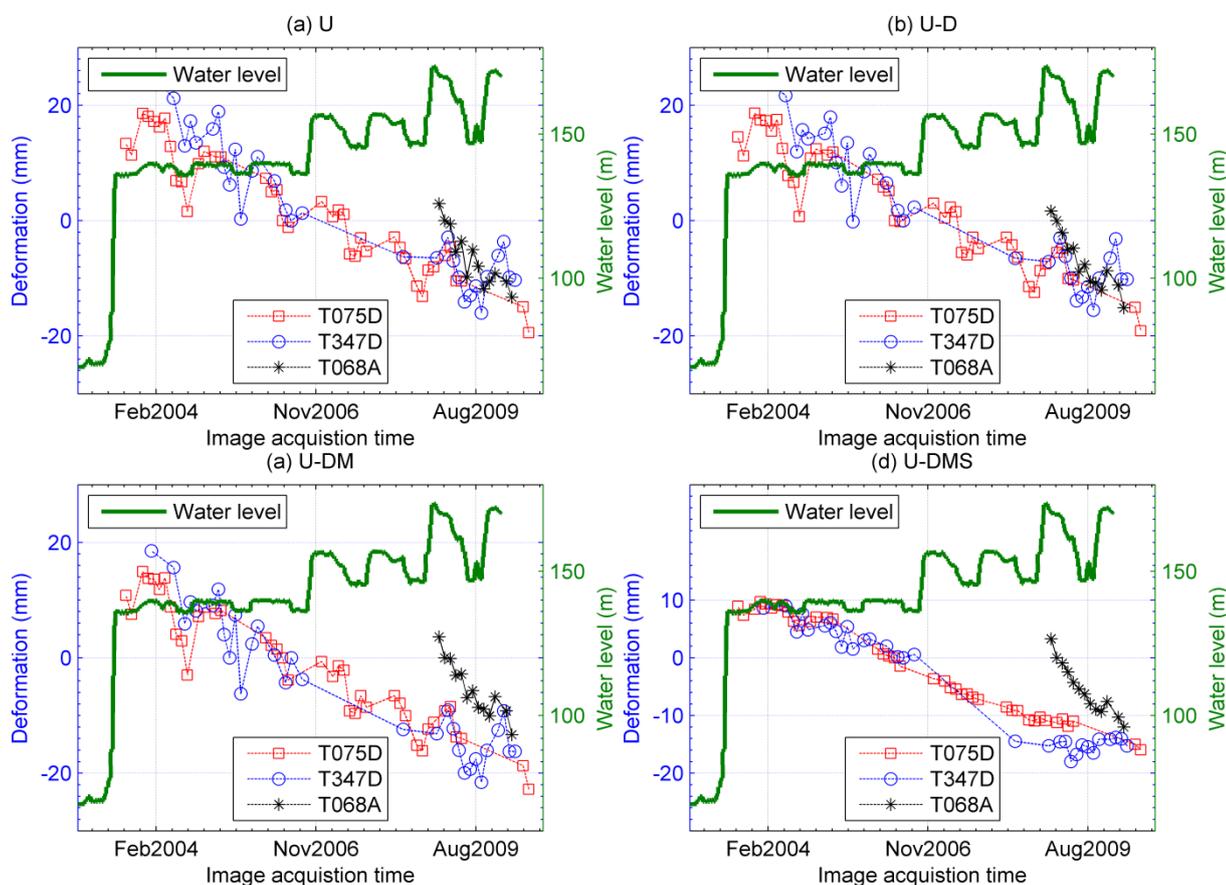


**Figure 3.26 An example of InSAR time series deformation in Huangtupo landslide of Badong, Three Gorges, China. (a) Unwrapped phase. (b) Unwrapped phase subtracts look angle error. (c) Unwrapped phase subtracts look angle error and AOE (atmospheric effects**

**and orbital error) in master image. (d) Unwrapped phase subtracts look angle error, AOE in master image and slave images. Radar line of sight displacements are given in square, circle and star symbols for descending Track 075, 347 and ascending Track 068 respectively. Water level of Yangtze River at the foot of the Huangtupo landslide body is the green solid line.**

The reliability of time series InSAR technique can be seen in Badong landslide study with strong correlation between seasonal deformation and water level change of Three Gorges Reservoir  (Liu *et al.*, 2013) (Fig 3.26). Impoundment water level is an independent observation to validate InSAR time series. It can be seen from Figure 3.26d that the seasonal displacement in Track 075D and Track 347D is lost when AOE (atmospheric effects and orbital error) estimation of slave images is subtracted from unwrapped phase. The seasonal deformation has leaked into slave AOE. So the use of AOE estimation for slave images should be careful when seasonal deformation signal is also of interest.

# Chapter 4 The sedimentary environment of the Yellow River delta

In this chapter, the geomorphological and geological context of the Yellow River delta is given to assess the possible deformation mechanisms in this region. Geomorphological information comes from literature, field investigation and laboratory work. Oil extraction has begun in the Yellow River delta since late 1960s. Some unclassified borehole logs, seismic profiles and relevant interpretations are available from publications. Structural information for Gudao oilfield is collected here to facilitate further geophysical modeling of the effects of oil extraction on Earth surface deformation.

## 4.1 Geomorphology and Geology of the Yellow River delta

### 4.1.1 Sediment load of Yellow River

The Yellow River has a catchment area of 752 000 $km^2$. The annual water discharge of Yellow River is only 49 $km^3$/yr, but average sediment concentration is 37.4 $kg/m^3$ (Jia and Wang, 2011, Wang et al., 2007, Wang et al., 2010). The Yellow River can be sub-divided into the Upper, Middle and Lower reaches (demarcation between neighbouring reaches are given in caption of Fig. 1.1 in Section 1.1).

**Table 4.1 Sediment load of Yellow River, after (Gao et al., 1989). The symbol "-" means unavailable data.**

|  | Upper reaches | Middle reaches | Lower reaches | Total river |
|---|---|---|---|---|
| Length (km) | 3742 | 1122 | 870 | 5464 |
| Catchment area (%) | 32% | 64% | _ | 100% |
| Sediment load ($kg/m^3$) | 6.67 | _ | _ | 37.4 |
| Total sediment yield (%) | 8.6% | $\geq$ 90% | _ | 100% |

Approximately, 90% of the total sediment load in Yellow River is provided by the Loess Plateau located in the Middle reach as a result of intensive soil erosion (Saito et al., 2001, Ren and Shi, 1986). The Loess Plateau (Wen et al., 2009) is an area of thick aeolian deposits mainly comprised of loosely compacted silt. The aeolian sediment of the Loess plateau is 100-200 m thick, is predominantly composed of 2-50 μm size particles, and is prone to erosion (Gao et al., 1989). The area covered by aeolian sediments is 430 000 $km^2$,

approximately 57% of the total catchment of Yellow River, of which 280 000 km$^2$ is severely incised (Huang et al., 2007).

Being confined between artificial levees, the lower reach has a total fall in elevation of about 95 m in 700 km. Due to continued aggradation, the Lower Yellow River flows in a perched channel over the surrounding floodplain behind the dikes, and only small tributaries join the river (Shi, 2005). The Lower Yellow River bed is rising by 0.1 m/yr (Sui et al., 2006). Reconstructed longitudinal profiles of its latest abandoned channel suggest that its riverbed has been raised by 15-20 m in 600 years. The floodplain land between the dikes is 9-15 m higher than the surrounding floodplain because of continuous siltation (Shi, 2005). Historical documents show 1593 avulsions in the past 3000 years, with 26 major avulsions (Xue, 1993).

Before the construction of the Sanmenxia Reservoir in the early 1960s, $1.6 \times 10^9$ t of sediment was transported to the Lower Yellow River from the Loess Plateau each year (Suo, 2004, Wang et al., 2005). A quarter of this sediment load was deposited in the channel of the Lower Yellow River, nearly half in the river delta and another quarter in the shallow water of the Bohai Sea (Gao et al., 1989). Since the 1960s, about 3147 reservoirs have been built in the Yellow River with total capacity of 57.4 km$^3$ (Jia and Wang, 2011). It is now a highly fragmented and regulated river. An example of this regulation is the Water-Sediment Regulation Scheme, a controlled release of floodwaters from the Xiaolangdi Reservoir, to expel sediments deposited in the reservoir and to scour the Lower reaches of the river every year in June since 2002 (Wang et al., 2010).

## 4.1.2 Sediment aggradation in the Yellow River delta

For most of the time, the Yellow River has flowed into the Bohai Sea, which is also the current situation. However, between 1128 and 1855 it entered the South Yellow Sea. The current course of the lower Yellow River downstream from Dongbatou resulted from a major avulsion in 1855 (Fig. 1.1 in Section 1.1). The Yellow River delta complex is divided into ten super lobes (Fig. 4.1) (Xue, 1993). Nine super lobes are located around the Bohai Sea and the rest one is on the western coast of the Yellow Sea.
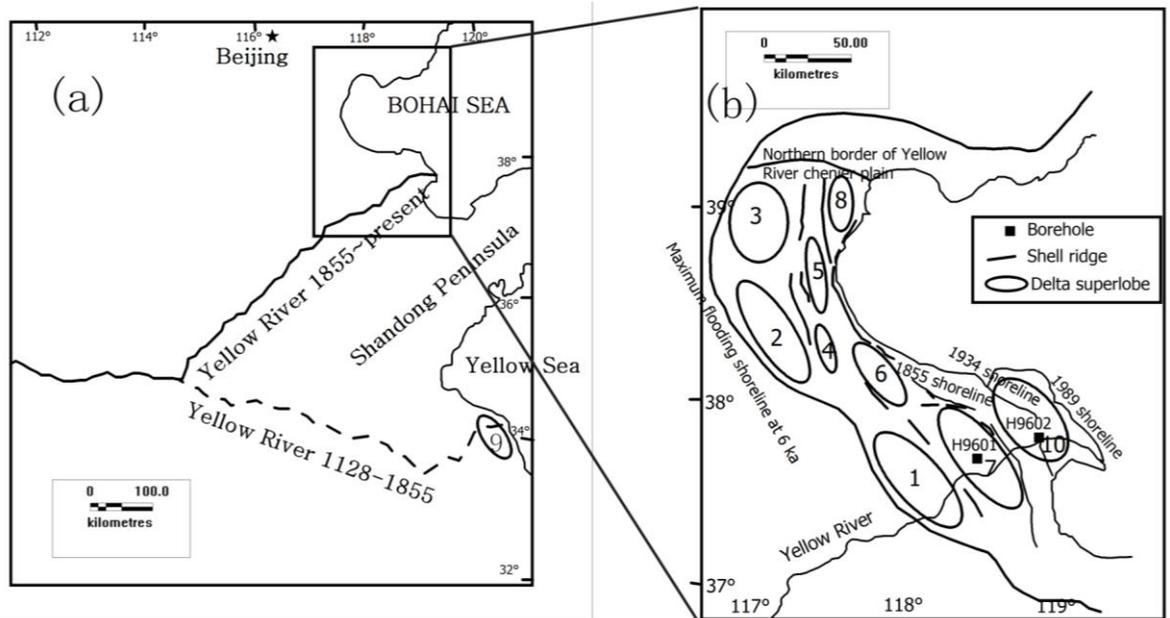
**Figure 4.1 Physiographic map of the Yellow River delta, after (Yi et al., 2003, Saito et al., 2000, Xue, 1993). The black solid border of (b) corresponds to the left smaller rectangle in (a). Lobe 9 is shown in (a), while Lobes 1 ~ 8 and 10 are shown in (b). The estimated age of each super lobe is 1: 6000-5000 yr BP, 2: 5000-4500 yr BP, 3: 4500-3400 yr BP, 4: 3400-3000 yr BP, 5: 3000 yr BP-602 BC, 6: 602 BC-11 AD, 7: 11 AD-1048, 8: 1048-1128, 9: 1128-1855, 10: 1855-present. Samples from borehole H9601 located landward of the 1855 shoreline and H9602 located seaward of the 1855 shoreline are used for detailed sediment analysis and high-resolution radiocarbon dating to clarify the relationship between delta progradation and chenier formation by Saito et al. (2000).**

The modern delta is Super lobe 10. Xue (1993) discussed the relationship between cheniers (shelly ridges) and the Holocene deltaic sequence in a cross section of the Yellow River delta. Depositional ages based on radiocarbon dates of molluscan shells of cheniers and borehole samples are given in their work (Fig. 4.2 and 4.3).
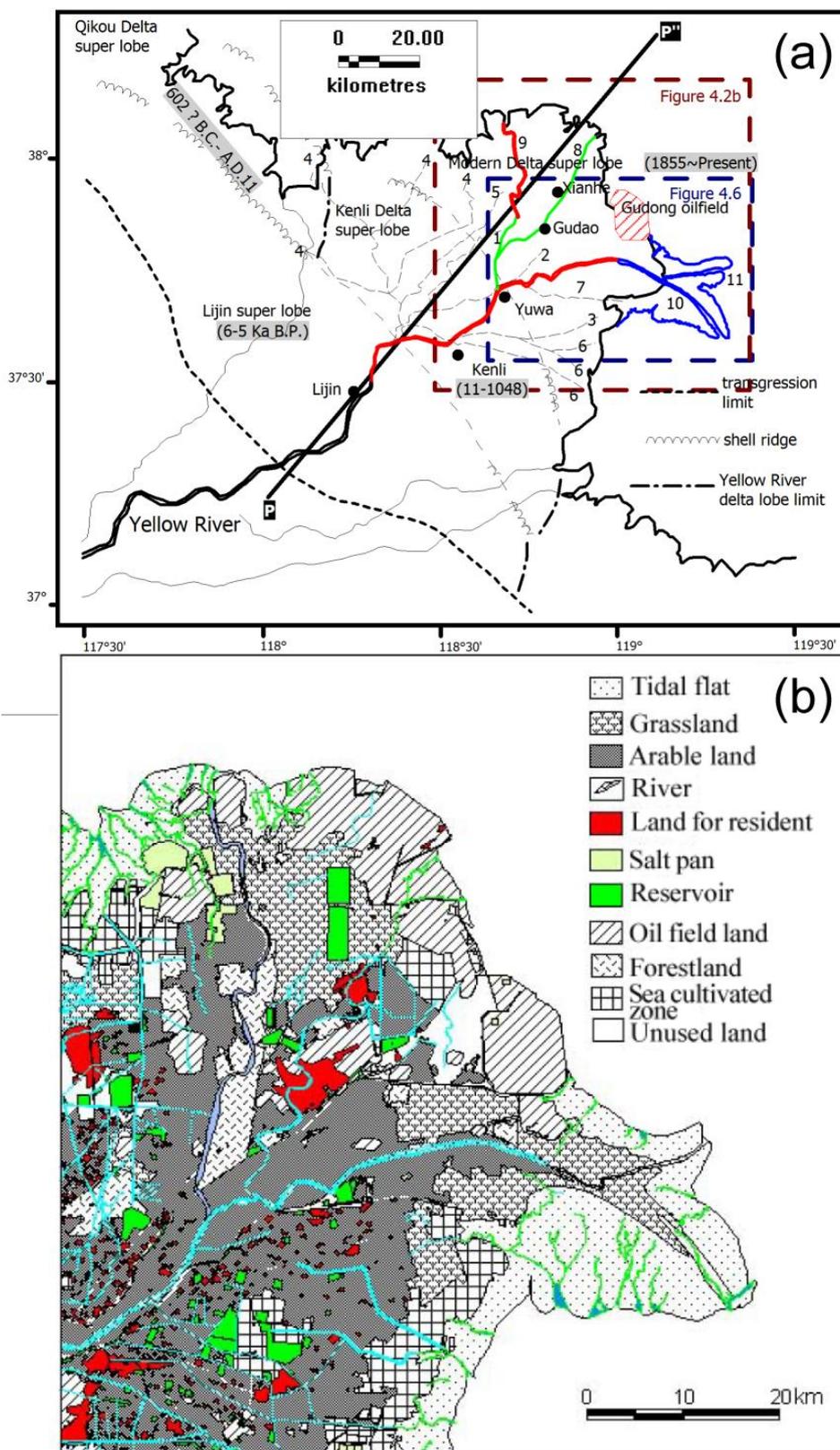
**Figure 4.2 (a) Migration of the Yellow River mouth since 1855. Black solid shoreline and delta lobes are from (Xue, 1993). Blue solid shoreline together with channels 10 and 11 are from (Wang et al., 2010). Channels 1-7 are from (Shi et al., 2003). Channels 8 and the green part of 9 are from (Chu et al., 2006). Channel adjustment time series from 1855 to present are marked on the map in serial number from 1 to 11. Gudong oilfield together with the red part of Channels 9 and 10 are from Google earth imagery. PP" is the profile trace on earth surface for the Figure 4.3. Yellow River delta Lobes 1 (6-5 Ka B.P.), 6 (602 B.C. - A.D.11), 7 (11-1048) and 10 (1855~ Present) in Fig. 4.1 are also displayed here with shell ridges and the extreme inland limit of transgression. (b) Land use and structure of the Yellow River delta, reproduced from (Zhou et al., 2001).**

Before the construction of the Xiaolangdi Reservoir in the Middle reaches of the Yellow River in 1999 more than $1.0 \times 10^9$ of sediment was discharged into the Bohai Sea each year (Wang et al., 2010). Approximately 90% of the sediment discharged to the sea is deposited within 30 km of the river mouth, generating a rapidly accreting and aggrading delta. Since the last migration of the channel of the Lower reaches in 1855, a mega delta (subaerial delta area > 5000 km$^2$) has been created (Fig. 4.2 and 4.3) (Shi, 2005, Wang et al., 2010). Within the modern delta, the position of the river's outlet to the sea changes on average every 10 years (Fig. 4.2). Three major recent changes (Wang et al., 2010, Chu et al., 2006, Shi, 2005) of the outlet are: (i) in 1964, the channel shifted from Shenxiangou Promontory to Diaokou promontory (Channels 8 to 9 in Fig. 4.2); (ii) in 1976, the channel mouth was artificially shifted south-eastward to Qingshuigou Promontory, and a new delta lobe began to form south of Laizhou Bay (Channels 9 to 10 in Fig. 4.2). (iii) another minor shift of the river channel was artificially induced in 1996, resulting in the present northeastward Q8 Promontory (Channels 10 to 11 in Fig. 4.2).
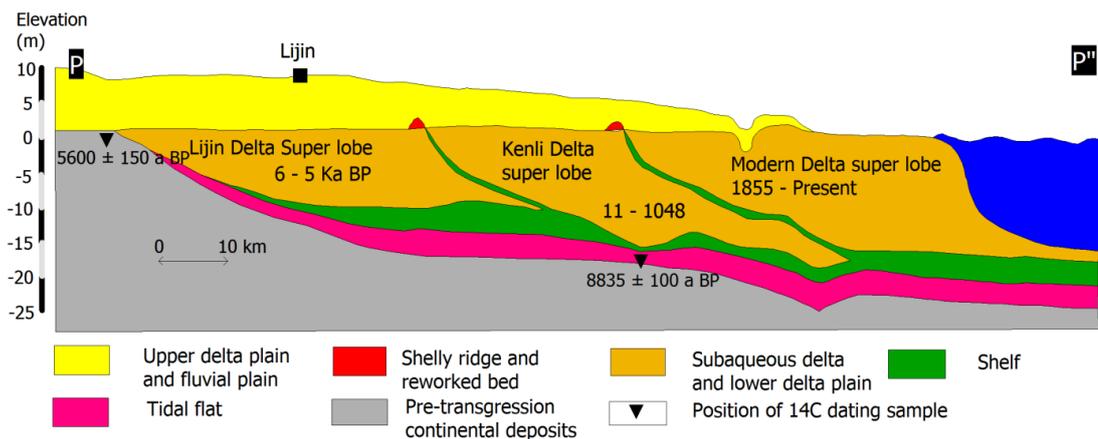


**Figure 4.3 Cross-section through three delta superlobes of the Yellow River delta complex: the Lijin delta superlobe, the Kenli delta superlobe and the modern delta superlobe, after (Xue, 1993). Elevation is above mean sea level. The location of this profile (PP") is given in Fig. 4.2.**

Recent coastline changes in the modern Yellow River delta are associated with the channel shifts. For example, the river mouth of Diaokou Promontory (Channel 9 in Fig. 4.2) extended about 10km seaward between February 1964 and April 1965. However, the coast near Diaokou Promontory retreated 6 km between 1976 and 1981 as the outlet of the Yellow River shifted to Qingshuigou Promontory (Channel 10 in Fig. 4.2) in 1976 (Ren and Shi, 1986). Multi temporal Landsat MSS and TM images from 1976 to 2000 were used to calculate the distance, accretion area, and erosion area due to shoreline movement between different image acquisitions (Chu et al., 2006). Another study explored the relationships between the accretion-erosion of land and the runoff and sediment load of the Yellow River (Cui and Li, 2011).

The rate of aggradation in the Yellow River delta is roughly indicated by Borehole G-96, near the 1964-1976 Diaokou Promontory of the Yellow River delta, where a subaqueous delta stratum with $^{14}$C age of 3850±80 BP occurs at a depth of -17.2 m (Gao et al., 1989). Detailed sediment analyses and high resolution radiocarbon dating were done on mollusc shells subsamples of the borehole taken from two sites on the present Yellow River: H9601 and H9602 (Fig. 4.1 and 4.4) in order to clarify the Holocene development of the Yellow River delta by *Saito et al*. (2000). The lower, middle and upper facies are terrestrial/fluvial facies, delta front to prodelta facies, and nature levee or flood plain facies respectively from their borehole analysis (Fig. 4.4). Both of H9601 and H9602 show rapid accumulation from 2 to 1 kaBP that can be correlated with super lobe 7 (11-1048 AD) (Fig. 4.1). There is a sharp contact at 17.5 m in H9602 from approximately 1 KaBP to 0.1 KaBP in radio carbon. It coincides with the 1855 river avulsion implying that the overlying sediment is correlated with super lobe 10 (Fig. 4.1) (Saito et al., 2000). Based on paleogeographic maps H9602 emerged from the sea in 1934 (Saito et al., 2000).

(a)

H9601 (Elevation +5.5 m)

| Depth (m) | C 14 age (a B.P.) | Hole I III | Lithology | Sample position | Lithological description | Sedimentary facies | Remarks |

Dark reddish grey clayer silt

Greyish brown clayer silt

Fluvial facies (natural levee or flood plain)

Greyish brown silt

Dark greyish brown silt-very fine sand

Very dark greyish brown very fine sand

Delta front to prodelta facies

Super lobe 7 (11-1048)

2150±50

1330-1335
1380-1385

Dark grey silt

13.5 m

1420-1425
1470-1475

Dark grey very fine sand

Super lobe 6 (602 BC -11 AD)

2590±40

15 m

3130±50
3120±50

1530-1535

3990±50
3620±50

1580-1585

Very dark grey clay

1620-1625

1743-1745
1780-1785

Greyish brown - dark greyish brown very fine sand

reworked of bed bearring molluscan shell

4630±60
3100±50
4180±60
4250±60
5310±50

1820-1825

Base of Holocene marine bed

5050±50

1930-1935
1970-1975

Sharp contact

2050-2055
2090-2095
2110-2115

Greyish brown very fine sand

Terrestrial/ fluvial facies

Late Pleistocene sediments

47000±1500
46730±1500

2210-2215
2250-2255

Grain size

very fine sand
silt
clay

Thin lamination

Molluscan shells

Concretion

Core recovered

Ripple cross lamination

Plant fragments

Bioturbated

**Figure 4.4 Boreholes H9601 (a) and H9602 (b) in the Yellow River delta (Yi et al., 2003, Saito et al., 2000). The locations of H9601 and H9602 are given in Fig. 4.1b.**

Based on deposit lithology, and soil mechanics relations, not on direct measurement, *Shi et al.* (2007) estimated that the total consolidation of the 14 m thick clay layers is approximately 1.44 m, and 1.52 m for the 20 m thick clay layers. According to their

calculation, consolidation of a 15m thick silt layer can be more than 95% complete in a period of about 12 hours to 1 week in the Yellow River delta. *Shi et al*. (2007) suggested that it is not necessary to estimate the consolidation of silt-dominated deposits as this proceeds so fast that consolidation after 1 week should be negligible. However, *Becker and Sultan* (2009) suggested that an older depositional centre (8000–2500 yr BP) in Nile Delta is still subsiding at 2~6 mm/yr, which is slower than the youngest depositional centre (3500-Present) in Nile Delta of 8 mm/yr, but still significant. The more likely places where relative sediment consolidation differences persist are recently deposited areas. For interpreting InSAR data, the relevant questions are: (i) how much consolidation is completed before the sediment column emerge above sea level, as the InSAR technique cannot measure displacement under water? (ii) Are the magnitudes of remaining relative sediment compaction rates detectable from InSAR data subject to noise and to the strength of other signals?

Addressing the impact of relative sediment consolidation differences is made difficult because other displacements may also contribute to the total Earth surface displacement. *Cheng* (1991) estimated the terrain of the bottom of the 1855~Present delta from 83 boreholes from the 1980s. From a previously digitized the bathymetric charts of 1855 (Wang and Huang, 1988), *Shi et al*. (2007) made a displacement map of delta bottom by comparing the borehole and bathymetric terrains (Fig. 4.5). Subsidence is observed at the bottom of the 1855~Present modern Yellow River delta with three subsidence centres seen on the map. Maximum subsidence is about 8~10 meters in over 125 years. This map indicates that there may be large displacements from underlying the modern Yellow River delta bottom and the displacement might be seen from the Earth's surface.
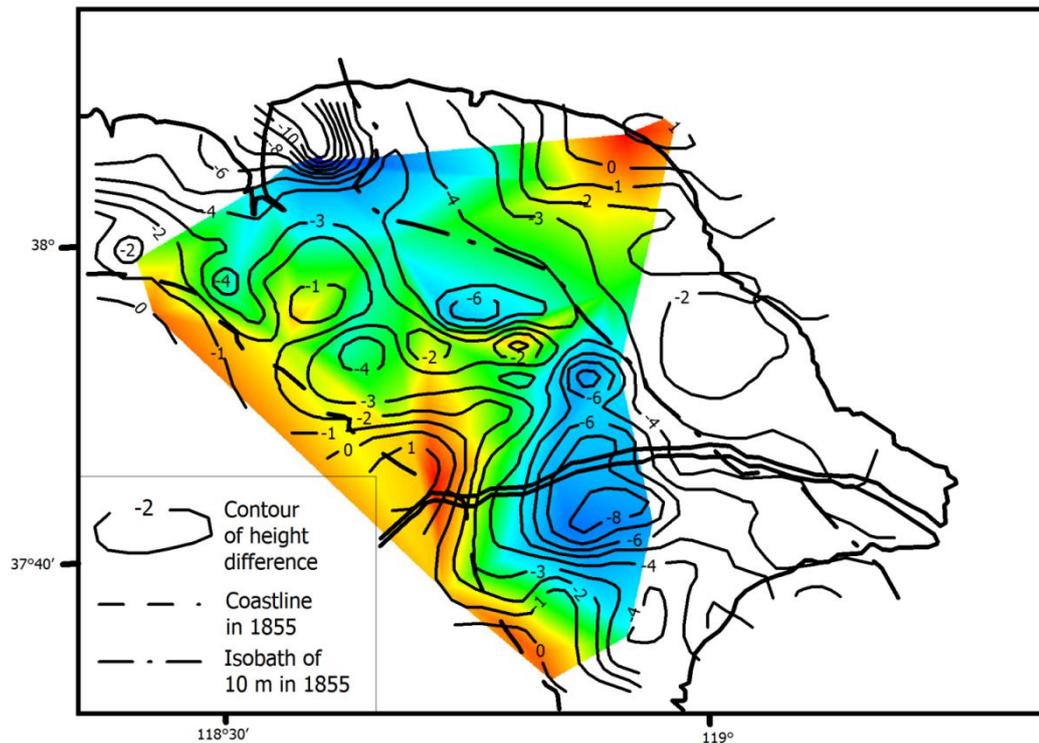
**Figure 4.5 Terrain changes of modern Yellow River delta bottom between 1855 and 1980s using bathymetry records and boreholes after (Shi et al., 2007, Cheng, 1991). The background is a triangular irregular network (TIN) interpolation of the contours. The contours are in one meter intervals. Negative values mean that the delta bottom is lowered.**

## 4.1.3 Shallow sediment samples from the Yellow River delta

Studies of zonal variations in particle size of the last glacial loess and case studies of modern dust storms have indicated that the aeolian dust accumulated on the Loess Plateau is mainly derived from the desert regions to the northwest (Sun, 2002b). In the Loess Plateau, quartz is the most abundant mineral comprising about 50% of the loess. Quartz, feldspar, mica and calcite together account for more than 90% of the total (Sun, 2002a, Jia and Wang, 2011).

Sediment samples were collected from the Yellow River delta in September 2010 (Fig. 4.6). Grain size was determined using a Coulter LS 230 laser diffraction particle size analyzer (Blott et al., 2004). The Laser firstly passes a projection lens, which gives beam of constant intensity, and secondly a Fourier lens, which converges this beam. The waterborne suspended particles flow through the sample cell in the path of the laser beam. Large particles scatter light at small angles relative to the laser beam and small particles scatter light at large angles (Hackley et al., 2004). The resultant scattering pattern is analyzed to calculate the size of the particle. Each sample, 21 in total, was analysed a minimum of two times, with a total of 6 runs, with further tests carried out for samples

with unusual particle size distribution patterns. Scanning Electron Microscopy (SEM) imaging was used to analyze the mineralogy, shape, roundness and sorting of the samples.
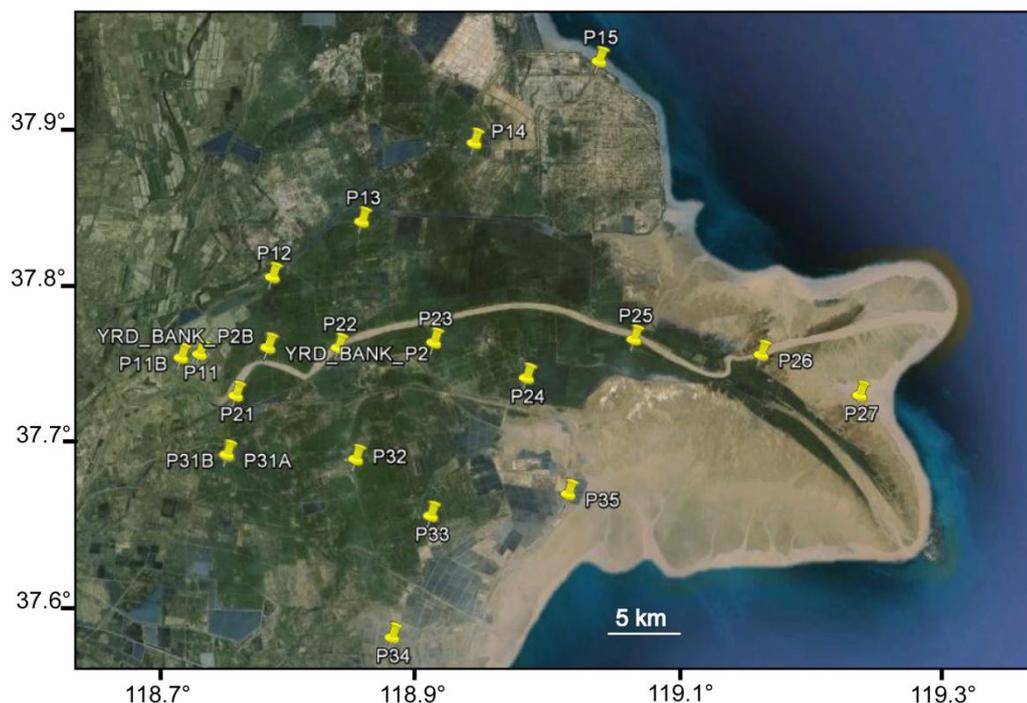


**Figure 4.6 Sampling locations in the Yellow River delta. Background is a Google earth image. Sample list is given in Appendix A.1.**
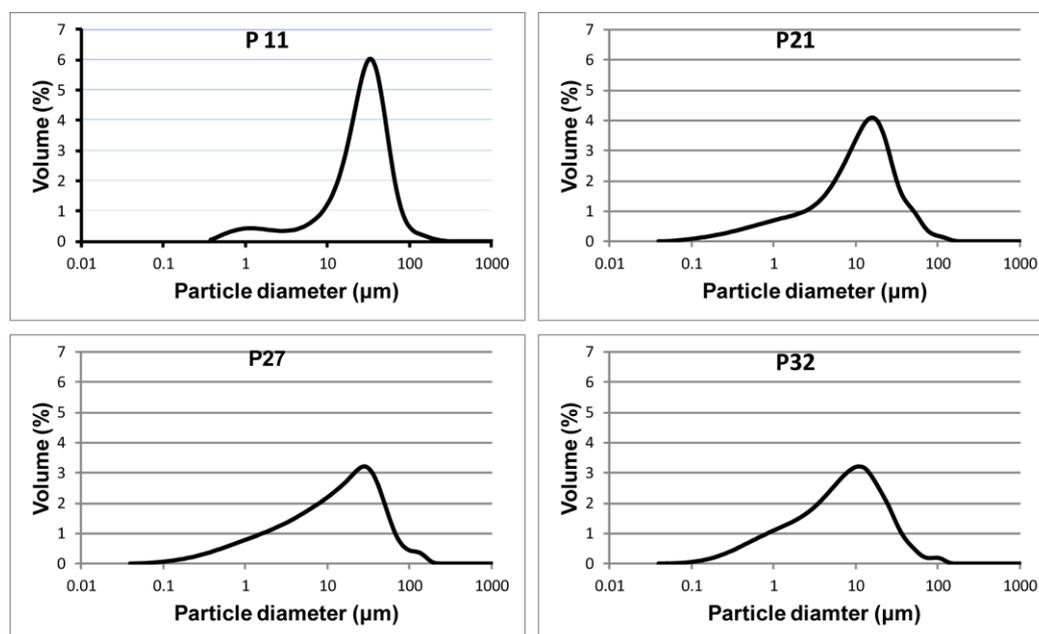


**Figure 4.7 Differential volume particle size for samples P11, P21, P27 and P32 from Yellow River delta. Differential volume particle size distribution is a function giving the fractional volume of particles falling within a series of specified size intervals versus the characteristic size for the interval (Hackley et al., 2004). Particle size of all samples are given in Appendix A.2**

Although several samples (e.g. P31A and P31B) include occasional coarse grains ranging up to 600 μm, nearly all of the sediment lies in the range from 0.04 ~ 200 μm (Fig. 4.7).

Except for samples YRD_BANK_P2, P31A and P31B, the mean particle size of the remaining 18 samples lies within the silt classification with modal sizes from 4-60 μm. The mean particle size for sediment samples collected over the delta is 25.89 μm (Table 4.2). The particle size supports the view that the provenance of sediments in Yellow River delta is loess.

**Table 4.2 Particle size statistics for shallow samples collected from the Yellow River delta. Mean is the average particle size. Sorting is the standard deviation of particle size, reflecting the spread of particles around the average (Blott and Pye, 2001). The skewness characterizes the asymmetry of a distribution to one side of the average (Blott and Pye, 2001). A positive value of skewness signifies a distribution with a tail extending towards greater particle size, whilst a negative value signifies a distribution with a tail extending towards smaller particle size (Press et al., 1997). The kurtosis measures the peakness or flatness relative to a normal distribution (Press et al., 1997) and is a degree of concentration of grains relative to the average (Blott and Pye, 2001). Sorting, skewness and kurtosis were calculated using the formulae given by Folk and Ward (1957). Note that phi units are defined as $phi = -log_2 D$ ie log to the base 2 of the size D, which is in mm.**

| Sample | Mean particle size (μm/microns) | Sorting (phi units) | Skewness | Kurtosis |
|---|---|---|---|---|
| P11 | 25.59 | 1.39 | -0.38 | 3.08 |
| P11B | 28.88 | 1.66 | -0.45 | 4.09 |
| P12 | 40.41 | 1.45 | -0.41 | 3.19 |
| P13 | 45.02 | 1.36 | -0.42 | 2.98 |
| P14 | 5.64 | 2.03 | -0.10 | 7.53 |
| P15 | 33.75 | 1.41 | -0.36 | 3.01 |
| YRD_BANK_P2 | 3.75 | 1.45 | -0.10 | 3.87 |
| YRD_BANK_P2B | 35.68 | 1.51 | -0.46 | 3.39 |
| P21 | 9.21 | 1.85 | -0.33 | 5.71 |
| P22 | 17.52 | 1.59 | -0.37 | 4.12 |
| P23 | 46.13 | 1.19 | -0.41 | 2.08 |
| P24 | 18.76 | 1.73 | -0.31 | 5.13 |
| P25 | 5.03 | 2.08 | -0.06 | 7.69 |
| P26 | 6.99 | 2.07 | -0.18 | 7.78 |
| P27 | 10.59 | 2.10 | -0.29 | 8.18 |
| P31A | 66.27 | 1.33 | -0.49 | 2.39 |
| P31B | 72.43 | 1.04 | -0.38 | 1.59 |
| P32 | 6.04 | 1.92 | -0.23 | 6.64 |
| P33 | 24.07 | 1.80 | -0.41 | 5.25 |
| P34 | 32.32 | 1.43 | -0.43 | 3.02 |
| P35 | 9.61 | 1.83 | -0.29 | 5.88 |
| Mean of mean particle size (μm) | 25.89 | | | |

Mineralogy was quantified using the software ImageJ (Ferreira and Rasband, 2006) The major elements are represented by different colour bands that can be isolated by filtering (thresholding) the image to determine the percentage of the area that the element constitutes. Mineralogy results from six SEM samples are given in Table 4.3. Quartz (Fig. 4.8) is found to be the dominant mineral with 60~65% abundance, which agrees well with the mineralogy of loess seen by *Nemecz et al*. (2000), but is 10~15% higher than the 50%

abundance of quartz in Loess Plateau seen by Sun (2002a). Note that the 50% abundance is in a selected size fraction, which is not clear in (Sun, 2002a) but can be ($<$20 μm) as in (Sun, 2002b). Calcite, feldspar and biotitie mica are also found with small abundances of 5-8%, 5-10% and 2-5% respectively. There are also 20-25% clay minerals, which are mainly smectite and illite.

**Table 4.3 Mineralogy results from six samples: P11, P15, P24, P27, P31A, and P34.**

| Mineral | Quartz | Calcite | K-feldspar and plagioclase feldspar | Biotite mica | Clay minerals |
|---------|--------|---------|-------------------------------------|--------------|---------------|
| Abundance | 60-65% | 5-8% | 5-10% | 2-5% | 20-25% |
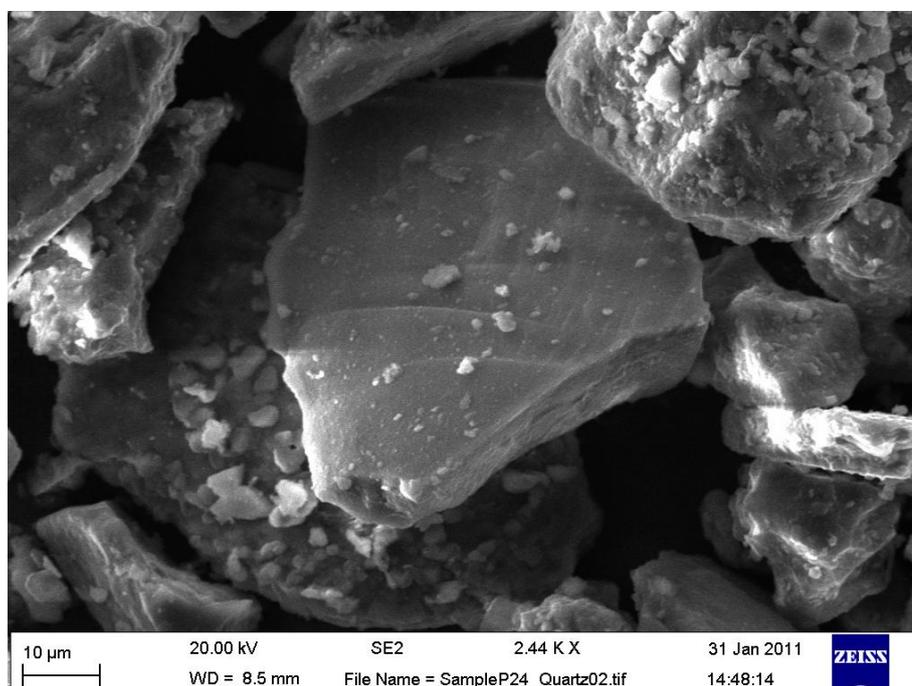


**Figure 4.8 SEM image showing a quartz grain in sample P24. This central quartz crystal exhibits the dominant angular, tabular form of quartz grains from the delta. Some clay-sized particles are coating the silt-sized particle behind.**

*Powers* (1953) proposed a roundness scale for sedimentary particles. The particles from four samples were divided into the six classes proposed by *Powers* [1953] and were split into two sphericity classes (Table 4.4). 10% of the particles belong to the high sphericity class and the other 90% particles have low sphericity e.g. the tabular quartz particle in Figure 4.8. In the low sphericity class, the sub-angular, angular and very angular particles account for 15.6%, 37.8% and 35.7% of the particles respectively, adding up to a total of 89.1%.

**Table 4.4 Roundness of 384 particles from four samples: P11, P24, P31A, and P34. The roundness of a particle depends on the sharpness of the edges and corners rather than the shape (Powers, 1953). For example, a smooth prolate spheroid will be belong to low sphericity model and well rounded scale with this standard.**

|              | High sphericity | Low sphericity |
|--------------|-----------------|----------------|
| Very angular | 0               | 137            |
| Angular      | 24              | 145            |
| Sub angular  | 14              | 60             |
| Sub rounded  | 1               | 3              |
| Rounded      | 0               | 0              |
| Well rounded | 0               | 0              |

These samples show similar physical properties to the Loess Plateau deposits, including the dominant quartz composition of 60~65% (Fig. 4.8), dominant silt size particles (10-60μm) and angular, tabular shape. This suggests that the particles deposited in the delta region are not obviously rounded during transport from the source region in the Loess plateau to the Yellow River delta, although the increase in quartz abundance does indicate some increase in sediment maturity.

Previous studies show rapid increase of roundness for fluvial pebbles in the first few kilometres from where they initiate (Gregory and Cullingford, 1974, Scott, 1967). However, *McPherson* (1971) find the downstream change in pebble size is the result of selective river transport not by abrasion due to the insignificant change of particle roundness. *Hoey and Bluck* (1999) further suggested that the main over downstream fining of river gravels can be the volume of sediment supplied from within the drainage basin. These studies are based on coarse fluvial particles. *Russell* (1955) suggested that sand-sized grains are actually rounded more slowly by abrasion than are larger particles. The dominant tabular, angular particles (Table 4.4) seen from the SEM images may suggest insignificant abrasion on silt sized particles.

Another kind of explanation is based on the effect of progressive sorting in transportation rather than abrasion on particles proposed by *Wadell* (1932). The transportation of sedimentary particles by water involves rolling and suspension. A sphere has the greatest relative volume with the smallest surface, indicative of a greater setting velocity than any other shape of the same volume and density (Wadell, 1932). If movement is by suspension, grains of low sphericity tend to be transported downstream to the place of final deposition. This is because the low sphericity particles remain longer in suspension due to higher surface volume ratio (Russell, 1955). If movement is dominantly by rolling, oppositely, grains of high sphericity roll more easily and rapidly than tabular grains of lower sphericity

(Russell, 1955). The dominant low sphericity particles (Table 4.4) in SEM images may also suggest a progressive sorting effect on particle shape by selection during transport.

*Russell* (1955) further pointed out that the effectiveness of this type of sorting has not been determined because most the bed load moves by saltation (Nishimura and Hunt, 2000) which is an intermediate stage between rolling and suspension. He also mentioned the suspended load of streams show the effects of sorting according to shape in the relative abundance of low sphericity grains. The Yellow River is characterized by suspension load rather than bed load (Wang et al., 2006, Qiao et al., 2010). Hence the transportation of particles by suspension (Halow, 1973) is considered reasonable.

Some key points from Section 4.1 are:

- The Loess plateau is the major source of the shallow sediments in the Yellow River delta. The research area within the modern Yellow River delta has been deposited after 1855. Shallow sediments composition differences are not expected to be related with obvious non-uniform displacement signals observed from InSAR as they are consistent across the delta.

- The observed tabular angular particle shape can be related to insignificant abrasion affecting silt-sized particles and the predominance of suspension as the particles were transported downstream.

## 4.2   Geology of the Gudao oilfield

The Gudao oilfield is located in the east part of the Zhanhua sag (Fig. 4.9) of the Jiyang depression (Fig. 4.10) in the Bohaiwan Basin. The Gudao oilfield reserves are $4 \times 10^8$ tonnes of oil and $47 \times 10^8 \, \text{m}^3$ of natural gas. The tertiary sandstone reservoir is a draped anticline (Lu et al., 2005, Zhang et al., 2004), which could form the petroleum trap (Hyne, 1991). The Gudao oilfield (Fig. 4.10) is controlled by Gunan fault to the south, Gubei fault zone to the north, and is gently dipping on its east and west sides This kind of structure facilitates the migration of petroleum from Bonan, Gunan and Gubei hydrocarbon sources to the Gudao oilfield (Lu et al., 2005).
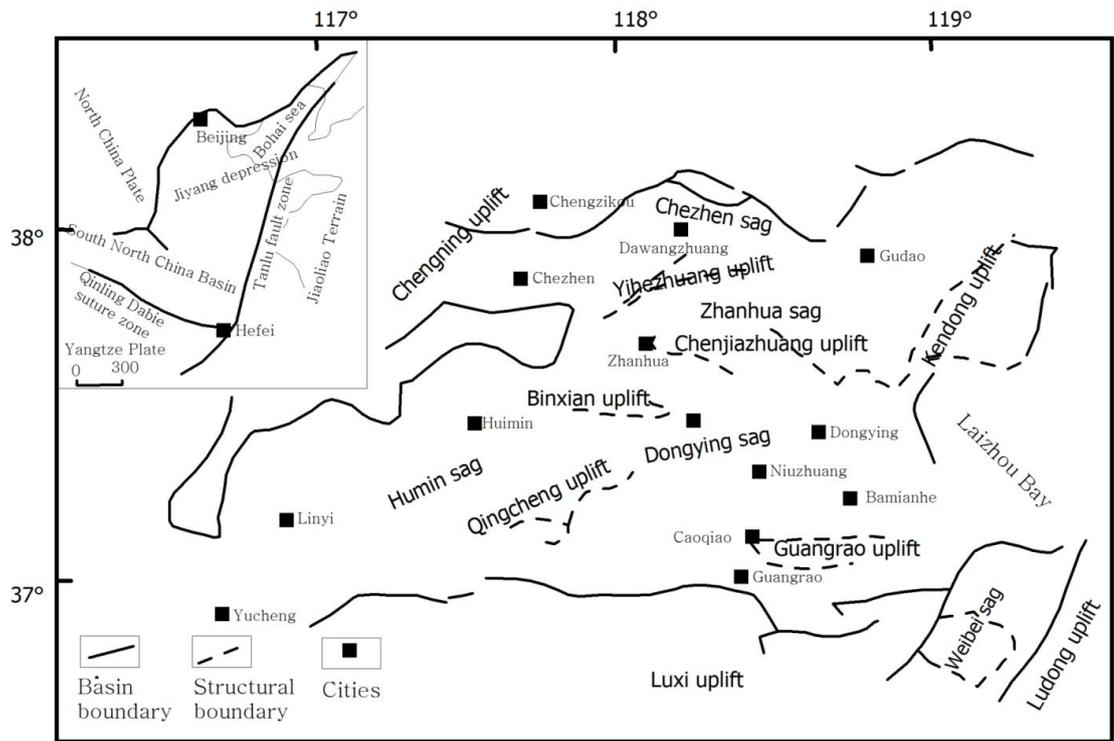
**Figure 4.9 Tectonic sketch of Jiyang depression (Gong et al., 2004, Zhu et al., 2005, Zhang et al., 2004).**

## 4.2.1 Stratigraphy
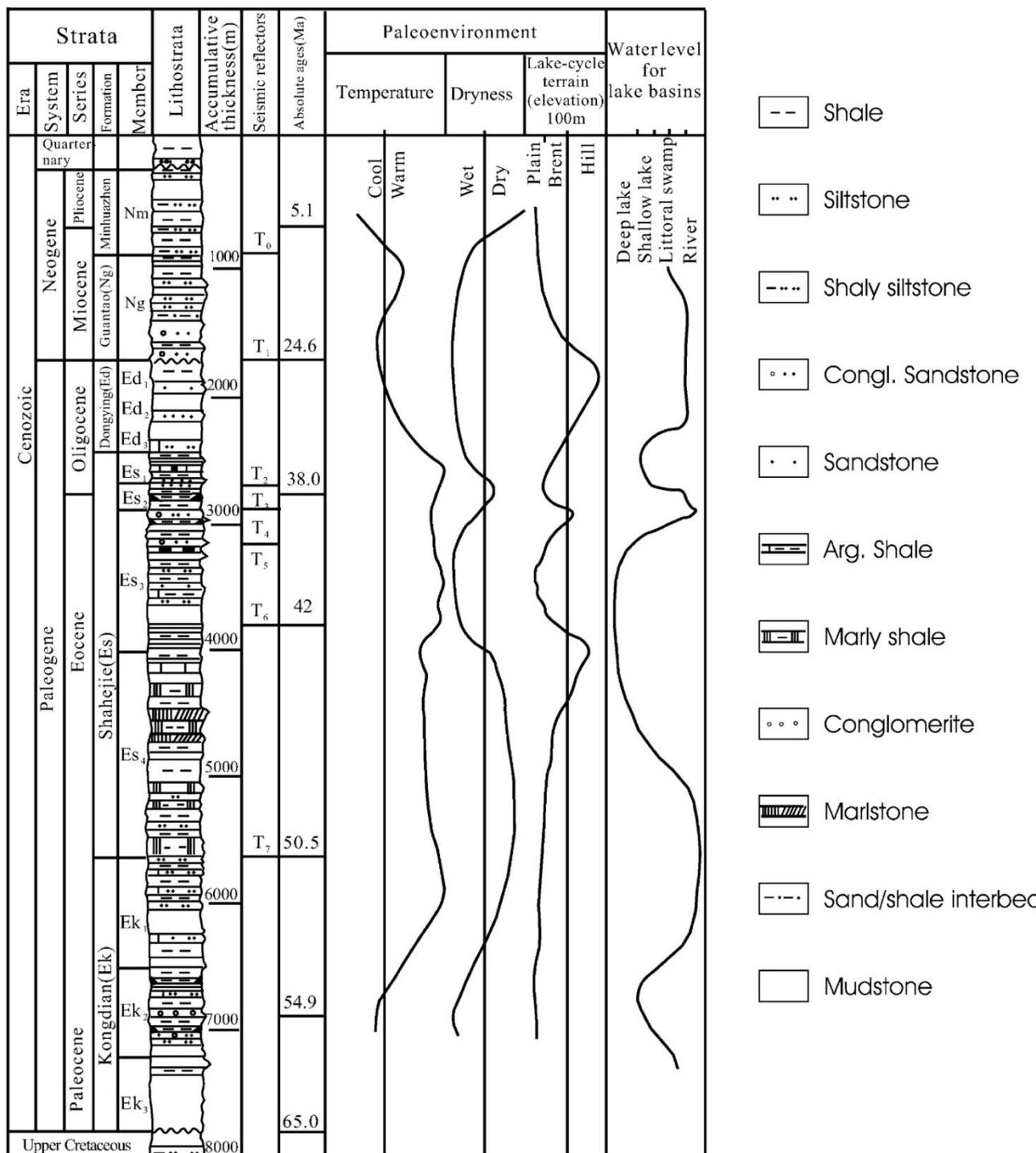


**Figure 4.10 Stratigraphy of Jiyang depression in Bohaiwan Basin, reproduced from (Zhang et al., 2004).**

The area of the current Northern China Plain (NCP) experienced widespread uplift and erosion after the second phase of Himalayan orogeny (Ren and Xiao, 2002). Within the Bohaiwan Basin, sediments are deposited on uplifts and sags in the Guantao formation, flattening the topography. Within the Gudao area, the developments are characterized by initial rift in Kongdian formation, rift filling in Shahejie formation, and sag filling in

Guantao and Minghuazhen formations by fluvial depositions (Xiong, 2011). For Gudao oilfield, oil bearing strata are within the Guantao and Minghuazhen formations (Fig. 4.10).

A sequence stratigraphic column of Guantao formation in Jiyang depression was also shown in another study (Sun, 2005). Sun identified the boundary between Neogene Guantao formation (Ng) and Neogene Minghuazhen formation (Nm) at 1250 m depth in borehole Gudong 14 as implying relatively deeper water delta front facies overlying relatively shallow water floodway facies which does not follow the sediment sequence expected for an aggrading delta.

The braided river deposit system is developed in Neogene Guantao formation (Ng) 7+8+9+10 members. Anastomosing river facies are found in upper Guantao formation 5+6 members(Lu et al., 2005). A meandering river and shallow water delta system deposited the Neogene Guantao formation (Ng) 3+4 members. Ng1+2 is characterized by meandering river facies in (Wang et al., 2004), but it is interpreted as anastomosing river facies in (Xiong, 2011), and it is described as flood plain facies in (Lu et al., 2005).

## 4.2.2 Structural geology of Gudao area

The Gudao area is located in Dongying City of Shandong province, and is to the north of the Yellow River mouth. It is located to the east of the Bonan oilfield, to the west of the Gudong oilfield, to the north of Hetan oilfield and to the south of Gubei slope zone (Fig. 4.11). The Gudao uplift is located between Gunan sag and Gubei slope zone. In the centre of Gudao uplift, lower Tertiary and Mesozoic strata are absent (Lu et al., 2005).

The upper part of Gudao uplift is the Gudao oilfield, whose main reservoir is the upper part of Guantao formation. The 15 km long and 6 km wide NEE-EW trending Gudao oilfield occupies about 90 km$^2$ with the oil reservoir of 1120~1350 m depth and 170~350 m thick (Xiong, 2011). Gudao oilfield occupies late Tertiary (Miocene) deposits, and is dominated by fluvial facies composed of clastic and argillaceous sedimentary rocks. It contains interbedded fine-grained sandstone, siltstone, and grayish-green, purplish-red mudstone (Xiong, 2011). Gas is produced from the Neogene Minghuazhen formation (Nm) and Neogene Guantao formation (Ng) 1+2 sand members. Ng1+2 sand members are 1120-1200 m deep with effective thickness of 2.6 m and reservoir store of 2.36 x 10$^6$ tonnes. Ng3+4+5+6 members form a well connected sandstone reservoir with significant oil storage. The oil is mainly stored in the Guantao formation sand members 3+4 with some

heavy oil in sand member 5. Oil is rarely present in the lower part of the Guantao formation or in the Shahejie formation (Lu et al., 2005, Xiong, 2011).
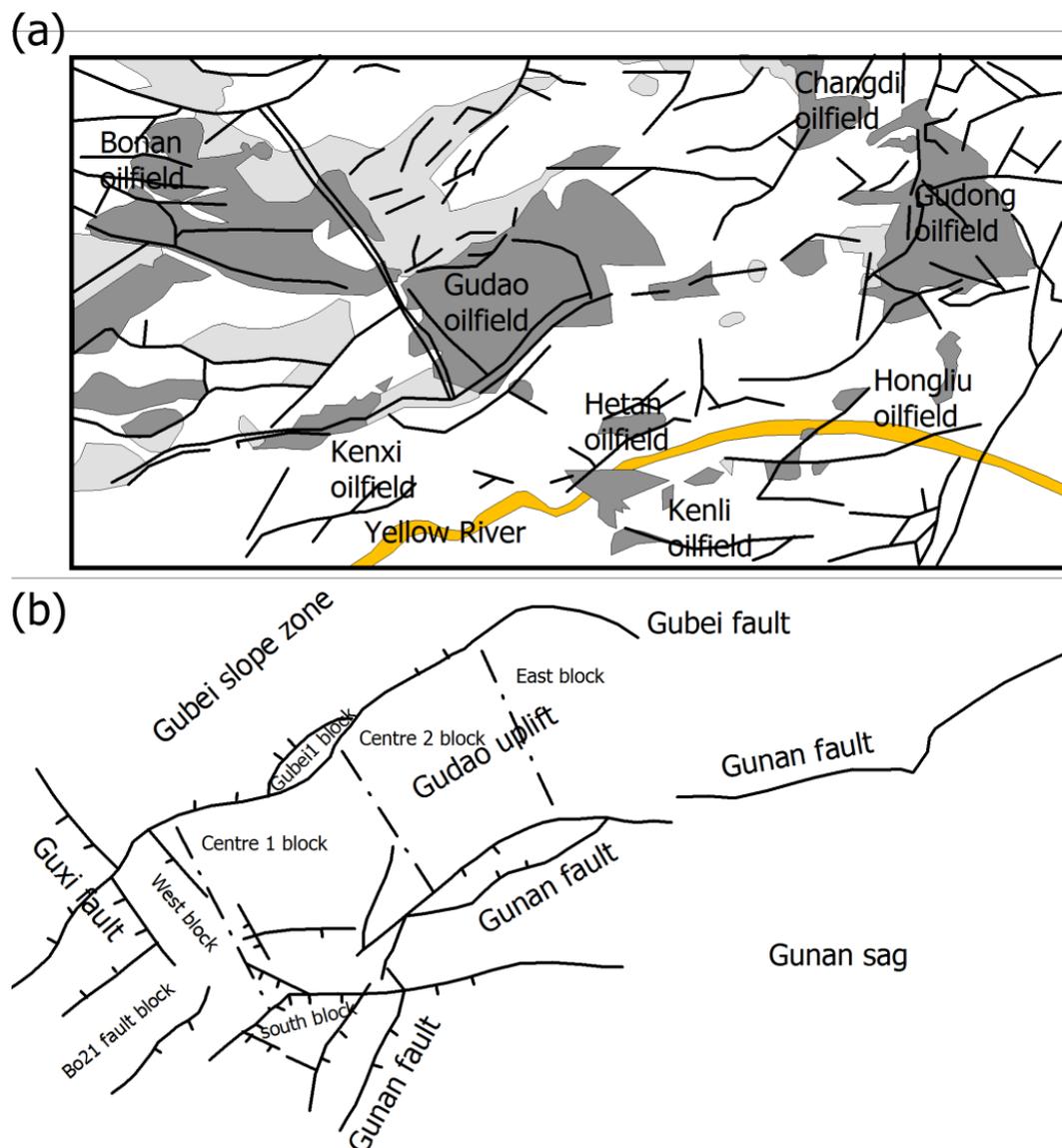


**Figure 4.11 Location and geological units of the Gudao oilfield, after (Lu et al., 2005). (a) The oilfields (dark grey), faults (black solid line) and Yellow River (Yellow strip) are shown. (b) Gunan sag, Gudao uplift and Gubei slope zone in the Gudao area are shown along with the Gubei, Guxi and Gunan faults. There are more than 20 faults, all normal faults (solid line), around Gudao uplift. There are 6 production blocks (bounded by dashed line) in the Gudao oilfield: Bo21 fault block; West block; Centre 1 block; Centre 2 block; East block and South block. Tags on the fault are dipping directions. Unfortunately, the scale and coordinates of this map are not given in (Lu et al., 2005).**

Gubei fault (Fig. 4.11) is 15 km long in Gudao area, roughly NE-SW striking, dipping 50 °~70 °to the northwest, with 50 m fault throw in Guantao formation and 1600 m fault throw in Ordovician (Yong, 2007). Gubei fault was more active in early Tertiary than late Tertiary with the expansion index decreased from 10.41 ~ 12.2 in Eogene (Palaeogene) Shahejie formation (Es) 2+3 members to 1.0 ~ 4.46 in Eogene (Palaeogene) Dongying

formation (Ed) and further to 0.92~1.36 in Neogene Minghuazhen formation (Nm) (Lu et al., 2005). Lu et al (2005) pointed out that the activity of Gubei fault is very low in Nm formation.

The total length of Gunan fault (Fig. 4.11) is 20 km in Gudao area, roughly NE-NEE striking, dipping 40 °~65 ° to SE-SSE, with fault throws of 1600 m in Ordovician (Yong, 2007), 1400 m in Eogene (Palaeogene) Shahejie formation (Es) 3 member (Lu et al., 2005) and 60 m in Neogene (Yong, 2007). In early Tertiary, tensional activity happened in Gunan fault, forming thick deposits in Gunan-Sanhecun sag with oil and gas resources (Lu et al., 2005, Yong, 2007). In the end of early Tertiary, compression activity took place in Gunan fault, lifting Gunan-Sanhecun sag. Gunan fault expansion indices decreased from 2.0~5.7 in Es2+3 to 0.9~1.14 in Nm.

Guxi fault (fractures) (Fig. 4.11) is smaller than Gubei and Gunan fault in size, NW striking, dipping 40 °~60 ° to the southwest. The activity of Guxi fault is weak before Eogene (Palaeogene) Dongying formation (Ed) with fault expansion index of 1.0 in Eogene (Palaeogene) Shahejie formation (Es) member 1. It is more active in Ed and Ng, getting weak again in Nm, with fault index of 3.26 in Ed, 1.17 in Ng2, 1.26 in Ng1 and 1.01 in Nm (Lu et al., 2005).

Gudao oilfield is connected with Gunan sag via Gunan fault, with Gubei sag via Gubei fault, and with Bonan sag via both the Guxi and Gubei faults (Lu et al., 2005, Hooper, 1991, Wang, 2011).

## 4.2.3 Reservoir Properties

Ng formation 3+4+5+6 members in Centre 1 block (Fig. 4.11) of Gudao oilfield are composed of fine sandstone, siltstone, argillaceous siltstone, and grayish green or purplish red mudstone from bottom up. The sandstone particles are poorly rounded, subangular, moderately sorted. Median particle size and other parameters are given in Table 4.5. Quartz has an abundance of 45~55%, feldspar 35~45% and detrital fragments contribute 10~20% (Lu et al., 2005). The Ng3 sand member is single wide channel with sand body pinching out in the channel margin and sand unit thickness of 2~6 m. Ng4+5 sand members have multiple channels as does Ng6 with part of the sand body pinching out in channel centre (Lu et al., 2005).

**Table 4.5 Upper Ng formation reservoir parameters in Centre 1 block of Gudao oilfield (Statistics from 12 cored wells) (Lu et al., 2005). Continuous porosity allows leakage and is distinguished from enclosed or blind porosity.**

|  | Ng1+2 | Ng3 | Ng4 | Ng5 | Ng6 |
|---|---|---|---|---|---|
| Median particle size (mm) | 0.117 | 0.121 | 0.118 | 0.142 | 0.201 |
| Sorting coefficient | 1.72 | 1.56 | 1.68 | N/A | N/A |
| Continuous porosity (%) | 35.1 | 33.7 | 32.5 | 33.1 | 32.1 |
| Air permeability ($10^{-3} \mu m^2$) | 1673 | 1340 | 1264 | 1486 | 3370 |
| Shale volume (%) | N/A | 10.1 | 10.3 | 9.4 | 8.0 |
| Carbonate volume (%) | 0.86 | 1.31 | 2.35 | 1.35 | 0.73 |

Ng formation 7+8+9+10 members in Centre 1 block are composed of sandstone and gravel. Mudstone in Ng8+9 is light grey or light grayish green. Mudstone in Ng7 is variegated, grayish yellow or purplish red. Purplish red mudstone is more common towards the surface in Ng7+8+9+10. Lithology often changes from gravel sandstone or fine grained sandstone directly to mudstone (Lu et al., 2005). The sandstone particles are poorly sorted, and their median particle size is 0.25-0.34 mm. Mineral abundance in Ng7+8+9+10 is 40-50% quartz and 20~40% feldspar, carbonates 20~30%, clays account for 5.0~12.0% of the rock, mainly in the cement. Dolomite content is generally 2%~3% (Lu et al., 2005).

Published data for Ng formation 3+4 members in northern Centre 2 block and Ng formation 3+4+5+6 members in South block of Gudao oilfield from (Lu et al., 2005) show some difference in mudstone content, particle roundness and sorting, but similar mineralogy with the Centre 1 block above.

During oil production, water is injected to increase pressure and stimulate production. Based on water saturation, the production is divided into low, medium, high or extremely high water cut stages. Gudao oilfield found in late 1960s started oil production in November 1971 and water injection began in April 1973. Operation is now at the high water cut stage. Specific values (Lu et al., 2005) showing shale volume decrease, median particle size decrease, porosity increase, permeability increase, and decrease of carbonates volume, shale volume, oil saturation and Irreducible water saturation from low to high water cut stages are given in Appendix B.1

Reservoir heterogeneity is observed in both horizontal and vertical directions in Gudao oilfield (Fig. 4.12). Insulating layers are impermeable or lowly permeable layers between sand bodies. The thickness of insulating layers can be $10^{-1} - 10^2$ meters and they can be

comprised of mudstone, shale or siltstone. A reservoir is divided into subcomponents by insulating layers or interlayer (Lu et al., 2005).
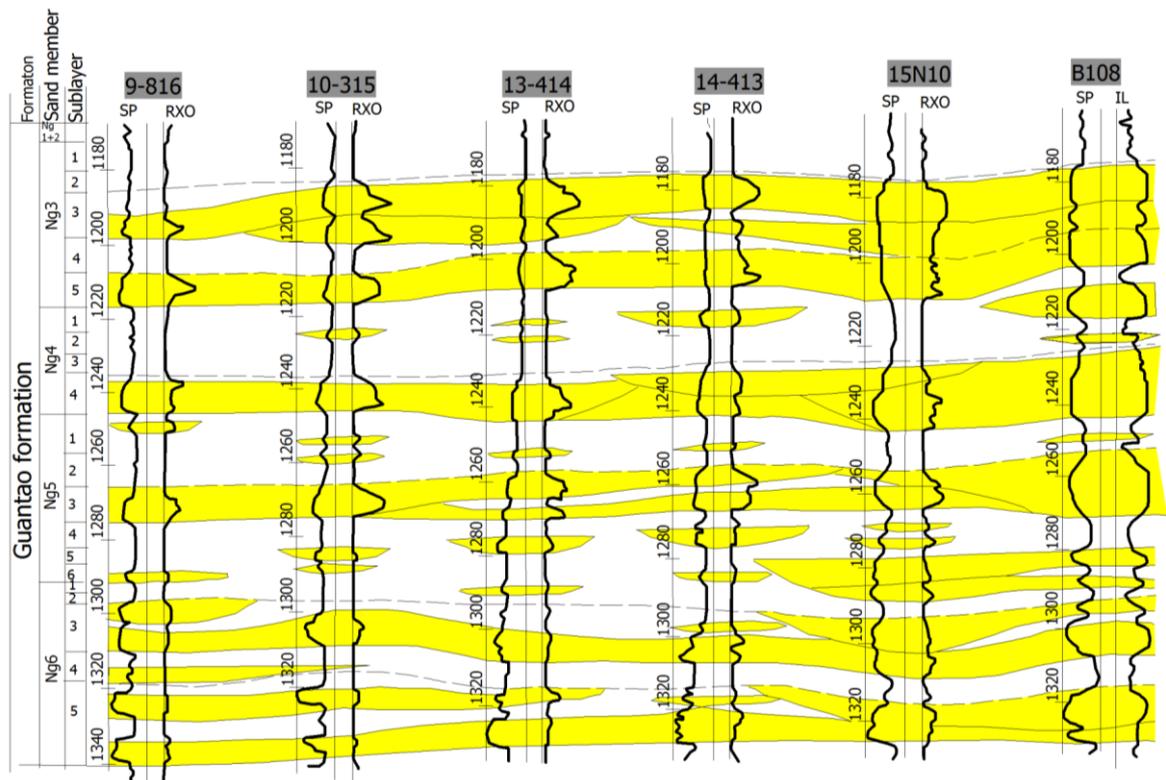


**Figure 4.12 Borehole cross section of upper Guantao formation 3-6 sand members, after (Lu et al., 2005). The SP is the Spontaneous potential (SP) curve, which is the natural potential difference between the borehole and the surface. SP log is used to characterize permeability, resistivity and correlations of the formations in oil industry. RXO (Flushed zone resistivity) is the resistivity of formation flushed zone in which movable fluid are replaced by mud during drilling. Channel sand is in Yellow. Borehole names are given on the top.**

Vertical reservoir thickness, effective thickness, porosity, permeability, shale volume, median particle size and oil saturation heterogeneity for the sub-layers in Ng3+4+5 sand members are given in Appendix B.2

Horizontal reservoir heterogeneity is related to the horizontal distribution, shape, continuity and permeability of sand bodies. For a single sand body, the shale volume, porosity, permeability can be variable in different directions (Lu et al., 2005) . The values are usually greater on average and more homogeneous in the direction parallel to the river than the perpendicular direction. Specific values are given in Appendix B.3

Some key points in Section 4.2 are:

- Gudao oilfield is a sandstone reservoir of 1120~1350 m depth and 170~350 m thick and porosity of 29~34%.

- Reservoir heterogeneities exist within the reservoir. Isotropic homogeneous medium is assumed for modelling, which might cause some differences between the observed and modelled displacement by reservoir compaction.

# Chapter 5 Surface displacements of the Yellow River delta from InSAR time series analysis

In this chapter, both PS and SBAS InSAR methods are employed to determine the Earth surface displacement fields in the Yellow River delta. Two adjacent tracks are used to obtain two independent surface displacements in this study. Comparisons between these two derived displacement fields are then performed to assess their accuracy.

## 5.1 Data availability

Affordable SAR data in Yellow River delta are from the C band ERS and Envisat Satellites. Although ERS and Envisat are in orbit for about 20 years in total, only three years Envisat ASAR data from 2007 to 2010 is used in this study for the following reasons:

- ERS-1 (July 1991~ March 2000) and ERS-2 (April 1995~ September 2011) data are available for the Yellow River delta. In 1990s, the Yellow River delta was mainly a vegetated area, whilst some residential and production area in Yellow River delta experienced fast development. As a result of temporal decorrelation, the density of stable pixels is too low for identification of displacement. ERS-2 has been operating without gyroscopes since February 2001, resulting in degradation of InSAR performance because of the high variation in Doppler Centre (DC) from one acquisition to another, which is known as Doppler decorrelation.

- Envisat ASAR data (March 2002 ~ May 2012) is also available for Yellow River delta. Although there are six radar images from Track 132 between 2003 and 2004, there is a two year data gap between 2005 and 2007. In October 2010, the orbit of the Envisat satellite was lowered by 17 km, which exceeds the length of critical baseline for InSAR. As a result, only Envisat ASAR data from 2007 to 2010 is used for this study.

Twenty-four SAR images from descending Track 132 (Table 5.1) and thirteen SAR images from descending Track 404 (Table 5.2) are used to determine surface displacements over the Yellow River Delta region in this study (Fig. 5.1). Descending refers to the travel of the satellite from north to south where observations are made from the east. Track 132 is in Image Swath 1 (IS1) mode with incidence angle range of 15.0°~22.9°. Track 404 is in

Image Swath 2 (IS2) mode with incidence angle of 19.2°~26.7°. For an identical pixel, the incidence angles of these two tracks are only slightly different.
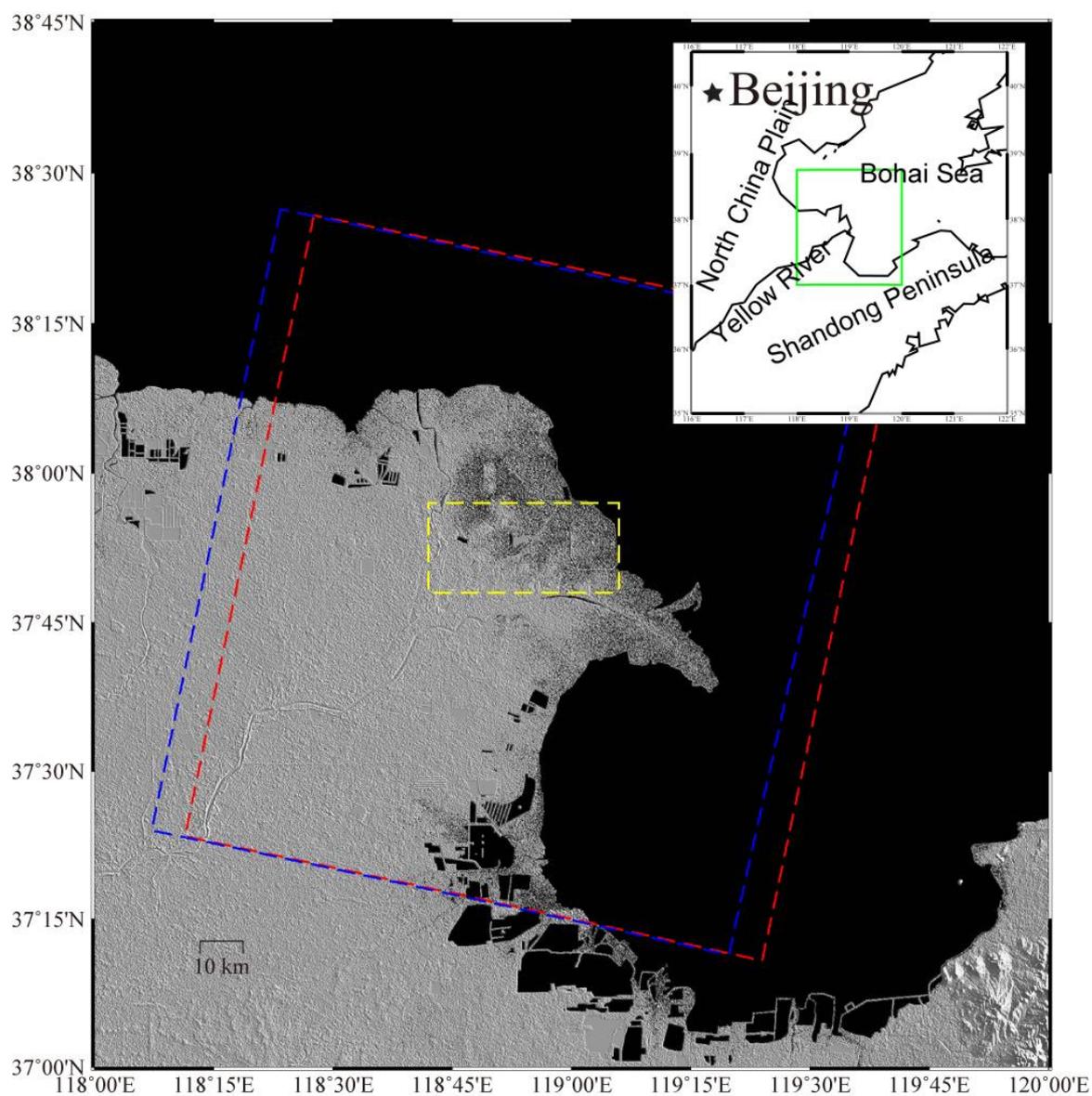


**Figure 5.1 Location of the study area in the Yellow River delta region. The study area is denoted by yellow dashed rectangle. The red dashed rectangle is Track 132. The blue dashed rectangle is Track 404. The green solid rectangle in the upper right small figure is the frame of large map. Background is SRTM, black areas are water surfaces (ocean and ponds). Yellow River can be vaguely seen on the DEM because of the dikes built for flood control.**

**Table. 5.1 SAR images archive of Track 132 (Reference date: 26-Jul-2007).**

| Scene No. | Acquisition date | Baseline perpendicular (m) | Scene No. | Acquisition date | Baseline perpendicular (m) |
|---|---|---|---|---|---|
| 1 | 01-Feb-2007 | -372 | 13 | 01-Jan-2009 | 158 |
| 2 | 08-Mar-2007 | 481 | 14 | 05-Feb-2009 | -292 |
| 3 | 12-Apr-2007 | -185 | 15 | 12-Mar-2009 | 520 |
| 4 | 17-May-2007 | -136 | 16 | 16-Apr-2009 | -208 |
| 5 | 21-Jun-2007 | 71 | 17 | 21-May-2009 | -24 |
| 6 | 26-Jul-2007 | 0 | 18 | 25-Jun-2009 | 342 |
| 7 | 08-Nov-2007 | 202 | 19 | 30-Jul-2009 | -6 |
| 8 | 17-Jan-2008 | -41 | 20 | 03-Sep-2009 | 312 |
| 9 | 21-Feb-2008 | -324 | 21 | 08-Oct-2009 | -99 |
| 10 | 27-Mar-2008 | 347 | 22 | 12-Nov-2009 | 289 |
| 11 | 23-Oct-2008 | 244 | 23 | 17-Dec-2009 | -308 |
| 12 | 27-Nov-2008 | -250 | 24 | 21-Jan-2010 | 267 |

**Table. 5.2 SAR images archive of Track 404 (Reference date: 05-September-2009).**

| Scene No. | Acquisition date | Baseline perpendicular (m) | Scene No. | Acquisition date | Baseline perpendicular (m) |
|---|---|---|---|---|---|
| 1 | 16-Jan-2007 | 592 | 7 | 07-Oct-2008 | 75 |
| 2 | 27-Mar-2007 | 535 | 8 | 16-Dec-2008 | -93 |
| 3 | 05-Jun-2007 | 125 | 9 | 31-Mar-2009 | 742 |
| 4 | 01-Jan-2008 | -275 | 10 | 05-May-2009 | 0 |
| 5 | 05-Feb-2008 | 200 | 11 | 09-Jun-2009 | 336 |
| 6 | 15-Apr-2008 | 335 | 12 | 27-Oct-2009 | 76 |

For the same set of SAR images, both PS and SBAS InSAR approaches are implemented using different networks (Fig. 5.2 and 5.3).
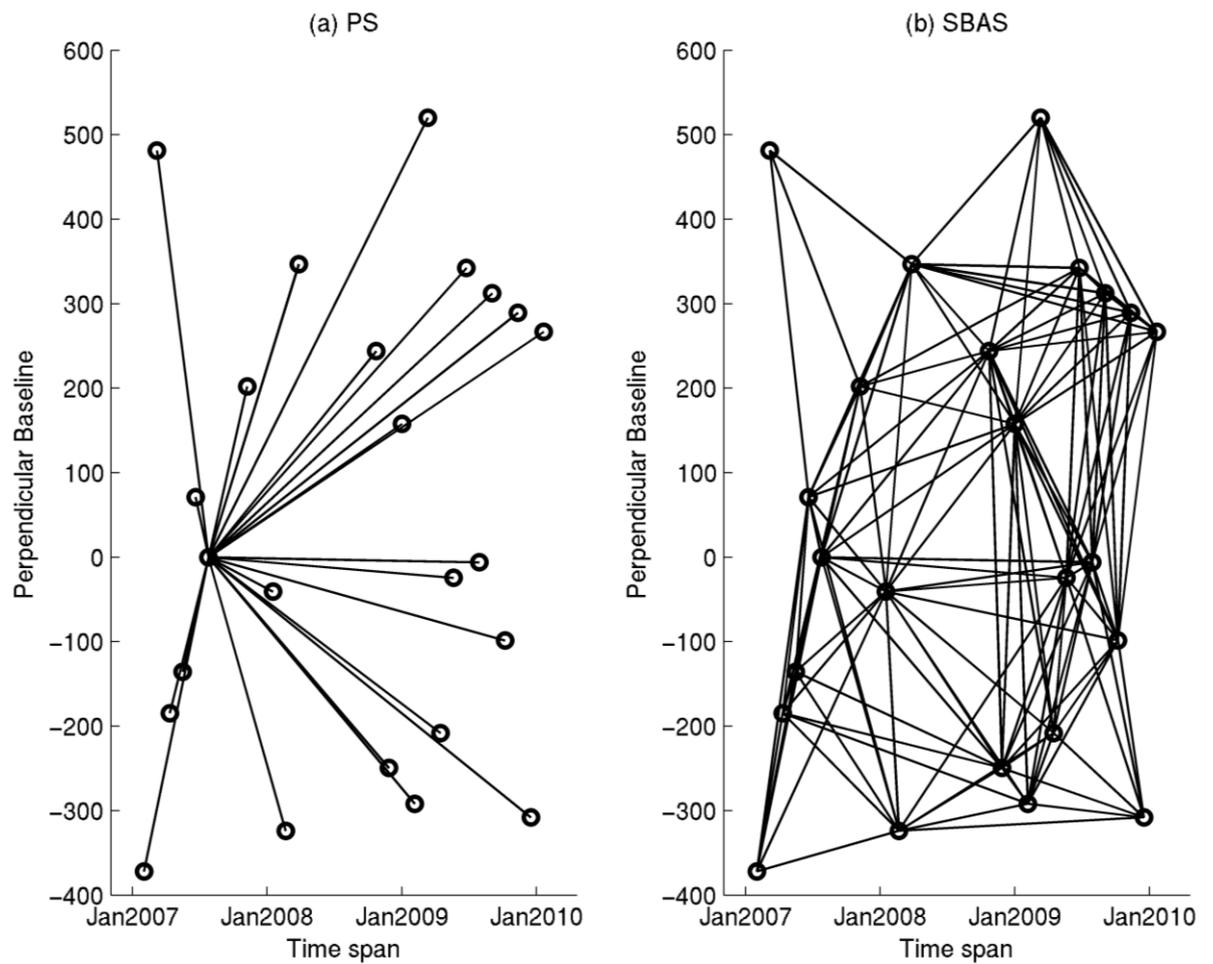
**Figure 5.2 Baseline network of Track 132. (a) PS network. (b) (Small baseline) SBAS network. Each circle is an SAR image and each edge is an SAR interferogram. PS interferograms are all connected with a single master scene, while multiple master scenes are used in the SBAS network.**
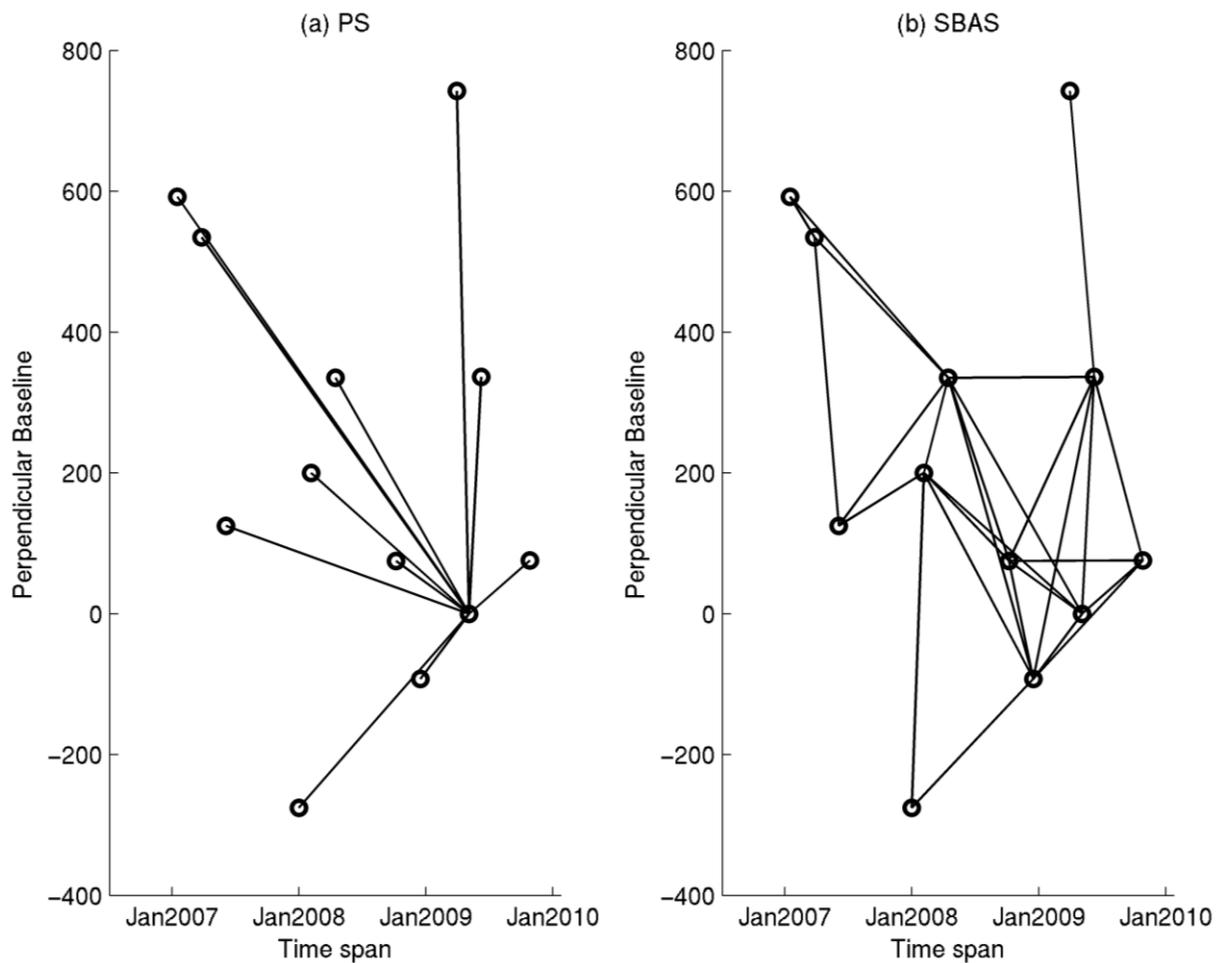
**Figure 5.3 Baseline network of Track 404. (a) PS network. (b) (Small baseline) SBAS network. Each circle is an SAR image and each edge is an SAR interferogram. PS interferograms are all connected with a single master scene, while multiple master scenes are used in SBAS interferograms.**

In the Yellow River delta, temporal decorrelation has a significant impact on interferograms (Fig. 5.4). The interferograms lose coherence fast with an increasing time interval. Compared with PS interferograms, SBAS interferograms have shorter spatial and temporal baselines. Hence interferograms with better coherence can be achieved by summing up several relevant interferograms in a small baseline network as shown in Figure 5.5.
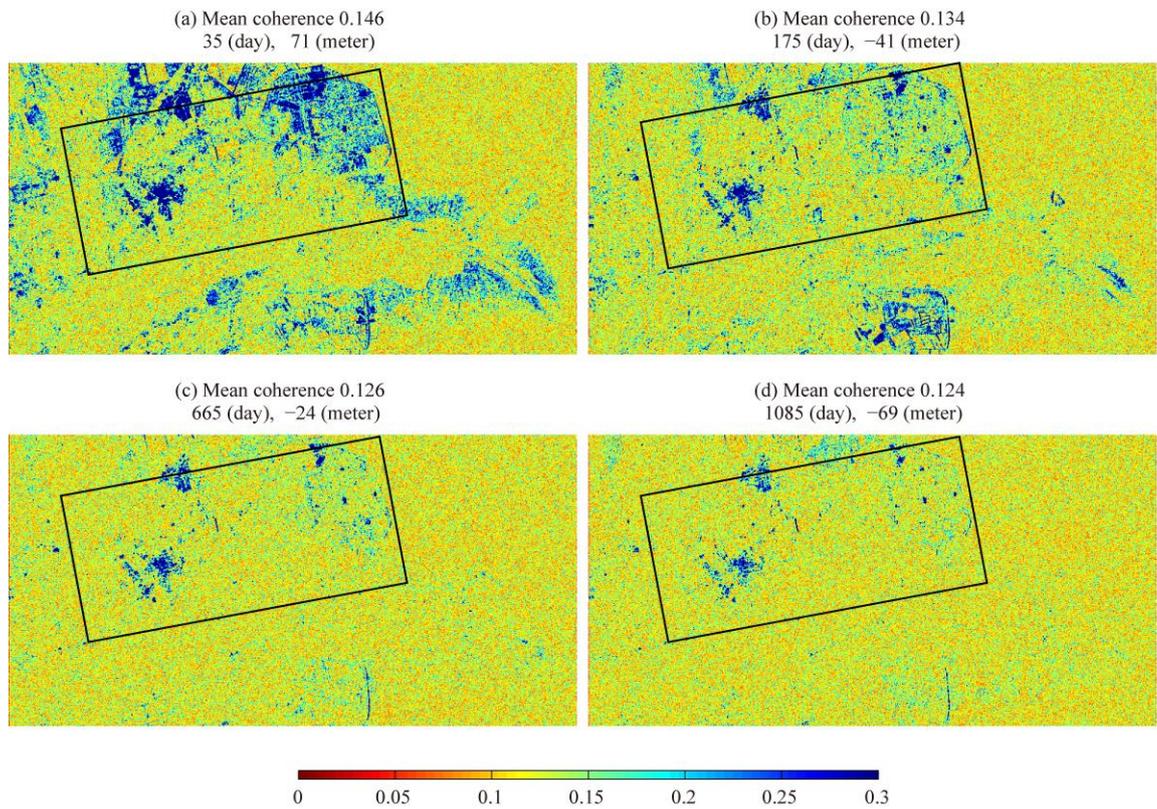
**Figure 5.4 Coherence of Yellow River delta interferograms in Track 132. There are $400 \times 775$ multi-looked pixels (near $100 \times 100$ m) in radar coordinates in the mapping area. Each interferogram (format: YYYYMMDD) is (a) $20070621 - 20070726$; (b) $20070726 - 20080117$; (c) $20070726 - 20090521$; (d) $20070726 - 20100715$. Since the percentages of pixels below coherence of 0.3 are 96.3%, 98.3%, 99.4%, and 99.6% for (a), (b), (c), and (d), the colour bar scale is set between 0 and 0.3. Pixels with coherences are below 0.2 account for 86.7%, 92.0%, 95.8% and 96.3% in (a), (b), (c), and (d) respectively. The area in black rectangle is retained after time series analysis.**
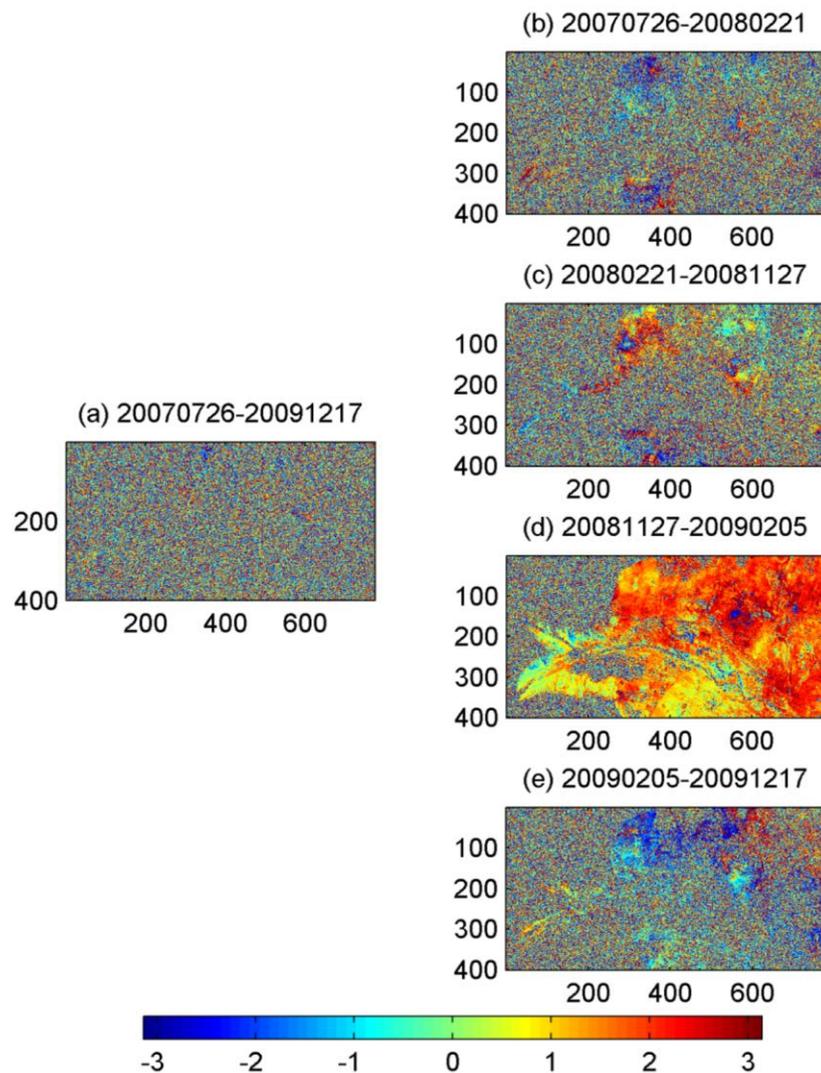
**Figure 5.5 Multi-looked interferograms of the Yellow River delta from Track 132. (a) PS interferogram of 875 days. (b), (c), (d) and (e) are four small baseline interferograms which can be added up to this period. Each title corresponds to the SAR acquisition times of the SAR images that form an interferogram.**

## 5.2 InSAR data processing

Satellite level 0 raw data is processed using the ROI_PAC package developed by Caltech/Jet Propulsion Laboratory (JPL) to generate SAR SLC images (Rosen et al., 2000). DORIS (Delft object-oriented radar interferometric software) developed by the Delft Institute of Earth Observation and Space Systems (DEOS) of Delft University of Technology is used to generate interferograms from SLC images (Kampes et al., 2003). StaMPS (Stanford method for persistent scatterers) is used to generate the displacement time series (Hooper, 2008, Hooper et al., 2007). Both PS and SBAS method incorporated in StaMPS are implemented for the Yellow River delta. PS (Fig. 5.6) and SDFP pixels (Fig. 5.7) are selected using phase analysis. The phase analysis includes the spatial correlation of phase values, the look angle error estimation with spatial baseline, and

statistics of the gamma values representing noise level of a pixel in time series (Section 3.3 in Chapter 3).
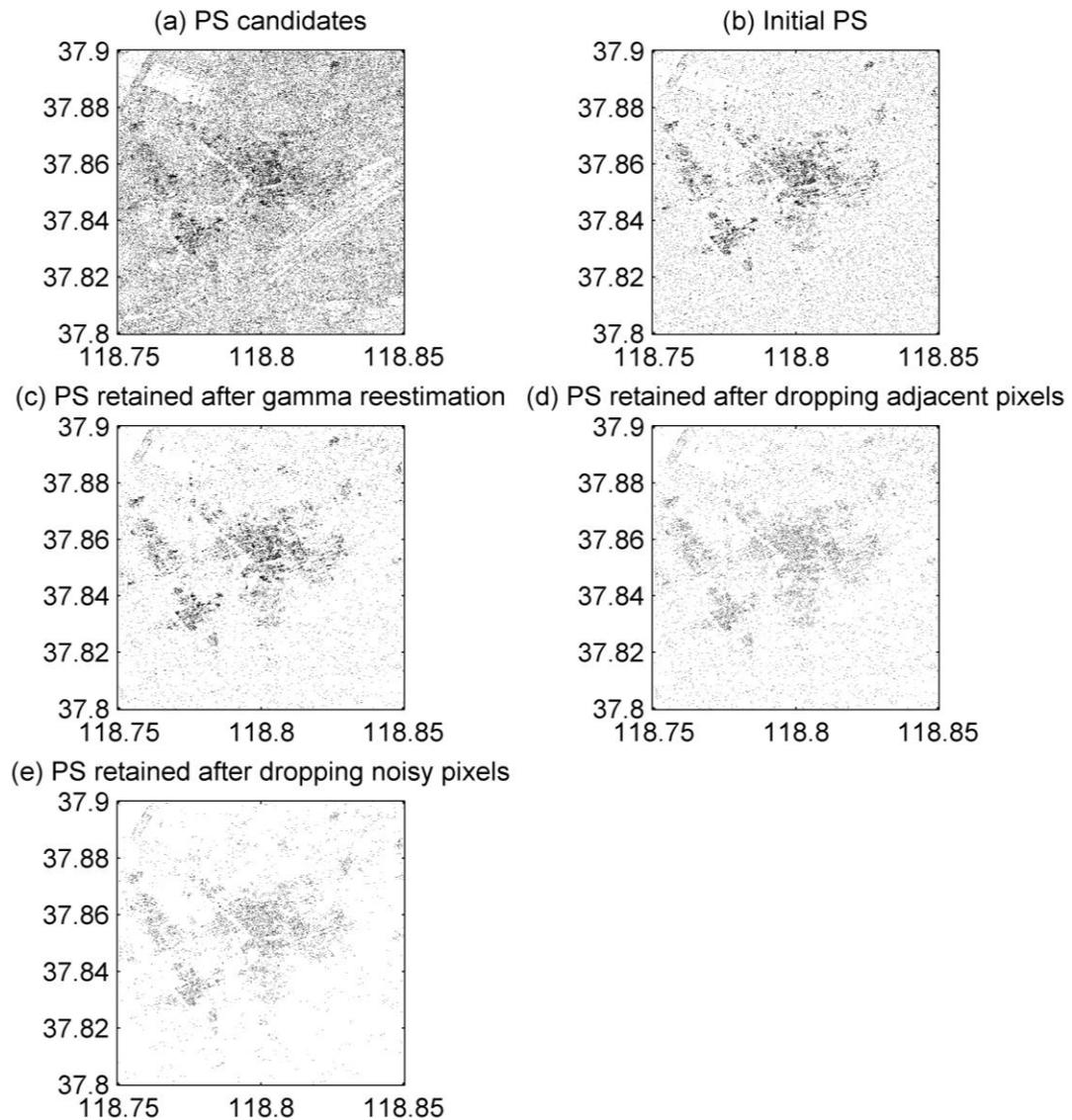


**Figure 5.6 An example of PS points retained after phase analysis in the Gudao Town of Yellow River delta from Track 132. (a) PS candidates under amplitude dispersion threshold. (b) Initial PS above gamma threshold. (c) PS points retained after gamma re-estimation. (d) PS retained after dropping adjacent pixels. Of all 600934 PS candidates in Yellow River delta, 219764 PS selected initially, 101746 PS refined after gamma re-estimation, 85834 PS are kept after dropping adjacent pixels, and 37830 are kept after dropping noisy pixels. Noisy PS pixels are dropped by evaluating the spatial phase differences of neighbouring PS pixels in time.**
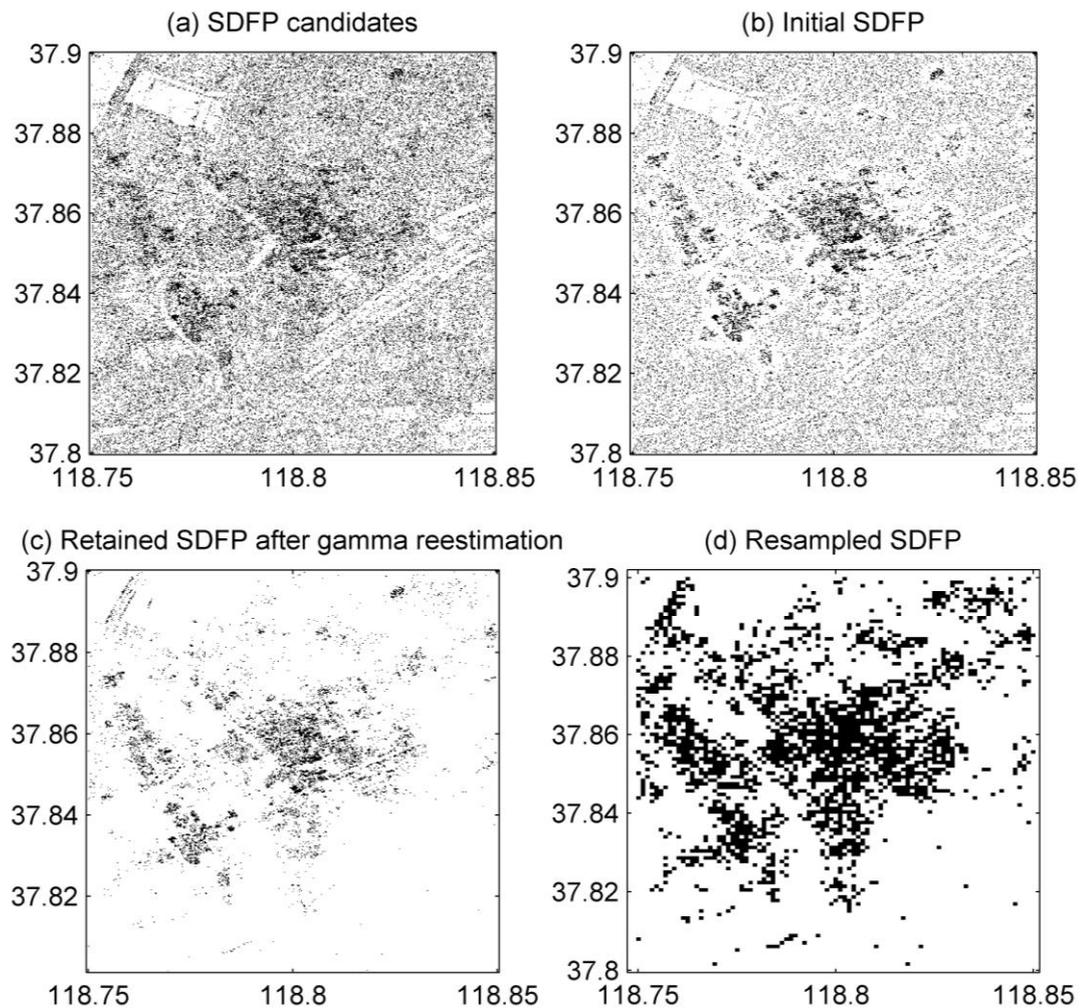
**Figure 5.7 An example of SDFPs retained after phase analysis in the Gudao Town of Yellow River delta from Track 132. (a) SDFP candidates under amplitude dispersion threshold. (b) Initial SDFPs above gamma threshold. (c) SDFPs retained after gamma re-estimation. (d) Resample of SDFP kept to $100 \times 100$ m grids. Of all 712385 SDFP candidates in Yellow River delta, 510361 SDFP are selected initially, 69456 SDFP are retained after gamma re-estimation, and 21290 SDFP are retained after resampling. For SDFP, the wrapped phases are not referenced to a common master, so their noises cannot be estimated the same way for PS. Instead of dropping adjacent and noisy pixels, resample is implemented for SDFPs to reduce their density and noise**

## 5.2.1 Nonlinearity in gamma threshold determination

With more PS candidates in the Yellow River delta than in Badong, there are more amplitude chunks and gamma thresholds for determination of gamma threshold line. It can be observed that $\gamma^{low\_thresh}$ increases with $D_A$ too. However, it turned out that relationship between $\gamma^{low\_thresh}$ and $D_A$ in Yellow River delta may not be as linear as Hooper suggested (Hooper et al., 2007), especially for the lower chunks of $D_A$ (Fig. 5.8). Although the nonlinearity is found, a linear fit is still adopted as the nonlinear behaviour cannot be easily approximated by a single function. For linear approximation, the lines fitted from 60 and 300 $D_A$ chunks are quite similar. However, for a non-linear function, like the logarithm

function used, the curves fitted changed a lot from 60 to 300 chunks. The fitted logarithm function is unsuitable for $D_A$ values which are smaller than mean value of the first chunk because logarithm decays fast when the base approaches zero. For some $D_A$ values, the base is smaller than zero, which makes the logarithm undefined. So it is impractical to fit a logarithm and apply for all the PS candidates.
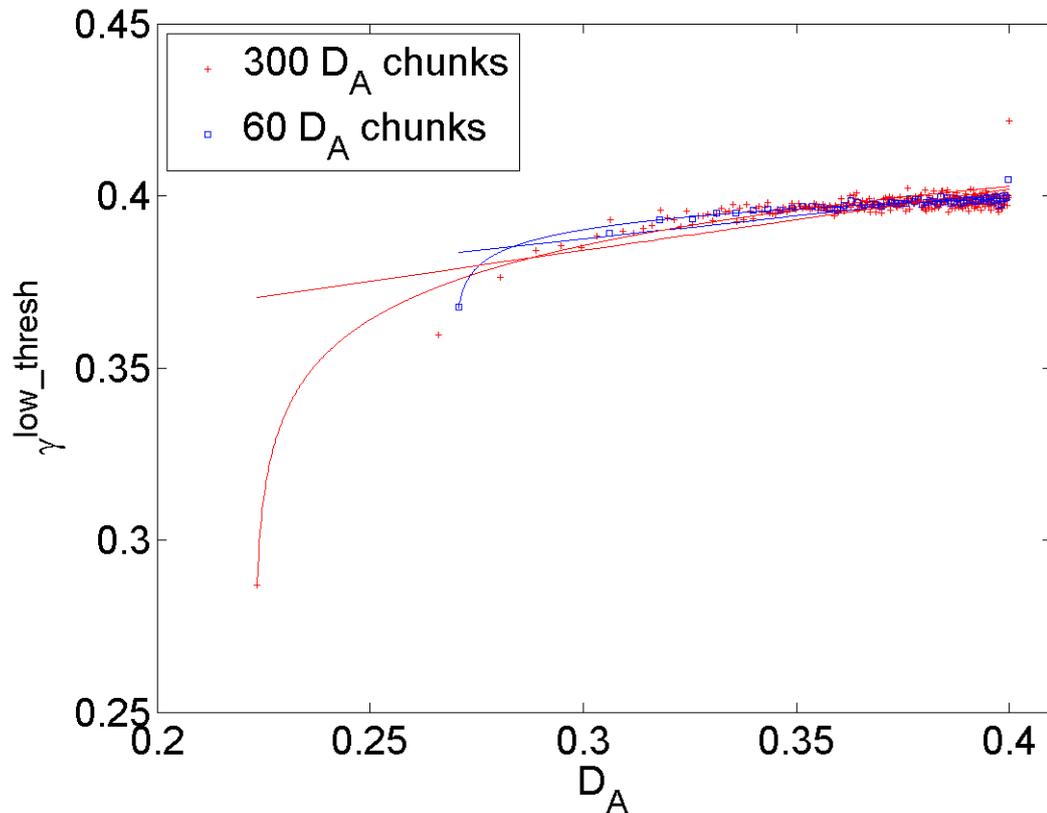


**Figure 5.8 Determination of PS selection threshold in Yellow River delta from Track 132. Blue squares represent the 60 $D_A$ chunks in Yellow River delta. Red pluses represent the 300 $D_A$ chunks. Each dot has the mean amplitude dispersion of the chunk as its horizontal coordinate and the low gamma threshold of the chunk as its vertical coordinate. The blue straight line and blue curve are the linear and logarithm function used to fit the 60 squares. The red straight line and red curve are the linear and logarithm functions used to fit the 300 pluses.**

The nonlinearity in lower $D_A$ range is related with the variability in distribution of PS candidates. Five chunks in 300 $D_A$ chunks are equal to one chunk in 60 $D_A$ chunks. If the distributions of $\gamma$ in the five $D_A$ chunks are similar, the pattern that they added up will be similar to each of them, resulting in a $\gamma^{low\_thresh}$ similar to the five individual $\gamma^{low\_thresh}$. This is obviously the circumstances in higher $D_A$ chunks. Thus the fitted lines are similar in this part. However, if the distributions of $\gamma$ in the five chunks are variable, the distribution pattern that they added up cannot be similar to the five chunks, resulting in a $\gamma^{low\_thresh}$ inconsistent to the five individual $\gamma^{low\_thresh}$. This is the circumstances in lower $D_A$ chunks (Fig. 5.9). The first $D_A$ chunk (Fig. 5.9a) will still skew to high gamma values even

with fewer candidates in each chunk. This is because higher phase stability is associated with lower amplitude dispersion.
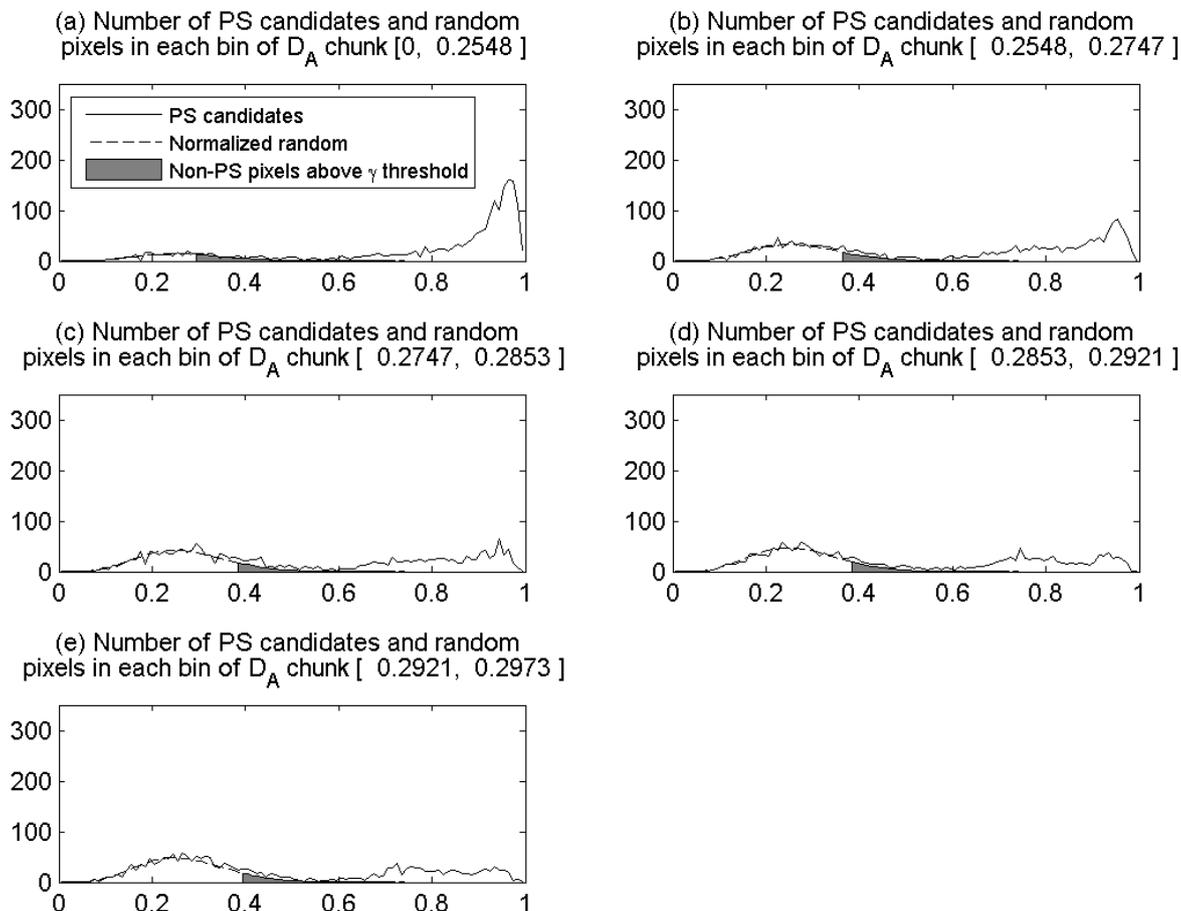


**Figure 5.9 Five examples of distribution of PS candidates and normalised random phases (non-PS pixels) in 300 $D_A$ chunks from Track 132. The horizontal axis is the 100 $\gamma$ bins equally set between 0 and 1. The vertical axis is the number of pixels in each bin. The random distribution is normalized using the total number of pixels in $\gamma$ binns from 0 to 0.31 of both distributions. The normalized random distribution for non-PS is in dashed line and the distribution for PS candidates is in solid line. The grey area is the distribution of non-PS pixels above the $\gamma^{low\_thresh}$ of this $D_A$ chunk.**

The PS selection is based on the use of same theoretical maximum non-PS pixel density 20 per km$^2$ for all chunks. If the density setting is too high for lower $D_A$ chunks with higher phase stability, the red straight threshold line is actually a correction of the $\gamma^{low\_thresh}$ in lower chunks. This section confirms that the relationship between $\gamma^{low\_thresh}$ and $D_A$ may vary in the lower chunks when same maximum non-PS density is set for all the $D_A$ chunks.

## 5.2.2 Phase unwrapping error

In SBAS case, phase unwrapping can be checked by looking the differences between unwrapped phase of small baseline interferograms and that predicted from the model

values for the single master phase. Spatially correlated residuals indicate unwrapping errors (Hooper, 2008). Incorrectly unwrapped interferograms are dropped from the unwrapping process (Fig. 5.10)
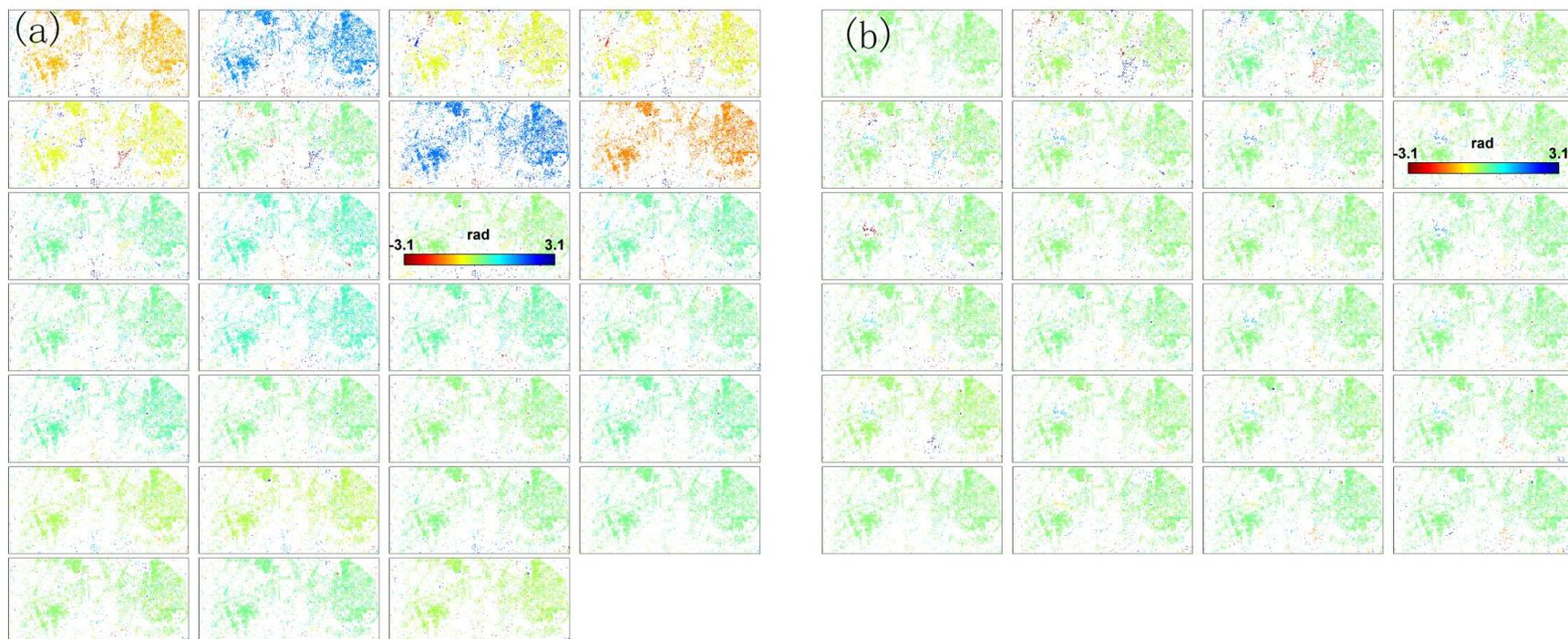
**Figure 5.10 Differences between unwrapped phase of small baseline interferograms and that predicted from the model values for the single master phase. (a) Differences from Track 404. The 2nd, 7th and 8th interferograms show obvious differences indicating phase unwrapping errors. Phase unwrapping errors in one interferogram can propagate to the modelled values of other interferograms. (b) Differences from Track 404 after removing the three small baseline interferograms. Other interferograms once affected also show normal differences. Unwrapping errors can sometimes be solved by increase the phase unwrapping grid size. However, when there are optional image combinations, it is unnecessary to sacrifice the resolution.**

## 5.2.3 DEM error and look angle error

Both the concepts of DEM error and look angle error have been used in InSAR time series analysis because they will influence the interferometric phase. It is necessary to distinguish the two terms although they are related. Look angle error is phase centre uncertainty. DEM error is height uncertainty. Hooper et al (2007) define the look angle error as the angle change of radar beam from looking at the geometric (assumed) centre to the phase centre of a pixel. It is estimated by using the sensitivity between phase and look angle in the form of $d\phi = -\frac{4\pi}{\lambda}B_\perp d\theta$ (Equation 2.25 in Section 2.2.2.2 of Chapter 2). In Li et al. (2009), the DEM error is the height change from the DEM to the actual height of a pixel. It does not only use the sensitivity between phase and look angle, but also use the sensitivity between height and look angle $dz = \rho sin\theta d\theta$ (Equation 2.27 in Section 2.2.2.3 of Chapter 2) to get the sensitivity between phase and height $dz = -\frac{\lambda}{4\pi}\frac{\rho sin\theta}{B_\perp}d\phi$ (Equation 2.28 in Section 2.2.2.3 of Chapter 2 and Equation 4 in Li et al. (2009)) for DEM error estimation. The two errors are not independent (Fig. 5.11). A vertical DEM error will cause a look angle error if $ST$ and $SV$ do not coincidentally overlap. Hooper et al. (2007) pointed out that even if the DEM is 100% accurate, there could still be look angle error as long as the geometric centre is not the phase centre.
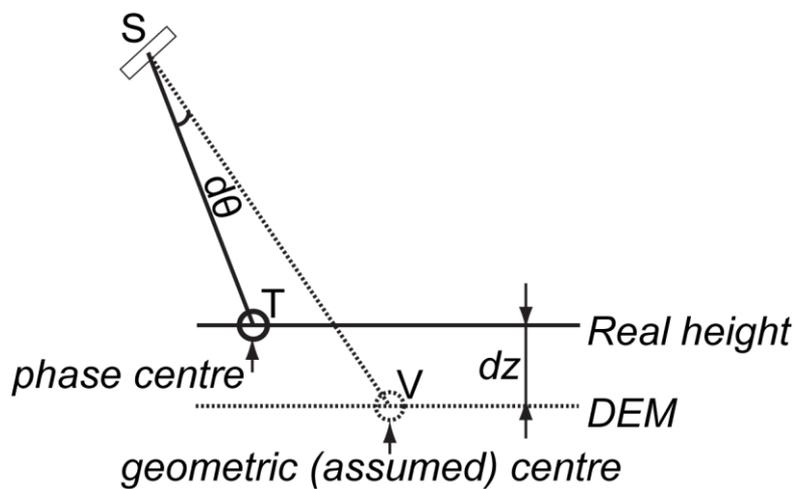


**Figure 5.11 DEM error and look angle error. S is the satellite. T is the real position of phase centre in the pixel. V is the assumed virtual position of target centre on DEM height.**
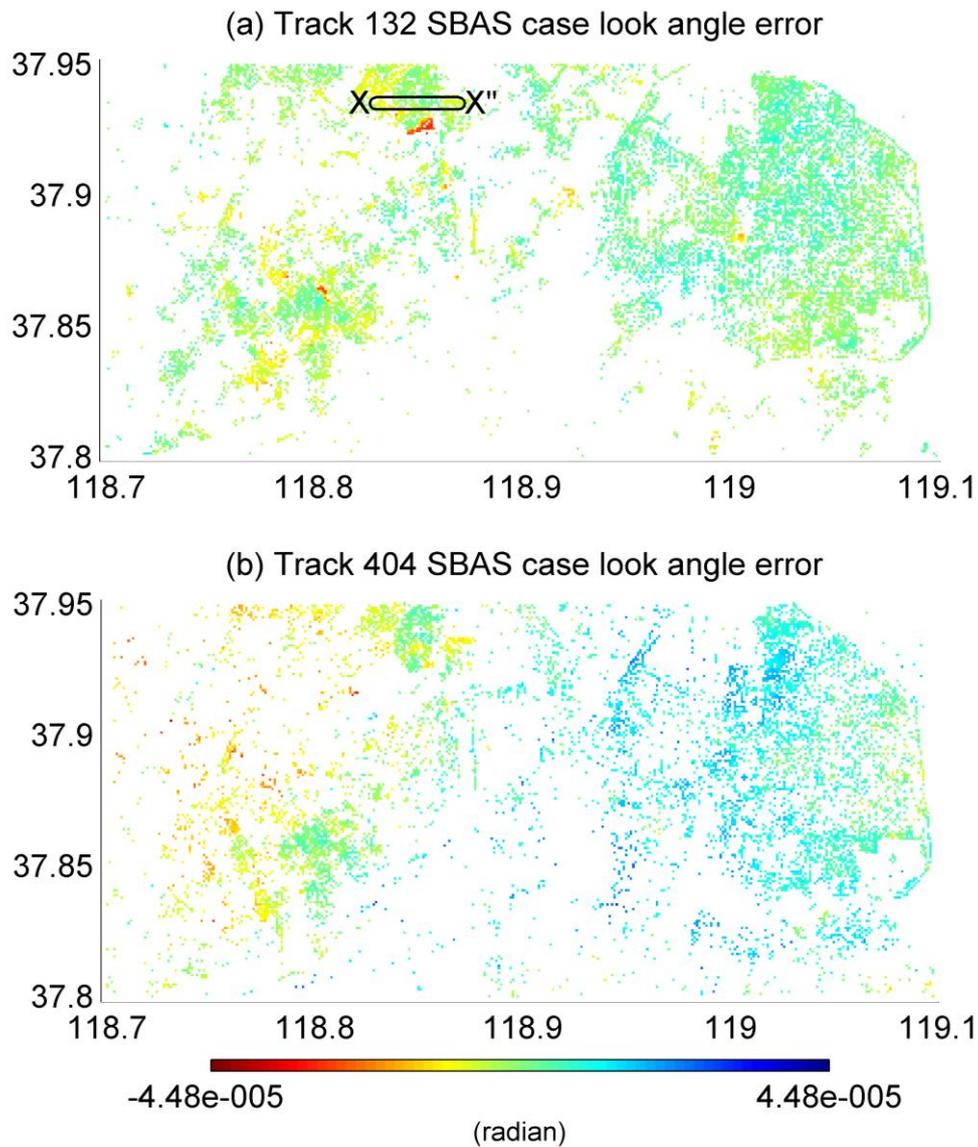
**Figure 5.12 Look angle error estimated from InSAR time series. Position of $X - X^{''}$ is marked in (a) for later use. Note that the radians here are look angle changes $d\theta$, not interferometric phase error $d\phi$, although the two can be converted using $d\phi = -\frac{4\pi}{\lambda} B_{\perp} d\theta$ (Equation 2.25 in Section 2.2.2.2).**

The topography of the Yellow River delta is quite gentle because it is formed in a coastal area by sediment aggradation. Large DEM errors are not expected here. The look angle errors are estimated in Yellow River delta (Fig. 5.12) from InSAR time series (Section 3.3.2 in Chapter 3). The estimated look angle errors of SBAS cases from Track 132 and Track 404 are analyzed for their correlation (Fig. 5.13a). Track 404 show greater changes for look angle errors. The look angle errors have similar patterns in some places between the two tracks e.g. similar fluctuations in swath $X - X^{''}$ (Fig. 5.13b).
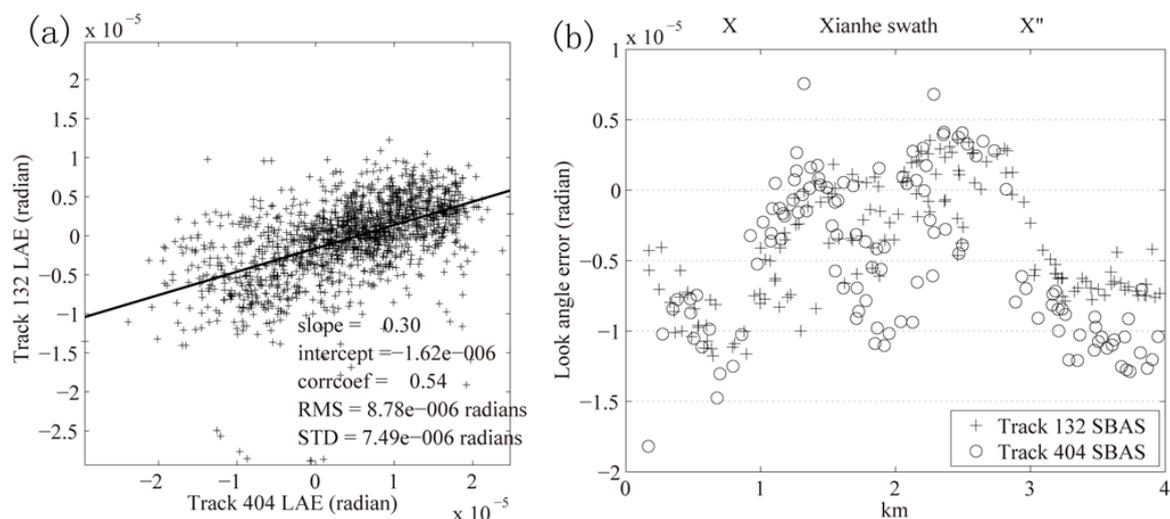
**Figure 5.13 (a) Correlation between look angle errors (LAE) from Track 132 and 404. (b) Look angle errors in Swath $X - X''$ of Xianhe Town in Yellow River delta. Position of $X - X''$ is marked in Fig. 5.11.**

## 5.2.4 Orbit error

Orbit error in Yellow River delta can be estimated by a best fit plane and subtracted from the unwrapped interferogram (Fig. 5.14) (Fialko, 2006). The best fit plane could also account for part of the long wavelength atmospheric effects (Ofeigsson et al., 2011).
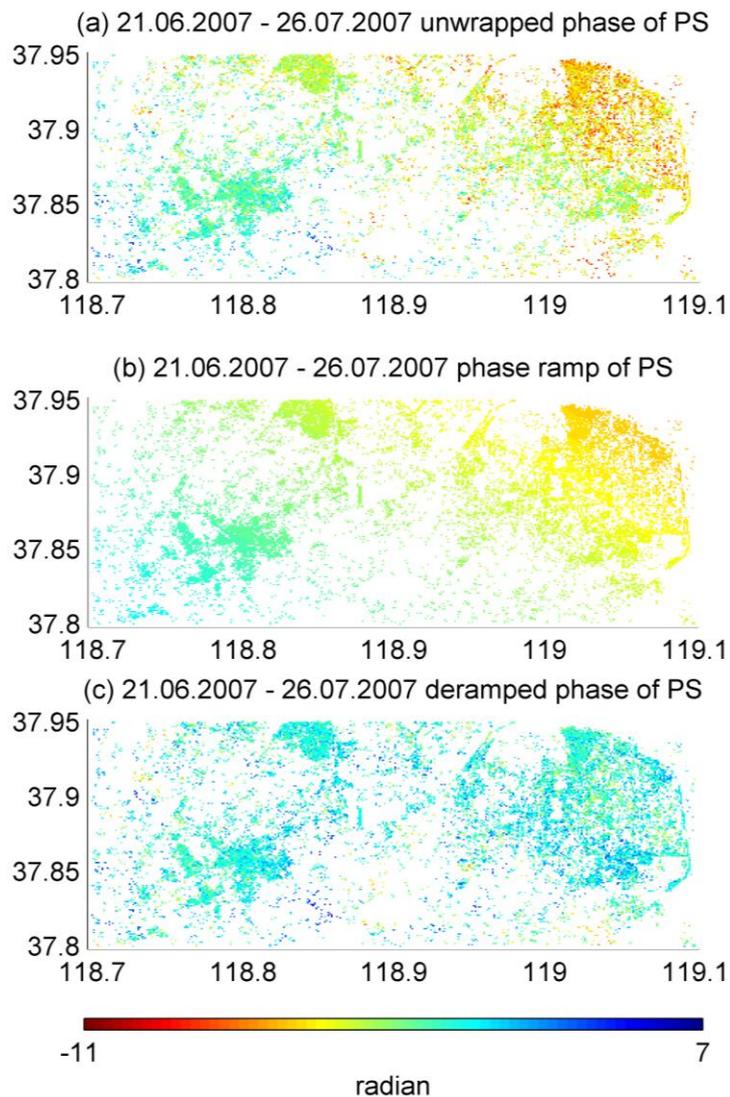
**Figure 5.14 Orbit ramp for unwrapped PS interferogram. (a) The unwrapped interferogram. (b) The phase ramp estimated by a best fit plane. (c) The corrected interferogram by subtracting (b) from (a).**

## 5.2.5 Atmospheric effects

It can be seen the phases by atmospheric heterogeneity from ERS tandem images of this area (Fig. 5.15). For the mapping area, the atmospheric difference can be 1 radian, which is about 0.16 phase cycles, corresponding to 4.5 mm of the LOS displacements for C band Envisat ASAR. The ERS tandem APS that atmospheric effects exhibit spatially correlated pattern. Deformation pattern are also spatially correlated. However, displacement usually stays in the same area while the APS pattern is variable from one image to another. For a single pixel, the deformation should be continuous in time, APS will cause unexpected signal in time series. The APS can be estimated according to its different spatial and temporal nature from displacement.
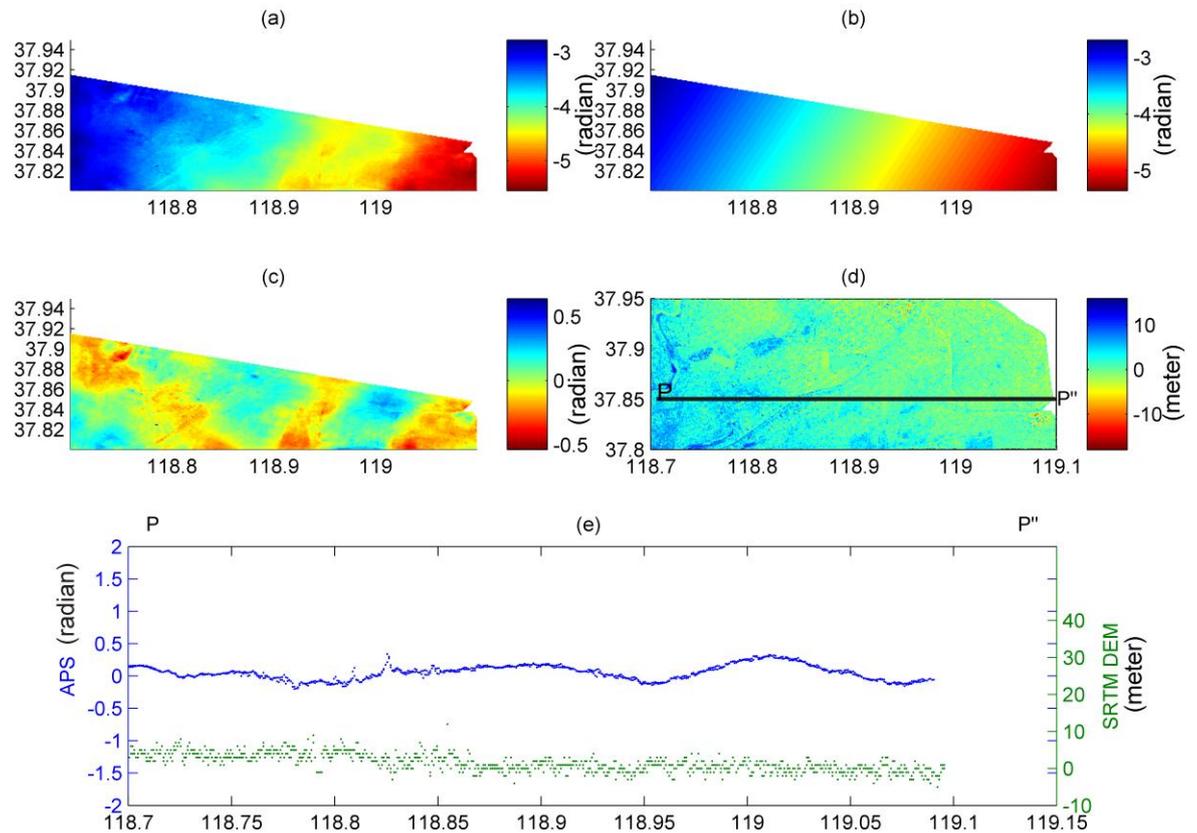
**Figure 5.15 (a) unwrapped ERS tandem mission interferogram 19951210-19951211, one day apart, 4 looks in range and 20 looks in azimuth, topography is removed; (b) phase ramp estimated from the unwrapped interferogram; (c) de-ramped unwrapped interferogram, leaving atmosphere effects; (d) SRTM of this area; (e) Diagonal Profile PP" of (c) and (d). The left vertical axis is the de-ramped unwrapped interferogram thought to be atmospheric signals. The right vertical axis is the 90 m resolution SRTM DEM.**

The master AOE is estimated by its presence in every interferogram. The slave AOE is estimated by temporal filtering and spatial filtering (Section 3.5 in Chapter 3). However the performance of atmospheric filtering varies from case to case, as it can lead to misestimation of displacement signals if both displacement and atmospheric noise represent similar patterns and temporal behaviours (Peltier et al., 2010). Some slave AOE estimations show similar pattern with displacements in this study. The displacements might have leaked into the slave atmospheric estimations. Hence only slave AOE estimations without suspicious patterns (e.g. pattern similar to the rate map) in displacement areas are used to improve the time series (Fig. 5.16).
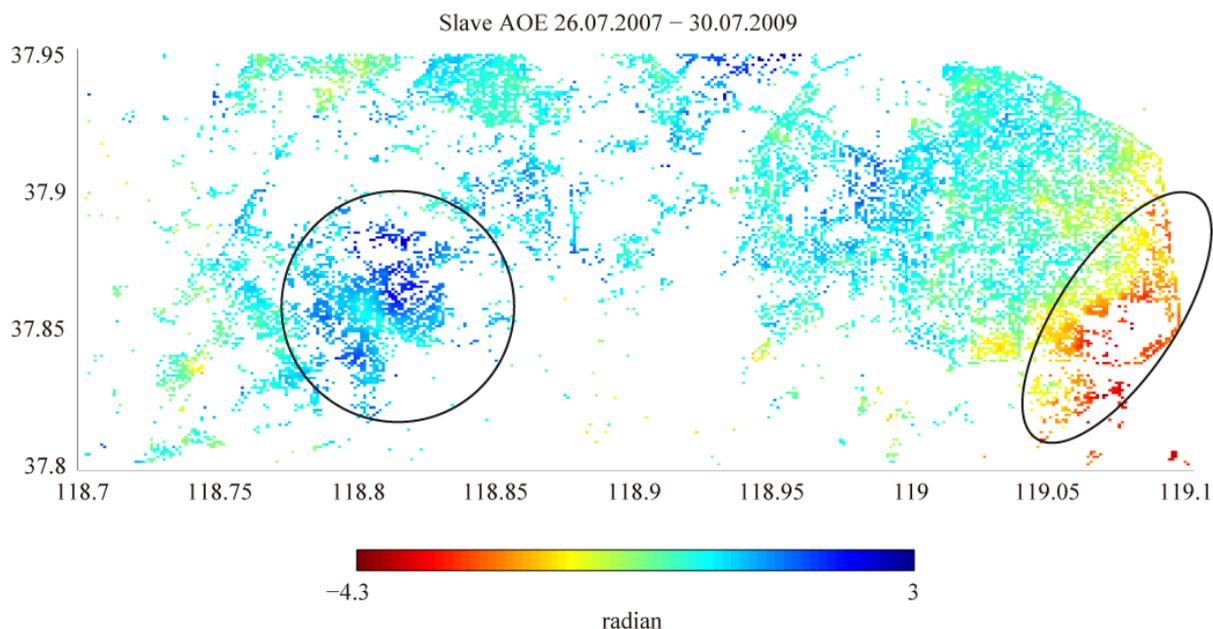
**Figure 5.16 An example of the slave AOE estimated from InSAR time series. The area in circle has some displacement estimated as slave AOE. The area in ellipse is not a displacement area in time series. Thus the apparent signals in the oval are the result of the slave AOE.**

As a flood plain, our research area in Yellow River delta show gentle topography (Fig. 5.15). As a result, the topography dependent APS (Shirzaei and Bürgmann, 2012, Jolivet et al., 2011, Plattner et al., 2010, Lin et al., 2010, Li et al., 2006a, Remy et al., 2003), which could stay in the same area and be misunderstood as displacement, are believed to be small.

## 5.3 InSAR Time series results

The displacement rates from Track 132 PS, Track 132 SBAS and Track 404 SBAS cases are shown in Figures 5.17 (a), (c) and (e) respectively. The single master processing of sparsely distributed images from Track 404 showed a quite noisy pattern and failed to give a reliable result. So the result of Track 404 PS case is not reported here. As no independent ground truth data are available in this area, the mean values of each image are firstly used as the reference phases in the time series analysis. The area without obvious displacements from the resulted rate map is then chosen as the reference area of Yellow River delta (Fig. 5.17b). Finally, the displacement time series are recalculated with the newly referenced phases.

## 5.3.1 Displacement rates

Two subsidence areas can be identified from the rates map (Fig. 5.17a, c, and e). The area which $A - A''$ and $B - B''$ cross is the Gudao Town. Swath $A - A''$ shows a subsidence bowl from 4 $km$ to 7 $km$ in distance with maximum rates of about 30 $mm/yr$ (Fig. 5.18a). The bowl maybe even wider but there is a lack of stable pixels further east. Swath $B - B''$ shows the subsidence from near 5 $km$ to near 8.5 $km$ with maximum rates of 30 $mm/yr$ (Fig. 5.18b). The other area which Swath $C - C''$ crosses is the Gudong Oilfield. A subsidence from 1 $km$ to 6 $km$ with maximum rates of 15 $mm/yr$ and another subsidence from 7 $km$ to 10 $km$ with maximum rates of 20 $mm/yr$ can be identified (Fig. 5.18c).
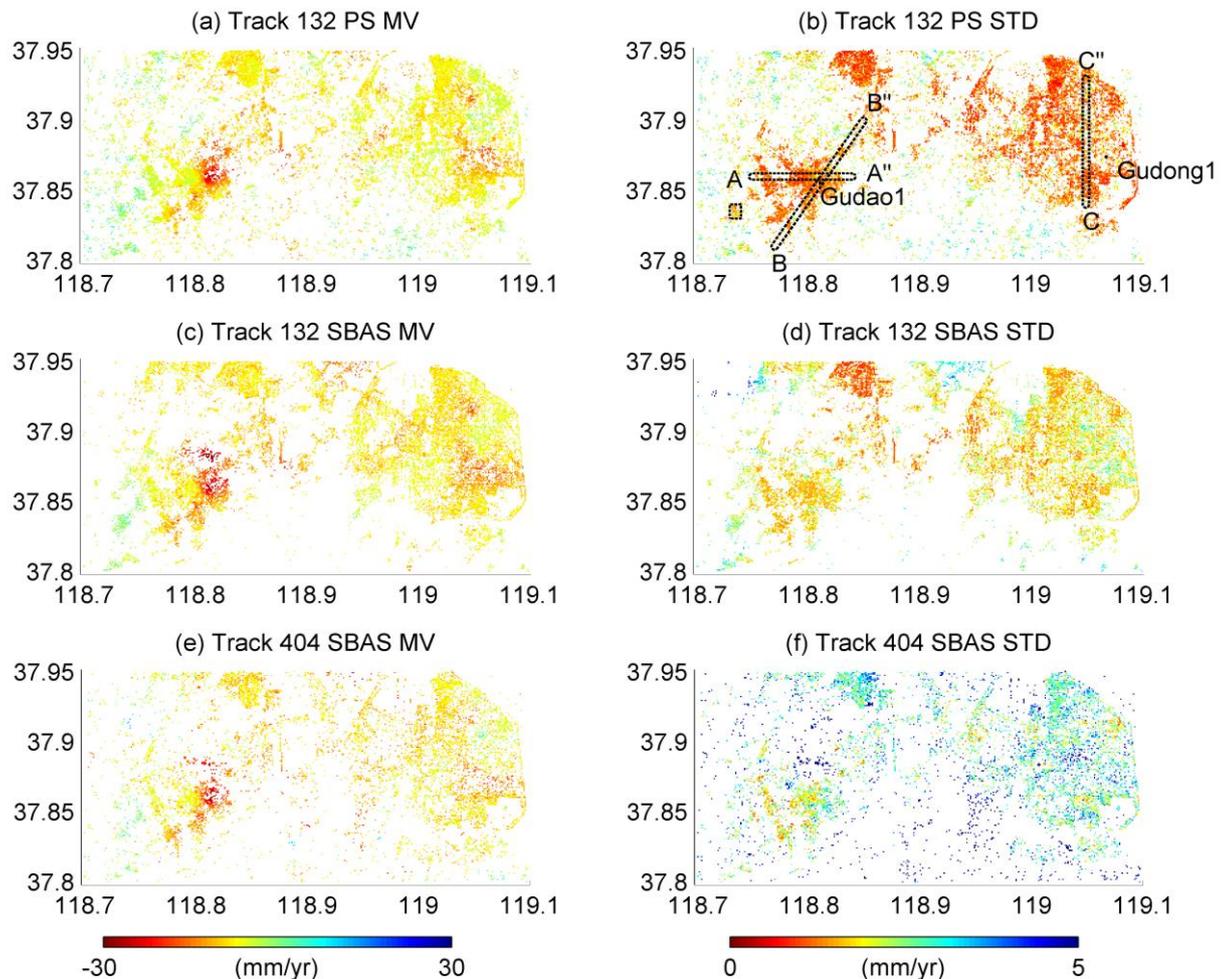


**Figure 5.17 (a) Track 132: Displacement rates from PS analysis, or Mean velocities (MV). (b) Standard deviations (STD) of displacement rates from Track 132 PS interferograms. (c) Track 132: Displacement rates from SBAS analysis. (d) Standard deviations of displacement rates from Track 132 SBAS interferograms. (e) Track 404: Displacement rates from SBAS. (f) Standard deviations of displacement rates from Track 404 SBAS interferograms.**

Positions of three 500 meter wide Swaths $-A^{''}$, $B-B^{''}$ and $C-C^{''}$ are marked in (b). Reference area is outlined by rectangle.
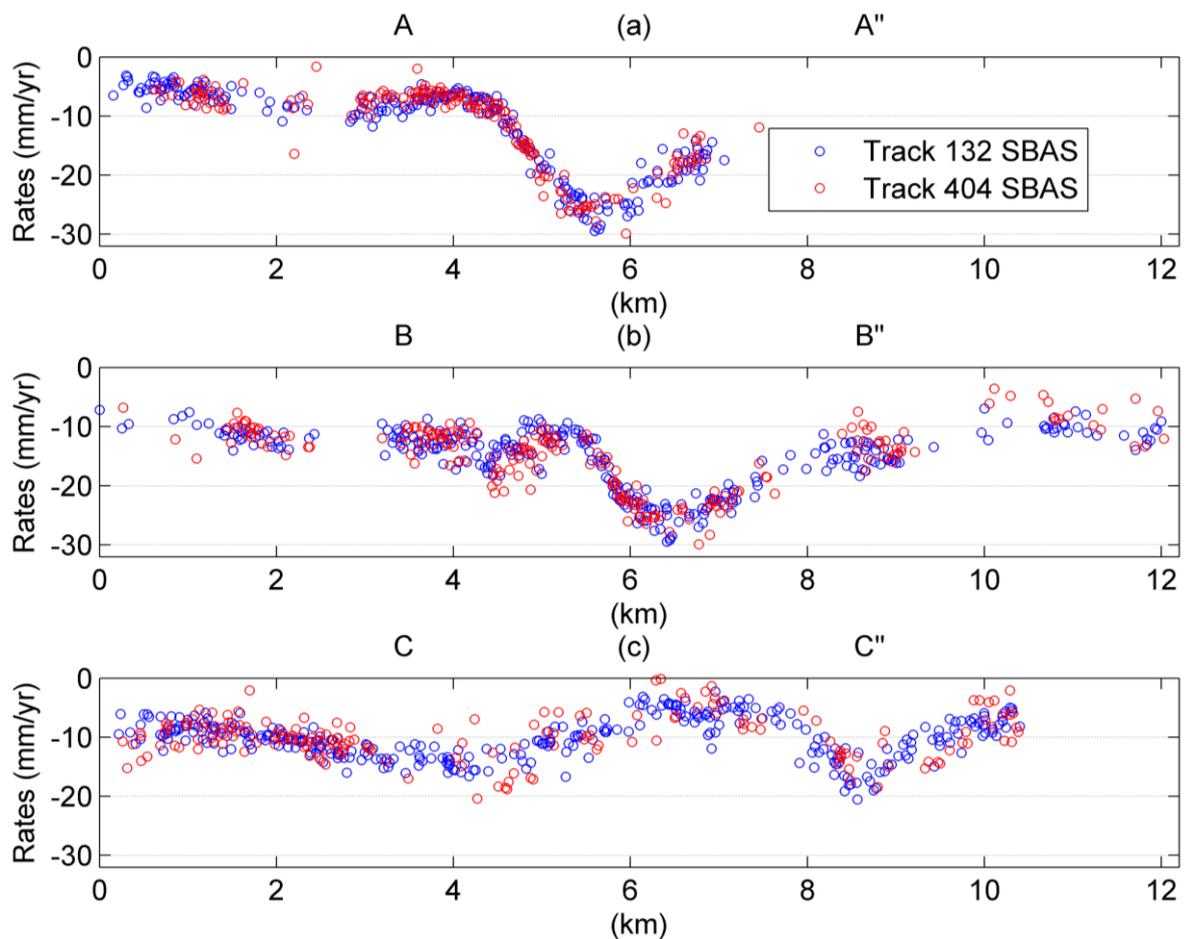


**Figure 5.18 Displacement rates of Yellow River delta estimated from Track 132 and 404 small baseline interferograms. Positions of three 500 meter wide Swaths $-A^{''}$, $B-B^{''}$ and $C-C^{''}$ are marked in Fig. 5.17b.**

 The standard deviations (Fig. 5.17b,d, and e) of the mean velocity at each pixel were calculated using bootstrapping method (Efron and Tibshirani, 1986) in StaMPS. This approach provides an estimate of the precision of the mean velocity estimates. There are two possible implications of the standard deviations: (1) the higher the standard deviation, the lower (worse) the precision of the corresponding mean velocity; and (2) as the mean velocity assumes linear deformation, a high standard deviation may suggest that this assumption is not sound, i.e. the deformation may not be temporally linear. It is likely that the instant deformation rate is greater than the mean velocity and deformation increments between adjacent images may provide better information on the displacement event. The standard deviations in both PS and SBAS cases from Track 132 are smaller than that from Track 404 SBAS case (Fig. 5.17). This should be because the number of SAR images in Track 132 is much greater than that in Track 404. The coefficient of variation (CV) is defined as the ratio of the standard deviations to the mean velocities (Tab. 5.3). The CV

estimator also confirms that mean rates are representing the time series displacements better in Track 132 than in Track 404.

**Table 5.3 The coefficient of variation (CV) for mean velocities.**

|  | $CV \leq 0.1$ | $0.1 < CV \leq 0.2$ | $0.2 < CV \leq 0.3$ |
|---|---|---|---|
| Track 132 PS case | 16.2% | 47.3% | 34.8% |
| Track 312 SBAS case | 4.35% | 44.7% | 32.7% |
| Track 404 SBAS case | 3.7% | 15.2% | 35.4% |

## 5.3.2 Displacement time series
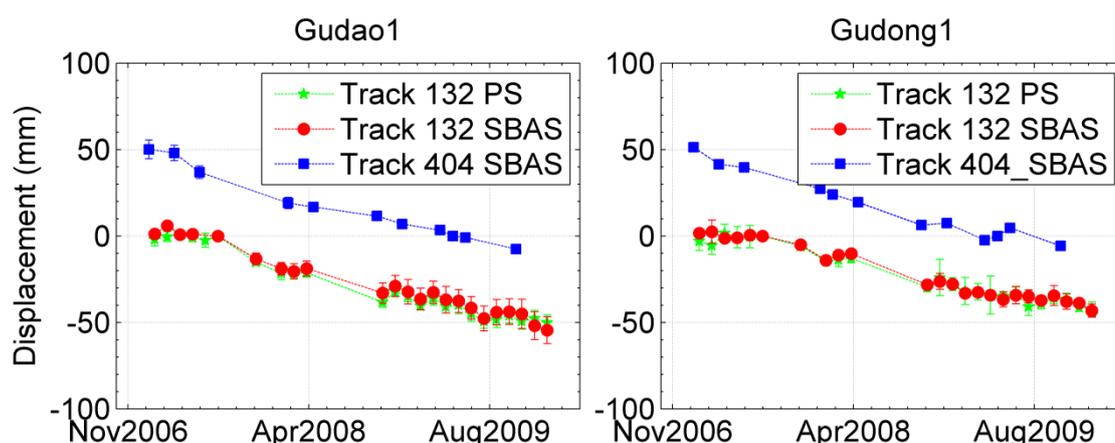


**Figure 5.19 Time series of Gudao1 and Gudong1 from Tracks 132 and 404 using PS and SBAS processing. Positions of Gudao1 and Gudong1 are given in Fig. 5.17b.**

Both Tracks 132 and 404 show Gudao1 and Gudong1 moving away from the satellite, indicating subsidence of about 50 $mm$ in three years time at the two points (Fig. 5.19). Offset between Tracks 132 and 404 are due to different reference dates used to optimize the configurations of spatial and temporal baselines of each dataset. PS and SBAS results of Track 132 are almost identical. Some differences between Tracks 132 and 404 may due to different temporal sampling of the motion. Although atmospheric effects are mitigated through time series analysis, residual atmospheric heterogeneity could still exist and obscure on the displacement. Fortunately, the levels of residual atmospheric effects do not affect the identification of displacement.
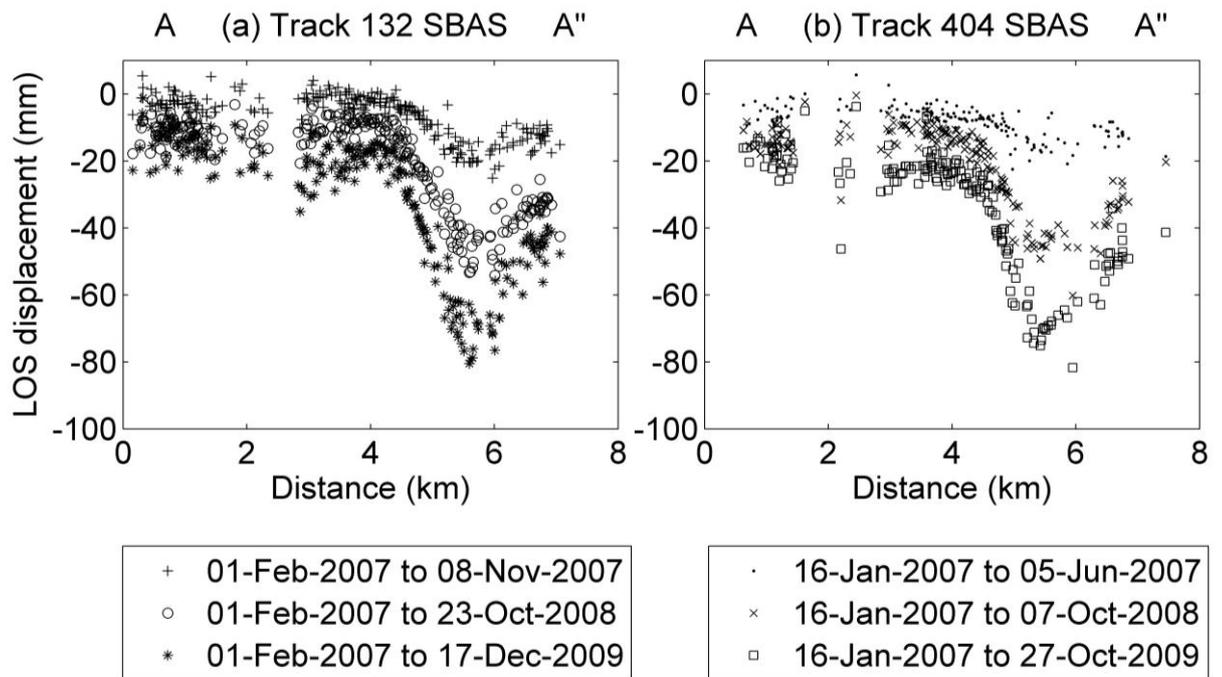
**Figure 5.20 (a) Displacements of Yellow River delta from Track 132 in three interferograms. (b) Displacements of Yellow River delta from Track 404 in three interferograms. Position of Swath $A - A^{''}$ is marked in Fig. 5.16b.**

The displacements in three different interferograms along Swath $A - A^{''}$ are given for Track 132 and 404 respectively (Fig. 5.20). Maximum displacement reached about $80 \ mm$ at about $5.5 \ km$ from both track. A step forward subsidence can be seen from the three interferograms for each track. The subsidence is near symmetric. Note that even when the displacement is totally symmetric, the line of sight displacement will show greater gradient on one side due to horizontal motions. The subsidence show greater gradient to the west of the peak just like that can be expected from a descending track.

## 5.4 Validation of InSAR results

### 5.4.1 Validation of displacement rates.
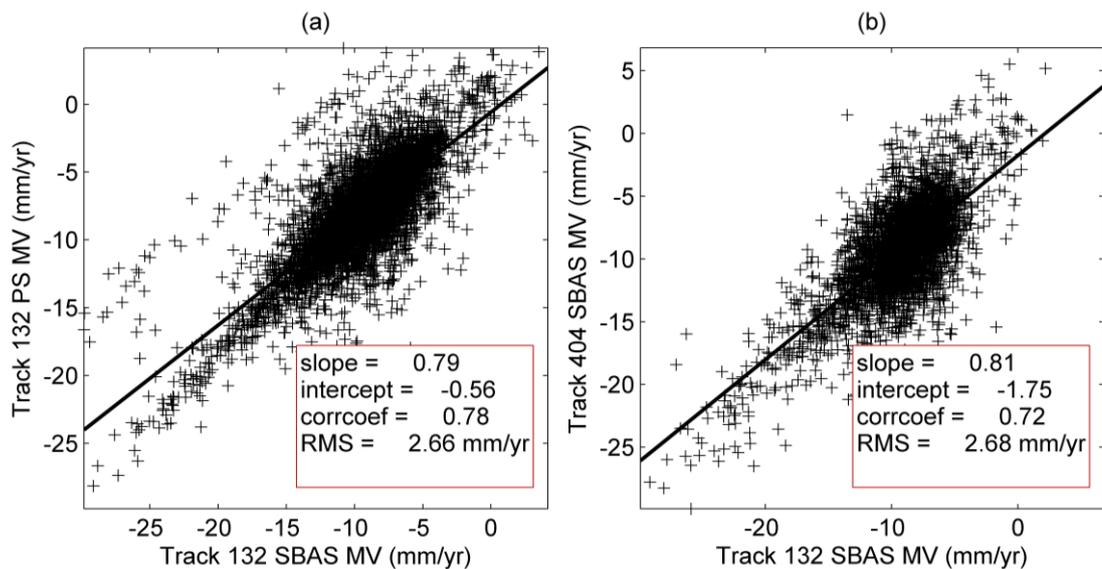


**Figure 5.21 Correlation between displacement rates. (a) Track 132 PS vs. Track 132 SBAS. (b) Track 404 SBAS vs. Track 132 SBAS.**

Correlation analysis is implemented for the mean velocities of common pixels from the two adjacent tracks. PS and SBAS cases from Track 132 show correlation of 0.78 (Fig. 5.21a), whilst SBAS cases from Track 404 and 132 show correlation of 0.72 (Fig. 5.21b). Comparing the mean rates between Track 404 SBAS case from Track 132 SBAS case (Fig. 5.22), 35.61% common pixels have absolute differences less than 1 mm/yr and 61.85% less than 2mm/yr. The overall RMS difference is 2.68 mm/yr between the two tracks.
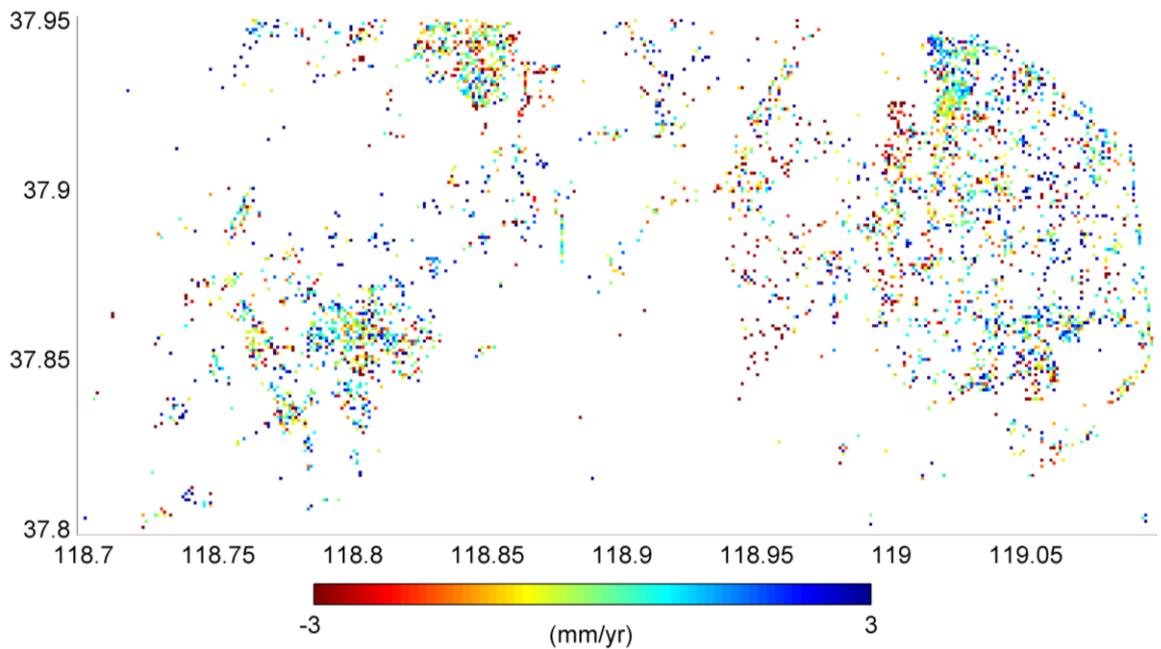
**Figure 5.22 Displacement rate differences by subtracting Track 132 from Track 404.**

## 5.4.2 Validation of displacement time series

In order to assess the accuracy of the InSAR time series results, the displacement values over the overlapping area between the two adjacent tracks can be compared with each other to calculate the root mean square (RMS) of their differences; it should be pointed out that the incidence angles of a single pixel over two adjacent tracks are different, but their impacts are (and can be) neglected in this study. RMS is estimated from the displacement differences between the estimated displacement values from Track 132 and the interpolated displacement values from Track 404 at the SAR acquisition times of Track 132. Note that the systematic offsets between different tracks in Fig 5.19 are due to different reference images used in the time series analysis.  The RMS differences between Track 132 and Track 404 are 4.5 mm for Gudao1 and 3.8 mm for Gudong1 respectively. For these two points, the RMS values between Tracks 132 and 404 are about one tenth of the magnitude of displacements. Pixels with time series RMS differences between the independent tracks below 3 mm, 5 mm and 10 mm, account for 11%, 60%, and 97% of the total common pixels, respectively.

## 5.4 Field visit



**Figure 5.23 Oil wells in Gudao Town. (a) a well in the Town just beside a residential compound. (b) oil wells on a grassland of Gudao Town.**



**Figure 5.24 (a) Oil collection and transportation unit joint station two in Gudao Oilfield. (b) Oil wells in Gudong oilfield.**

Field investigation in the Yellow River delta was carried out in summer 2010. Oil wells are found in Gudao Town (Fig. 5.23) and Gudong oilfield (Fig. 5.24). The two places happen to be the two displacement areas detected from InSAR time series. Hence the subsidence bowls in Gudao Town and Gudong oilfield of Yellow River delta should be mainly (if not completely) due to oil extractions.
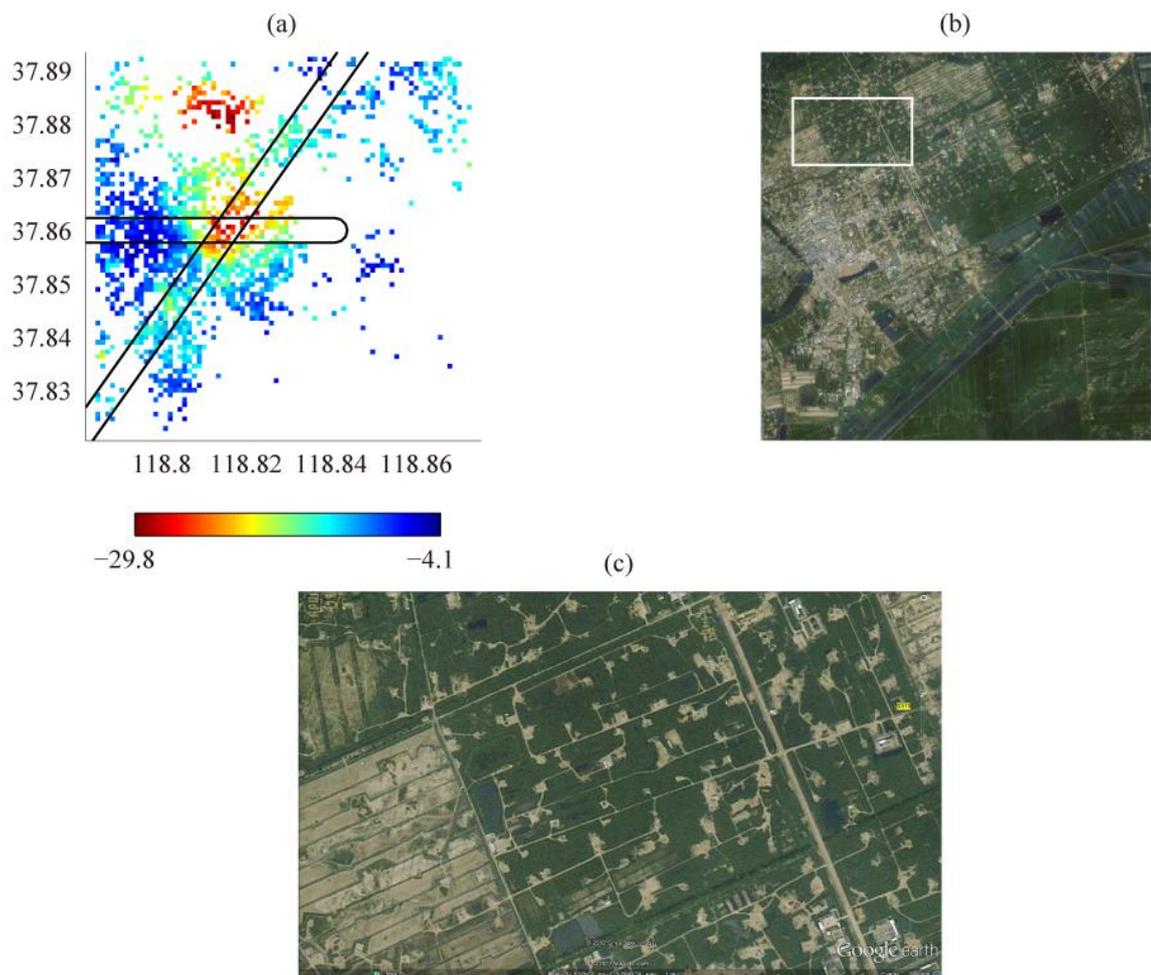
**Figure 5.25 (a) Displacement rates in Gudao Town from Track 132 SBAS case. The swaths shown above are in black solid line. (b) Google Earth view of the same area as shown in (a). The bright dots distributed in green area are the oil wells observed from the field visit. (c) Zoom in on (b) of the area in white rectangle. The oil wells are connected with the road grids.**

The subsidence in Gudao Town has two bowls (Fig. 5.25a). The northern bowl is in the green land to the north of the urban area. The central bowl is in the northeast part of the town. The two swaths in Gudao Town just cross the central bowl, and the northern bowl was not seen from both swaths. Subsidence also exists between the two bowls with greater rates than the area with dense buildings in Gudao Town. The empty area has no SDFP, thus the subsidence there remains unknown.
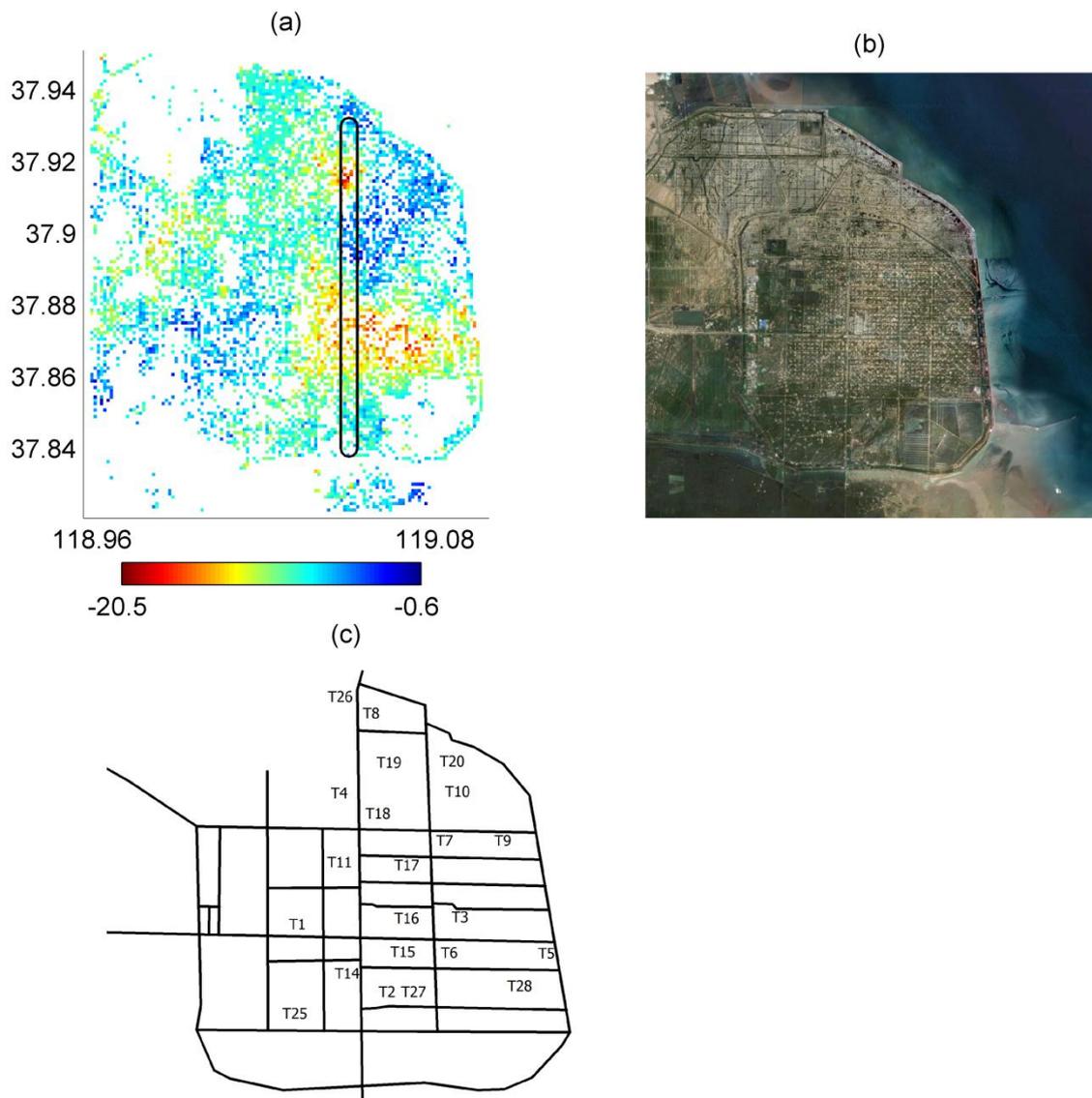
**Figure 5.26 (a) Displacement rates in Gudong oilfield from Track 132 SBAS case. The swaths shown above are in black solid line. (b) Google Earth view of the same area as shown in (a). (c) Positions of oil extraction teams in Gudong Oilfield retrieved from filed visit. The solid lines are the roads in this area.**

In Gudong oilfield, the northern subsidence bowl is likely in the positions of oil extraction Team 18 and Team 19 (Fig. 5.26). The southern subsidence bowl is larger covering the extent of T16, T3, T14, T15, T15, T5, T2, T27, and T28 (Fig. 5.26).

Some findings of this chapter are:

- The relationship between Gamma thresholds and amplitude chunks may be nonlinear in lower amplitude chunks when same maximum non-PS density is set for all the $D_A$ chunks.

- Subsidence is detected from both Tracks 132 and 404 in Yellow River delta with consistency in rates and time series.

- Association between subsidence and oil extraction are found in Gudao Town (oilfield) and Gudong oilfield.

# Chapter 6 Subsidence modelling in the Yellow River delta

In this chapter, the subsidence caused by hydrocarbon production is modelled using the Mogi model (Mogi, 1958), the ellipsoidal model (Yang et al., 1988) and the poroelastic disk reservoir model (Segall et al., 1994). The three models are firstly applied to a simulated displacement field based on the subsidence of the Lacq gas field in south-western France (Segall et al., 1994). Secondly, the models are applied to a near axisymmetric subsidence in the Gudao oilfield of the Yellow River delta region obtained from InSAR observations between 2007 and 2010 (Section 5.4).

## 6.1 Models for subsidence
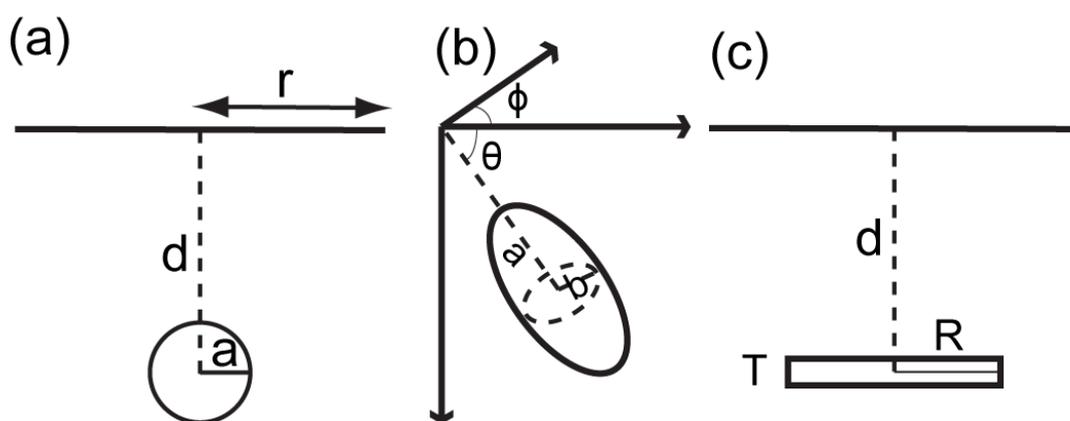


**Figure 6.1 Schematic characterisation for (a) Mogi, after (Mogi, 1958), (b) Ellipsoidal source, after (Yang et al., 1988), and (c) Poroelastic disk reservoir (Segall et al., 1994).**

In Section 6.1, three models: Mogi, ellipsoidal source and disk reservoir are reviewed. They have different geometries: a sphere, an ellipsoidal and a disk respectively as shown in Figure 6.1. All the three models will be used to model simulated data and the Earth surface displacement in the Gudao oilfield.

### 6.1.1 Mogi model

Mathematical expression of surface displacement from a centre of dilation in the elastic half space (also known as a semi-infinite elastic solid) was first solved by Anderson (1936). Yamakawa (1955) and Mindlin and Cheng (1950) also derived similar expressions for a spherical source:

$$u_z(r, 0) = (1 - v)\frac{\Delta P a^3}{G}\frac{d}{(r^2 + d^2)^{3/2}} \qquad (6.1a)$$

$$u_r(r, 0) = (1 - v)\frac{\Delta P a^3}{G}\frac{r}{(r^2 + d^2)^{3/2}} \qquad (6.1b)$$

where $u_z(r, 0)$ and $u_r(r, 0)$ are vertical and horizontal displacements, respectively, of the Earth surface, $v$ (non dimensional) is Poisson's ratio, $G$ (Pascal) is shear modulus, $\Delta P$ (Pascal) is pressure change, $a$ (meter) is the radius and $d$ (meter) is the depth of the spherical source, and $r$ (meter) is the distance to the source centre projected on the Earth surface (Fig. 6.1a). Mogi (1958) applied these expressions with Poisson's ratio of 0.25 to Sakurazima Volcano and found a good agreement between the predicted vertical displacement and the actual displacement of bench marks. For this application aiming at modelling the surface displacement from the change in volume, the expressions are in the form of:

$$u_z(r, 0) = \frac{3\Delta V}{4\pi}\frac{d}{(r^2 + d^2)^{3/2}} \qquad (6.2a)$$

$$u_r(r, 0) = \frac{3\Delta V}{4\pi}\frac{r}{(r^2 + d^2)^{3/2}} \qquad (6.2b)$$

The Mogi model has four degrees of freedom: the three dimensional coordinates of the spherical source centre and the source volume. For the application to the Gudao oilfield in Yellow River delta, Equations (6.2a) and (6.2b) are used. Optionally for the Gudao oilfield, Poisson's ratio is varied from Mogi's (1958) application due to the different material within magmatic chamber and hydrocarbon reservoir. Furthermore, drained and un-drained reservoir material exhibit different Poisson's ratios e.g. 0.17 to 0.34 for Berea sandstone (Hart and Wang, 1995).

## 6.1.2 Ellipsoidal source

As Mogi's model is unsuitable for non symmetric deformation, *Davis et al.* (1974) extended the spherical inflation centre to a vertically elongated pseudo-chamber to better accord with the observations in Kilauea Volcano, Hawaii. Davis (1986) further extended the Mogi model to a point ellipsoidal source. Yang and Davis (1988) derived the analytical solution of an arbitrarily oriented, prolate, spheroid cavity, of finite dimensions in an elastic half space. The point ellipsoidal source model has the greatest number of degrees of freedom and gives accurate estimates in the far field. However, Yang et al. (1988) pointed

out that the finite ellipsoidal source be used for observations at near field after comparing point ellipsoidal and finite ellipsoidal models with the observation data in Kilauea volcano (Yang et al., 1988). For volcano applications with fixed Poisson's ratio, the finite prolate spheroid model has eight degrees of freedom, three dimensional coordinates for ellipsoidal centre, source excess pressure, semi-major and semi-minor axes, and strike and dip of the major axis (Fig. 6.1b). Pages of model equations and relevant expressions of intermediate variables are given in (Yang et al., 1988). The finite prolate spheroid model is also used for the Gudao oilfield. Additionally, Poisson's ratio can be optionally varied and considered an additional degree of freedom.

### 6.1.3 Poroelastic model

Biot (1941) proposed a general theory of three dimensional consolidation to treat porous media in the same way as elastic solids. Nur and Byerlee (1971) incorporated the effect of pore pressure on strain for an isotropic linear poroelastic medium. The strain $\epsilon_{ij}$ induced by the stresses $\sigma_{ij}$ and the pore pressure $P$ is:

$$\epsilon_{ij} = \frac{1}{2G}\left(\sigma_{ij} - \frac{1}{3}\sigma_{rr}\delta_{ij}\right) + \frac{1}{9K}\left(\sigma_{rr}\delta_{ij}\right) + \frac{1}{3H}\left(P\delta_{ij}\right) \qquad (6.3)$$

Where $\sigma_{ij}$ is the tensor notation of stress acting in the $i$ direction on the plane perpendicular to the $j$ direction. $\sigma_{ij}$ are the axial stresses when $i = j$, and shear stresses when $i \neq j$. Strains $\epsilon_{ij}$ use same tensor notation as stresses $\sigma_{ij}$. $\delta_{ij}$ is Kroenecker's delta function (Andrews and Phillips, 2003) and the repeated subscript $rr$ refers to summation. $K$ is the un-drained bulk modulus and $H$ is an effective modulus introduced by Biot (1941) to measure the compressibility of the soil for a change in water pressure. In order to clarify, the full form of Equation (6.3) is:

$$
\begin{pmatrix} \epsilon_{11} & \epsilon_{12} & \epsilon_{13} \\ \epsilon_{21} & \epsilon_{22} & \epsilon_{23} \\ \epsilon_{31} & \epsilon_{32} & \epsilon_{33} \end{pmatrix} = \frac{1}{2G}\begin{pmatrix} \sigma_{11} - \frac{\sigma_{11}+\sigma_{22}+\sigma_{33}}{3} & \sigma_{12} & \sigma_{13} \\ \sigma_{21} & \sigma_{22} - \frac{\sigma_{11}+\sigma_{22}+\sigma_{33}}{3} & \sigma_{23} \\ \sigma_{31} & \sigma_{32} & \sigma_{33} - \frac{\sigma_{11}+\sigma_{22}+\sigma_{33}}{3} \end{pmatrix} +
$$

$$
\frac{1}{9K}\begin{pmatrix} \sigma_{11} + \sigma_{22} + \sigma_{33} & 0 & 0 \\ 0 & \sigma_{11} + \sigma_{22} + \sigma_{33} & 0 \\ 0 & 0 & \sigma_{11} + \sigma_{22} + \sigma_{33} \end{pmatrix} + \frac{1}{3H}\begin{pmatrix} P & 0 & 0 \\ 0 & P & 0 \\ 0 & 0 & P \end{pmatrix} \qquad (6.4)
$$

Equation (6.3) aims to give the strain in terms of the parts due to deviatoric stress (first term), hydrostatic stress (second term), and the pore pressure (third term). Using this form,

it is easier to see the effect of the three stress (pressure) terms on the volume strain $\epsilon_{rr}$ (Nur and Byerlee, 1971):

$$\epsilon_{rr} = \epsilon_{11} + \epsilon_{22} + \epsilon_{33} = \frac{\sigma_{rr}}{3K} + \frac{\alpha P}{K} \tag{6.5}$$

where $\alpha$ is the Biot pore pressure coefficient $0 \ll \alpha \ll 1$ (Segall et al., 1994),

$$\alpha = \frac{K}{H} \tag{6.6}$$

The pore pressure coefficient can also be expressed as (Nur and Byerlee, 1971):

$$\alpha = 1 - \frac{K}{K_s} \tag{6.7}$$

where $K_s$ is the bulk modulus of the grains in the material. With increasing porosity, $K$ is reduced, $K_s$ is unchanged, and $\alpha$ increases. Hence $\alpha$ is an increasing function of porosity (Segall, 1992) with values approaching zero meaning low porosity while as they approach one means high porosity. It can be seen from Equation (6.5) that the hydrostatic stress acts to change the shape but has no effect on the volume strain. The volume strain is related with the mean stress $\sigma_{rr}/3$ and the pore pressure $P$ in Equation (6.5). Segall et al. (1994) point out that if the reservoir were free from constraints (i.e. stress $\sigma_{rr} = 0$), it would contract by $\alpha P/K$. If the reservoir was perfectly constrained (i.e. volume strain $\epsilon_{rr} = 0$ ), it would be driven into tension $\sigma_{rr} = -3\alpha P$. The real situation is that the reservoir contracts by less than $\alpha P/K$ and the rocks are stressed. Segall (1992) used the Biot pore pressure coefficient $\alpha$ and Poisson's ratio $\nu$ to rewrite the constitutive Equation (6.3) as:

$$2G\epsilon_{ij} = \sigma_{ij} - \frac{\nu}{1+\nu}\sigma_{kk}\delta_{ij} + \frac{(1-2\nu)\alpha}{1+\nu}P\delta_{ij} \tag{6.8}$$

The equilibrium equations (Fjær et al., 1992) are

$$\frac{\partial \sigma_{ij}}{\partial x_j} + f_i = 0 \tag{6.9}$$

where $f_i$ are body forces. The kinematic relations between strain and displacement are:

$$\epsilon_{ij} = \frac{1}{2}\left(\frac{\partial u_i}{\partial x_j} + \frac{\partial u_j}{\partial x_i}\right) \tag{6.10}$$

With Equations (6.8), (6.9) and (6.10), the displacement and the pore pressure are coupled by Segall (1992) as:

$$G\nabla^2 u_i + \frac{\mu}{(1-2v)}\frac{\partial^2 u_j}{\partial x_i \partial x_j} - \alpha\frac{\partial P}{\partial x_i} + f_i = 0 \qquad (6.11)$$

Green's function (Greenberg, 1971) is a type of function to solve inhomogeneous differential equation. The displacement Green's function for Equation (6.11) is defined by (Segall, 1992) as follows, and is restricted to axisymmetric configurations:

$$g_z(r, 0) = -(1 - 2v)\rho \int_0^\infty k J_0(kr) J_0(k\rho) exp^{-kd} dk \qquad (6.12a)$$

$$g_r(r, 0) = (1 - 2v)\rho \int_0^\infty k J_1(kr) J_0(k\rho) exp^{-kd} dk \qquad (6.12b)$$

where $g_z(r, 0)$ is the vertical Green's function at the free surface and $g_r(r, 0)$ is the radial Green's function at the free surface. The vertical and radial displacements are solved by integrals of pressure distribution (Segall et al., 1994) as

$$u_r(r, 0) = \frac{\alpha}{G}\iint_0^\infty P(\rho, d)\, g_r(r, 0; \rho, d) d\rho dd \qquad (6.13a)$$

$$u_z(r, 0) = \frac{\alpha}{G}\iint_0^\infty P(\rho, d)\, g_z(r, 0; \rho, d) d\rho dd \qquad (6.13b)$$

For the Gudao oilfield, a simplified disk reservoir (Fig. 6.1c) (Segall et al., 1994, Geertsma, 1973) located at a depth of $d$ with a radius of $R$ and thickness of $T$, and with uniform pressure decline is applied (Fig. 6.1c).

$$\begin{cases} P(\rho, z) = \Delta P\, H(R - \rho) & d - \frac{T}{2} \le z \le d + \frac{T}{2} \\ \quad P(\rho, z) = 0 & otherwise \end{cases} \qquad (6.14)$$

For a poroelastic disk reservoir, the calculated vertical displacement alone is compared with data from levelling (Segall et al., 1994).

$$u_z(r, 0) = -\frac{\alpha(1-2v)T\Delta P}{G} R \int_0^\infty J_1(kR) J_0(kr) exp^{-kd} dk \qquad (6.15a)$$

Using InSAR observations, as well as using vertical displacement, the radial displacement is also considered as it contributes to changes in the radar line of sight direction. Radial displacement is calculated as:

$$u_r(r, 0) = \frac{\alpha(1-2v)T\Delta P}{G} R \int_0^\infty J_1(kR)J_1(kr)exp^{-kd}dk \qquad (6.15b)$$

The integrals for products of Bessel functions are given by Eason et al. (1955) in the form of elliptic integrals. The poroelastic disk reservoir is applied to Yellow River delta. This model has seven degrees of freedom including the three dimensional coordinate for the centre of the disk, thickness and radius of the reservoir, pressure change within the reservoir, and the Biot coefficient of the reservoir. Optionally, Poisson's ratio can be varied.

## 6.1.4 Model comparisons

The three models (Table 6.1) assume different shapes of the deformation source (Fig. 6.1): a point sphere, an ellipsoid, and a circular disk with known thickness. Compared with Mogi model sphere, the finite ellipsoidal source is able to model the effects of source asphericity and orientation (Yang et al., 1988). The Mogi equations used are a first approximation and require the radius of the sphere to be negligible compared to the dimension of depth, hence it is considered to be a point sphere (Mogi, 1958). Equation (6.1) shows that the radius of the sphere and the change of pressure cannot be obtained independently (Mogi, 1958). The source strength can be characterized by the product $\Delta P \times V$ (Fialko and Simons, 2000). Using an ellipsoidal source allows the determination of the characteristic source dimensions only if the source dimensions are not negligible compared with the source depth (Fialko and Simons, 2000). The Mogi and the ellipsoidal models have been used for modelling both magma reservoirs (Manconi and Casu, 2012, Amoruso and Crescentini, 2011, Amelung et al., 2000) and geothermal reservoirs (Fialko and Simons, 2000, Mossop and Segall, 1997, Gambino and Guglielmino, 2008). Both the Mogi and the ellipsoidal source models assume deformation of a continuous elastic medium. In contrast, the poroelastic disk reservoir relates both the elastic (solid) part and the porous (fluid) part in the material. Hence, this model is physically closer to the reality of hydrocarbon reservoir compaction. The theory of poroelastic stressing and induced seismicity has been used to interpret seismic activities or faulting detected in oil reservoirs (Rutledge et al., 1998, Zoback and Zinke, 2002), geothermal reservoirs (Majer et al., 2007), and even in a wider crust context (Harris, 1998, Grasso and Sornette, 1998).

**Table 6.1 Summary of model differences**

|  | Assumption | Free parameters |
|---|---|---|
| Mogi | An infinitesimal spherical chamber | Spherical centre coordinates, the source volume |
| Ellipsoidal source | An finite prolate spheroid chamber | ellipsoidal centre coordinates, source excess pressure, major axis, minor axes, strike of major axis, dip of the major axis, Poisson's ratio |
| Disk reservoir | An symmetric disk reservoir | disk centre coordinates, disk thickness, disk radius, reservoir pressure change, Biot coefficient, Poisson's ratio (if unknown) |

# 6.2 Simulations

## 6.2.1 Simulated subsidence

The purpose of the simulation is to test different models for hydrocarbon induced subsidence in a site where detailed subsurface information are known, in order to evaluate the reliability of the inverted parameter estimates. Previous work has suggested that a symmetrical displacement field is simulated based on forward modelling of poroelastic deformation (Segall et al., 1994). The anticline dome structure oil reservoir provides greater subsidence in the centre field and approximates the levelling better than the disk reservoir in Lacq (Segall et al., 1994). However, it is beyond the scope of this thesis to model an anticline dome structure reservoir in the Gudao oilfield because the limited available data, structure contours without coordinates and with unequal difference in height between adjacent contour lines, suggest that the reservoir in the Gudao oilfield is flat lying (Lu et al., 2005). To the best of our knowledge, the distribution of pore pressure in the Gudao oilfield is unknown. Hence the simulation of the Gudao oilfield is limited to assuming a disk reservoir with uniform pressure. The reservoir parameters for simulation are based on the Lacq oil field (Table 6.2) (Segall et al., 1994). The poroelastic model itself is also tested with added noise for the simulated data to assess its stability during inversion.

**Table 6.2 Simulation parameters for the Lacq gas field using a disk reservoir with uniform pressure [Table one of Segall et al. [1994] (Segall et al., 1994)**

| Quantity | Poisson's ratio | Biot Coefficient | Shear modulus | Reservoir thickness | Pressure decline | Reservoir radius | Reservoir depth | Source centre east | Source centre north |
|---|---|---|---|---|---|---|---|---|---|
| Symbol | $\nu$ | $\alpha$ | $G\ (GPa)$ | $T\ (m)$ | $\Delta P\ (MPa)$ | $R\ (km)$ | $d\ (km)$ | $X_c\ (\,km)$ | $Y_c\ (km)$ |
| Value | 0.25 | 0.25 | 23 | 250 | 60 | 7 | 3.5 | 20 | 20 |

## 6.2.2 Spherical point source for synthetic data

Following many previous studies (Fialko and Simons, 2000, Ofeigsson et al., 2011, Masterlark et al., 2010), Poisson's ratio is initially taken as 0.25 and is fixed. However, measurements have shown how Poisson's ratio can vary with liquid content; for example, data from the Berea sandstone, a good reservoir rock recognized by petroleum industry with relatively high porosity and permeability, laboratory measurements show the drained Poisson's ratio of 0.17 and un-drained 0.34 (Hart and Wang, 1995). Poisson's ratio ranges between $-1$ and 0.5 for isotropic elastic materials (Ting and Chen, 2005), but with the exception of some artificial materials Poisson's ratio values range between 0 and 0.5. Hence, Poisson's ratio is bounded between 0 and 0.5 for inversion of synthetic data. Four categories are implemented in the following inversion by combination of noise and Poisson's ratio (Table 6.3). The RMS errors of the Mogi parameters are given together with other models in Table 6.6 for comparison.

The inversion is implemented using a nonlinear least squares algorithm (Coleman and Li, 1996). Each parameter that needs to be determined from inversion is given a lower and upper boundary, which form the lower and upper boundaries for the parameter group. From the parameter space confined by the boundaries, the nonlinear least square algorithm will find the optimal parameter group which minimize the misfit between model and the data.

Firstly, the simulated data are inverted directly with the Mogi model without added noise. The location of the source centre is well represented by this model (Table 6.3). However, the modelled depth of 6.9 $km$ is almost twice the depth of 3.5 $km$ used for simulation (Table 6.2), with RMS error of 3.4 $km$ (Table 6.6). Is this because the displacement in central field is overestimated by 25% for about 10 mm (Fig. 6.3)? The centre field can be better matched by giving displacements in central field extra weighting (e.g. using the displacement value itself as weighting) in the process of inversion, which however results in even deeper depth at 8.8 km. The differences in depth between simulation and inversion are intrinsically related with discrepancies in model geometry and the effect by including pore pressure effect. The necessity of including inelastic effects for modelling subsidence was found by *Kosloff et al.* (1980b, 1980a) when they try to use finite element method and measured reservoir pressure changes to model observed subsidence in Wilmington oilfield. The poroelastic model used for simulation also includes the inelastic effects. The model differences are seen in the simulation case.

The volume change obtained from Mogi model is not one of the parameters used for simulation through forward modelling of disk reservoir. The Poisson's ratio is fixed or varied. When it is varied within bounds, Poisson's ratio is overestimated by 24% with RMS of 0.12. For simulated subsidence without added noise, only the subsidence centre is accurately determined from inversion using Mogi model.

**Table 6.3 Mogi model parameters of the best fit group, for four cases: fixed and variable Poisson's ratio, in each case with or without added noise. A: Mogi *without* added noise and with *bounded* Poisson's ratio. B: Mogi *without* added noise and with *fixed* Poisson's ratio. C: Mogi *with* added noise and with *bounded* Poisson's ratio. D: Mogi *with* added noise and with *fixed* Poisson's ratio.**

| Quantity | Source centre east | Source centre north | Depth | Volume change | Poisson's ratio | Variance of misfit |
|---|---|---|---|---|---|---|
| Symbol | $X_c$ $(km)$ | $Y_c$ $(km)$ | $d$ $(km)$ | $\Delta V$ $(m^3)$ | $v$ | $(mm^2)$ |
| Truth | 20 | 20 | 3.5 | $- - - - -$ | 0.25 | $- - - - -$ |
| A | $20.0 \pm 0.0003$ | $20.0 \pm 0.0003$ | $6.93 \pm 0.001$ | $1.3 \times 10^7 \pm 1.9 \times 10^6$ | $0.31 \pm 0.11$ | $2.8 \pm 0.001$ |
| B | $20.0 \pm 0.0$ | $20.0 \pm 0.0$ | $6.94 \pm 0.00$ | $1.1 \times 10^7 \pm 2.8 \times 10^3$ | $0.25 \ (fixed)$ | $2.9 \pm 0.0$ |
| C | $20.2 \pm 0.04$ | $20.0 \pm 0.03$ | $4.9 \pm 0.06$ | $7.1 \times 10^6 \pm 9.1 \times 10^5$ | $0.41 \pm 0.09$ | $31.4 \pm 0.25$ |
| D | $20.2 \pm 0.01$ | $20.0 \pm 0.01$ | $4.9 \pm 0.02$ | $5.5 \times 10^6 \pm 2.0 \times 10^4$ | $0.25 \ (fixed)$ | $31.7 \pm 0.12$ |

Secondly, random noise is added to the simulated displacement field, equivalent to 30% of the simulated deformation, for a total of 100 trials to get 100 groups of best fit Mogi parameters (Fig. 6.2). On one hand many small noises fluctuate at the level of about 20 *mm*, while on the other hand adding two much noise will affect the model inversion. The estimated source centre from these simulations with added noise is only 0.2 *km* away from the centre for the simulation without added noise (Table 6.3). With added noise, the estimated depth is shallower at 4.9 *km*, which is still 1.4 *km* deeper than the depth for simulation. The reduced depths result in lower RMS differences of 1.4 *km* compared with the 3.5 *km* RMS difference of the categories without added noise. The volume change of the Mogi source is smaller than that obtained from the data without added noise (Table 6.3). The estimated Poisson's ratio of 0.41 is approaching the upper limit set in inversion and biased with RMS of 0.18 against the value for simulation. For simulated subsidence with added noise, similarly only the subsidence centre is accurately determined from inversion using Mogi model.

There is a direct trade-off between Poisson's ratio and the volume change (Fig. 6.2), which can be foreseen from Equations (6.1). There is a linear trade off between volume change and depth for Mogi when the Poisson's ratio is fixed in our observation though it is not

plotted here. A similar trade off between volume change and depth when using the Mogi model has been observed in volcano modelling cases e.g. Kenyan volcanoes, East African Rift (Biggs et al., 2009), Long Valley Caldera (Feng and Newman, 2009), and Three Sisters volcanic centre, Oregon (Riddick and Schmidt, 2011).
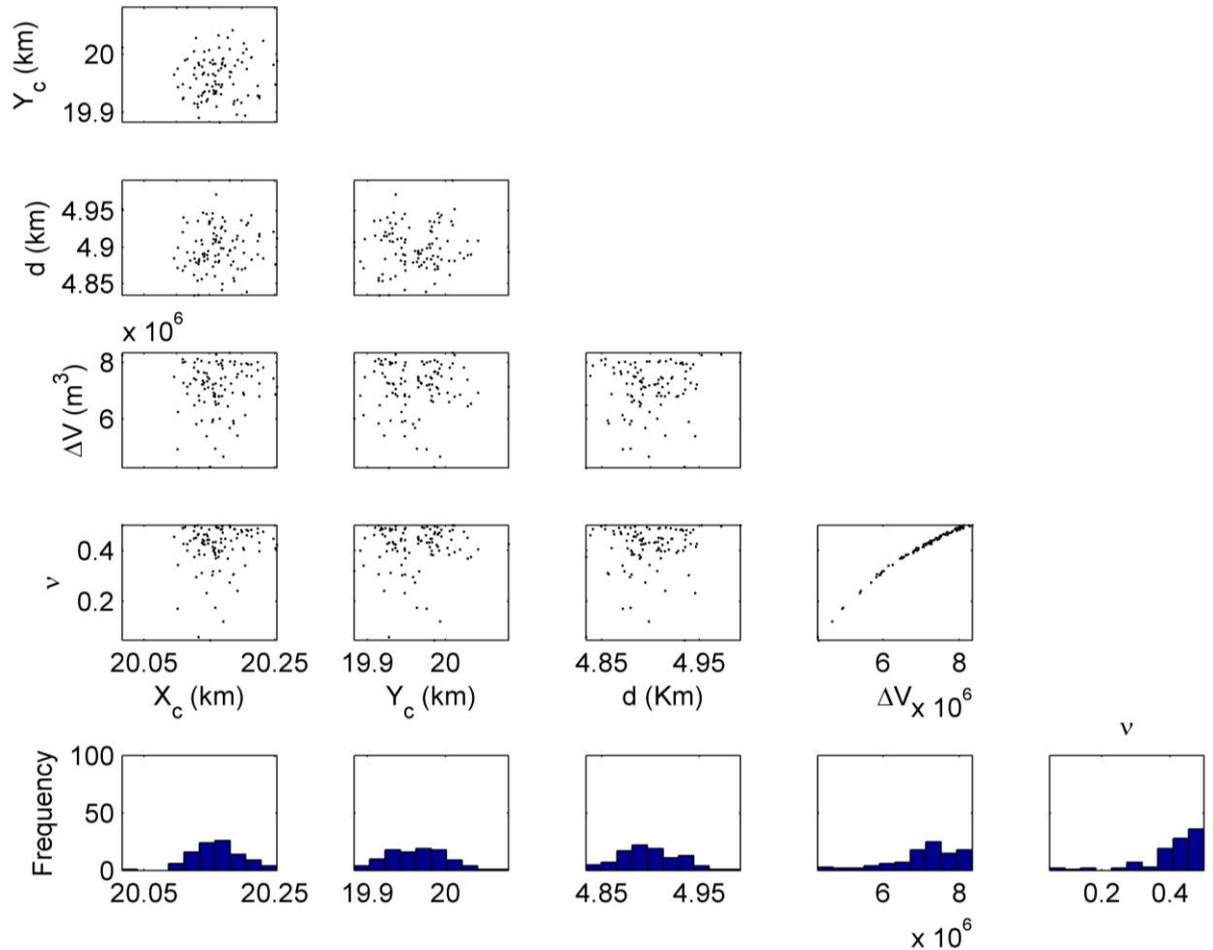


**Figure 6.2 Matrix plot for 100 groups of best fit Mogi model parameters for the simulation data with added noise. Each dot has one parameter as horizontal coordinate and the other parameter from the same optimal group as the vertical coordinate e.g. all the elements in the first column have centre east as the horizontal coordinate, whilst all the elements in the last second row have Poisson's ratios as the vertical coordinate. A well confined parameter shows symmetric distribution in histogram or dots plot. A wide scatter means the parameter is unstable. A line may means one parameter is well confined or there is a trade-off between two parameters.**

There is a tendency for the best fit subsidence using a Mogi type model to be more concentrated near the centre field (Fig. 6.3). The results over predict the subsidence in the centre and under predict the subsidence in the flanks, leaving a donut shape residual, which has also been reported in magma reservoir modelling (Biggs et al., 2009).
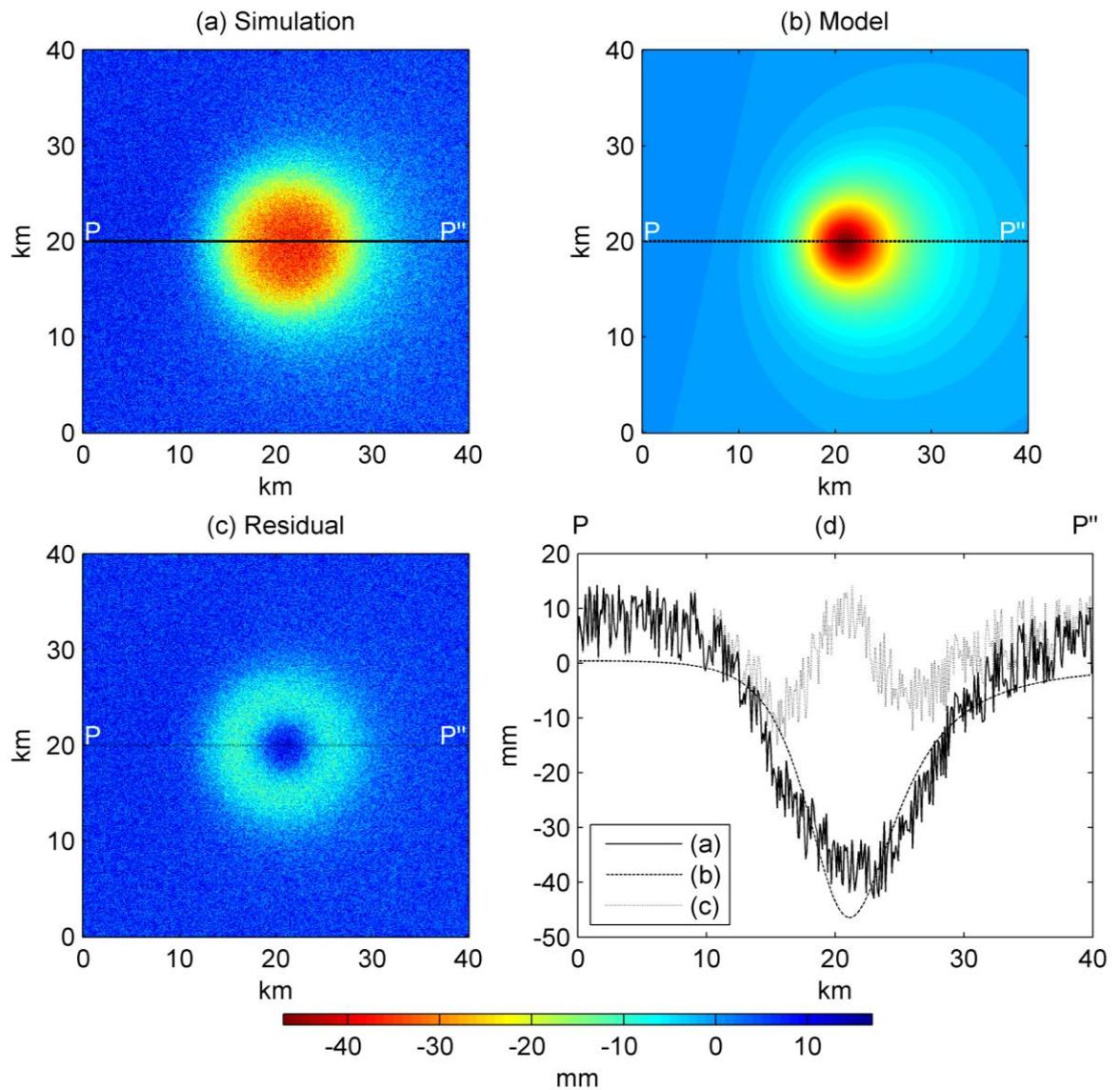
**Figure 6.3 (a) simulated displacement using Poroelastic model on earth surface with added noise. (b) Best fit Mogi model for the simulated displacement field. (c) Residuals between simulation and model. (d) Profiles of the simulation, model and residuals.**

## 6.2.3 Ellipsoidal source for synthetic data

Like the Mogi model, the ellipsoidal source parameters are also obtained from the simulated displacement with or without added noise. Poisson's ratio is either fixed at 0.25 or varied between 0 and 0.5. There are also four categories for ellipsoidal source modelling (Table 6.4).

**Table 6.4 Best fit ellipsoidal deformation model obtained from inversion, for four cases: fixed and variable Poisson's ratio, in each case with or without added noise. Shear modulus is fixed at $23\ GPa$ as used for simulation. A: Ellipsoidal source *without* added noise and with *bounded* Poisson's ratio. B: Ellipsoidal source *without* added noise and with *fixed* Poisson's ratio. C: Ellipsoidal source *with* added noise and *bounded* Poisson's ratio. D: Ellipsoidal source *with* added noise and *fixed* Poisson's ratio.**

| Quantity | Source centre east | Source centre north | Depth | Pressure change | Semi major axis | Semi minor axis | Strike | Plunge | Poisson's ratio | Variance of misfit |
|---|---|---|---|---|---|---|---|---|---|---|
| Symbol | $X_c$ (km) | $Y_c$ (km) | $d$ (km) | $\Delta P$ (MPa) | $a$ (km) | $b$ (km) | $\phi$ (deg) | $\theta$ (deg) | $\nu$ | ($mm^2$) |
| Truth | 20 | 20 | 3.5 | 60 | $-\ -\ -\ -\ -$ | $-\ -\ -\ -\ -$ | $-\ -\ -\ -\ -$ | $-\ -\ -\ -\ -$ | 0.25 | $-\ -\ -\ -\ -$ |
| A | $20.0 \pm 0.01$ | $20.0 \pm 0.01$ | $6.4 \pm 0.01$ | $0.20 \pm 0.25$ | $11.8 \pm 1.6$ | $11.2 \pm 1.7$ | $84.8° \pm 46.9°$ | $1.0° \pm 0.6°$ | $0.50 \pm 0.00004$ | $2.5 \pm 0.003$ |
| B | $20.0 \pm 0.001$ | $20.0 \pm 0.001$ | $6.4 \pm 0.009$ | $0.04 \pm 0.02$ | $27.2 \pm 3.2$ | $26.9 \pm 3.3$ | $77.4° \pm 41.9°$ | $0.1° \pm 0.001°$ | 0.25 (fixed) | $2.5 \pm 0.004$ |
| C | $19.9 \pm 0.14$ | $20.0 \pm 0.10$ | $4.1 \pm 0.1$ | $10.2 \pm 53.4$ | $6.6 \pm 1.5$ | $3.0 \pm 2.6$ | $177.0° \pm 128.8°$ | $4.8° \pm 14.5°$ | $0.50 \pm 0.0002$ | $30.3 \pm 0.2$ |
| D | $20.1 \pm 0.04$ | $20.0 \pm 0.04$ | $4.1 \pm 0.04$ | $0.13 \pm 0.09$ | $15.8 \pm 2.5$ | $15.0 \pm 2.6$ | $137.1° \pm 119.5°$ | $0.2° \pm 0.4°$ | 0.25 (fixed) | $30.5 \pm 0.01$ |

The pressure change within ellipsoidal source is non-dimensional and is given in terms of shear modulus (Yang et al., 1988). Making use of the shear modulus for simulation, the excess pressure is given in Mega Pascals (Table 6.4). On one hand, semi-major or semi-minor axes are subject to trade-offs with excess source pressure if their lengths are much smaller than the source depth (Fialko and Simons, 2000). On the other hand the solution becomes inaccurate when the radius of curvature of the upper surface of a prolate spheroid source becomes comparable to the source depth (Fialko and Simons, 2000). *Amoruso and Crescentini* (2011) concluded that any approach based on Eshelby's results for an infinite medium (Eshelby, 1957) and the half-space point force solution by *Mindlin* as the fundamental Green's function is applicable only if the free surface causes negligible deviations from the uniform pressure condition at the cavity boundary. The ellipsoidal source uses both *Mindlin's* half space solution and *Eshelby's* model for the case of a prolate spheroid. The deviations of its solution are smaller than few percent if the ratio of depth to the upper surface of the ellipsoid to its minimum radius of curvature (Fig. 6.4) is greater than 1.5 (Yang et al., 1988, Amoruso and Crescentini, 2011).
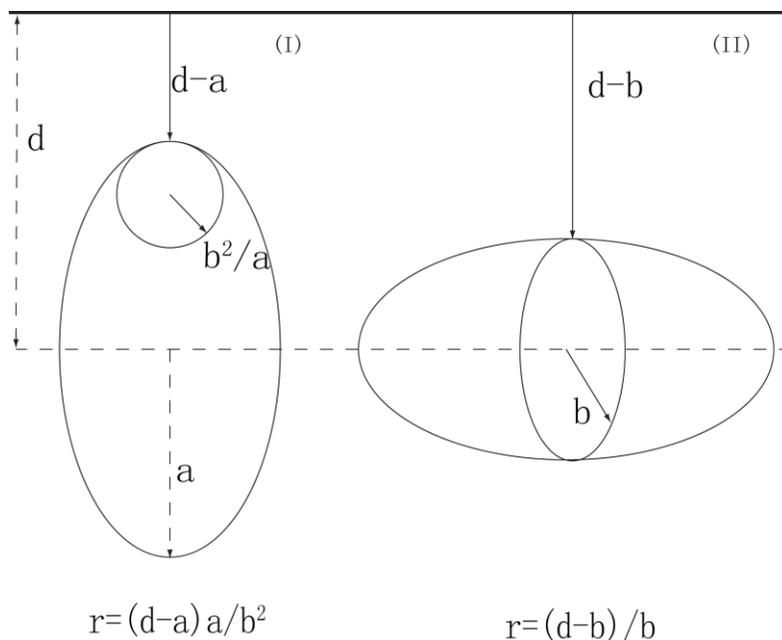


**Figure 6.4 Two examples of ratio of depth to the upper surface of the ellipsoid to minimum radius of curvature of upper surface (Yang et al., 1988). (I) dipping angle of 90°. The depth to the upper surface is *d-a*, and the minimum radius of curvature is $b^2/a$. (II) dipping angle of 0°. The depth to upper surface is *d-b*, and the minimum radius of curvature is *b*.**

In three of the four categories, the major and minor axes are of comparable length (categories A, B and D in Table 6.4), thus the minimum curvature is about the length of the semi-major and semi-minor axes and greater than the depth. The ratios in categories A, B, and D are thus smaller than 1, indicating inaccurate solutions. Actually, part of the ellipsoid is outside the elastic half space in categories A, B, and D by exceeding the earth surface. In category C, assuming the part of depth inside the ellipsoid is $x$, the depth to upper surface will be $d - x$. Assuming the minimum radius of curvature for upper surface is $R_{u,min}$ and the minimum radius of curvature for whole ellipsoid is $R_{min}$ ($R_{min} = b^2/a$), since $x \geq b$ and $R_{u,min} \geq R_{min}$, the ratio of Category C will be:

$$r = \frac{d-x}{R_{u,min}} \leq \frac{d-b}{R_{u,min}} \leq \frac{d-b}{R_{min}} = \frac{(d-b)a}{b^2} = 0.81 < 1 \qquad (6.16)$$

As $r < 1$, the ellipsoidal source is not applicable in Category C (Fialko and Simons, 2000). This suggests that the ellipsoidal source is not the first choice for modelling axisymmetric displacement. Large uncertainties of the strike angle obtained from inversion are also seen (Table 6.4).

## 6.2.4 Poroelastic disk reservoir for synthetic data

As previously for Poisson's ratio, both fixed and bounded Biot coefficients are considered. Through different combinations of noise, Poisson's ratio and Biot coefficient, a total of eight categories are implemented in inversion (Table 6.5). Their RMS errors with the parameters for simulation are given in (Table 6.6).

**Table 6.5 Best fit disk reservoir obtained from inversion for eight cases: fixed and variable Poisson's ratio, fixed and variable Biot coefficient, in each case with or without added noise. Shear modulus is fixed at $23\ GPa$ as used for simulation. A: Bounded Poisson's ratio and bounded Biot coefficient without added noise for disk reservoir. B: Fixed Poisson's ratio and bounded Biot coefficient without added noise for disk reservoir. C: Bounded Poisson's ratio and fixed Biot coefficient without added noise for disk reservoir. D: Fixed Poisson's ratio and fixed Biot coefficient without added noise for disk reservoir. E: Bounded Poisson's ratio and bounded Biot coefficient with added noise for disk reservoir. F: Fixed Poisson's ratio and bounded Biot coefficient with added noise for disk reservoir. G: Bounded Poisson's ratio and fixed Biot coefficient with added noise for disk reservoir.  H: Fixed Poisson's ratio and fixed Biot coefficient with added noise for disk reservoir.**

| Quantity | Source centre east | Source centre north | Depth | Radius | Thickness | Pressure change | Biot coefficient | Poisson's ratio | Variance of misfit |
|---|---|---|---|---|---|---|---|---|---|
| Symbol | $X_c\ (km)$ | $Y_c\ (km)$ | $d\ (km)$ | $R\ (km)$ | $T\ (m)$ | $\Delta$P (MPa) | $\alpha$ | $\nu$ | $(mm^2)$ |
| Truth | 20 | 20 | 3.5 | 7 | 250 | 60 | 0.25 | 0.25 | $-----$ |
| A | $20.0 \pm 0.10$ | $20.0 \pm 0.10$ | $4.1 \pm 0.8$ | $6.7 \pm 0.5$ | $192.5 \pm 109.9$ | $31.7 \pm 17.3$ | $0.73 \pm 0.2$ | $0.13 \pm 0.11$ | $0.26 \pm 0.26$ |
| B | $20.0 \pm 0.03$ | $20.0 \pm 0.03$ | $3.5 \pm 0.06$ | $7.0 \pm 0.1$ | $194.0 \pm 90.5$ | $33.9 \pm 18.9$ | $0.76 \pm 0.2$ | $0.25\ (fixed)$ | $0.02 \pm 0.03$ |
| C | $20.0 \pm 0.01$ | $20.0 \pm 0.02$ | $3.5 \pm 0.06$ | $7.0 \pm 0.05$ | $257.4 \pm 86.6$ | $43.8 \pm 14.6$ | $0.25\ (fixed)$ | $0.11 \pm 0.09$ | $0.04 \pm 0.03$ |
| D | $20.0 \pm 0.005$ | $20.0 \pm 0.01$ | $3.5 \pm 0.02$ | $7.0 \pm 0.02$ | $289.0 \pm 67.2$ | $54.7 \pm 12.7$ | $0.25\ (fixed)$ | $0.25\ (fixed)$ | $0.009 \pm 0.009$ |
| E | $20.1 \pm 0.16$ | $20.0 \pm 0.17$ | $2.1 \pm 0.7$ | $6.7 \pm 0.5$ | $190.3 \pm 103.2$ | $28.3 \pm 18.4$ | $0.61 \pm 0.20$ | $0.17 \pm 0.11$ | $19.6 \pm 0.8$ |
| F | $20.1 \pm 0.18$ | $20.0 \pm 0.19$ | $2.1 \pm 0.5$ | $6.7 \pm 0.39$ | $204.4 \pm 94.1$ | $24.8 \pm 12.5$ | $0.67 \pm 0.22$ | $0.25\ (fixed)$ | $19.5 \pm 0.7$ |
| G | $20.1 \pm 0.3$ | $20.0 \pm 0.3$ | $2.4 \pm 0.6$ | $6.7 \pm 0.4$ | $242 \pm 93$ | $39.8 \pm 17.3$ | $0.25\ (fixed)$ | $0.14 \pm 0.11$ | $19.2 \pm 1.0$ |
| H | $20.1 \pm 0.15$ | $20.0 \pm 0.16$ | $2.1 \pm 0.3$ | $6.9 \pm 0.26$ | $249.5 \pm 69.5$ | $42.0 \pm 11.6$ | $0.25\ (fixed)$ | $0.25\ (fixed)$ | $19.0 \pm 0.5$ |

The source centre is accurately positioned through inversion with the RMS errors under 0.2 $km$ for all eight categories. In the four categories with added noise, no matter which kind of configurations are used for Poisson's ratio and the Biot coefficient, the modelled depths are all shallow compared to the simulated value with RMS errors of the order of 1.5 $km$ (Table 6.6). The RMS error of depth is reduced to less than 1 $km$ when both Poisson's ratio and Biot coefficient are bounded and there is no added noise. The RMS error of depth is reduced significantly to less than 0.1 $km$ when Poisson's ratio or Biot coefficient is fixed without added noise (Table 6.6). The reservoir radius is reliably recovered with RMS errors under 10% of the radius in all eight categories. The RMS errors of reservoir thickness increased when Poisson's ratio and the Biot coefficient are varied, from 30% to 50% of the reservoir thickness (Table 6.6). The disk reservoir underestimates the pressure change by 10% when there is no added noise and both Poisson's ratio and the Biot coefficient are fixed. It further underestimates the pressure change by 30-50% in its other five categories (Table 6.5). The RMS errors of pressure decline also rose with the flexibility of the Poisson's ratio and Biot coefficient, and the presence of extra noise (Table 6.6). The Biot coefficient is substantially over-estimated when it is bounded. Poisson's ratio is under-estimated when it is bounded.
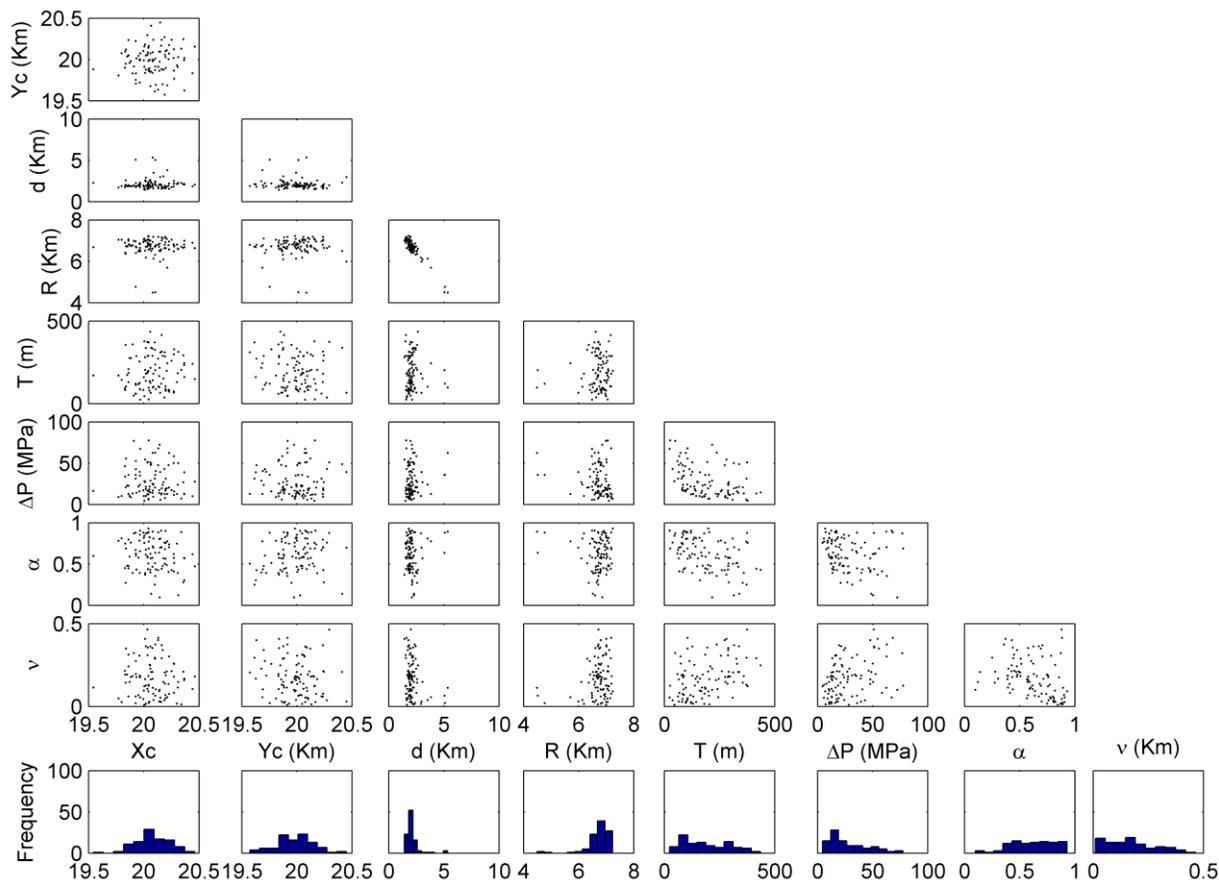
**Figure 6.5 Matrix plot for 100 groups of best fit poroelastic model parameters for the simulation data with added noise, bounded Biot coefficient, and bounded Poisson's ratio.**

Note that there is a trade-off between the radius and the depth of the reservoir when the lateral dimension of the reservoir gets smaller (Row R and column d in Figure 6.5). The trade-off between the pressure decline and the reservoir thickness is not obvious in Figure 6.5. However, this is clearer when there is no additional noise and Poisson's ratio is fixed or when both Biot coefficient and Poisson's ratio are fixed regardless of the noise condition.

The simulated data is well predicted by a disk reservoir as expected because the synthetic data is also simulated with a poroelastic disk reservoir model although 30% random noise is added (Fig. 6.6).
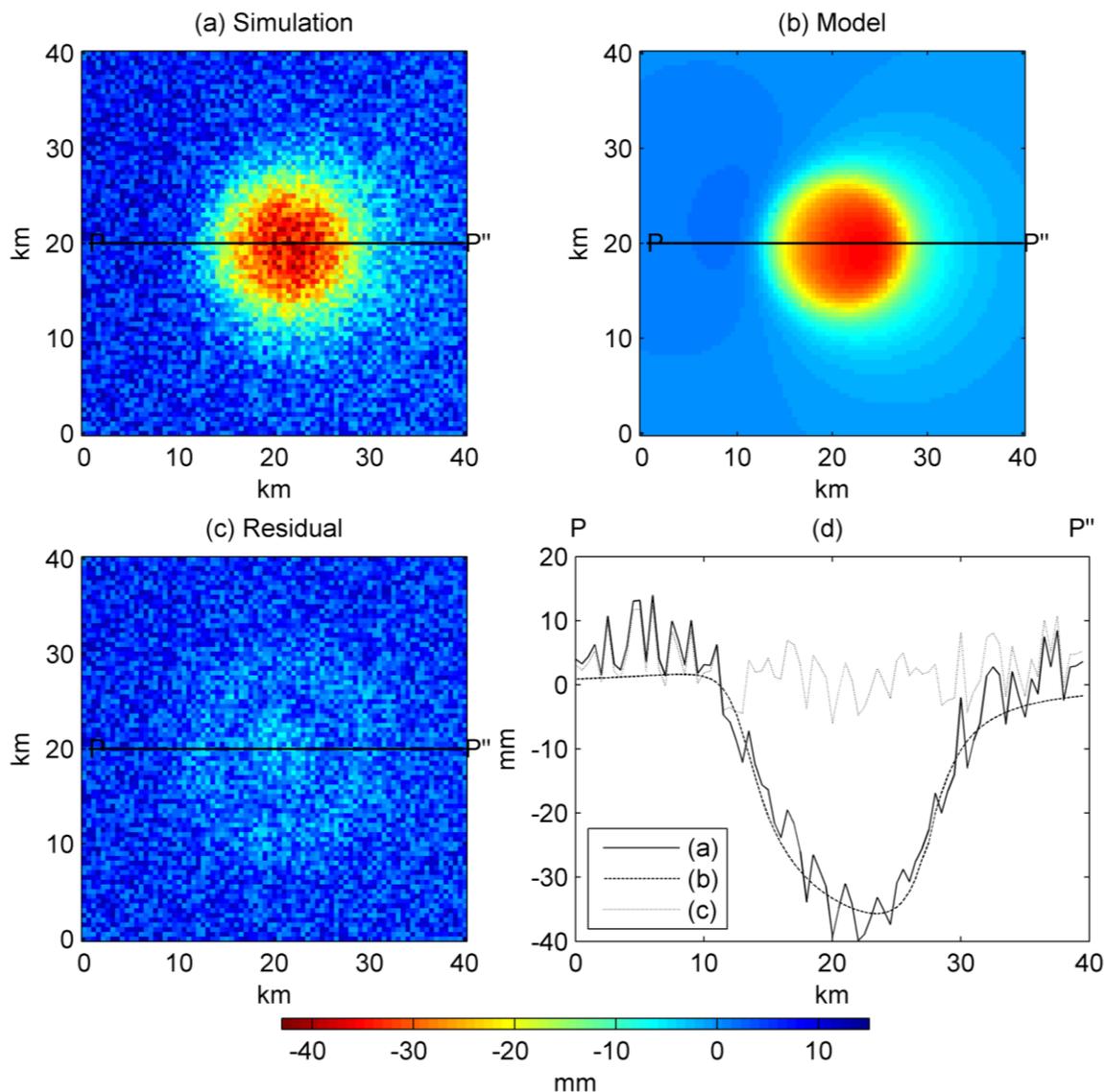
**Figure 6.6 (a) simulated displacement using Poroelastic model on earth surface with added noise. (b) Best fit poroelastic disk reservoir model with bounded Poisson's ratio and bounded Biot coefficient for the simulated displacement filed. (c) Residuals between simulation and model. (d) Profiles of the simulation, model and residuals.**

## 6.2.5 Comparisons of model parameters for synthetic data

As the ellipsoidal source is not applicable for the simulated dataset, only the parameters obtained from inversions of the simulated displacement using spherical Mogi type point deformation source and poroelastic disk reservoir are compared. Both the two models are able to retrieve the source centre for simulation. The added noise makes no significant difference to the modelled position of the source centre.

The Mogi model overestimates the depth of the deformation source. The disk reservoir estimates the depth better when there is no additional noise. The added noise reduces the depth of estimated source depth for the two models, reducing the overestimation of the depth for Mogi source, but causing underestimation of the depth for the disk reservoir. This explains why the RMS errors of depth response oppositely to the addition of noise for the elastic and poroelastic models.

The radius of the Mogi source cannot be estimated independently. The Mogi source cannot estimate the pressure change independently without extra information. The Mogi and ellipsoidal sources show different distribution patterns of Poisson's ratio with the disk reservoir by approaching the upper limit. The findings based on the simulation cases are:

- Disk reservoir model differs from Mogi by including inelastic effects.

- For Mogi source, the added noise affects the depth and volume except source centre. The Poisson's ratio affects the volume but has negligible effect on depth and source centre. The Poisson's ratio cannot be reliably obtained from inversion and should be fixed. The advantage of Mogi source is that it gives confined solutions although sometimes with significant offsets in the simulated case. The disadvantage of Mogi is limited information on the source dimensions.

- For disk reservoir, the added noise affects all parameters except the source centre and radius of the reservoir. The Biot coefficient affects the reservoir thickness and pressure decline, with negligible effect on source centre, reservoir depth and radius. The Poisson's ratio only affects the reservoir thickness and pressure decline slightly, with negligible effect on source centre, reservoir depth and radius. The Poisson's ratio is obtained with uncertainty. The advantage of disk reservoir is that most geometric parameters can be reliably obtained, although some parameter are not accurately obtained (e.g. pressure rely on the knowledge of material parameters such as Poisson's ratio and Biot coefficient).

**Table 6.6 RMS differences between model parameters obtained from inversion and used for simulation**

| Model RMS | Noise added (Y/N) | Poisson's ratio fixed (Y/N) | Biot coefficient fixed (Y/N/-) | $X_c$ (km) | $Y_c$ (km) | $d$ (km) | $\Delta P$ (MPa) | $\nu$ | $T$ (m) | $R$ (km) | $\alpha$ |
|---|---|---|---|---|---|---|---|---|---|---|---|
| Mogi | N | N | ___ | 0.01 | 0.003 | 3.43 | ___ | 0.12 | ___ | ___ | ___ |
| Mogi | N | Y | ___ | 0.01 | 0.003 | 3.40 | ___ | ___ | ___ | ___ | ___ |
| Mogi | Y | N | ___ | 0.17 | 0.05 | 1.41 | ___ | 0.18 | ___ | ___ | ___ |
| Mogi | Y | Y | ___ | 0.17 | 0.04 | 1.41 | ___ | ___ | ___ | ___ | ___ |
| Disk reservoir | N | N | N | 0.07 | 0.09 | 0.97 | 33.1 | 0.17 | 123.5 | 0.55 | 0.52 |
| Disk reservoir | N | Y | N | 0.03 | 0.04 | 0.06 | 32.1 | ___ | 106.0 | 0.06 | 0.55 |
| Disk reservoir | N | N | Y | 0.02 | 0.02 | 0.06 | 21.7 | 0.16 | 86.5 | 0.06 | ___ |
| Disk reservoir | N | Y | Y | 0.006 | 0.02 | 0.02 | 13.7 | ___ | 77 | 0.02 | ___ |
| Disk reservoir | Y | N | N | 0.18 | 0.17 | 1.51 | 36.6 | 0.14 | 118.8 | 0.55 | 0.41 |
| Disk reservoir | Y | Y | N | 0.21 | 0.19 | 1.44 | 37.3 | ___ | 104.1 | 0.49 | 0.48 |
| Disk reservoir | Y | N | Y | 0.36 | 0.31 | 1.25 | 26.6 | 0.15 | 93 | 0.51 | ___ |
| Disk reservoir | Y | Y | Y | 0.17 | 0.16 | 1.47 | 21.4 | ___ | 69.1 | 0.29 | ___ |

# 6.3 Modelling subsidence in the Yellow River delta

An area in the Gudao oilfield with near axisymmetric displacement is modelled using the same three models as above, the spherical deformation source Mogi type model, the ellipsoidal source and the poroelastic disk reservoir. The disk reservoir is expected to give reliable estimates for reservoir geometries based on the simulation experience.

## 6.3.1 Spherical point source in Gudao oilfield

Unfortunately oil production data in the Yellow River delta is proprietary and cannot be obtained. The modelled depth can be compared with a published study that estimates the Gudao oilfield to be $1120\sim1350\ m$ in depth (Lu et al., 2005). When the InSAR displacement is inverted directly, the estimated depth from Mogi model is $500\sim730\ m$ deeper than this with added noise and $920\sim1150$ deeper with no added noise. This could be caused by an unknown global bias, which is due to inaccurate reference level (Biggs et al., 2009) or other uniform signals. Hence the global bias is incorporated into the model by co-estimating an offset between the model and the InSAR displacement (Muntendam-Bos et al., 2008). It is treated simply by adding a constant term to the modelled displacement during inversion. The non linear least square algorithm will find the optimum solution which minimizes the misfit between the model with offset and the data. Alternatively, the mean phase of each image is again used as the reference phase for InSAR. The two methods actually have similar results later (Table 6.7).

As in the simulation case above, Poisson's ratio obtained from inversion approaches the upper theoretical limit of 0.5 when the Mogi sources is implemented in the Gudao oilfield. So a more strict bounds $[0.17, 0.34]$ are set for Poisson's ratio based on the laboratory measurements of drained and un-drained Poisson's ratios of six kinds of sandstone (Hart and Wang, 1995, Detournay and Cheng, 1993). As expected, the Poisson's ratio approaches the restricted upper limit again when inverted. Fortunately, the Poisson's ratio is well confined at 0.25 from the disk reservoir later, so it is fixed to this value for Mogi model.

**Table 6.7 Mogi model parameters obtained from inversion for four cases: offset co-estimation or mean value as InSAR reference, in each case with or without added noise. A: Mogi with no added noise and offset estimated. B: Mogi with added noise and offset estimated. C: Mogi with no added noise and mean value as InSAR reference. D: Mogi with added noise and mean value as InSAR reference.**

| Quantity | Source centre east | Source centre north | Depth | Volume change | offset | Variance of misfit |
|---|---|---|---|---|---|---|
| Symbol (unit) | $X_c$ $(km)$ | $Y_c$ $(km)$ | $d$ $(km)$ | $\Delta V$ $(m^3)$ | $(mm)$ | $(mm^2)$ |
| $A$ | $2.2 \pm 0.0003$ | $2.4 \pm 0.0003$ | $1.37 \pm 0.002$ | $4.1 \times 10^5 \pm 1.1 \times 10^3$ | $19.9 \pm 0.03$ | $63.6 \pm 0.00007$ |
| $B$ | $2.2 \pm 0.03$ | $2.4 \pm 0.03$ | $1.37 \pm 0.07$ | $4.2 \times 10^5 \pm 4.3 \times 10^4$ | $10.2 \pm 1.2$ | $89.3 \pm 3.3$ |
| $C$ | $2.2 \pm 0.0003$ | $2.3 \pm 0.0002$ | $1.24 \pm 0.0002$ | $3.3 \times 10^5 \pm 91$ | ____ | $63.1 \pm 0.0003$ |
| $D$ | $2.1 \pm 0.01$ | $2.3 \pm 0.007$ | $0.80 \pm 0.008$ | $1.3 \times 10^5 \pm 1765$ | ____ | $99.3 \pm 1.01$ |

Firstly, the displacement field from InSAR observation is modelled directly without added noise. Secondly, random noise equivalent to 30% displacement is added to examine the sensitivity of the estimated parameters (Table 6.7). The procedures are followed for the two methods used to account for the global bias. There are thus four categories in Mogi model.

When the offset is estimated to account for global bias, the modelled subsidence centres are both [2.2, 2.4] *km* with or without the added noise. The modelled depths are the same at 1.37 *km*, which are 20~250 *m* deeper than the published depth. The modelled volume change increased by 2% with added noise. The offset reduced by 49% while the variance of misfit increased by 40% with added noise.

When the mean phase value is referenced to account for global bias, the modelled subsidence centres are [2.1~2.2, 2.3] *km*. The modelled depth without added noise is just 5 *m* deeper than the mean value of the published depth. It is 440 *m* shallower with the added noise, which was also found in the simulation above. The volume change reduced with added noise by 61% like the simulation case. A 57% increase of the variance of misfit is likely to be caused by the presence of noise.

It can be seen that the parameter stability of the first method is better, but the accuracy of depth is higher for the second method (mean reference) when there is no additional noise.
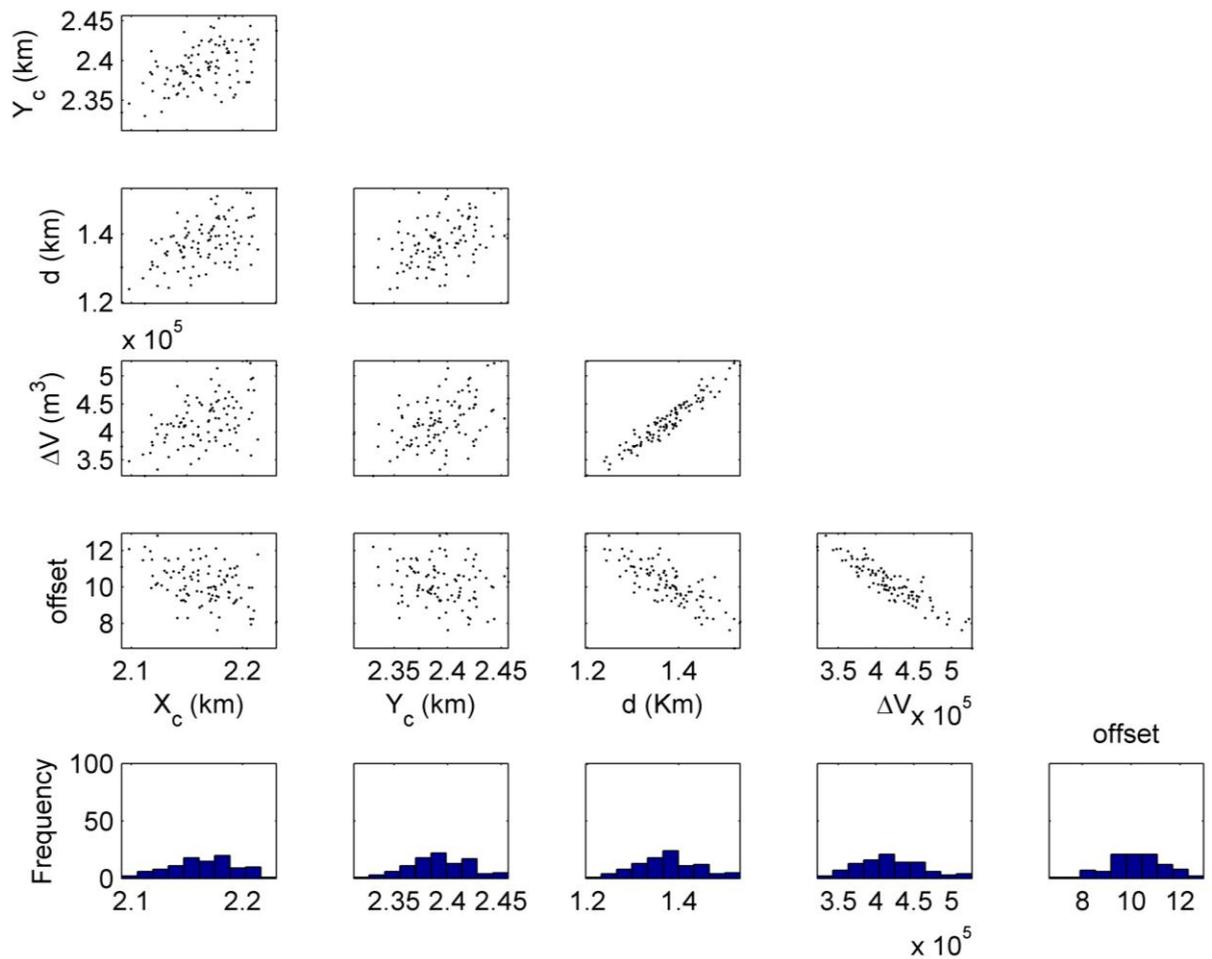


**Figure 6.7 Matrix plot for 100 groups of best fit Mogi model parameters for the InSAR derived displacement with added noise and offset estimated in Gudao Town.**

It can also be seen from the matrix plot (Fig. 6.7) that there is a direct trade-off between change of volume and the depth. Trades-offs between offset and depth, and between offset and volume change are also seen.
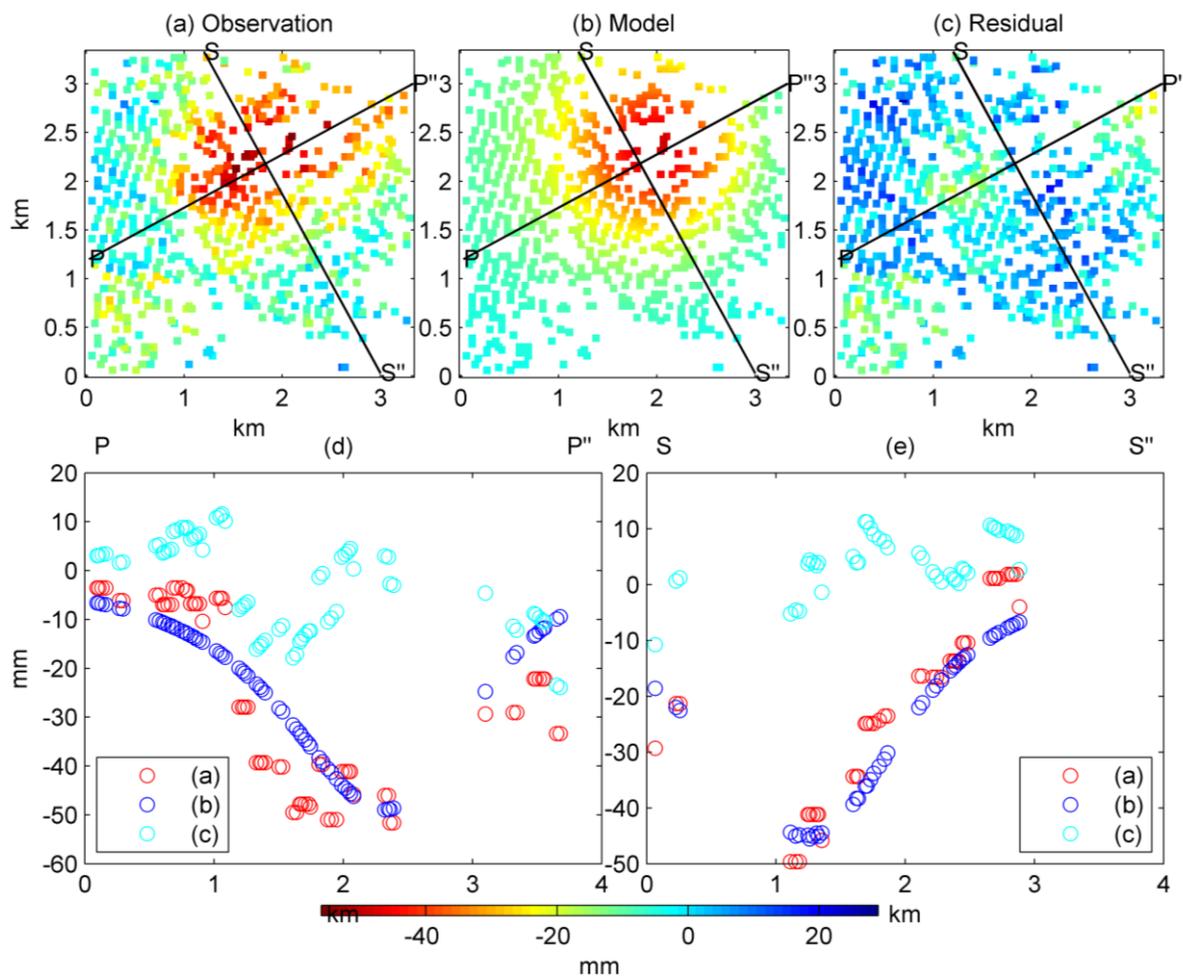
**Figure 6.8 (a) InSAR derived line of sight cumulative displacement field in Gudao Town between 20070201 and 20100121 with mean value as InSAR reference and no added noise. (b) Best approximated displacement field using a single Mogi deformation source. (c) Residuals between InSAR and modelled displacements. (d) Profile P-P" of (a), (b) and (c). (e) Profile S-S" of (a), (b) and (c).**

The Mogi model might have underestimated the displacement in the lower left corner of the mapping area (Fig. 6.8). The area of displacement in the lower left corner shows some separation from the central area of subsidence and may be related to a separate source. The area of near symmetrical displacement is only $3 \times 3 \ km$ in which the relative displacement is up to 67 $mm$. The observation on the profile PP", which is on the elongated direction of the near symmetric subsidence, can be seen as three clusters from SW to NE (Figure 6.8d). The left cluster (0-1 $km$ along the profile) shows little change without systematic gradient. The model fails to fit this part and systematically overestimates subsidence (positive residuals). The central cluster (1-2.5 $km$) shows more subsidence than the left cluster and exhibits a displacement gradient although with obvious fluctuations. The model underestimates subsidence here and has residuals up to 20 $mm$. The right cluster (2.5-4 $km$) has only a few pixels and these show less subsidence than the central cluster. Overall the three clusters suggest a bowl shape subsidence field. The observation on the profile SS",

which is perpendicular to PP'', show general good fit but with residuals up to 10 *mm* near 2 *km* and 3 *km*.

## 6.3.2 Ellipsoidal source in Gudao oilfield

When the InSAR displacement is inverted directly, the estimated depth ellipsoidal source model is 6.4~6.6 *km* deeper than published depth with added noise and 7.1~7.3 *km* deeper with no added noise. The offset estimation method is tried but the result obtained from inversion is ill conditioned with unstable solution. Hence only the mean reference method is used to account for the global bias for ellipsoidal source. As expected, the Poisson's ratio approaches the restricted upper limit again when the displacement is inverted using ellipsoidal sourced. Hence Poisson's ratio is fixed to 0.25, which is confined from the disk reservoir later.

The shear modulus of the sandstone reservoir in the Gudao oilfield is unknown. Detournay and Cheng (1993) reported the shear modulus and porosity for six types of sandstones, of which we can fit a linear relationship (Fig. 6.9). The porosity of the Gudao oilfield is 29~34% (Lu et al., 2005) corresponding to shear modulus of $2.7 \sim 0.7 GPa$ on the line of Figure 6.9. Kovacik (2008, 2001) demonstrate good linear fits between shear modulus and porosity for $Th_2O$ when porosity is under 0.25. In his results, linear fitting underestimates the shear modulus by 6% near porosity of 0.3 and by 30% near porosity of 0.4. Hence the decline of shear modulus accompanying increasing porosity is likely to slow down when the porosity exceeds 25% for sandstone. The shear modulus for sandstone is in the range of $1.2 \sim 41.6 \ GPa$ (Bell, 2007). For the Gudao oilfield, shear modulus 2.5 $GPa$ is adopted for the ellipsoidal source and the disk reservoir models.
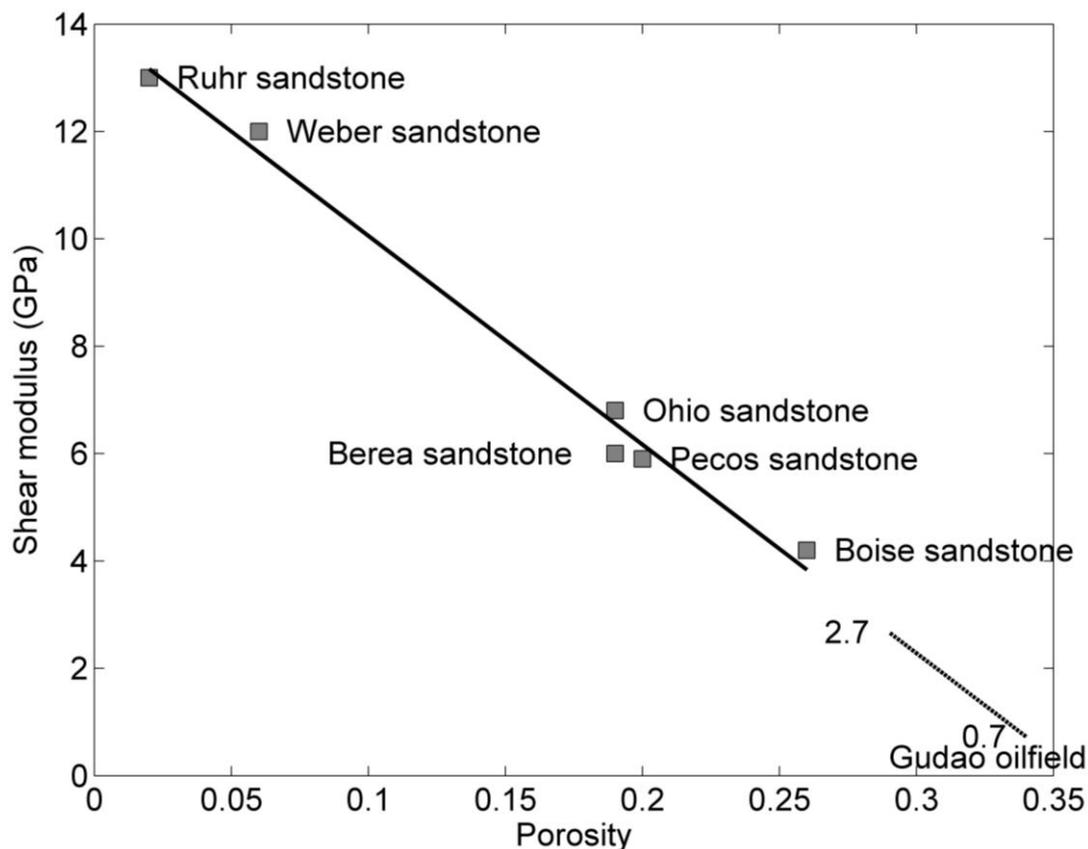
**Figure 6.9 The shear modulus and porosity of different kinds of sandstone, after (Detournay and Cheng, 1993). Each square is a type of sandstone. Black solid line is the fitted linear relationship between shear modulus and the porosity. The dashed line is the linear extrapolation of the solid line to the porosity reported for the Gudao oilfield.**

**Table 6.8 Ellipsoidal model parameters. A: Ellipsoidal source with no added noise and mean value as InSAR reference. B: Ellipsoidal source with added noise and mean value as InSAR reference.**

| Quantity | Source centre east | Source centre north | Depth | Pressure change | Semi major axis | Semi minor axis | Strike | Plunge | Variance of misfit |
|---|---|---|---|---|---|---|---|---|---|
| Symbol (unit) | $X_c$ (km) | $Y_c$ (km) | $d$ (km) | $\Delta P$ (MPa) | $a$ (km) | $b$ (km) | $\phi$ (deg) | $\theta$ (deg) | $mm^2$ |
| A | $2.1 \pm 0.1$ | $3.1 \pm 0.1$ | $1.59 \pm 0.05$ | $1.4 \pm 3.7$ | $1.94 \pm 0.15$ | $0.59 \pm 0.19$ | $327.0° \pm 1.0°$ | $42.0° \pm 1.0°$ | $47.7 \pm 0.01$ |
| B | $1.9 \pm 0.3$ | $2.5 \pm 0.3$ | $0.59 \pm 0.02$ | $0.0015 \pm 0.0036$ | $5.49 \pm 1.02$ | $5.37 \pm 1.04$ | $302.1° \pm 2.7°$ | $12.9 \pm 1.3°$ | $85.9 \pm 2.4$ |

The InSAR derived displacement field is modelled both without added noise and with addition of 30% random noise. The ellipsoidal model is not applicable for displacment with added noise (Cateogry B in Table 6.8) because the ellipsoid exceeds the Earth surface. The soultion obtained without added noise (Cateogry A in Table 6.8) show 0.1 *km* uncertainty in positioning of the source centre. The depth obtained from inversion is

240~470 *m* deeper than the published reservoir depth. The pressure change obtained from inversion shows significant uncertainty. The big dipping angle does not reflect a flat lying reservoir.
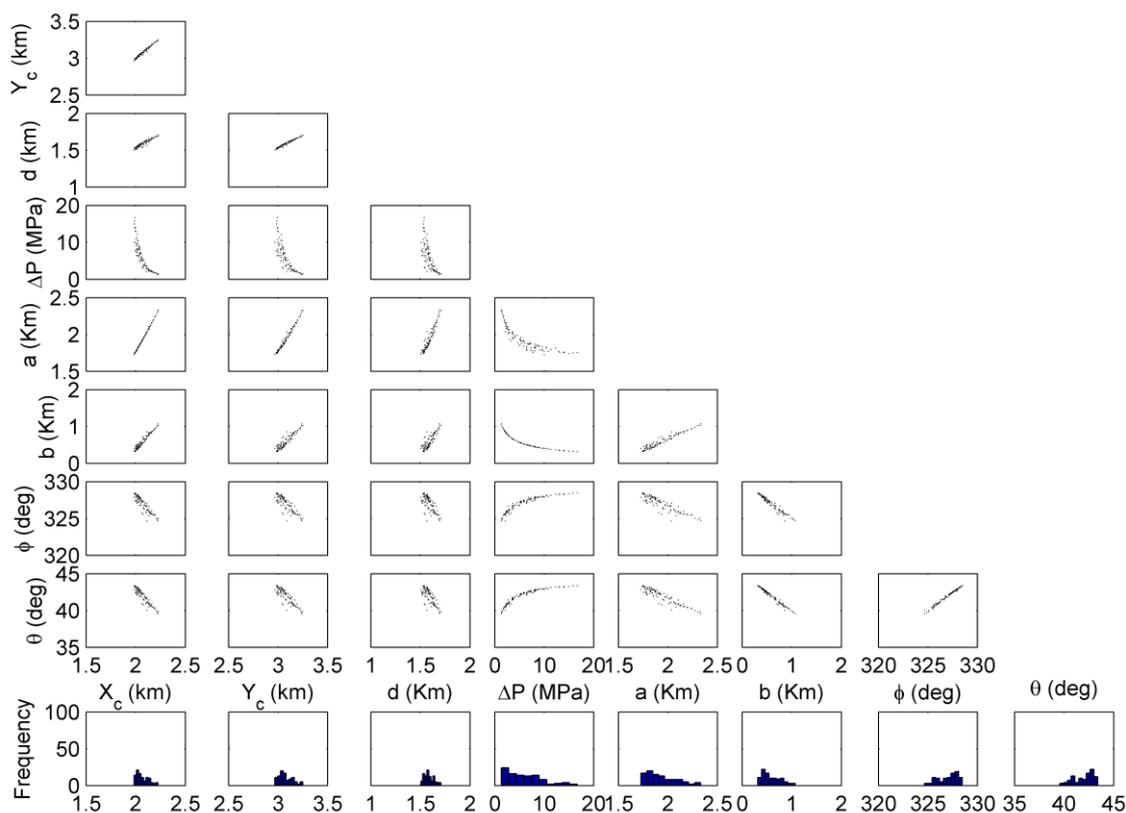


**Figure 6.10 Matrix plot for 100 groups of best fit ellipsoidal model parameters for InSAR derived displacement with mean phase value as reference and with no added noise in Gudao Town. The solutions with added noise are not applicable (Category B) and not plotted.**

Trade-offs is seen between every two parameters (Figure 6.10). Trade off between b and $\Delta P$ was used to explain unrealistic big pressure values in Coos geothermal field (Fialko and Simons, 2000).
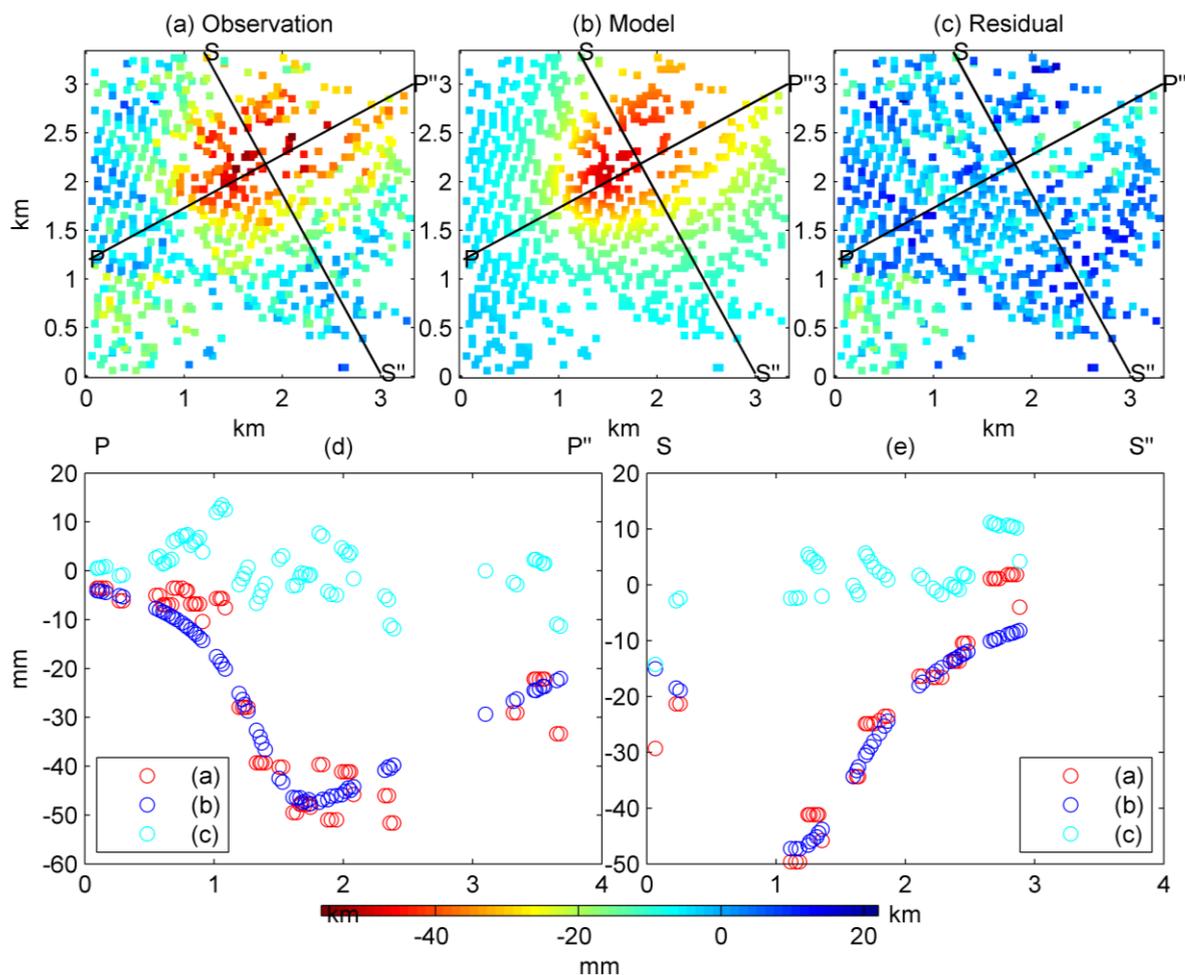
**Figure 6.11 (a) InSAR derived line of sight cumulative displacement field in Gudao Town between 20070201 and 20100121 with mean value as InSAR reference and no added noise. (b) Best approximated displacement field using an ellipsoidal deformation source. (c) Residuals between InSAR and modelled displacements. (d) Profile P-P" of (a), (b) and (c). (e) Profile S-S" of (a), (b) and (c).**

The optimised ellipsoidal source model exhibits a better overall fit than the spherical Mogi source, with smaller error variances compared to Mogi when there is no added noise for both models. The better fit of a ellipsoidal source was also observed in modelling of the Coso geothermal field (Fialko and Simons, 2000) and was explained by the greater number of degrees of freedom (dip, strike, etc) associated the ellipsoidal source than for the spherical source. It can be seen that the ellipsoidal source model can match the bottom of observed displacement in centre cluster of the profile (Fig. 6.11). Note that, in the left cluster (0-1$km$ along PP" in Figure 6.11d), the ellipsoidal source also produces a systematic over-estimation of subsidence as did the Mogi model.

## 6.3.3 Poroelastic disk reservoir in Gudao oilfield

When the InSAR displacement is inverted directly, the estimated depth is 720~950 $m$ deeper than the published depth with no added noise and 500~730 $m$ deeper with added noise. The offset estimation was tried but the depth is ill conditioned with uncertainty of

790 $m$ with added noise and 1040 $m$ without added noise. Hence the mean reference method is used to account for the global bias. The Poisson's ratio is bounded between 0.17 and 0.34 based on laboratory measurements of six kinds of sandstone (Detournay and Cheng, 1993).

**Table. 6.9 Poroelastic disk reservoir model parameters. A: Disk reservoir with no added noise and mean value as InSAR reference. B: Disk reservoir with added noise and mean value as InSAR reference.**

| Quantity | X | Y | Depth | Pressure change | Disk reservoir thickness | Disk reservoir radius | Biot coefficient | Poisson's ratio | Variance of misfit |
|---|---|---|---|---|---|---|---|---|---|
| Symbol (unit) | $X_c\ (km)$ | $Y_c\ (km)$ | $d\ (km)$ | $\Delta P\ (MPa)$ | $T\ (m)$ | $R\ (km)$ | $\alpha$ | $\nu$ | $(mm)^2$ |
| A | 1.45 $\pm$ 0.02 | 2.38 $\pm$ 0.01 | 1.45 $\pm$ 0.02 | 26.1 $\pm$ 11.2 | 222.2 $\pm$ 95.6 | 0.70 $\pm$ 0.03 | 0.52 $\pm$ 0.17 | 0.25 $\pm$ 0.03 | 71.7 $\pm$ 0.29 |
| B | 1.56 $\pm$ 0.04 | 2.35 $\pm$ 0.04 | 0.87 $\pm$ 0.13 | 19.2 $\pm$ 14.4 | 190.4 $\pm$ 105.6 | 0.77 $\pm$ 0.14 | 0.45 $\pm$ 0.18 | 0.26 $\pm$ 0.03 | 93.4 $\pm$ 1.17 |

The displacement field from InSAR observations are modelled with poroelastic disk reservoir both without added noise and with addition of 30% random noise (Table 6.9). The source centre location only changes slightly when noise is added. The estimated depth is 100~330 $m$ deeper than the published depth without added noise. The estimated reservoir depth is 250~480 $m$ shallower than the published depth with added noise, as in the simulated case. The estimated pressure decline is 26% less with added noise. Actual pressure change data are unavailable for comparsion. The estimated disk reservoir thickness is around 220 $m$ which is in agreement with the actual total reservoir thickness of 170~350 m (Lu et al., 2005). The modelled Biot coefficient is centred around 0.52 with similar uncertainty of 0.17 for both noise conditions. The Biot coefficient can be validated if core samples provide the following parameters.

$$\alpha = \phi \mathrm{K} C_{pc} \tag{6.17}$$

$$C_{pc} = -\frac{1}{V_p}\left(\frac{\partial V_p}{\partial P_{conf}}\right)_p \tag{6.18}$$

where $\phi$ is the porosity, K is undrained bulk modulus, $C_{pc}$ is change in pore volume induced by a change in confining pressure at constant pore pressure (Segall et al., 1994). All these parameters have to be determined from laboratory measurements. Core sample porosity of Gudao oilfiled is 29~34% (Lu et al., 2005), but the undrained bulk modulus

and the pore compressibility are unknown. Poisson's ratio is centred around 0.25 with uncertainty of 0.03 for both noise situations. The modelled Poisson's ratio is used earlier in Mogi source and ellipsoidal source. Variance of misfit increased with added noise.
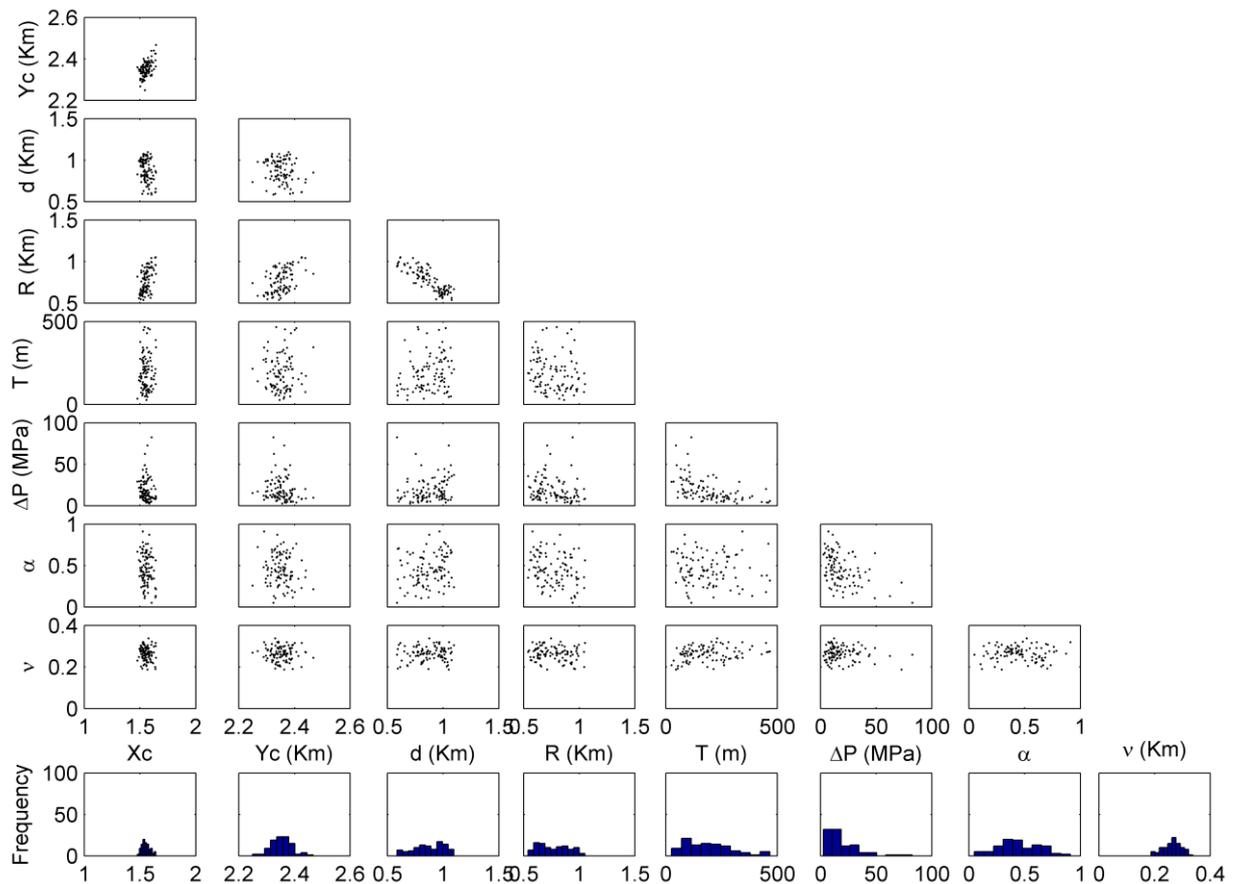


**Figure 6.12 Matrix plot for 100 groups of best fit poroelastic disk reservoir parameters for InSAR derived displacement with mean phase value as reference and with added noise in Gudao Town.**

The parameters are plotted against each other to examine the trade-offs (Fig. 6.12). The source centre is well confined with symmetrical distributions. The reservoir depth and radius have more fluctuations in distributions. The reservoir thickness, Biot coefficient and the Poisson's ratio are distributed in a wider range. Trade-off is observed between reservoir radius and depth. Along profile PP", the modelled displacement seems an upper envelope for the central and right clusters and passes below the left cluster in the profile (Fig. 6.13). From profile SS" which demonstrates higher displacement gradient, the model overestimates the displacements in the flanks. On one hand, the problem is related with the non axisymmetry of the deformation. On the other hand, it may be related with the heterogeneity of pressure distribution in the reservoir and can be solved by considering non uniform pressure drop, if the actual pressure change distributions within the reservoir are known and can be approximated in terms of a radial symmetric function.
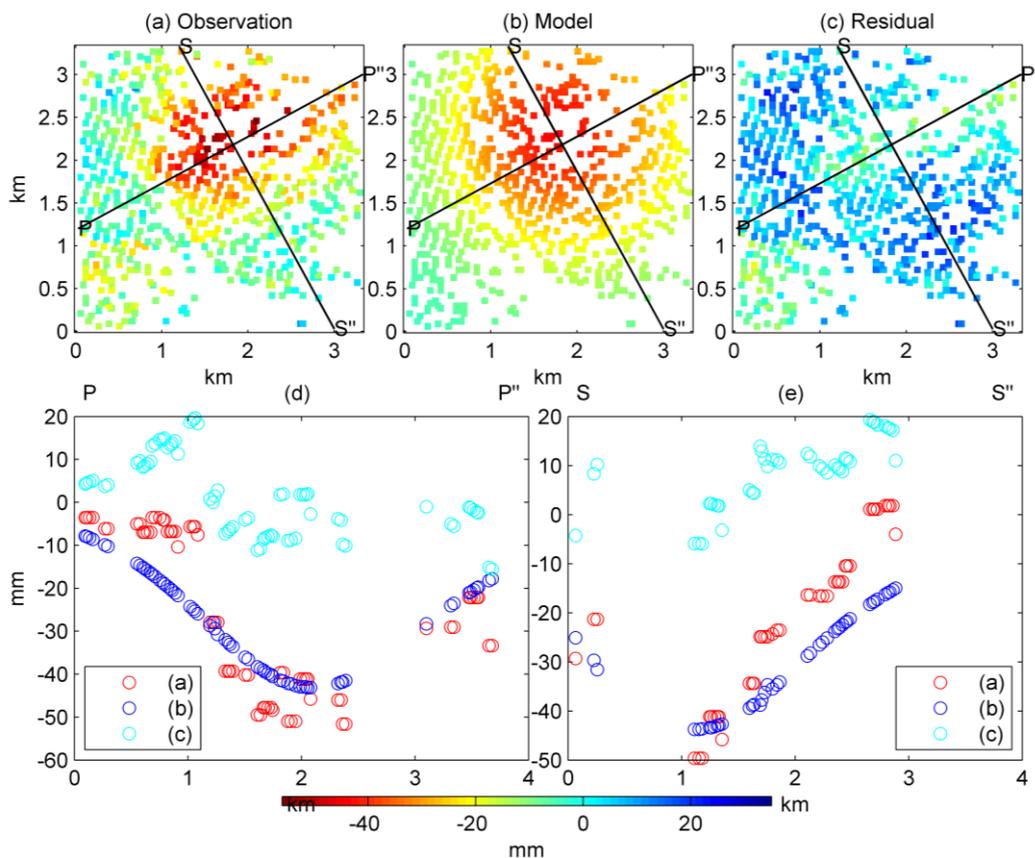
**Figure 6.13 (a) InSAR derived line of sight cumulative displacement field in Gudao Town between 20070201 and 20100121 with mean value as InSAR reference and no added noise. (b) Best approximated displacement field using a disk reservoir model. (c) Residuals between InSAR and modelled displacements. (d) Profile P-P" of (a), (b) and (c). (e) Profile S-S" of (a), (b) and (c).**

## 6.3.4 Comparisons of model parameters for InSAR observation

**Table. 6.10 Common model parameters and published parameters for the spherical source, ellipsoidal source and the disk reservoir models.**

| Quantity | Source centre east | Source centre north | Depth | Pressure change | Disk reservoir thickness | Variance of misfit |
|---|---|---|---|---|---|---|
| Symbol (unit) | $X_c$ (km) | $Y_c$ (km) | $d$ (km) | $\Delta P$ (MPa) | $T$ (m) | $(mm^2)$ |
| Published values | ____ | ____ | 1.12~1.35 | ____ | 170~350 | ____ |
| Mogi, no added noise | $2.2 \pm 0.0003$ | $2.3 \pm 0.0002$ | $1.24 \pm 0.0002$ | ____ | ____ | $63.1 \pm 0.0003$ |
| Mogi, added noise | $2.1 \pm 0.01$ | $2.3 \pm 0.007$ | $0.80 \pm 0.008$ | ____ | ____ | $99.3 \pm 1.01$ |
| Ellipsoid, no added noise | $2.1 \pm 0.1$ | $3.1 \pm 0.1$ | $1.59 \pm 0.05$ | $1.4 \pm 3.7$ | ____ | $47.7 \pm 0.01$ |
| Disk, no added noise | $1.45 \pm 0.02$ | $2.38 \pm 0.01$ | $1.45 \pm 0.02$ | $26.1 \pm 11.2$ | $222.2 \pm 95.6$ | $71.7 \pm 0.29$ |
| Disk, added noise | $1.56 \pm 0.04$ | $2.35 \pm 0.04$ | $0.87 \pm 0.13$ | $19.2 \pm 14.4$ | $190.4 \pm 105.6$ | $93.4 \pm 1.17$ |

Here parameters are given in Table 6.10. The modelled source centre position is different for the spherical source, ellipsoidal source and the disk reservoir models in the Gudao oilfield. Mogi estimates the depth accurately. Disk reservoir and the ellipsoidal source overestimate the depth by about 200 *m* and 350 *m* respectively. Both the ellipsoidal source and the disk reservoir estimate the source pressure change. The disk reservoir gives greater pressure change with smaller relative uncertainty than ellipsoidal source. Only the disk reservoir model estimates the reservoir thickness, and this agrees with the actual total thickness. Both the disk reservoir and the ellipsoidal source estimate the dimensions of the sources but with different geometric definitions. Both the Poisson's ratios of Mogi and ellipsoidal source use the Poisson's ratio confined from disk reservoir.

## 6.4 Comparison of model parameters for simulation and InSAR observation

The same three models have been implemented for both the synthetic data and for the displacement field of the Gudao oilfield measured from InSAR observations. The synthetic data is a symmetrical displacement in the radar line of sight direction. This regular geometry makes it easier for the models to identify the source centre than is the case for the InSAR observations. The addition of noise results in shallower estimated depths for both the synthetic data and the real data. The depth were overestimated by Mogi and underestimated by disk reservoir in simulation. For InSAR observation, Mogi estimates the depth successfully, whilst the disk reservoir overestimates the depth slightly, and a bit more overestimation for the ellipsoidal source. Pressures and estimated with uncertainty for both ellipsoidal source and disk reservoir. Mogi has no estimation for source dimensions. Ellipsoidal source has greater degrees of freedom in geometry and a best approximation is seen for the InSAR observation compared with Mogi and the disk reservoir when there is no additional noise. The radius is estimated with small uncertainty in both the synthetic and real cases by the disk reservoir. The reservoir thickness is estimated with comparable uncertainty for the synthetic and real cases by disk reservoir model. The Poisson's ratios approach the upper limit for Mogi and ellipsoidal source. The Poisson's ratio is estimated with smaller uncertainty in the real case than in the synthetic case by disk reservoir. The Biot coefficient is estimated with similar uncertainty in both cases although the real Biot coefficient in the Gudao oilfield is unknown.

For the synthetic data, the disk reservoir gives the least RMS errors. Bear in mind that the synthetic data is simulated using a disk reservoir. For the Gudao oilfield, the actual

sandstone reservoir size, actual production volume, in-situ pressure change, and core material parameters will be helpful to determine the performance of the three models. Here are some findings based on current work:

- The offset estimation method can be used for Mogi to compensate the global bias for modelling. While for ellipsoidal source and disk reservoir, which have more model parameters, the global bias should be addressed before modelling using independent ground truth such as GPS and levelling. The global bias will cause overestimation for source depth for all three models.

- Random noise will cause the underestimation for source depth and other model parameters.

- Both Mogi and disk reservoir give more stable results than the ellipsoidal source. Trade-offs can be strong for ellipsoidal source. The ellipsoidal source needs to be examined to see if it is applicable.

- Poisson's ratio cannot be reliably estimated from inversion for either Mogi or ellipsoidal sources. For Mogi source, Poisson's ratio needs to be measured directly to provide accurate volume change estimation. For ellipsoidal source, Poisson's ratio and shear modulus should be measured directly. For the disk reservoir, Biot coefficient should be measured directly to have better estimation for pressure change and thickness. Shear modulus should also be measured to better estimate the pressure change. For low porosity sandstone reservoir, the shear modulus can be fitted if porosity is known.

# Chapter 7 Conclusions

Subsidence in river deltas causes relative sea level rise, coastline change, wetland loss and flooding, and so places high risk on local communities. Attention has been drawn to land subsidence in the Yangtze River delta and Pearl delta regions in China because economic dynamos with over 10 million populations are located there, but less attention is paid to the Yellow River delta region although 1.64 million people, 65 oil field with $75 \times 10^8$ tonnes oil reserve, and a National Nature reserve of 1530 km$^2$ are situated there (Chen et al., 2012). Based on three years of ASAR imagery, I have mapped the surface displacements in the Yellow River delta region and modelled the InSAR observations with respect to three different deformation mechanisms.

## 7.1 InSAR results

The InSAR results were given in Chapter 5. This section will synthesize the InSAR results to answer the research questions.

*Question 1: Is it feasible to use InSAR to monitor surface movements in the Yellow River Delta region*? *How accurate can the InSAR results be?*

With its sub centimetre accuracy, regular data acquisition (35 repeat interval for ASAR), and previous successful application to subsidence, InSAR was used to monitor surface movements in the Yellow River delta. Areas of subsidence were observed in Gudao oilfield and Gudong oilfield. The mean velocities reached about 30 mm/yr in Gudao oilfield with a bowl shaped velocity profile gradually decreasing to lower rates at margins. The subsidence in Gudong oilfield does not have a regular shape, and can be thought as two separate subsidence centres. The mean velocities of the northern subsidence in Gudong reached about 15 mm/yr, whilst the velocity of the southern subsidence in Gudong reaches about 20 mm/yr.

The accuracy of InSAR measurements can be lowered by various error sources, whose effects are mitigated by applying time series InSAR processing techniques. The accuracy of InSAR measurement is assessed from Track 132 and 404 with similar incidence angles. The mean velocity field shows a standard deviation of 2.7 mm/yr and correlation of 0.72 between two adjacent tracks. The time series are consistent in displacement trend although seasonal differences remain which may be due to residual atmospheric effects. Pixels with

time series RMS differences between the independent tracks below 3 mm, 5 mm and 10 mm, account for 11%, 60%, and 97% of the total common pixels, respectively.

*Questions 2: What is the major cause of surface displacement in the Yellow River delta region?*

To identify possible reasons for the observed subsidence, field investigation was conducted in the Yellow River delta. The Gudao Town, Xianhe Town and Gudong oilfield to the north of the current Yellow River channel, the aquafarms to the south of current channel and the Yellow River Delta National Nature Reserve (YRDNNR) in the cuspate delta, were inspected. The areas showing coherent subsidence bowls from the InSAR observations are associated with the Gudao and Gudong oilfields, in which oil extraction dates back to the late 1960s and late 1980s, respectively. Oil extraction is very likely the major cause of non-uniform subsidence observed in Yellow River delta.

*Question 3: Is the major cause the sole reason for subsidence?*

It should be noted that the PS (persistent/permanent scatterers) and SDFP (slowly decorrelating filtered phase) pixels detected in the Yellow River delta region are mainly due to man-made activities and structures, oil fields and towns. Most of the natural and farmed vegetated areas give no stable radar back scattering, leaving empty zones in the InSAR results. The subsidence rates in areas with no or sparsely distributed PS or SDFP points remain unknown. It is difficult to conclude if there is any other cause contributing to surface subsidence in addition to oil extraction in whole delta region. However, some evidences suggest that other reasons contribute to the total subsidence. In Gudao oilfield, using the Mogi model, an offset of 20 mm is estimated for three years displacement. In Xianhe Town, the majority of pixels show subsidence of 8~12 mm/yr. The model results for these two areas suggest relatively uniform signals without the bowl shape characterized by oil extraction. It is suggested that the uniform subsidence may due to other sources.

It has been reported that other deltas in the world are also subsiding: 0.5 ~ 8 mm/yr in the Nile delta from old to young deposit centres due to sediment compaction (Becker and Sultan, 2009), 5~10 mm/yr in the Mississippi delta by compaction of Holocene organic rich deposits (Tornqvist et al., 2008), 1~2 mm/yr in the Fraser River delta by consolidation of Holocene shallow sediments, and 3~8 mm/yr again in the Fraser river delta due to artificial loading (Mazzotti et al., 2009). Sediment compaction and loading may also

contribute to the total subsidence in Yellow River delta. From InSAR measurement, the uniform rate detected in Gudao oilfield can be 7 mm/yr.

*Questions 4: What are the limitations for applying InSAR to the Yellow River delta?*

The InSAR results given are for a rectangular area of about 40 km by 15 km to the north of the Yellow River channel including Gudao Town, Xianhe Town and Gudong oilfield. The ASAR images processed covered a larger area of about 2200 km$^2$, including the aquafarms to the south of current channel and Yellow River Delta National Nature Reserve (YRDNNR) in the cuspate delta. The three areas however are not connected with each other, leaving 10 km wide gaps with no PS or SDFP detected. The YRDNNR can be seen as a group of isolated islands of PS or SDFP pixels. Some PS or SDFP pixels in YRDNNR were visited and turned out to be the facilities of Shengli oilfield located in the natural reserve. The aquafarms produce some radar signals from the concrete edges of the ponds. The connections between stable pixels in aquafarms are also poor. Phase jumps are seen between the three areas and even within the spatial extent of YRDNNR or aquafarms after unwrapping, indicating phase unwrapping errors. Hence the YRDNNR and aquafarms area cannot be included in the analysis although we are interested in their displacement. Coherence is a limitation for InSAR application in Yellow River delta because if affects the density of stable pixels that can be detected. For phase unwrapping purposes, the phases of neighbouring pixels are required to be within the same phase cycle. If the neighbouring PS or SDFP pixels are far away from each other, it is uncertain if their wrapped phases are within the same cycle.

Without the absolute displacement of an area as the reference for time series, a stable area has to be assumed for time series InSAR. Setting different reference phases does not affect the relative displacement between any two points of the same acquisition, but it affects the relative phases of a single pixel in time, resulting in referenced time series and rates. Hence a truly stable reference area is vital for precise InSAR time series especially for detecting displacements of below 1 cm per year, which is probably the range for displacement due to sediment compaction and loading.

## 7.2 Modelling results

The modelling results were given in Chapter 6. This section synthesizes the modelling results to answer the study's research questions.

*Question 1: Which mechanisms have been used to model the surface movements caused by oil extraction? Why are different models used? What are the differences between them?*

The mechanism modelled is the earth surface displacement by subsurface fluid extraction. Specifically, oil extraction will reduce the oil or gas reserve in reservoir, decreasing the pressure within the reservoir. Reduced pore pressure will increase the effective stress and cause the reservoir to shrink. Reservoir compaction will in turn cause subsidence at earth surface (Fjær et al., 1992).

Following model inversion, for those parameters, e.g. depth, that are already known, the estimated model parameters can be compared with the observed data. Estimates of unknown parameters can only be compared with the range of values expected on the basis of previous studies and also between models to see if they are consistent.

The Mogi and ellipsoidal source models have previously been successfully used to model subsidence due to volcanic activities (Amelung et al., 2000, Lu et al., 2010) and geothermal extraction (Mossop and Segall, 1997, Fialko and Simons, 2000).Surface displacements in volcanoes are usually related with chamber deflation or inflation, which are caused by volcano eruption or magma intrusion. Geothermal plants extract water from the ground for geothermal energy, causing reservoir compaction and thermal contraction, which also result in surface displacement. Since these successful applications of the Mogi and ellipsoidal source models are for surface displacement due to subsurface fluid movement, these same models were used to model Gudao oilfield where subsidence is related with oil extraction.

A third model geometry, the disk reservoir, has been successfully used to model subsidence in the Lacq gas field (Segall et al., 1994). This model also produced good agreement with surface levelling and with known reservoir parameters in Lacq. Hence this approach is also used for the Gudao oilfield.

In terms of the deforming medium, the Mogi and ellipsoidal source are elastic models, whilst the disk reservoir is a poroelastic model which couples stress and pressure changes of the pore fluid. In terms of geometry, the Mogi model assumes an infinitesimal point source. The ellipsoidal source model used here is a finite prolate spheroid, and the disk reservoir assumes a symmetrical disk. The ellipsoidal source has the greatest number of

degrees of freedom and does not assume axial symmetry as both the Mogi and disk reservoir models do.

*Question 2: Can the most appropriate models match the observed displacements? Is there any reason for the residuals? How close are the models to the reality?*

From simulation, the disk reservoir is expected to be the most appropriate for modelling subsidence in Gudao oilfield. In practice, generally good fits to the observed InSAR displacements are seen for all the three models, after inversion. Misfits in the lower left corner of the model domain (Fig 6.8c in Section 6.3.1 of Chapter 6) may be related with another deformation source. The ellipsoidal source fits the observed displacement better than either the Mogi or the disk reservoir because of its more flexible model geometry.

The InSAR observations may also introduce some noise as well as real displacements. The models are all set in an isotropic homogenous medium, which simplifies the real ground condition. It is difficult to determine how much the InSAR noise or model simplification contributes to the total residuals, but this does not affect seeing their effect on model results together. InSAR observations show around 20 mm fluctuation in central cluster along P-P". Both the Mogi source and the ellipsoidal source can match the mean value of the fluctuations but at different positions along the profile (Fig. 6.8d in Section 6.3.1 and 6.11d in Section 6.3.2 of Chapter 6). The disk reservoir model, instead of matching the mean of the fluctuation, however, matches the upper surface of the observed displacement. So the noise together with the simplification of ground condition has greater impact on disk reservoir model than for the Mogi and ellipsoidal source. Even though, which model performs best still depends on whether or not the joined impact of noise and simplification is symmetric around the real displacement. If their impact is symmetric, Mogi and ellipsoidal source will match the real displacement better. If their impact is a systematic overestimation of displacement, disk reservoir will match the real displacement better.

All three models predict depth for the fluid extraction that are close to the actual oilfield depth. Other parameters need to be examined by the ground truth. The pressure appears poorly constrained for ellipsoidal source and the disk reservoir. It takes Lacq gas field about 30 years to have 60 MPa pressure change and 60 mm maximum subsidence with a linear maximum rate of 1 mm/MPa in the centre field and pressure change of 2MPa/yr (Segall et al., 1994). Excluding the 20 mm uniform subsidence, the three years subsidence due to oil extraction in Gudao oilfield is 62 mm which is of the same order of subsidence

in Lacq. The shear modulus used for the Gudao and Lacq reservoirs are 2.5 GPa (sandstone reservoir) and 23 GPa (carbonate reservoir) respectively. So the sandstone reservoir of Gudao oilfield needs less pressure change to produce same level of subsidence because sandstone is weaker than carbonate. That is why for nearly the same level of subsidence, Gudao oilfield shows less pressure decline than that of Lacq. So mathematically, it seems reasonable to have greater rate of 3mm/MPa in Gudao than in Lacq. However, the pressure drop of the order of 20 MPa in three years time estimated by disk reservoir is unexpected. Pressure change of 7 MPa/yr in Gudao does not reflect the truth that water injection has been implemented since 1973 to maintain the pressure in the reservoir (Lu et al., 2005). Better estimation can be achieved by using accurate reservoir parameters, especially the material parameters, such as shear strength, Poisson's ratio and the Biot coefficient.

*Question 3: What is the limitation of modelling application in the Yellow River delta?*

Due to the axisymmetric configuration of Mogi and disk reservoir models, subsidence with arbitrary shapes cannot be modelled, although they can be modelled through superposition of ellipsoidal sources, which however ignores source interaction (Fialko and Simons, 2000). The model is limited to an area with near axisymmetric displacement in Gudao oilfield.

It is also difficult to get good ground truth data for many parameters, e.g. material parameter, pressure change, volume change and reservoir geometry, so full testing of the model is difficult.

Reservoir properties are not homogeneous in directions parallel or perpendicular to the river (Lu et al., 2005). The Yellow River has changed course frequently and produced different sedimentary units in the delta since 1855 (Shi and Zhang, 2003). Material heterogeneity is also a limitation for modelling application

*Question 4: Is subsidence a major problem? Can it be predicted?*

From InSAR observation and modelling, uniform subsidence observed in Xianhe Town may not be a problem in the short time. In a long term, subsidence associated with relative sea level rise and storm surge can increase flooding risk for Xianhe Town. If the uniform subsidence of 8~12 mm/yr in Xianhe Town is by loading, then the rate will decrease to the

level of the area without loading in 3-5 decades based on the observation in Fraser delta (Mazzotti et al., 2009).

Non-uniform subsidence in Gudao Town and Gudong oilfield can be a problem by forming local low-lying areas prone to flooding and difficult to drain. The subsidence rate is generally linear in three years time with maximum rate of 30 mm/yr in Gudao and 15~20 mm/yr in Gudong. The 7 mm/yr uniform subsidence will decrease to a lower rate if it is by loading. The non uniform subsidence depends on future oil production, water injection and how the reservoir responds to the changes. Future observation is helpful to see if the rate is still linear in a longer time interval.

## 7.3 Contributions and implications of this research.

Through this research, the surface displacement over the part of the Yellow River delta region has been mapped using two independent InSAR tracks. Using time series InSAR techniques (Hooper, 2008), stable pixels were extracted from phase analysis. Orbit errors, look angle errors, and atmospheric effects are mitigated in order to produce accurate time series of the displacement field between 2007 and 2010. The time series and mean subsidence rates are consistent between the two tracks. The subsidence in part of Gudao oilfield has been modelled using three different models, which have been validated with source depth and other data.

A clear association between subsidence and the locations of significant and ongoing oil extraction can be identified from the displacement maps. These results may be helpful for local people and environment agencies in the Gudao and Gudong oilfield regions. Gudong oilfield is located in a tidal flat area close to the Bohai Sea. A sea wall of 17 km long, 5 m high and 10 m wide has been built to protect the oil installations from high tides and waves to facilitate oil production in 1986. The sea wall was repaired after a 50 year (return period) storm surge in 1992. With decreasing sediment discharge of Yellow River to the sea, average erosion along the seawall reached 0.73 m between 1998-2003 with maximum water depth of 4~5 m near the sea wall (Li et al., 2008). The ongoing subsidence will decrease the height of ground surface and increase the relative sea level. There is a flooding risk if high tides overtop the wall, although this sea wall is robust and the Bohai Gulf is not so frequently affected by typhoons.

Gudao oilfield is located near to, an inside parts of Gudao Town with population of 35000. The subsidence rate difference can reach 25 mm/yr over a 2 km distance. The rate will affect the stability of man-made structures, which in turn pose threaten to human lives. Building safety inspection is still strongly suggested for Gudao Town.

## 7.4 Future research and applications

Using InSAR observations of the Yellow River delta, displacement mapping is limited to parts of the delta because of poor coherence and subsequent difficulty of phase unwrapping. Greater coherence can be achieved using a longer wavelength satellite e.g. the L band ALOS/PALSAR satellite that was lost in April 2011. Alternatively, using shorter revisit intercals can also improve the coherence e.g. revisit time of 11 days for the X band TerraSAR-X (Adam et al., 2009) and 4~37 hours for Cosmo-SkyMed satellites compared with 35 days of Envisat ASAR images used in this thesis. However, X band will still suffer decorrelation in non-urban areas, although high coherence presents in urban areas (Monells et al., 2010). Hence the application of L band data (e.g. ALOS data archive from 2006~2011 and it is follow-on mission ALOS 2 in preparation) in Yellow River delta will be of interest to detect displacement over a wider area than in this thesis.

For modelling surface displacement due to oil extraction, reservoir geometry, core parameters, contemporary pressure data and volume change information will all help to better constrain the model parameters. However, the data that exist to constrain these parameters are confidential at present. Improvements can also be made by improving the geometry assumed in the poroelastic model. Such an approach is usually implemented using finite element numerical models (FEM). Several studies using finite element modelling for subsidence in oilfield have been published (Lewis and Sukirman, 1994, Lewis and Sukirman, 1993, Kosloff et al., 1980b, Kosloff et al., 1980a, Capasso and Mantica, 2006). Implementation of FEM requires a static 3D model of the reservoir and of the surrounding region, describing all its geological, lithological, stratigraphical and petrophysical aspects (e.g. the shapes of the layers and the trend of the faults, initial porosity and permeability), and a dynamic model regarding the characteristics of the fluids, the rock and the well system (Capasso and Mantica, 2006), which also requires lots of knowledge that remains unknown or confidential for the Yellow River delta.

Shorter revisit time of new SAR satellites will provide a fast build up of high resolution dataset in a short time. This provides the opportunities to test models in a new way by looking at the model perform over shorter time periods.

# Appendix A Sediment samples

## A.1 Sample list

**Table A.1 Sample location, depth and description.**

| Name | Location | Sampling depth | Description |
|---|---|---|---|
| P11 | N37.75523 E118.73203 | 67.5 cm | Cotton field |
| P11B | N37.75304 E118.71769 | 2.3 m | Water channel bank being dug by excavator |
| P12 | N37.80281 E118.78826 | 86 cm | Water pond bank |
| P13 | N37.83706 E118.85735 | 46 cm | Water channel besides rice field |
| P14 | N37.88557 E118.94435 | 50 cm | The bank of a small river |
| P15 | N37.93583 E119.04099 | 50 cm | Low land beside a oil well |
| YRD_BANK_P2 | N37.75941 E118.78487 | 20 cm | Cotton field |
| YRD_BANK_P2B | N37.75925 E118.78472 | Water level | Suspension samples of the Yellow River |
| P21 | N37.72969 E118.76011 | 37 cm | Reed marsh |
| P22 | N37.75926 E118.83928 | N/A | A soil block left by a excavator |
| P23 | N37.76266 E118.91313 | 31 cm | Reed marsh |
| P24 | N37.74088 E118.98489 | N/A | A soil block left by a excavator beside a water channel |
| P25 | N37.76453 E119.06784 | N/A | A soil block left by a excavator beside a water channel |
| P26 | N37.75501 E119.16621 | N/A | A soil block left by a excavator beside a water channel |
| P27 | N37.72985 E119.24225 | Water level | Suspension sample |
| P35 | N37.66939 E119.01701 | N/A | A soil block left by a excavator beside ponds |
| P34 | N37.58096 E118.88108 | 47 cm | Lowlands beside ponds |
| P33 | N37.65590 E118.91074 | 69 cm | Reed marsh |
| P32 | N37.69075 E118.85283 | 21 cm | Cotton field |
| P31A | N37.69342 E118.75330 | 2.5 m | Water channel without much water |
| P31B | N37.69342 E118.75331 | 1.4 m | Above P31A |

# A.2 Particle size distribution
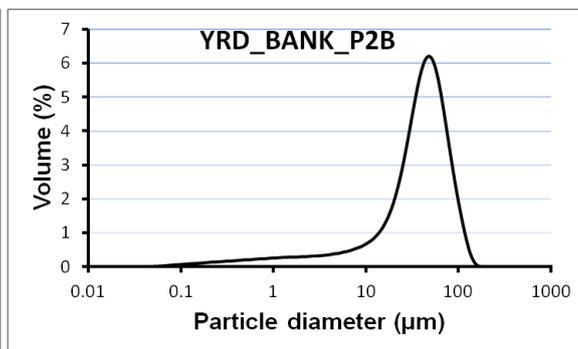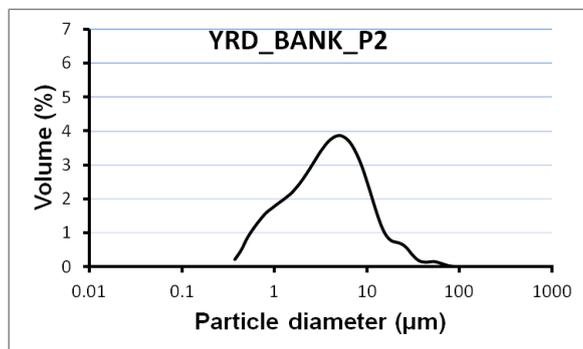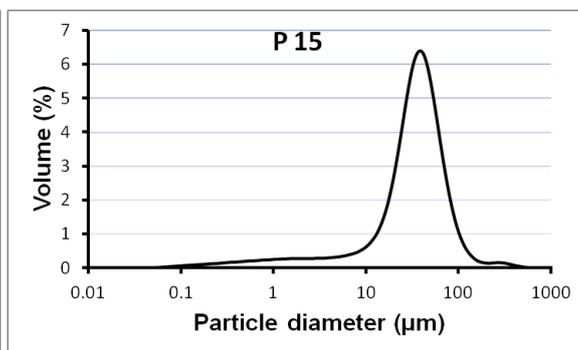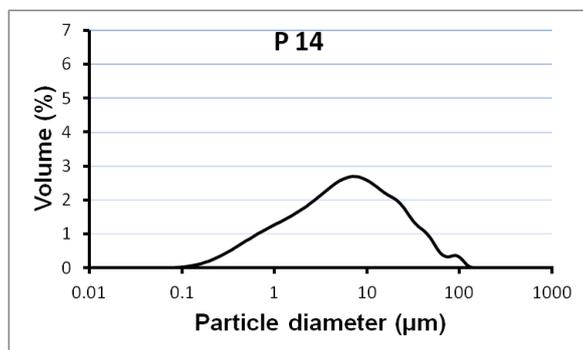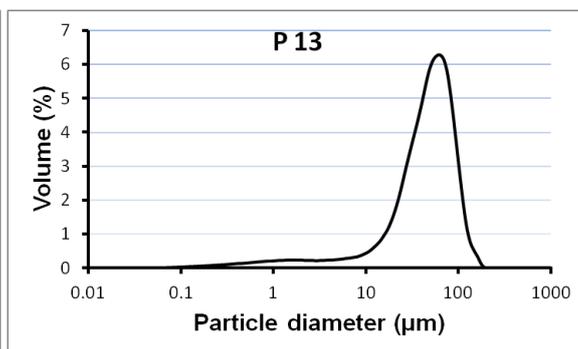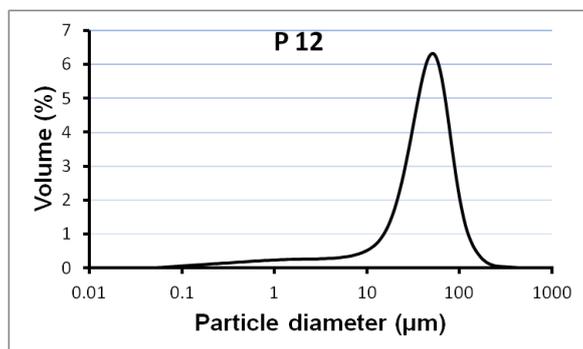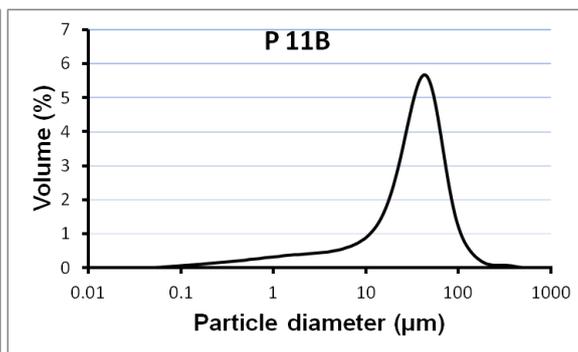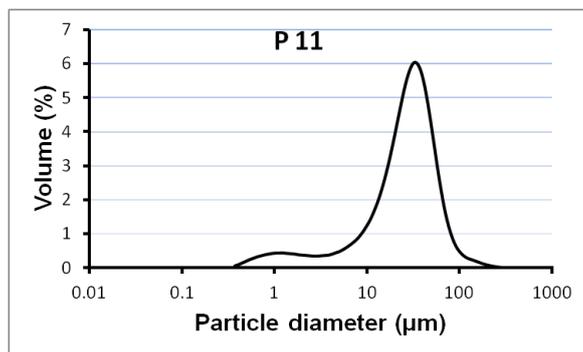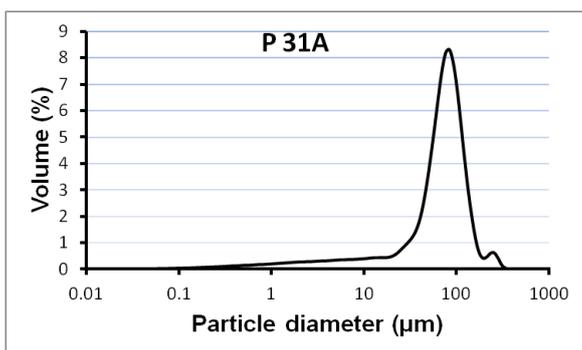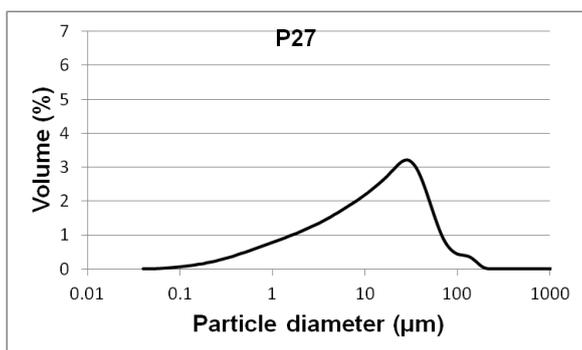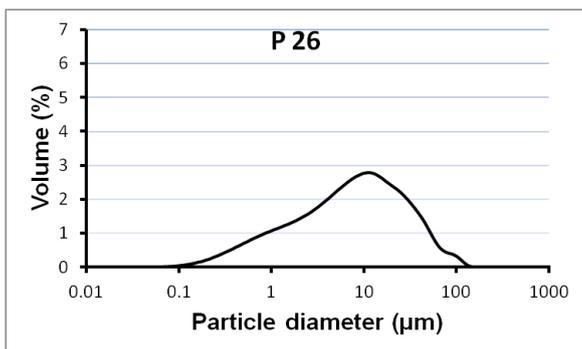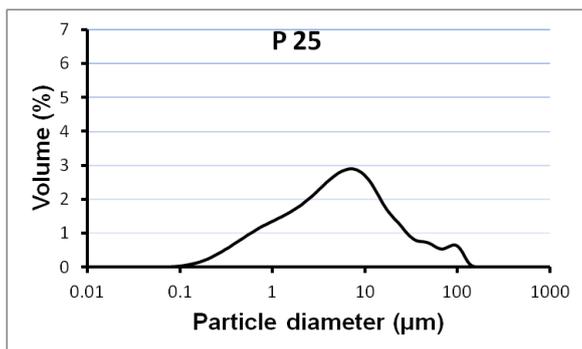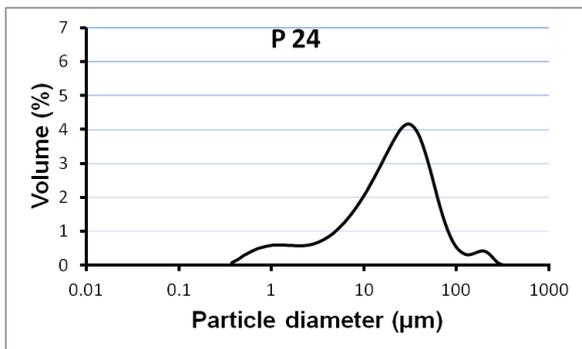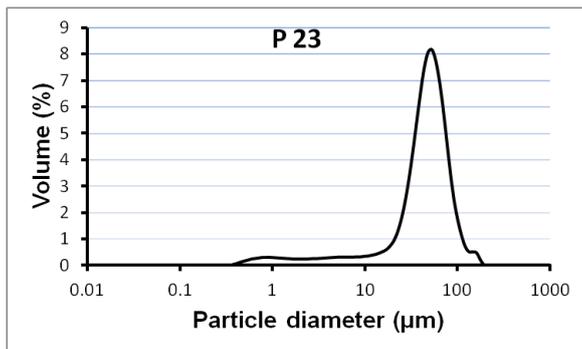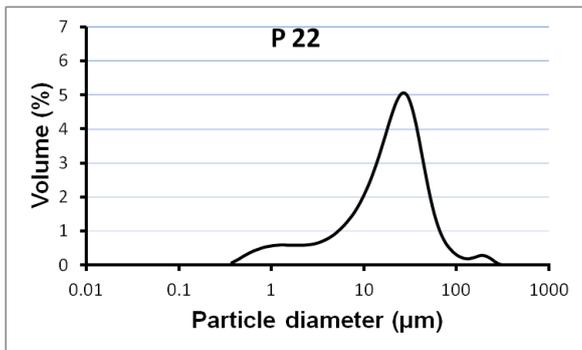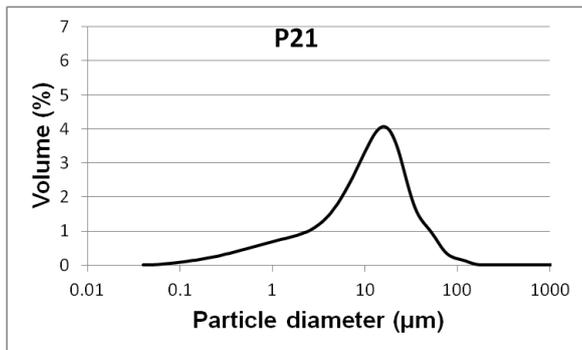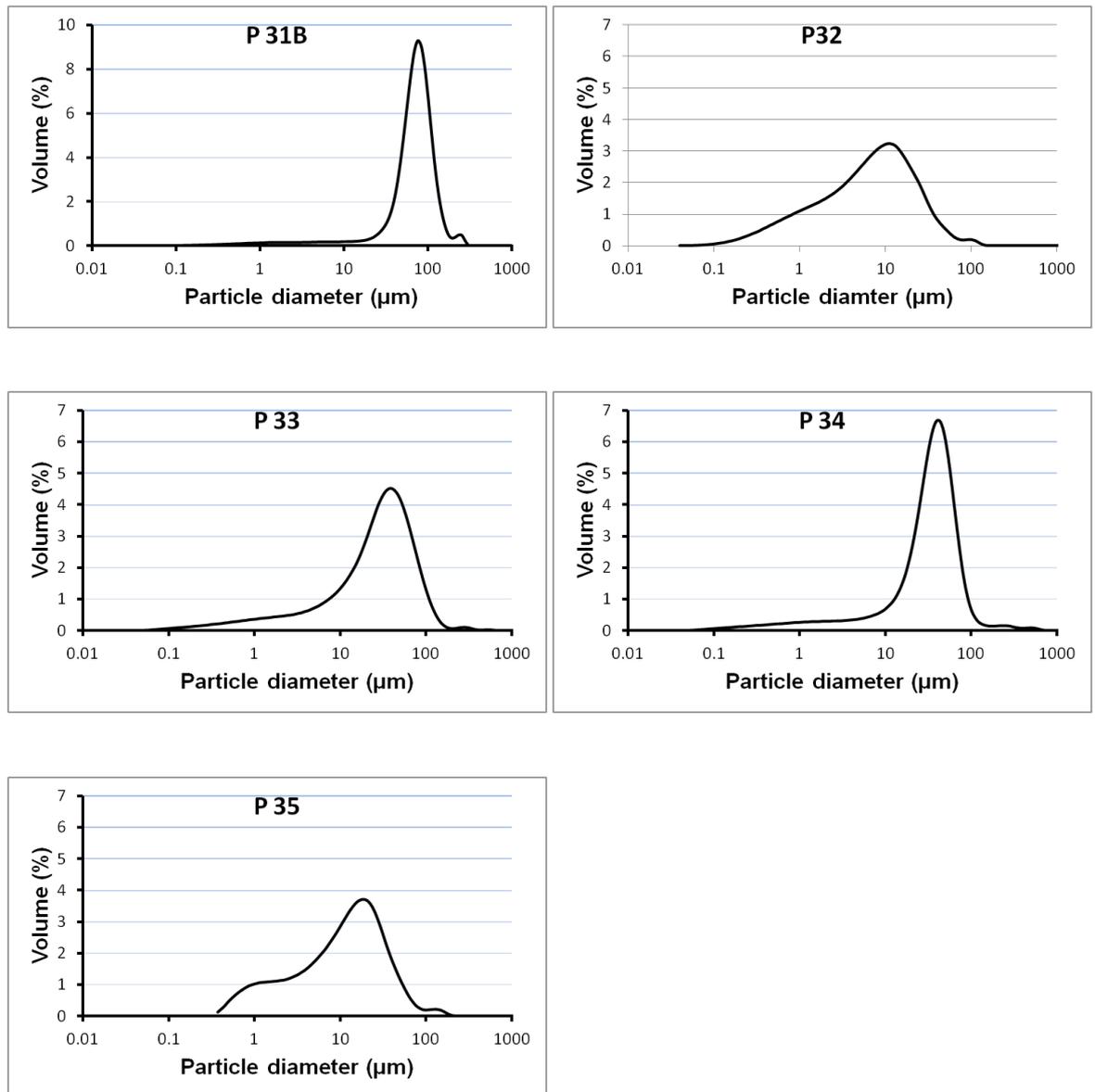
**Figure A.1 Differential volume particle size for all 21 samples (Table 4.2 in Section 4.1.3 of Chapter 4) from Yellow River delta.**

# Appendix B Gudao oilfield additional reservoir properties

## B.1 Influence of water injection

Due to long term water injection, reservoir material and porosity parameters have changed significantly. A lot of small particles have been washed away, resulting in lower clay or shale volume (Vsh) and higher median particle size (Md) (Table. B.1) (Lu et al., 2005).

**Table B.1 Shale volume (Vsh) and median particle size (Md) at different production stages (Lu et al., 2005).**

|  | Low water cut stage | | Medium to high water cut stage | | Extremely high water cut stage | |
|---|---|---|---|---|---|---|
|  | Vsh (%) | Md (mm) | Vsh (%) | Md (mm) | Vsh (%) | Md (mm) |
| Siltstone to fine grained sandstone | 10~20 | 0.1~0.14 | 8~12 | 0.11~0.15 | <5 | 0.14~0.18 |
| Fine grained sandstone to medium grained sandstone | 8~12 | 0.13~0.16 | 5~8 | 0.14~0.21 | <5 | 0.16~0.25 |

Porosity is inversely proportional to clay content. Fluvial facies in Guantao formation are characterized by high porosity, high permeability and medium oil saturation. The original porosity was in the range 22-43%, with most values 32-37%. The original air permeability was 0.12-7.9 $\mu m^2$. During water injection, the physical properties of reservoir rocks changed to different extents in different water saturation stages. Both shale and carbonate volumes have reduced, while median particle size, porosity and permeability have increased (Table B.2) (Lu et al., 2005). Mean porosity has increased from 33.3% in the low water cut stage to 38.7% in the extremely high water cut stage, with permeability increasing from 1.44 to 16.73 $\mu m^2$.

**Table B.2 Reservoir rock properties at different water saturation stages (Lu et al., 2005). Irreducible water saturation (sometimes called critical water saturation) defines the maximum water saturation that a formation with a given permeability and porosity can retain without producing water. This water, although present, is held in place by capillary forces and will not flow. Critical water saturations are usually determined through core analysis.**

|  | Porosity (%) | Permeability (x $10^{-3}$ $\mu m^2$) | Median particle size (mm) | Carbonates content (%) | Clay contents (%) | Oil saturation | Irreducible water saturation (%) |
|---|---|---|---|---|---|---|---|
| Low water cut stage | 33.3 | 1437 | 0.121 | 2.16 | 11.2 | 61.8 | 36 |
| Medium to high water cut stage | 35.6 | 2104 | 0.142 | 1.78 | 1.78 | 56.9 | 32.2 |
| Extremely high water cut stage | 38.7 | 16730 | 0.165 | 0.97 | 0.97 | 51.4 | 27.4 |

# B.2 Reservoir heterogeneity in vertical direction of Gudao oilfield

Vertically the Ng3 sand member has 9 sub layers with vertical heterogeneity (Table B.3). Units Ng3[5] and Ng3[3] units form the main reservoirs in Ng3 because of their outstanding effective thickness and permeability. Sub-layers Ng3[1], Ng3[2] and Ng3[4] are relatively less used as a result of low effective thickness or poor permeability. Effective thickness is usually related with sandstone thickness, structural height and permeability (Lu et al., 2005).

**Table B.3 Reservoir parameters in Guantao formation sand member 3 (Lu et al., 2005).**

|  | $Ng_3^1$ | $Ng_3^2$ | $Ng_3^{3^1}$ | $Ng_3^{3^2}$ | $Ng_3^{3^3}$ | $Ng_3^4$ | $Ng_3^{5^1}$ | $Ng_3^{5^2}$ | $Ng_3^{5^3}$ |
|---|---|---|---|---|---|---|---|---|---|
| Reservoir thickness (m) | 2.4 | 2.73 | 2.88 | 2.88 | 2.89 | 4.42 | 2.63 | 2.91 | 3.85 |
| Effective thickness (m) | 1.11 | 1.42 | 1.74 | 2.01 | 2.47 | 2.12 | 1.32 | 1.86 | 2.34 |
| Porosity (%) | 31.46 | 32.45 | 32.99 | 34.27 | 34.00 | 33.35 | 32.84 | 33.63 | 33.63 |
| Permeability ( $10^{-3}$ $\mu m^2$) | 2418 | 2239 | 2358 | 2743 | 2363 | 1779 | 2457 | 2844 | 2162 |
| Shale volume (%) | 15.59 | 15.67 | 13.7 | 11.26 | 12.85 | 12.75 | 13.77 | 11.63 | 11.55 |
| Median particle size (mm) | 0.08 | 0.09 | 0.11 | 0.14 | 0.12 | 0.11 | 0.10 | 0.14 | 0.13 |
| Oil saturation (%) | 45.77 | 50.59 | 55.80 | 60.12 | 60.86 | 57.46 | 53.95 | 56.88 | 62.94 |

In terms of reservoir heterogeneity, Ng4 has 7 sub-layers, of which the Ng4[4] is the most developed sand body, followed by the Ng4[2] sand body (Table B.4). These form the main reservoirs in Ng4 sand member. The spacer layers in Ng4 are thick with only minor sand body overlay between Ng4[3] and Ng4[4]. Ng4[4] is characterized by high effective thickness, permeability, oil saturation, a large oil bearing area, and well developed upper and lower insulating layers (Lu et al., 2005).

**Table B.4 Reservoir parameters in Guantao formation sand member 4 (Lu et al., 2005).**

| | $Ng_4^1$ | $Ng_4^{2^1}$ | $Ng_4^{2^2}$ | $Ng_4^3$ | $Ng_4^{4^1}$ | $Ng_4^{4^2}$ | $Ng_4^{4^3}$ |
|---|---|---|---|---|---|---|---|
| Reservoir thickness (m) | 3.19 | 3.71 | 3.89 | 3.73 | 2.99 | 3.38 | 3.01 |
| Effective thickness (m) | 1.72 | 2.56 | 2.97 | 1.82 | 2.50 | 2.11 | 1.74 |
| Porosity (%) | 31.42 | 32.77 | 33.68 | 32.72 | 32.57 | 33.95 | 33.32 |
| Permeability ( $10^{-3}$ μm$^2$) | 1512 | 2406 | 2374 | 2079 | 2041 | 2275 | 1612 |
| Shale volume (%) | 14.18 | 12.11 | 10.57 | 12.92 | 12.86 | 10.71 | 12.15 |
| Median particle size (mm) | 0.08 | 0.13 | 0.13 | 0.11 | 0.12 | 0.13 | 0.12 |
| Oil saturation (%) | 51.32 | 56.34 | 58.31 | 50.92 | 52.96 | 53.53 | 48.06 |

There are 9 sublayers in Ng5, of which Ng5$^3$ and Ng5$^4$ are the main reservoirs of Ng5 (Table B.5). Because of the low effective thickness and poor oil saturation, recoverable reserves in Ng5 are small. There are 5 sublayers in Ng6, of which Ng6$^1$ and Ng6$^2$ are mostly overlapping and so can be seen as one layer. Insulating layers between Ng6$^3$, Ng6$^4$, and Ng6$^5$ are thick, and rarely overlap. Although the sublayers in Ng6 are thick, their effective thickness and oil saturation are not satisfactory for oil extraction (Lu et al., 2005).

**Table B.5 Reservoir parameters in Guantao formation sand member 5 (Lu et al., 2005).**

| | $Ng_5^1$ | $Ng_5^2$ | $Ng_5^{3^1}$ | $Ng_5^{3^2}$ | $Ng_5^{3^3}$ | $Ng_5^{4^1}$ | $Ng_5^{4^2}$ | $Ng_5^5$ | $Ng_5^6$ |
|---|---|---|---|---|---|---|---|---|---|
| Reservoir thickness (m) | 2.21 | 2.66 | 2.17 | 2.36 | 2.56 | 2.74 | 2.66 | 3.72 | 4.16 |
| Effective thickness (m) | 0.35 | 1.34 | 0.96 | 1.01 | 1.20 | 1.47 | 1.55 | 2.14 | 2.02 |
| Porosity (%) | 30.98 | 31.53 | 31.23 | 31.85 | 32.19 | 32.27 | 33.58 | 32.79 | 33.24 |
| Permeability ( $10^{-3}$ μm$^2$) | 1934 | 1166 | 1984 | 1932 | 1995 | 2770 | 2385 | 2022 | 2491 |
| Shale volume (%) | 15.64 | 14.23 | 14.67 | 14.74 | 14.15 | 13.29 | 10.43 | 11.47 | 11.93 |
| Median particle size (mm) | 0.10 | 0.11 | 0.11 | 0.10 | 0.10 | 0.12 | 0.15 | 0.13 | 0.15 |
| Oil saturation (%) | 33.98 | 46.17 | 49.67 | 45.81 | 48.36 | 50.20 | 52.86 | 50.23 | 47.31 |

# B.3 Reservoir heterogeneity in horizontal direction of Gudao oilfield

The porosity and permeability show horizontal heterogeneity across the different sand bodies. For example, in sand member 3-5 of the Central 2 block of Gudao oilfield, different sedimentary facies show different porosity and permeability (Table B.6).

**Table B.6 Horizontal porosity and permeability differences across different sedimentary facies (Lu et al., 2005).**

| | | Sandbar | Channel | Channel margin | Floodplain |
|---|---|---|---|---|---|
| Porosity | Mean (μ) | 35% | 34% | 32% | 31% |
| | Coefficient of variation (σ/μ) | 0.076 | 0.075~0.095 | 0.08~0.135 | 0.115~0.215 |
| Permeability | Range ($10^{-3} \mu m^2$) | 1~6 | 0.5~2.5 | 0.2~1.5 | 0.1~3 |
| | Coefficient of variation (σ/μ) | 0.069 | 0.774 | 0.82 | 1.29 |

The heterogeneity also exists in different directions of the same sand body. The larger coefficient of variation value in the direction perpendicular to the river means more significant heterogeneity in this direction than the direction parallel to the river (Table B.7).

**Table B.7 Horizontal shale volume and porosity differences in a single sand body (Lu et al., 2005).**

| | | $Ng3^3$ sand member | | $Ng4^4$ sand member | |
|---|---|---|---|---|---|
| | | Parallel to the river | Perpendicular to the river | Parallel to the river | Perpendicular to the river |
| Shale volume | Range | 5%~20% | 5~35% | 2%~20% | 4%~35% |
| | Mean (μ) | 9.7% | 21.4% | 7.8% | 19.2% |
| | coefficient of variation (σ/μ) | 0.450 | 0.633 | 0.465 | 0.683 |
| Porosity | Range | 32%~42% | 21%~37% | 33%~39% | 21%~41% |
| | Mean (μ) | 36.4% | 32.0% | 35.9% | 31.8% |
| | coefficient of variation (σ/μ) | 0.078 | 0.183 | 0.095 | 0.196 |

The porosity is greater on average and more homogeneous in the direction parallel to the river than the perpendicular direction (Table B.6). The porosity gradually reduces in the direction of shoal (sandbar)-channel fill-channel margin-floodplain, when its coefficient of variation gradually increases (Lu et al., 2005).

The permeability is less changed in the direction parallel to the river also with higher mean values (Table B.8).

**Table B.8 Horizontal permeability differences in a single sand body (Lu et al., 2005).**

| | $Ng3^2$ sand member | | $Ng3^3$ sand member | |
|---|---|---|---|---|
| Permeability | Parallel to the river | Perpendicular to the river | Parallel to the river | Perpendicular to the river |
| Range ($10^{-3}\,\mu m^2$) | 610~3076 | 270~2926 | 354~3980 | 14.4~2270 |
| Mean ($\mu$) ($10^{-3}\,\mu m^2$) | 1375 | 969 | 2033 | 690 |
| Coefficient of variation ($\sigma/\mu$) | 0.6 | 1.171 | 0.555 | 1.332 |

# Appendix C Publication

The following pages reproduce the published paper below which constitutes the work from Chapter 3.

Liu, P., Li, Z., Hoey, T., Kincal, C., Zhang, J., Zeng, Q. & Muller, J.-P., 2013. Using advanced InSAR time series techniques to monitor landslide movements in Badong of the Three Gorges region, China, *International Journal of Applied Earth Observation and Geoinformation*, 21, 253-264, doi:10.1016/j.jag.2011.10.010.

Permission (licence number 3038251338934) for Peng Liu to reproduce this paper in this thesis (both print and electronic format) has been granted by Elsevier for free.

Contents lists available at SciVerse ScienceDirect

# International Journal of Applied Earth Observation and Geoinformation

# Using advanced InSAR time series techniques to monitor landslide movements in Badong of the Three Gorges region, China

Peng Liu [a,*], Zhenhong Li [a], Trevor Hoey [a], Cem Kincal [a,b], Jingfa Zhang [c], Qiming Zeng [d], Jan-Peter Muller [e]

[a] School of Geographical and Earth Sciences, University of Glasgow, Glasgow G12 8QQ, United Kingdom
[b] Geological Engineering Department, Dokuz Eylul University, 35160 Buca-Izmir, Turkey
[c] Institute of Crustal Dynamics, China Earthquake Administration, Beijing 100085, China
[d] Institute of Remote Sensing and GIS, Peking University, Beijing 100871, China
[e] Mullard Space Science Laboratory, Department of Space and Climate Physics, University College London, Surrey RH5 6NT, United Kingdom

## ARTICLE INFO

## ABSTRACT

The Three Gorges occupy 193 km of the middle reaches of the Yangtze River between Fengjie in Chongqing and Yichang in Hubei Province, China. Due to steep valley-side slopes and long-term river incision, landslides are a major hazard in the Three Gorges region. In this study, we employ the SBAS InSAR technique to process Envisat SAR images collected between 2003 and 2010. Our time series results enable identification of two distinct landslides with deformation rates of up to 10–15 mm/yr in Badong County, and field evidence is used to verify the positions of these failures. With both descending and ascending observations, two-dimensional velocity fields in north and up directions are recovered to better understand the landslide movements. Obvious correlation between seasonal landslide movements and water level changes is observed, which not only provides strong support of our InSAR time series results, but also indicates the impacts of water level changes to landslide activities.

© 2011 Elsevier B.V. All rights reserved.

## 1. Introduction

The Yangtze River, the third longest in the world and the longest in China, is a major waterway that has been the location of human settlement for millennia (Beardsley et al., 1985; Wright and Nittrouer, 1995). The Three Gorges region, in the middle reaches of the Yangtze River where it is deeply incised into bedrock, is an area of known geological hazards including landslides and rock falls. Construction of the Three Gorges dam (Shen and Xie, 2004; Wang, 2002) began in 1994, and since June 2003 the dam has provided hydro-electrical power and has assisted downstream flood control. The Three Gorges reservoir is approximately 663 km long and up to 1576 m wide at the designed highest water level of 175 m above sea level (SCGPCCEO, 2008). The average water level rise after the dam's construction is about 110 m and the water level varies between 145 m and 175 m bi-annually. The frequency of water level change is greater than under pre-existing natural conditions (Yin and Li, 2001). Consequently, the changeable hydro-geological conditions of the landslide zones will affect slope stability in the region, in addition to the threat from heavy

summer precipitation (He et al., 2008). These slope instabilities include the reactivation of old landslides and the triggering of new failures in the new settlements which house 1.27 million immigrants (Liu et al., 2004; SCGPCCEO, 2009). In the third period of the hazard prevention and control project of the Three Gorges region from 2005 to 2011, 2977 potentially unstable sites were identified of which 2686 were classified as slump-masses but only 255 of these sites have been treated with engineering methods (Caijing Magazine, 2009).

Significant landslides occurred in the Three Gorges region prior to the dam construction. Two landslides occurred in the Huangtupo zone, Badong County on June 10th 1995 and November 20th 1995 causing a total of 5 deaths and 9 injuries (Wu et al., 2006). On June 12th 1985, 1371 local residents were evacuated when surveyors observed the beginning of a landslide (Wang and Tan, 1991). After evacuation, about $30 \times 10^6 \, \text{m}^3$ of landslide debris destroyed the whole of Xintan Town, blocked one-third of the width of the Yangtze River and triggered a wave in the river up to 54 m above the normal flow level along a 42 km river reach (Wang and Tan, 1991). This example shows the scale of the pre-dam hazard and illustrates how landslide monitoring successfully saved lives following long-term landslide monitoring in the region. Unfortunately, frequent monitoring of large areas is difficult due to the nature of the terrain affecting both conventional surveys and inhibiting GPS signals.

* Corresponding author. Tel.: +44 0141 330 5400; fax: +44 0141 330 4894.
E-mail address: p.liu.1@research.gla.ac.uk (P. Liu).

Interferometric Synthetic Aperture Radar (InSAR) employing radar waves transmitted from spaceborne antennae and backscattered from the Earth's surface can be used to detect range changes between different radar acquisitions (Massonnet and Feigl, 1998). With its wide coverage and sub-centimeter accuracy, InSAR has been used to study dynamic surface processes including earthquakes and faults (Massonnet et al., 1993; Gourmelen et al., 2010), volcano dynamics (e.g. Massonnet et al., 1995; Lu et al., 2010; Lu and Dzurisin, 2010), glacier movement (Goldstein and Engelhardt, 1993), subsidence and landslides (e.g. Fruneau et al., 1996; Colesanti and Wasowski, 2006; Strozzi et al., 2010; Tomas et al., 2010). However, the application of conventional InSAR is limited by three major factors: error in the digital elevation model (DEM) used in interferometric processing; temporal and spatial decorrelation; and atmospheric effects.

Firstly, each interferogram contains topographic information in the form of fringes, known as topography fringes. To measure ground surface deformation, the topography fringes should be removed. This is usually implemented using a DEM (e.g. SRTM DEM, ASTER GDEM) and satellite geometry information. Both the uncertainty in DEM itself and the inaccurate satellite geometry information generate DEM errors in the topography removal step. As the impact of DEM errors on interferograms is a function of perpendicular baselines, DEM errors can be estimated with multiple interferograms.

Secondly, changes in the scattering properties of the Earth surface, often caused by changes in vegetation or dielectric properties of soil, are referred to as temporal decorrelation effects (Zebker and Villasenor, 1992). The Three Gorges region has high and spatially variable vegetation densities (e.g. in the Yichang City area, near the Three Gorges, Zhang et al. (2009a) report land cover as: 41.4% forest, 28.8% cultivated crops, 1.8% dense grass, 6.7% medium and sparse grass, 10.9% shrubs, 7.2% water, 3.0% urban residential and 0.2% bare land), which causes significant decorrelation. The longer the time interval between radar images, the greater the temporal decorrelation can be. Spatial decorrelation occurs due to different incidence angles of radar beams during radar scanning (Zebker and Villasenor, 1992). The longer the perpendicular baseline (i.e. satellite separation) between the radar images, the higher the likelihood of spatial decorrelation.

Thirdly, the phase delay in radio signal propagation through the atmosphere (especially the part due to tropospheric water vapour) represents one of the major limitations of repeat-pass InSAR (Hanssen, 2001; Li et al., 2005, 2006, 2009a,b). Zebker et al. (1997) suggested that a 20% spatial or temporal change in relative humidity could result in a 10–14 cm error in deformation measurement retrievals, independent of baseline parameters.

All the three abovementioned issues can be addressed with the Small BAseline Subset (SBAS) InSAR technique, which uses interferograms with small baselines to minimize the effects of baseline decorrelation and inaccuracies in topographic data used (e.g. Berardino et al., 2002; Mora et al., 2003; Lanari et al., 2007; Hooper, 2008). The Badong area of the Three Gorges has previously been studied by Perissin and Ferretti (2007) and Wang et al. (2008) using both Quasi Persistent Scatterers technique (QPS) and StaMPS/PS technique (Hooper et al., 2007). They detected two subsidence areas on the south bank of Yangtze River using four-year Envisat ASAR descending track data from Tracks 075 and 347 collected between August 2003 and June 2007 (Wang et al., 2008).

Corner reflectors can be used as stable targets during radar acquisitions, and have been utilised in the Three Gorges region (Xia et al., 2004). Corner reflectors can maximize the radar cross section and backscattering power, so a pixel containing a corner reflector should appear as a bright point on a radar amplitude image. Ten Artificial Triangular Trihedral Corner Reflectors were installed in the Three Gorges to study mass movements. An experiment

with manual adjustments of the corner reflector heights showed a high ratio of failure detection mainly due to atmospheric effects (Xia et al., 2004). This highlights the difficulties of using InSAR in this region, which also suggests the importance of the mitigation of atmospheric effects to obtain a reliable solution. In this paper, we focus on the Badong region (Fig. 1) and identify land movements using the StaMPS/SBAS technique (Hooper, 2008) with Envisat ASAR datasets spanning seven years. Firstly, the small baseline method is used to detect coherent pixels throughout the seven years by forming a robust small baseline interferometric network with reliable interferometric pairs (Fig. 2). Secondly, unlike QPS, StaMPS/SBAS does not require any assumed deformation model, so no *prior* knowledge of the temporal pattern of deformation is required. Thirdly, previous studies (e.g. Wang et al., 2008) only show surface displacement signals in the radar line of sight (LOS). In this paper, two descending (i.e. Tracks 075 and 347) and one ascending (i.e. Track 068) tracks are employed to derive 2D landslide surface movements. Fourthly, correlations between water level changes, rainfall and landslide movements are investigated.

## 2. Advanced InSAR time series techniques

The small baseline approach proposed by Berardino et al. (2002) combines interferograms with a small perpendicular baseline, small time interval and small Doppler centre frequency difference to create a dataset which minimizes the spatial decorrelation and topographic error for the group of small baseline interferograms. Minimum coherence of 0.5, decorrelation time of 1500 days and critical baseline of 1070 m are set to find the initial small baseline network. Visual inspection is then applied to exclude the interferograms with low coherence in the small baseline network.

The slowly decorrelating filtered phase (SDFP) pixels are selected in further time series analysis because radar echoes from SDFP pixels have Gaussian circular statistics and are independent from noise, remaining detectable over a long time period (Hooper, 2008). For SDFP pixels dominated by Gaussian scattering mechanisms, amplitude dispersion $D_{A}$ is used as a good indication of phase stability to reduce the number of SDFP candidates (Hooper, 2008). The selection of amplitude dispersion follows the method introduced in Peyret et al. (2011). A wide range of amplitude dispersion index thresholds are set to process the small baseline interferogram datasets. A higher threshold results in a denser SDFP map, but the chance of including unreliable deformation may also increase. Above a certain threshold, the mean velocity pattern ceases to conform to the ones with lower thresholds. Therefore, the highest threshold which keeps the mean velocity similarity with lower thresholds is chosen. In this study, an amplitude dispersion threshold of 0.6 was adopted to increase computational efficiency during the search for SDFP pixels. After amplitude analysis, the SDFP pixels are refined using the spatial correlation of phase measurements (Hooper, 2008).

Integer cycle ambiguities of the wrapped phase of SDFP pixels are estimated using the three-dimensional SNAPHU phase unwrapping approach (Chen and Zebker, 2001; Hooper and Zebker, 2007). The unwrapped interferograms are then inverted to obtain the time series of phase change of SDFP pixels using a least-squares method (Schmidt and Bürgmann, 2003). In this study a $2\pi$ phase change corresponds to a range change of 28.1 mm (i.e. half-wavelength) for conversion from phase to range.

Spatially correlated DEM error due to inaccurate DEM mapping is estimated by bandpass filtering of surrounding pixels, and spatially uncorrelated DEM error due to phase centre deviation can be estimated through its correlation with the perpendicular baseline (Hooper, 2008). The estimated DEM errors are then removed in our results. The effects of atmospheric delay in the reference
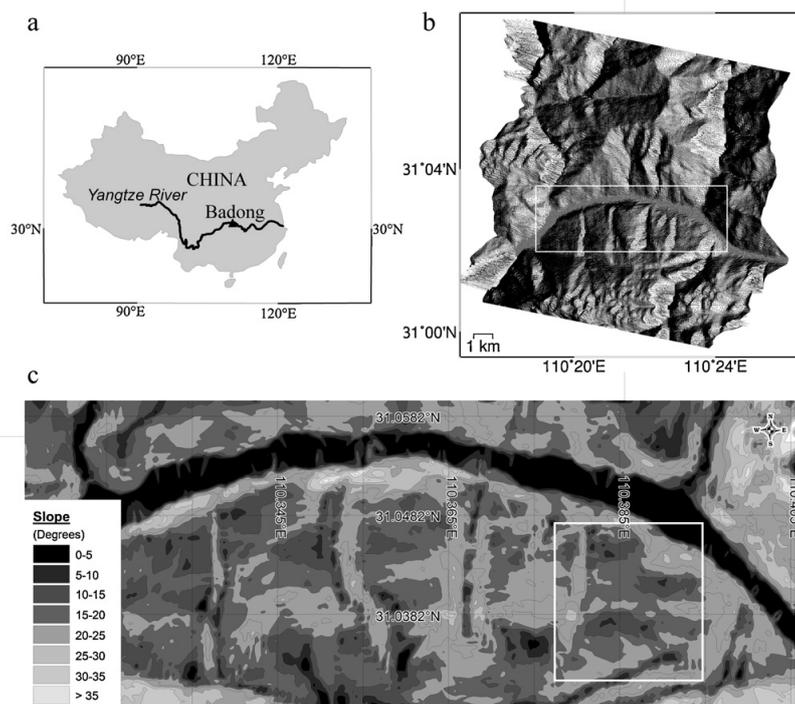
**Fig. 1.** (a) Location of Badong (black triangle) in China; (b) Envisat-ASAR intensity image of Badong. White rectangular represents the boundary for the mapped area in Fig. 4; (c) slope map of Badong, with the same spatial coverage as the mean velocity map (Fig. 4). The area mapped in Fig. 3b is outlined by the white rectangle.

SAR image can be estimated as the signals present in every relevant interferogram, and atmospheric effects in slave images can be derived using spatial and time filtering. However the performance of atmospheric filtering varies from case to case, as it can easily lead to misestimation of deformation signals if both deformation and atmospheric noise represent similar patterns and temporal behaviors (Peltier et al., 2010). In this study, we therefore estimated a best-fit plane of each unwrapped interferogram to account for orbit errors and long wavelength atmospheric effects (Ofeigsson et al., 2011), because the area of interest is small ($\sim$2.5 km $\times$ 8.0 km). A comparison between InSAR time series with atmospheric filtering and those with a best-fit plane suggested that higher deformation consistency between adjacent descending tracks was achieved when a best-fit plane was used to account for atmospheric effects.

## 3. Study area

### 3.1. Data

Three groups of Envisat ASAR images were used to investigate the Badong landslides: 41 images from Track 075 collected between August 2003 and July 2010 (Fig. 2a), 31 images from Track 347 collected between January 2004 and April 2010 (Fig. 2b), and 13 images from Track 068 collected between December 2008 and March 2010 (Fig. 2c). The former two are descending tracks where Badong is observed by the Envisat ASAR antenna from the east, while the last one is an ascending track where Badong is observed from the west. The radar line of sight (LOS) deformations are thus different as are the real surface displacements projected onto different LOS directions.

### 3.2. Geological setting

#### 3.2.1. Geological setting of the Badong area

The Three Gorges is formed by severe incision of Palaeozoic and Mesozoic limestone dominated mountains although there is a debate on the timing (Li et al., 2001; Richardson et al., 2010). According to Liu et al. (2004), landslides in Badong mainly occur in soft lithology blocks that are composed of sandstone, thin limestone and shale formations. General geological conditions of Badong are given in Fig. 3(a).

#### 3.2.2. Geological setting of the Huangtupo landslide

The Huangtupo area was constructed after May 1984 as much of the old Badong County is now beneath the Three Gorges reservoir water level. There are $\sim$20k residents in the area potentially affected by the Huangtupo landslide, at least until the completion of a new district, Shennongxi, to which Huangtupo residents will be further relocated. Two landslide events occurred in the Huangtupo Zone of Badong County (Fig. 1) on June 10th 1995 and November 20th 1995, respectively, which highlights the continuing risk and the necessity of continued landside monitoring.

The Huangtupo landslide is located between two narrow, steep gullies draining into the Yangtze River (Fig. 3(b)). The surface of the Huangtupo landslide has gradients of approximately 40°, 15–20° and 30–35° in the upper, middle and lower parts, respectively.

Wu et al. (2006) reported that the Huangtupo landslide has two Triassic geological units: $T_2b^2$ and $T_2b^3$ (Fig. 3(b)). The upper Unit $T_2b^2$ is approximately a 10 m thick pelite alternating with pelitic siltstone layers containing 40–65% clay minerals, predominantly illite. Unit $T_2b^3$ is a 364 m thick pelitic limestone. Failure of Unit
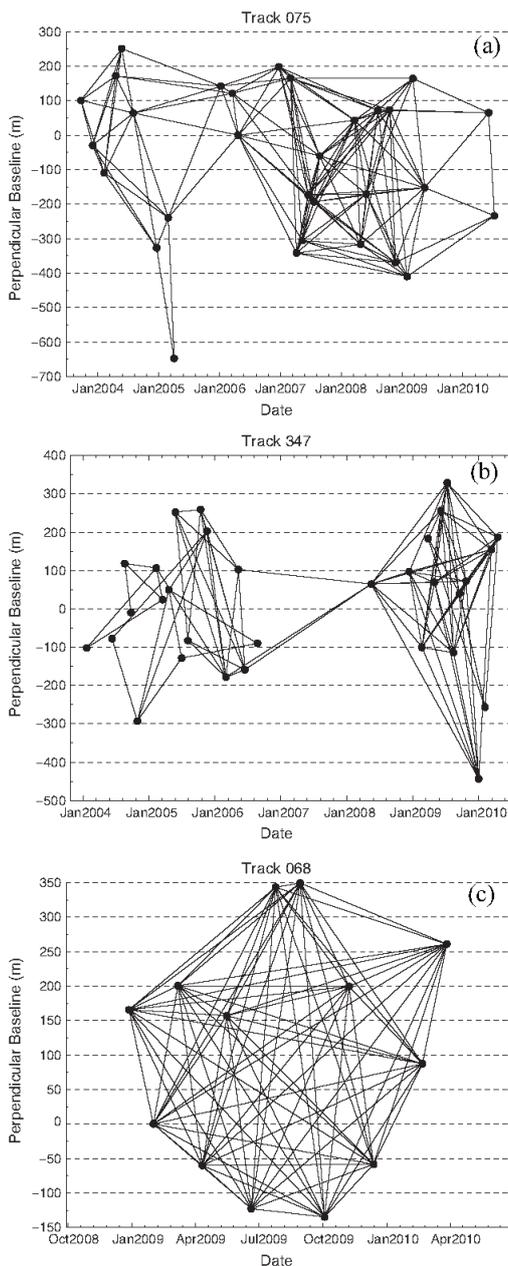
**Fig. 2.** Perpendicular baseline (satellite separation) as a function of time for: (a) Track 075 (descending); (b) Track 347 (descending); and (c) Track 068 (ascending). *Note*: Circles represent individual SAR images and lines indicate the small baseline interferograms formed from two different SAR images.

$T_2b^2$ from the upper part of the Huangtupo landslide covered some lower areas so some of this older $T_2b^2$ is found on the top of the younger $T_2b^3$ in the middle part of the landslide (Wu et al., 2006). Limited borehole data from the Yangtze River Water Resources Commission show that Huangtupo is a deep-seated landslide, with
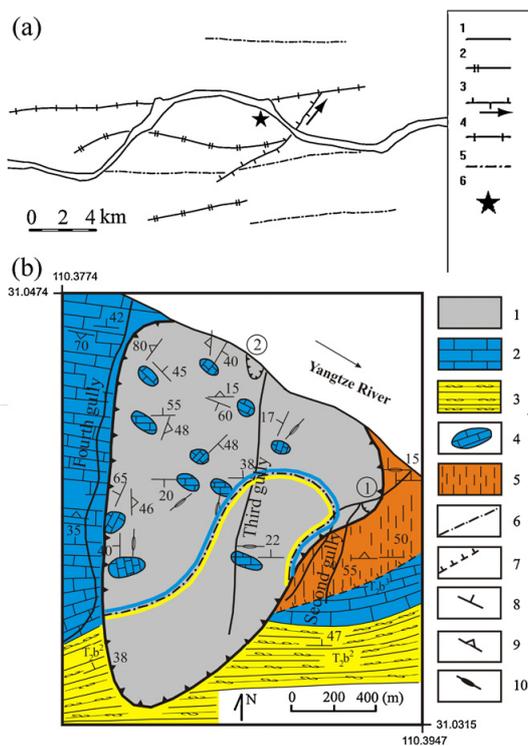


**Fig. 3.** (a) Geological structure of Badong (adapted from Deng et al., 2000). Legends: 1: banks of Yangtze River; 2: dipping faults to the north; 3: strike-slip faults; arrow in direction of slip; 4: syncline; 5: anticline; 6: rough location of Huangtupo. (b) Geological map of the Huangtupo landslide (adapted from Deng et al., 2000; Tang and Hu, 2009). 1: Huangtupo Landslide; 2: pelitic limestone, Badong formation; 3: pelite alternating with pelitic siltstone, Badong formation; 4: loose rock fall deposits; 5: location of ongoing rock creep and toppling; 6: landslide boundary between purplish-red debris originating from 3 and khaki materials from 4; 7: boundary of area of toppling failure; 8: surface slope direction; 9: cleavage attitude; 10: perpendicular cleavage. Points marked ① and ② are the 1995 landslide locations.

a failure surface depth of about 50–100 m and has a volume of $40 \times 10^6 \, m^3$ (Wu et al., 2006).

## 4. Time series results

### 4.1. Mean velocities

As no independent ground truth data are available in this area, Badong city council building was chosen as a reference. This is because no landslide risk has been reported here. The mean value of all the pixels in the reference area (which varied from 4 to 6 on different images) is set to zero for each Track. The two landslides identified in Fig. 4 are referred to here as the West and East landslides. Liu et al. (2004) reported there are seven known landslides in Badong. However, the locations and dimensions of the landslides given by Liu et al. (2004) are not completely consistent with the landslide trace pattern described by Wu et al. (2009). The East landslide is the Huangtupo landslide described in Deng et al. (2000), Tang and Hu (2009) and Wu et al. (2009). The west landslide lies close to the west of Zhaoshuling landslide described in Liu et al. (2004) (Fig. 4). Because of the lack of obvious deformation signals in Zhaoshuling landslide, only Huangtupo landslide in Liu et al. (2004) is discussed in this study.
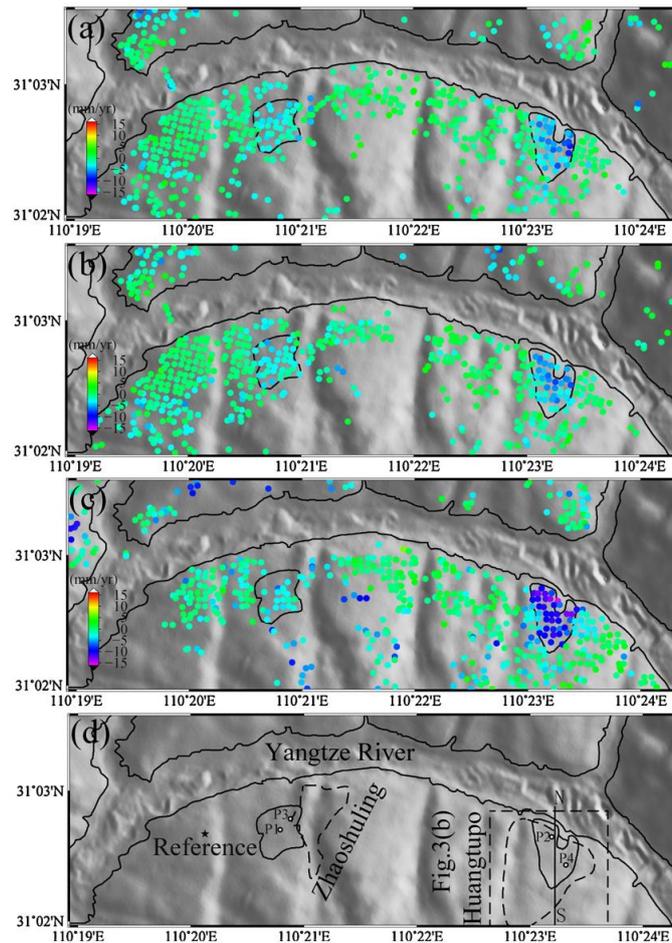
**Fig. 4.** (a) Mean velocity derived from InSAR Time Series of Track 075 (descending) between August 2003 and July 2010; (b) mean velocity from Track 347 (descending) between January 2004 and April 2010; (c) mean velocity from Track 068 (ascending) between December 2008 and March 2010; (d) the background is a shaded SRTM DEM with illumination effects. Badong city occupies the entire image south of the Yangtze River. West and East landslides and their outlines are shown in (d), along with the Yangtze River banks. The area of Zhaoshuling landslide and the area mapped in Fig. 3(b). The black star represents the reference area. Four points P1, P2, P3 and P4 are marked here for time series analysis. Line SN is marked for profile in Fig. 11.

The standard deviation of the mean velocity at each coherent pixel provides an estimate of the precision of the mean velocity estimates (Fig. 5). There are two possible implications of the standard deviations: (1) the higher the standard deviation, the lower (worse) the precision of the corresponding mean velocity; and (2) as the mean velocity assumes linear deformation, a high standard deviation may suggest that this assumption is not sound, i.e. the deformation may not be temporally linear. It is likely that the instant deformation rate is greater than the mean velocity and deformation increments between adjacent images may provide better information on the hazard. The two adjacent Tracks 075 and 347 are used to assess the accuracy of the mean velocity estimates in the study (Section 4.2) to improve confidence in the estimates of mean velocity. The coefficient of variation (CV) is defined as the ratio of the standard deviations (Fig. 5) to the mean velocities (Fig. 4). The CV values range from 0 to 0.3 for most SDFP pixels in landslide areas of Tracks 075, 347 and 068, so the mean velocities derived from Tracks 075 (Fig. 4a), 347 (Fig. 4b) and 068 (Fig. 4c) are robust estimates of deformation at SDFP pixels in the landslide

area. Although the standard deviations for Track 068 (Fig. 5c) on most pixels in the East and West landslides are relatively low as 1–3 mm/yr, the standard deviations (Fig. 5c) for pixels adjacent to the Yangtze River in the East landslide areas are still as high as 5–7 mm/yr. The short data period of 15 months for the 13 SAR images from Track 068 may account for this variability, especially as deformation adjacent to the river may be influenced by water level fluctuations in the dam.

### 4.2. Validation of InSAR time series

Data from both landslides show progressive lowering of the ground surface, and data from different tracks are generally consistent (Fig. 6). Overall deformation is of the order of 20–40 mm over a seven-year period, but phases of both relative upward ground movement and more rapid downward movement are identified.

The two adjacent descending tracks (i.e. Tracks 075 and 347) have similar incidence and azimuth angles, and both span the full time interval between 2004 and 2010. Comparisons between these

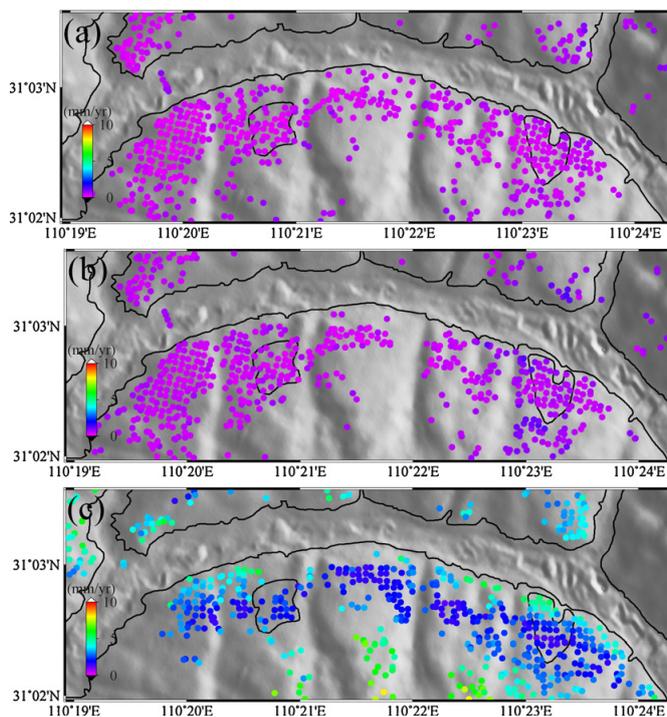**Fig. 5.** Standard deviation of the mean velocity derived from InSAR time series from: (a) Track 075 (descending); (b) Track 347 (descending); and (c) Track 068 (ascending). The background is a shaded DEM from SRTM. The outline of the East and West landslides along with the Yangtze River are shown.

tracks are used to assess the accuracy of InSAR derived time series results. As both Tracks 075 and 347 were acquired within the same incidence angle of 23° in Swath I2 mode, the deformations compared are still in the radar line of sight.

RMS is estimated by the displacement differences between the estimated displacement values from Track 347 and the interpolated displacement values from Track 075 at the SAR acquisition times of Track 347. The systematic offset due to different reference images is also considered. The RMS values for Points P1, P2, P3 and P4 in Fig. 4 are 1.68, 5.91, 3.11 and 2.57 mm, respectively. For these four points, the RMS values between Tracks 075 and 347 are much smaller than the magnitude of deformation, which suggests that the deformation time series is consistent between the two tracks.

The mean velocities derived from the deformation time series are also compared for each common pixel of Tracks 075 and 347 (Fig. 7). Although these velocity differences are up to 5 mm/yr, 57% of pixels have differences less than 1 mm/yr. This consistency in velocities suggests that the deformation time series and velocities from our study are reliable.

### 4.3. Two-dimensional velocity fields

Descending and ascending tracks have different incidence and azimuth angles and provide different perspectives on ground movement. Previous studies have used multiple interferograms with different geometries to recover 2D and/or 3D surface displacement fields (Fialko and Simons, 2001; Wright et al., 2004; Gourmelen et al., 2007; Bechor and Zebker, 2006). A similar approach is used to investigate 2D velocity fields in Badong with three LOS mean velocity maps from Tracks 068, 075 and 347. The similar satellite geometries for 075 and 347 does not allow full

recovery of 3D north, east and vertical velocities, but 2D north and vertical velocities can be recovered assuming that there is no movement in the west–east direction. During field inspection of the Huangtupo area, parallel surface cracks were observed in hill slope materials, roads and buildings at different elevations with a W–E orientation, suggesting that landslide movement is likely to be dominated by north and vertical components. Their observation equations can be written as

$$\begin{pmatrix} \sin\phi_{075}\sin\theta_{075} & \cos\theta_{075} \\ \sin\phi_{068}\sin\theta_{068} & \cos\theta_{068} \\ \sin\phi_{347}\sin\theta_{347} & \cos\theta_{347} \end{pmatrix} \begin{pmatrix} V_n \\ V_u \end{pmatrix} = \begin{pmatrix} V_{LOS075} \\ V_{LOS068} \\ V_{LOS347} \end{pmatrix} \qquad (1)$$

where $\phi$ is the azimuth of the satellite heading vector (positive from North) and $\theta$ is the radar incidence angle. Subscripts 075, 068 and 347 are the track numbers, and $n$ and $u$ refer to north and vertical (upwards positive) movements, respectively.

Eq. (1) can be rewritten as:

$$A \cdot V = LOS \qquad (2)$$

where $A$ is the $3 \times 2$ coefficient matrix by satellite geometry, $V$ is the $2 \times 1$ velocity matrix and $LOS$ is the $3 \times 1$ line of sight matrix for Tracks 075, 068 and 347. Applying orthogonal projections to the inconsistent system of Eq. (2), a least squares solution of the 2D velocity field $V$ will also be a solution to the associated normal system:

$$A^T \cdot A \cdot V = A^T \cdot LOS \qquad (3)$$

The least square solution of the 2D velocity field $V$ (Fig. 8) is thus given by:

$$V = (A^T \cdot A)^{-1} \cdot A^T \cdot LOS \qquad (4)$$
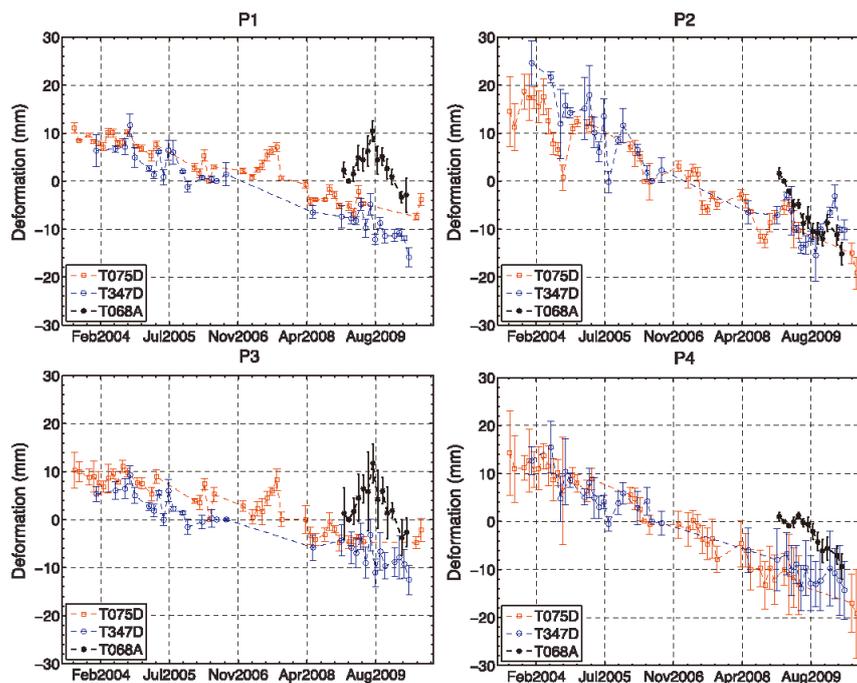
**Fig. 6.** Time series deformation for P1, P2, P3 and P4 in the radar line of sight (LOS) direction. Negative values mean that the ground surface moves away from the satellite, most likely indicating landslides. Red, blue and black colors represent Tracks 075, 347 and 068, respectively. Error bars represent the standard deviations of the deformation values for all SDFP points within a 200 m × 200 m square window, centred with the given point. Points P1 and P3 are from the West landslide, and Points P2 and P4 are from the East landslide. (For interpretation of the references to color in the figure caption, the reader is referred to the web version of the article.)

Using Eq. (5),

$$B = (A^T \cdot A)^{-1} \cdot A^T \tag{5}$$

Eq. (4) can be simply written as:

$$V = B \cdot LOS \tag{6}$$

Based on Eq. (6), the standard deviations of the north and vertical velocity can be calculated from the standard deviations of LOS velocities (Fig. 5) following uncertainty propagation theory (Dijkstra, 2010):

$$\text{cov}(V) = B \cdot \text{cov}(LOS) \cdot B^T \tag{7}$$

The full form of Eq. (7) can be written as:

$$
\begin{pmatrix} \sigma_n^2 & COV_{nu} \\ COV_{un} & \sigma_u^2 \end{pmatrix} = B \cdot
\begin{pmatrix} \sigma_{075}^2 & COV_{075,068} & COV_{075,347} \\ COV_{068,075} & \sigma_{068}^2 & COV_{068,347} \\ COV_{347,075} & COV_{347,068} & \sigma_{347}^2 \end{pmatrix} \cdot B^T \tag{8}
$$

In the equations above, $T$ and $(\ )^{-1}$ represent matrix transpose and inversion, respectively. $\sigma_{075}^2$, $\sigma_{068}^2$ and $\sigma_{347}^2$ are the variances of the velocities of Tracks 075, 068 and 347, respectively, which were calculated in Section 4.1 from the radar line of sight deformation time series. $COV_{075,068}$ is the covariance between the velocities of Tracks 075 and 068. The off-diagonal covariance terms in Eq. (8) are all zero as the different Tracks provide independent, uncorrelated observations. $\sigma_n^2$ and $\sigma_u^2$ are the variances for north and vertical velocities, respectively, expressed as standard deviations $\sigma_n$ and $\sigma_u$ and mapped in Fig. 9.

For the East landslide, movements in both the downward and northward directions can be seen from the two dimensional velocity fields (Fig. 8). Uncertainty in the north velocity field is high as the mean standard deviation of all the pixels is 8.29 mm/yr (Fig. 9a). Two explanations may account for this large standard deviation: the first is the large standard deviation in Track 068 along the Yangtze River due to short data interval (Fig. 5c); the other is low
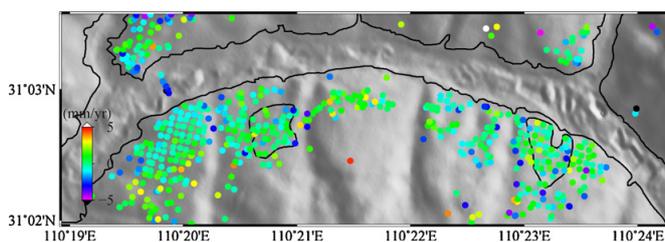


**Fig. 7.** Velocity differences between Tracks 075 and 347 for the common pixels found on a shaded DEM. The map is produced by subtracting the velocity value from Track 347 from that from Track 075. The outline of the East and West landslides along with Yangtze River are shown.

P. Liu et al. / International Journal of Applied Earth Observation and Geoinformation 21 (2013) 253–264
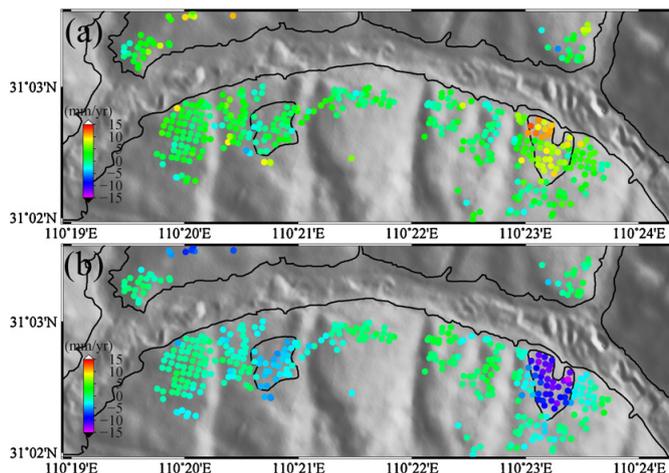


**Fig. 8.** (a) North component of the velocity field derived from Tracks 068, 075 and 347; (b) vertical component of the velocity field derived from Tracks 068, 075 and 347. Background for both is shaded DEM relief. The outline of the East and West landslides along with the Yangtze River are shown.

sensitivity of InSAR observation to the north component due to near vertical radar looking angles and the near polar orbits. The vertical velocity standard deviations are small with the mean value of 3.84 mm/yr. Most pixels from the upper slopes show vertical velocity standard deviations from 2–3 mm/yr, while most pixels adjacent to the Yangtze River have values of 5–7 mm/yr (Fig. 9b). The downward movements of the upper part of the East landslide are reliable as its 2–3 mm/yr standard deviations are much smaller than the 7–12 mm/yr vertical rate (Fig. 8b). For the West landslide, although common pixels for Tracks 075, 068 and 347 are sparse, downward movements could still be identified (Fig. 8b) with low standard deviations (Fig. 9b).

## 5. Landslide analysis

### 5.1. Surface movements of the west and east landslides

Points P1 and P2 are located on the west and east landslides, respectively (Fig. 4d). The RMS values between T075D and T347D

for P1 and P2 are 1.7 mm and 5.9 mm, respectively. These RMS values are much smaller than the total deformation that P1 and P2 exhibit. The high consistency between these two adjacent tracks provides confidence that our time series results from P1 and P2 are reliable. Both descending tracks 075 and 347 show that the cumulative LOS deformation magnitudes of P1 and P2 are 20 mm and 30 mm, respectively. Not only are the LOS deformation magnitudes different between P1 and P2, but also the pattern of deformation between successive SAR acquisitions are different. For example, point P2 (Fig. 6) on the East (Huangtupo) landslide has a consistent 20 mm drop from January 2004 to October 2004 at both Tracks 075 and 347. This is not observed at P1 on the West landslide. Similarly, P1 (Fig. 6) shows a constant rise of 6 mm from March 2007 to July 2007 from Track 075. This is not observed from P2 either. No radar image from Track 347 covers that time period. These differences suggest that movements of P1 (West landslide) and P2 (East landslide) are not correlated, and both the pattern and magnitude of their movements are different. There is correspondence between the two points on the West (P1 and P3) and the two points on the
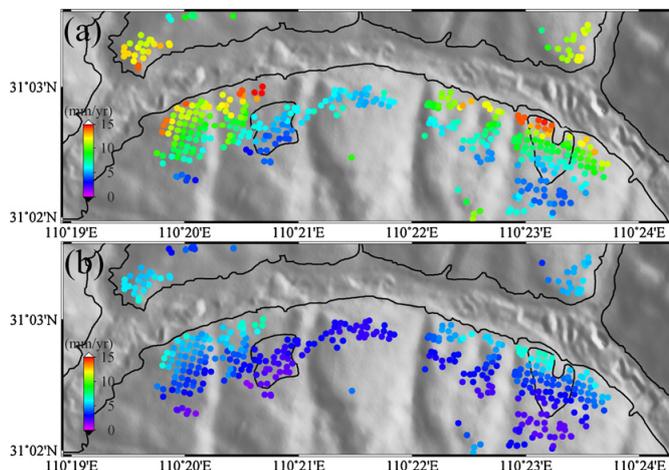


**Fig. 9.** (a) Standard deviation of the north component of the velocity field derived from Tracks 068, 075 and 347; (b) standard deviation of the vertical component of the velocity field derived from Tracks 068, 075 and 347. Background as Fig. 8. The outline of the East and West landslides along with Yangtze River are shown.

East (P2 and P4) landslide, suggesting that movement on each slide is affecting the whole of the feature.

### 5.2. Correlation analysis with water level and rainfall

Discrepancies in the time series deformation signals (Fig. 6) between different tracks could be due to different look angles and different temporal sampling of temporally variable events. All the tracks exhibit similar patterns of seasonal fluctuations (Fig. 6). On the other hand, both rainfall and water level exhibit strong seasonality in this region. Generally, rainfall between May and September accounts for 61–70% of the 1100–1522 mm annual precipitation in west Hubei province (Bao et al., 2009). Water level records show that the Three Gorges Dam began its first water impoundment on 1st June 2003. On 15th June 2003, the water level reached 135 m; on 21st September 2006, Three Gorges Dam began water impoundment to 156 m, which was reached on 27th October 2006; experimental water impoundment to 175 m started on 28th

September 2008, with peak level of 172.8 m on 10th November 2008; after a water level drop, another round of water impoundment began on 15th September 2009 with peak level of 171.43 m on 24th November 2009 (Dai et al., 2010; Zhang et al., 2009b). The water level of Three Gorges Reservoir can be divided into three different stages: 135 m, 156 m and 175 m impoundments with individual local peaks of I, II, III, IV, V, VI, VII and VIII (Fig. 10).

Correlation between water level fluctuations and landslide seasonal signals can be identified in P2 from the East landslide (Fig. 10). For instance: (a) water level between VII and VIII of 30 m pre-dam water level change in impoundment 175 m matches the simultaneous deformations of P2 in Track 347 when no Track 075 image is available; (b) water level between V and VI, and then between VI and VII of around 15 m water level change in impoundment 156 m match the deformation from Track 075 in P2 when Track 347 images are rarely distributed and none Track 068 image is available; (c) water level between III and IV of the order of 5 m in impoundment 135 m matches the deformation from Track 347 in
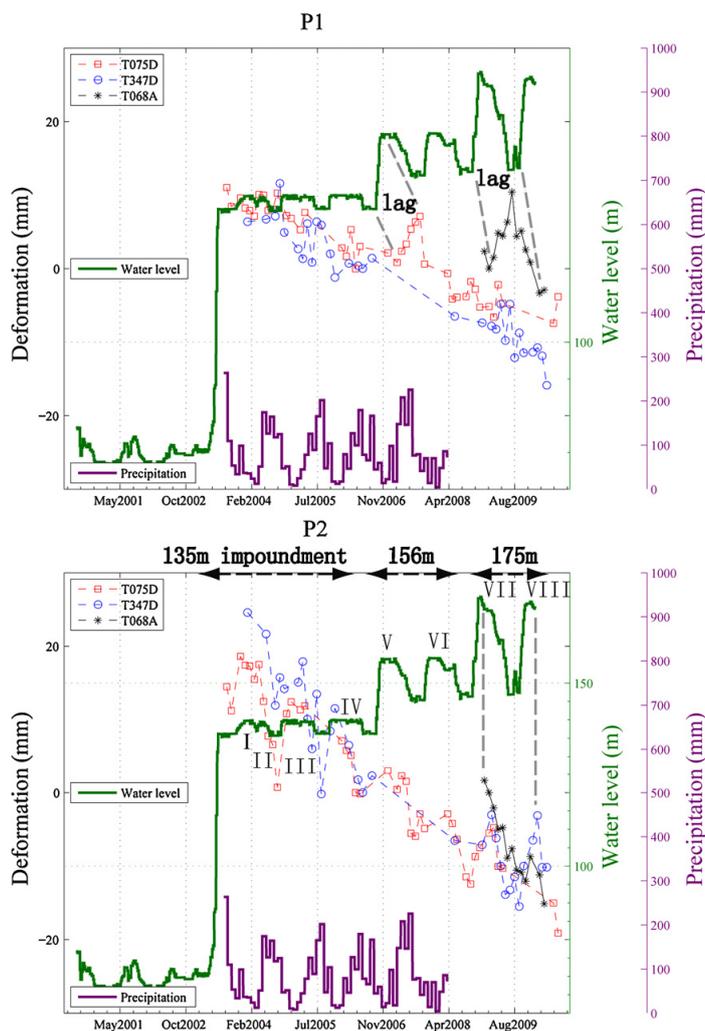


**Fig. 10.** Surface displacement time series of P1 and P2 in radar line of sight direction, pre-dam water level and monthly rainfall in Three Gorges Reservoir. Rainfall data comes from Li et al. (2010). Water level data comes from Dai et al. (2010).
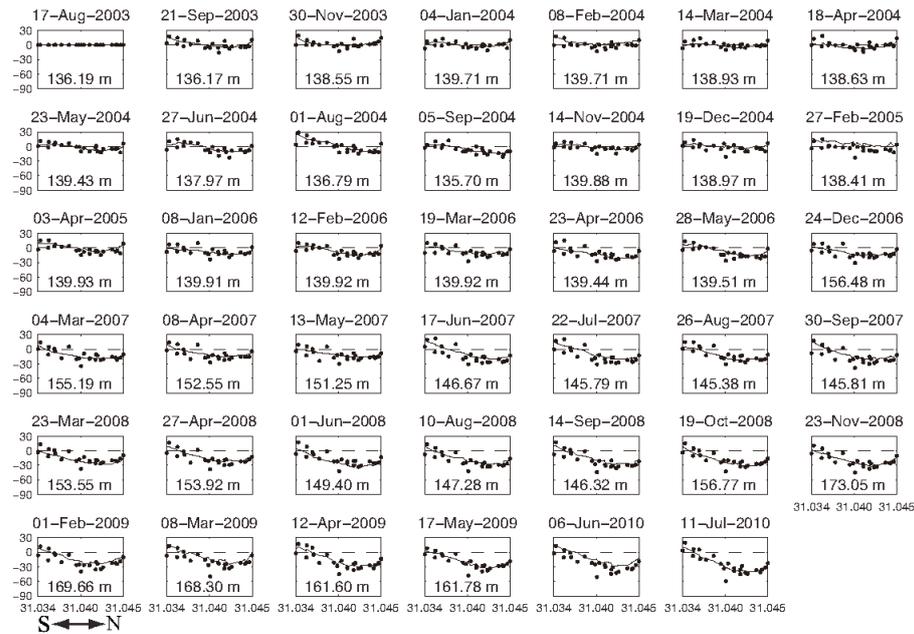
**Fig. 11.** Deformation profile SN of the Huangtupo landslide from Track 075. Line SN is marked in Fig. 4d. All the deformation is relative to the first scene on 17 August 2003. Dashed line in each scene stands for zero deformation. Each black dot represents a SDFP pixel in Profile SN. The approximated deformation tendencies of the dots are given in solid lines in each scene. Available pre-dam water level in SAR acquisition date is also given.

P2 when Track 075 images poorly cover this period; (d) water level in impoundment 135 among I, II and III in the order of 5 m impact the deformation of P2 in both Tracks 075 and 347. Seasonal deformation can be estimated simply by removing a long term linear rate from the observed InSAR deformation. In the three different impoundments, the seasonal deformation responds with different sensitivity to the water level change. The change of water level in impoundment 135 m is only 5 m compared with the next two impoundments of 15 m and 30 m (Fig. 10), but the seasonal deformation of P2 is −10–5 mm in impoundment 135 m compared with the next two impoundments of −5–3 mm and −6–5 mm. For P1 from the West landslide, a lag in correlation between water level and landslide seasonal signals can be identified sometimes (Fig. 10). For instance: (a) water level peak VII matches the deformation from Track 068 by a lag in P1; (b) water level rise during peak V matches the deformation from Track 075 by a lag in P1.

The drop of pre-dam water level in the Three Gorges Reservoir during the first five months of each year is to make enough reservoir capacity for big flood between May and September as a result of intense precipitation. Correlation between landslide activities and monthly rainfall is also investigated. For P2, it seems the local deformation valleys meet precipitation peaks (Fig. 10). This may be due to the fact that the water level has began to drop before the rainy season and therefore the local deformation valley correlated with this water level drop may meet the rainy season. For P1, correlation between deformation and rainfall is not clear.

The long-term deformation tendency is shown by the InSAR time series results (Figs. 6 and 11). Evidence of ongoing deformation was confirmed by field observations, with cracks in buildings and roads within the landslide areas. The cracks on concrete surfaces may be caused by landslides but as concrete weathers its tensile strength may change leading to cracking on the surface (Roy et al., 1999). Cracks were also observed in rocks – again this may be

affected by weathering that may exert sufficient pressure to separate rock fragments (Chen et al., 2000). However, cracking was found in rocks that have only been at the surface since the construction of the new city which may indicate that these cracks pre-date relocation and indicate longer-term landsliding. Also, the eastern, Huangtupo, landslide detected here has previously been identified and located in the same position (Wu et al., 2006).

## 6. Discussion and conclusion

In this paper, InSAR time series techniques have been successfully applied to identify surface deformation in Badong County, Three Gorges region, China from 2003 to 2010. Our time series results in Badong show consistent linear movement trends between two descending tracks with an overall RMS value of <2 mm, which enables the identification of the East landslide and the West landslide. They are two distinct landslides with different moving patterns and magnitudes. The locations of the East landslide identified in this study is consistent to the one suggested in previous studies (Deng et al., 2000; Tang and Hu, 2009; Wu et al., 2009). With both ascending and descending tracks, two-dimensional velocity fields in north and vertical directions have been recovered. The eastern landslide is moving northward (downslope) at the rate of 4–5 mm/yr while exhibiting a downward rate of 7–12 mm/yr. The western landslide is moving at the rate of 2–3 mm/yr with movement mainly vertically downward. Correlations between landslide seasonal deformations and water level changes are observed for both the eastern and western landslides, although these kinds of responds exhibit different time lag and different sensitivity in each impoundment.

A possible mechanism for such river bank landslides is that when the water level adjacent to the slope falls rapidly the groundwater level cannot dissipate quickly enough, leaving an artificially

high water table. This subjects the slope to a hydraulic pressure drive, leading to potential instability. We do not know if the water level changes affect the long term rate of landslide in Badong. The long term rate in our study period is relatively stable in seven years. Although correlations between water level fluctuation and seasonal landslide signals are observed, we cannot exclude the impacts of other factors such as cumulative precipitation and natural geological condition. It is beyond the scope of this paper to conclude if water filling by the dam affected the landslide rate because ASAR data are not available before 2003, the year that the dam started to function (Fig. 10).

In situ direct shear tests were carried out in a limited number of landslides investigation projects in this region by Wen et al. (2007). The slip zones of the large landslides in the Three Gorges region reach their in situ residual strength at shear displacement longer than 20 mm (normally 40–50 mm) (Wen et al., 2007). Greater magnitude of deformation is observed in the lower part of the Huangtupo landslide from the profile plot in Fig. 11. The two-dimensional velocity fields give vertical rates of 7–12 mm/yr in Huangtupo. The deformation rate of sliding zone can be greater than this vertical rate. As a result, the shear displacement in our study period is greater than 50 mm. The shear stress may have reached the steady state under which it remains constant while the shear strain increases.

The mean surface slope map (Fig. 1c) shows no clear correlation between landslide activity as represented by the mean velocity map (Fig. 4) and topographic slope. This may indicate that these landslides are not shallow landslides; the movement of which is generally correlated with topographic slope (Montgomery and Dietrich, 1994). This finding is consistent with the landslide depth previously suggested for the Huangtupo landslide (Wu et al., 2006).

This paper has demonstrated the capability of the small baseline InSAR technique for monitoring landslide hazards, even in regions with steep slopes and dense vegetation. It is suggested that this technique could be used on a continuous basis to monitor landslide activity and hazard in Badong and for other landslide sites in the Three Gorges area.

## Acknowledgements

## References

Bao, H., Mo, X., Yu, W., You, W., Kang, X., 2009. Uncertainty evaluation of the stability of the Huanglashi landslide in the Three Gorges of the Yangtze River. In: Wang, F., Li, T. (Eds.), Landslide Disaster Mitigation in Three Gorges Reservoir, China. Springer, Berlin, Heidelberg, pp. 475–485.

Beardsley, R.C., Limeburner, R., Yu, H., Cannon, G.A., 1985. Discharge of the Changjiang (Yangtze River) into the East China Sea. Cont. Shelf Res. 4 (1-2), 57–76.

Bechor, N.B.D., Zebker, H.A., 2006. Measuring two-dimensional movements using a single InSAR pair. Geophys. Res. Lett. 33 (16), L16311.

Berardino, P., Fornaro, G., Lanari, R., Sansosti, E., 2002. A new algorithm for surface deformation monitoring based on small baseline differential sar interferograms. IEEE Trans. Geosci. Remote Sens. 40, 2375–2383.

Caijing Magazine, 2009. Deterioration of Some Landslides after Water Level Rising of Three Gorges Reservoir, http://www.caijing.com.cn/2009-04-07/110134214.html (in Chinese).

Chen, C.W., Zebker, H.A., 2001. Two-dimensional phase unwrapping with use of statistical models for cost functions in nonlinear optimization. J. Opt. Soc. Am. A 18 (2), 338–351.

Chen, J., Blume, H.P., Beyer, L., 2000. Weathering of rocks induced by lichen colonization – a review. CATENA 39 (2), 121–146.

Colesanti, C., Wasowski, J., 2006. Investigating landslides with space-borne Synthetic Aperture Radar (SAR) interferometry. Eng. Geol. 88 (3–4), 173–199.

Dai, M., Yao, Y.S., Chen, J.H., Qin, X.J., Wang, Q.L., 2010. Relationship between seismic activity and pre-dam water level in Three Gorges Reservoir. Yangtze River 41 (7), 12–14 (in Chinese).

Deng, Q.L., Zhu, Z.Y., Cui, Z.Q., Wang, X.P., 2000. Mass rock creep and landsliding on the Huangtupo slope in the reservoir area of the Three Gorges Project, Yangtze River, China. Eng. Geol. 58 (1), 67–83.

Dijkstra, T.K., 2010. Latent variables and indices: Herman Wold's basic design and partial least squares. In: Vinzi, V.E., Chin, W.W., Henseler, J., Wang, H. (Eds.), Handbook of Partial Least Squares Concepts, Methods and Applications. Springer, Heidelberg, Dordrecht, London, New York, pp. 23–46.

Fialko, Y., Simons, M., 2001. The complete (3-D) surface displacement field in the epicentral area of the 1999 MW 7.1 Hector Mine Earthquake, California, from space geodetic observations. Geophys. Res. Lett. 28 (16), 3063–3066.

Fruneau, B., Achache, J., Delacourt, C., 1996. Observation and modelling of the Saint-Étienne-de-Tinée landslide using SAR interferometry. Tectonophysics 265 (3–4), 181–190.

Goldstein, R.M., Engelhardt, H., 1993. Satellite radar interferometry for monitoring ice sheet motion: application to an Antarctic ice stream. Science 262 (5139), 1525–1530.

Gourmelen, N., Amelung, F., Casu, F., Manzo, M., Lanari, R., 2007. Mining-related ground deformation in Crescent Valley, Nevada: implications for sparse GPS networks. Geophys. Res. Lett., 34.

Gourmelen, N., Amelung, F., Lanari, R., 2010. Interferometric synthetic aperture radar-GPS integration: interseismic strain accumulation across the Hunter Mountain fault in the eastern California shear zone. J. Geophys. Res. 115 (B9), B09408.

Hanssen, R., 2001. Radar Interferometry: Data Interpretation and Error Analysis. Springer, New York.

He, K., Li, X., Yan, X., Guo, D., 2008. The landslides in the Three Gorges Reservoir Region, China and the effects of water storage and rain on their stability. Environ. Geol. 55 (1), 55–63.

Hooper, A., Segall, P., Zebker, H., 2007. Persistent scatterer interferometric synthetic aperture radar for crustal deformation analysis, with application to Volcano Alcedo Galapagos. J. Geophys. Res. 112, B07407, doi:10.1029/2006JB004763.

Hooper, A., Zebker, H.A., 2007. Phase unwrapping in three dimensions with application to InSAR time series. J. Opt. Soc. Am. A: Opt. Image Sci. Vis. 24 (9), 2737–2747.

Hooper, A., 2008. A multi-temporal InSAR method incorporating both persistent scatterer and small baseline approaches. Geophys. Res. Lett. 35, L16302.

Lanari, R., Casu, F., Manzo, M., Zeni, G., Berardino, P., Manunta, M., Pepe, A., 2007. An overview of the small BAseline subset algorithm: a DInSAR technique for surface deformation analysis. Pure Appl. Geophys. 164 (4), 637–661, doi:10.1007/s00024-00007-00192-00029.

Li, J., Xie, S., Kuang, M., 2001. Geomorphic evolution of the Yangtze Gorges and the time of their formation. Geomorphology 41 (2–3), 125–135.

Li, Z., Muller, J.-P., Cross, P., Fielding, E.J., 2005. Interferometric synthetic aperture radar (InSAR) atmospheric correction: GPS, Moderate Resolution Imaging Spectroradiometer (MODIS), and InSAR integration. J. Geophys. Res., 110.

Li, Z., Fielding, E.J., Cross, P., Muller, J.-P., 2006. Interferometric synthetic aperture radar atmospheric correction: GPS topography-dependent turbulence model. J. Geophys. Res. 111 (B2), B02404, 02410.01029/02005JB003711.

Li, Z., Fielding, E.J., Cross, P., 2009a. Integration of InSAR time-series analysis and water-vapor correction for mapping postseismic motion after the 2003 Bam (Iran) earthquake. IEEE Trans. Geosci. Remote Sens. 47 (9), 3220–3230.

Li, Z., Fielding, E.J., Cross, P., Preusker, R., 2009b. Advanced InSAR atmospheric correction: MERIS/MODIS combination and stacked water vapour models. Int. J. Remote Sens. 30 (13), 3343–3363.

Li, D., Yin, K., Leo, C., 2010. Analysis of Baishuihe landslide influenced by the effects of reservoir water and rainfall. Environ. Earth Sci. 60 (4), 677–687.

Liu, J.G., Mason, P.J., Clerici, N., Chen, S., Davis, A., Miao, F., Deng, H., Liang, L., 2004. Landslide hazard assessment in the Three Gorges area of the Yangtze river using ASTER imagery: Zigui-Badong. Geomorphology 61 (1–2), 171–187.

Lu, Z., Dzurisin, D., Biggs, J., Wicks, C., Mcnutt, S., 2010. Ground surface deformation patterns, magma supply, and magma storage at Okmok volcano, Alaska, from InSAR analysis: 1. Interruption deformation, 1997–2008. J. Geophys. Res. 115, B00B02.

Lu, Z., Dzurisin, D., 2010. Ground surface deformation patterns, magma supply, and magma storage at Okmok volcano, Alaska, from InSAR analysis: 2. Coeruptive deflation, July–August 2008. J. Geophys. Res. 115, B00B03.

Massonnet, D., Rossi, M., Carmona, C., Adragna, F., Peltzer, G., Feigl, K., Rabaute, T., 1993. The displacement field of the Landers earthquake mapped by radar interferometry. Nature 364 (6433), 138–142.

Massonnet, D., Briole, P., Arnaud, A., 1995. Deflation of Mount Etna monitored by spaceborne radar interferometry. Nature 375 (6532), 567–570.

184

Massonnet, D., Feigl, K.L., 1998. Radar interferometry and its application to changes in the Earth's surface. Rev. Geophys. 36 (4), 441–500.

Montgomery, D.R., Dietrich, W.E., 1994. A physically-based model for the topographic control on shallow landsliding. Water Resour. Res. 30 (4), 1153–1171.

Mora, O., Mallorqui, J.J., Broquetas, A., 2003. Linear and nonlinear terrain deformation maps from a reduced set of interferometric SAR images. IEEE Trans. Geosci. Remote Sens. 41 (10), 2243–2253.

Ofeigsson, B.G., Hooper, A., Sigmundsson, F., Sturkell, E., Grapenthin, R., 2011. Deep magma storage at Hekla volcano, Iceland, revealed by InSAR time series analysis. J. Geophys. Res. 116 (B5), B05401.

Peltier, A., Bianchi, M., Kaminski, E., Komorowski, J.C., Rucci, A., Staudacher, T., 2010. PSInSAR as a new tool to monitor pre-eruptive volcano ground deformation: validation using GPS measurements on Piton de la Fournaise. Geophys. Res. Lett. 37 (12), L12301.

Perissin, D., Ferretti, A., 2007. Urban-target recognition by means of repeated spaceborne SAR images. IEEE Trans. Geosci. Remote Sens. 45 (12), 4043–4058.

Peyret, M., Dominguez, S., Cattin, R., Champenois, J., Leroy, M., Zajac, A., 2011. Present-day interseismic surface deformation along the Longitudinal Valley, eastern Taiwan, from a PS-InSAR analysis of the ERS satellite archives. J. Geophys. Res. 116 (B3), B03402.

Richardson, N.J., Densmore, A.L., Seward, D., Wipf, M., Li, Y., 2010. Did incision of the Three Gorges begin in the Eocene? Geology 38 (6), 551–554.

Roy, S.K., Poh, K.B., Northwood, D.O., 1999. Durability of concrete – accelerated carbonation and weathering studies. Build. Environ. 34 (5), 597–606.

Schmidt, D.A., Bürgmann, R., 2003. Time-dependent land uplift and subsidence in the Santa Clara valley, California, from a large interferometric synthetic aperture radar data set. J. Geophys. Res. 108 (B9), 2416.

Shen, G., Xie, Z., 2004. Three Gorges Project: chance and challenge. Science 304 (5671), 681.

State Council Gorges Project Construction Committee Executive Office (SCGPCCEO), 2008. The Three Gorges Projects's Water Coverage for Chongqing and Hubei Provinces, http://www.3g.gov.cn/xxxq.ycs?GUID=1915 (in Chinese).

State Council Gorges Project Construction Committee Executive Office (SCGPCCEO), 2009. The Three Gorges Projects has Relocated 1.27 Million People, Resettlement Task is Basically Completed, http://www.3g.gov.cn/xxxq.ycs?GUID=3114 (in Chinese).

Strozzi, T., Delaloye, R., Kääb, A., Ambrosi, C., Perruchoud, E., Wegmüller, U., 2010. Combined observations of rock mass movements using satellite SAR interferometry, differential GPS, airborne digital photogrammetry, and airborne photography interpretation. J. Geophys. Res. 115 (F1), F01014.

Tang, H., Hu, X., 2009. Research on the characteristics and slope deformation regularity of the Badong formation in the Three Gorges Reservoir area. Landslide Disaster Mitigation in Three Gorges Reservoir, China, vol. 8. Springer, Berlin, Heidelberg, pp. 7–113.

Tomas, R., Herrera, G., Lopez-Sanchez, J.M., Vicente, F., Cuenca, A., Mallorquì, J.J., 2010. Study of the land subsidence in Orihuela City (SE Spain) using PSI data: distribution, evolution and correlation with conditioning and triggering factors. Eng. Geol. 115 (1–2), 105–121.

Wang, F.W., Tan, Z.D., 1991. The forming mechanism and sliding character of Xintan Landslide. J. Yangtze River Sci. Res. Inst. 8 (3), 28–34 (In Chinese).

Wang, J., 2002. Three Gorges project: the largest water conservancy project in the world. Public Admin. Dev. 22, 369–375.

Wang, T., Liao, M.S., Perissin, D., Rocca, F., 2008. Deformation monitoring by long term D-InSAR analysis in Three Gorges area, China. In: Paper Presented at Proceedings of IGARSS 2008, Boston, MA, 6–11 July, 2008.

Wen, B.P., Aydin, A., Duzgoren-Aydin, N.S., Li, Y.R., Chen, H.Y., Xiao, S.D., 2007. Residual strength of slip zones of large landslides in the Three Gorges area, China. Eng. Geol. 93 (3–4), 82–98.

Wessel, P., Smith, W.H.F., 1998. New, improved version of generic mapping tools released. Eos Tran. AGU 79 (47), 579.

Wright, L.D., Nittrouer, C.A., 1995. Dispersal of river sediments in coastal seas – 6 contrasting cases. Estuaries 18 (3), 494–508.

Wright, T.J., Parsons, B.E., Lu, Z., 2004. Toward mapping surface deformation in three dimensions using InSAR. Geophys. Res. Lett., 31.

Wu, S., Wang, H., Han, J., Shi, J., Shi, L., Zhang, Y., 2009. The application of fractal dimensions of landslide boundary trace for evaluation of slope instability. In: Wang, F., Li, T. (Eds.), Landslide Disaster Mitigation in Three Gorges Reservoir, China. Springer, Berlin, Heidelberg, pp. 465–474.

Wu, X., Yu, Q.C., He, M.C., Zhao, X., 2006. Formation mechanism of Huangtupo Landslide in reservoir of Three Gorges Project. J. Hydraulic Eng. 37 (8), 969–976 (in Chinese).

Xia, Y., Kaufmann, H., Guo, X.F., 2004. Landslide monitoring in the Three Gorges area using D-InSAR and corner reflectors. Photogramm. Eng. Remote Sens. 70 (10), 1167–1172.

Yin, H.F., Li, C.G., 2001. Human impact on floods and flood disasters on the Yangtze River. Geomorphology 41 (2–3), 105–109.

Zebker, H.A., Villasenor, J., 1992. Decorrelation in interferometric radar echoes. IEEE Trans. Geosci. Remote Sens. 30 (5), 950–959.

Zebker, H., Rosen, P., Hensley, S., 1997. Atmospheric effects in interferometric synthetic aperature radar surface deformation and topographic maps. J. Geophys. Res. 102 (B4), doi:10.1029/96JB03804, ISSN: 0148-0227.

Zhang, A.B., Liu, X.X., Di, W.J., 2009a. Derivation of the green vegetation fraction from TM data of Three Gorges area. Proc. Earth Planet. Sci. 1 (1), 1152–1157.

Zhang, Z., Luo, X., Wu, J., 2009b. Study on the possible failure mode and mechanism of the Xietan landslide when exposed to water level fluctuation. In: Wang, F., Li, T. (Eds.), Landslide Disaster Mitigation in Three Gorges Reservoir, China. Springer, Berlin, Heidelberg, pp. 375–385.

# References

Adam, N., Xiaoxiang, Z. & Bamler, R., 2009. Coherent stacking with TerraSAR-X imagery in urban areas. *in Urban Remote Sensing Event, 2009 Joint*, pp. 1-6.

Amelung, F., Jonsson, S., Zebker, H. & Segall, P., 2000. Widespread uplift and 'trapdoor' faulting on Galapagos volcanoes observed with radar interferometry, *Nature,* 407**,** 993-996.

Amoruso, A. & Crescentini, L., 2011. Modelling deformation due to a pressurized ellipsoidal cavity, with reference to the Campi Flegrei caldera, Italy, *Geophys. Res. Lett.,* 38**,** L01303.

Anderson, E.M., 1936. The dynamics of the formation of cone sheets, ring dykes, and cauldron subsidences. *in R. Soc. Edinburgh*, pp. 128-157.

Andrews, L.C. & Phillips, R.L., 2003. *Mathematical Techniques for Engineers and Scientists,* edn, Vol., pp. Pages, SPIE-The International Society for Optical Engineering, Bellingham.

Bamler, R. & Hartlz, P., 1998. Synthetic aperture radar interferometry, *Inverse Problems,* 14**,** R1-R54.

Becker, R.H. & Sultan, M., 2009. Land subsidence in the Nile Delta: inferences from radar interferometry, *Holocene,* 19**,** 949-954.

Bell, F.G., 2007. *Basic Environmental and Engineering Geology,* edn, Vol., pp. Pages, Taylor & Francis.

Berardino, P., Fornaro, G., Lanari, R. & Sansosti, E., 2002. a new algorithm for surface deformation monitoring based on small baseline differential sar interferograms, *IEEE TRANSACTIONS ON GEOSCIENCE AND REMOTE SENSING,* 40**,** 2375-2383.

Biggs, J., Anthony, E.Y. & Ebinger, C.J., 2009. Multiple inflation and deflation events at Kenyan volcanoes, East African Rift, *Geology,* 37**,** 979-982.

Biggs, J., Lu, Z., Fournier, T. & Freymueller, J.T., 2010. Magma flux at Okmok Volcano, Alaska, from a joint inversion of continuous GPS, campaign GPS, and interferometric synthetic aperture radar, *J. Geophys. Res.,* 115**,** B12401.

Biggs, J., Wright, T., Lu, Z. & Parsons, B., 2007. Multi-interferogram method for measuring interseismic deformation: Denali Fault, Alaska, *Geophysical Journal International,* 170**,** 1165-1179.

Biot, M.A., 1941. General Theory of Three Dimensional Consolidation, *Journal of Applied Physics,* 12**,** 155-164.

Blott, S.J., Croft, D.J., Pye, K., Saye, S.E. & Wilson, H.E., 2004. Particle size analysis by laser diffraction, *Geological Society, London, Special Publications,* 232.

Blott, S.J. & Pye, K., 2001. GRADISTAT: A grain size distribution and statistics package for the analysis of unconsolidated sediments, *Earth Surface Processes and Landforms,* 26**,** 1237-1248.

Boesch, D.F., Josselyn, M.N., Mehta, A.J., Morris, J.T., Nuttle, W.K., Simenstad, C.A. & Swift, D.J.P., 1994. Scientific Assessment of Coastal Wetland Loss, Restoration and Management in Louisiana, *Journal of Coastal Research***,** i-103.

Brown, W.M. & Porcello, L.J., 1969. An introduction to synthetic-aperture radar, *Spectrum, IEEE,* 6**,** 52-62.

Buckley, S.M., Rosen, P.A., Hensley, S. & Tapley, B.D., 2003. Land subsidence in Houston, Texas, measured by radar interferometry and constrained by extensometers, *J. Geophys. Res.,* 108.

Capasso, G. & Mantica, S., 2006. Numerical Simulation of Compaction and Subsidence Using ABAQUS. *in 2006 ABAQUS Users' Conference*.

Cavalié, O., Lasserre, C., Doin, M.P., Peltzer, G., Sun, J., Xu, X. & Shen, Z.K., 2008. Measurement of interseismic strain across the Haiyuan fault (Gansu, China), by InSAR, *Earth and Planetary Science Letters,* 275**,** 246-257.

Chan, Y.K. & Koo, V.C., 2008. An introduction to Synthetic Aperture Radar (SAR), *Progress In Electromagnetics Research B,* 2.

Chen, C.W. & Zebker, H.A., 2001. Two-dimensional phase unwrapping with use of statistical models for cost functions in nonlinear optimization, *J. Opt. Soc. Am. A,* 18**,** 338-351.

Chen, K., Yuan, J. & Yan, C., 2012. CHINA Shandong Yellow River Delta National Nature Reserve.

Cheng, G.D., 1991. *Depositional processes and model of the modern Yellow River delta (in Chinese).* edn, Vol., pp. Pages, Geological Press, Beijing.

Chlieh, M., de Chabalier, J.B., Ruegg, J.C., Armijo, R., Dmowska, R., Campos, J. & Feigl, K.L., 2004. Crustal deformation and fault slip during the seismic cycle in the North Chile subduction zone, from GPS and InSAR observations, *Geophysical Journal International,* 158**,** 695-711.

Chu, Z.X., Sun, X.G., Zhai, S.K. & Xu, K.H., 2006. Changing pattern of accretion/erosion of the modern Yellow River (Huanghe) subaerial delta, China: Based on remote sensing images, *Mar. Geol.,* 227**,** 13-30.

Coleman, T.F. & Li, Y.Y., 1996. An interior trust region approach for nonlinear minimization subject to bounds, *SIAM J. Optim.,* 6**,** 418-445.

Colesanti, C., Ferretti, A., Novali, F., Prati, C. & Rocca, F., 2003. SAR monitoring of progressive and seasonal ground deformation using the permanent scatterers technique, *Geoscience and Remote Sensing, IEEE Transactions on,* 41**,** 1685-1701.

Colesanti, C. & Wasowski, J., 2006. Investigating landslides with space-borne Synthetic Aperture Radar (SAR) interferometry, *Eng. Geol.,* 88**,** 173-199.

Cui, B.-L. & Li, X.-Y., 2011. Coastline change of the Yellow River estuary and its response to the sediment and runoff (1976-2005), *Geomorphology,* 127**,** 32-40.

Cui, B.S., Tang, N., Zhao, X.S. & Bai, J.H., 2009. A management-oriented valuation method to determine ecological water requirement for wetlands in the Yellow River Delta of China, *J. Nat. Conserv.,* 17**,** 129-141.

Davis, P.M., 1986. Surface Deformation Due to Inflation of an Arbitrarily Oriented Triaxial Ellipsoidal Cavity in an Elastic Half-Space, With Reference to Kilauea Volcano, Hawaii, *J. Geophys. Res.,* 91**,** 7429-7438.

Davis, P.M., Hastie, L.M. & Stacey, F.D., 1974. Stresses within an active volcano -- with particular reference to kilauea, *Tectonophysics,* 22**,** 355-362.

Detournay, E. & Cheng, A.H.-D., 1993. *Fundamentals of Poroelasticity,* edn, Vol., pp. Pages, Pergamon Press.

Eason, G., Noble, B. & Sneddon, I.N., 1955. On Certain Integrals of Lipschitz-Hankel Type Involving Products of Bessel Functions, *Philosophical Transactions of the Royal Society of London. Series A, Mathematical and Physical Sciences,* 247**,** 529-551.

Efron, B. & Tibshirani, R., 1986. Bootstrap Methods for Standard Errors, Confidence Intervals, and Other Measures of Statistical Accuracy, *Statistical Science,* 1**,** 54-75.

Elliott, J.R., Biggs, J., Parsons, B. & Wright, T.J., 2008. InSAR slip rate determination on the Altyn Tagh Fault, northern Tibet, in the presence of topographically correlated atmospheric delays, *Geophys. Res. Lett.,* 35**,** L12309.

Eshelby, J.D., 1957. The Determination of the Elastic Field of an Ellipsoidal Inclusion, and Related Problems, *Proceedings of the Royal Society of London. Series A. Mathematical and Physical Sciences,* 241**,** 376-396.

Fang, H. & Xu, J., 2000. Land Cover and Vegetation Change in the Yellow River Delta Nature Reserve Analyzed with Landsat Thematic Mapper Data, *Geocarto International,* 15.

Farr, T.G., 2007. The Shuttle Radar Topography Mission, *Rev. Geophys,* 45.

Feigl, K.L., Agnew, D.C., Bock, Y., Dong, D., Donnellan, A., Hager, B.H., Herring, T.A., Jackson, D.D., Jordan, T.H., King, R.W., Larsen, S., Larson, K.M., Murray, M.H., Shen, Z.K. & Webb, F.H., 1993. Space geodetic measurement of curstal deformation in central and southern california, 1984-1992, *J. Geophys. Res.-Solid Earth,* 98**,** 21677-21712.

Feng, G., Ding, X., Li, Z., Jiang, M., Zhang, L. & Omura, M., 2012. Calibration of an InSAR-Derived Coseimic Deformation Map Associated With the 2011 Mw-9.0 Tohoku-Oki Earthquake, *Geoscience and Remote Sensing Letters, IEEE,* 9**,** 302-306.

Feng, L. & Newman, A.V., 2009. Constraints on continued episodic inflation at Long Valley Caldera, based on seismic and geodetic observations, *J. Geophys. Res.,* 114**,** B06403.

Ferreira, T. & Rasband, W., 2006. ImageJU. S. National Institutes of Health, Bethesda, Maryland, USA.

Ferretti, A., Fumagalli, A., Novali, F., Prati, C., Rocca, F. & Rucci, A., 2011. A New Algorithm for Processing Interferometric Data-Stacks: SqueeSAR, *Geoscience and Remote Sensing, IEEE Transactions on,* 49**,** 3460-3470.

Ferretti, A., Monti-Guarnieri, A., Prati, C., Rocca, F. & Massonnet, D., 2007. *InSAR Principles: Guidelines for SAR Interferometry Processing and Interpretation,* edn, Vol., pp. Pages, ESA Publications, The Netherlands.

Ferretti, A., Prati, C. & Rocca, F., 2001. Permanent scatterers in SAR interferometry, *Geoscience and Remote Sensing, IEEE Transactions on,* 39**,** 8-20.

Fialko, Y., 2004. Evidence of fluid-filled upper crust from observations of postseismic deformation due to the 1992 M(w)7.3 Landers earthquake, *J. Geophys. Res.-Solid Earth,* 109.

Fialko, Y., 2006. Interseismic strain accumulation and the earthquake potential on the southern San Andreas fault system, *Nature,* 441**,** 968-971.

Fialko, Y., Khazan, Y. & Simons, M., 2001. Deformation due to a pressurized horizontal circular crack in an elastic half-space, with applications to volcano geodesy, *Geophysical Journal International,* 146**,** 181-190.

Fialko, Y. & Simons, M., 2000. Deformation and seismicity in the Coso geothermal area, Inyo County, California: Observations and modeling using satellite radar interferometry, *J. Geophys. Res.,* 105**,** 21781-21793.

Fielding, E.J., Blom, R.G. & Goldstein, R.M., 1998. Rapid Subsidence Over Oil Fields Measured by SAR Interferometry, *Geophys. Res. Lett.,* 25.

Fjær, E., Holt, R.M., Horsrud, P., Raaen, A.M. & Risnes, R., 1992. Petroleum related rock mechanics. *in Developments in Petroleum Science*, pp. 338, ed Chilingarian, G. V. EISEVIER SCIENCE PUBLISHERS B.V.

Folk, R.L. & Ward, W.C., 1957. Brazos River bar [Texas]; a study in the significance of grain size parameters, *Journal of Sedimentary Research,* 27**,** 3-26.

Fornaro, G., Pascazio, V., Schirinzi, G. & Serafino, F., 2005. Improved resolution image focusing by multi-pass ENVISAT ASAR data *in FRINGE 2005 Workshop*, Frascati.

Foster, J., Brooks, B., Cherubini, T., Shacat, C., Businger, S. & Werner, C.L., 2006. Mitigating atmospheric noise for InSAR using a high resolution weather model, *Geophys. Res. Lett.,* 33**,** L16304.

Fournier, T., Pritchard, M.E. & Finnegan, N., 2011. Accounting for Atmospheric Delays in InSAR Data in a Search for Long-Wavelength Deformation in South America, *Geoscience and Remote Sensing, IEEE Transactions on,* 49**,** 3856-3867.

Fruneau, B., Achache, J. & Delacourt, C., 1996. Observation and modelling of the Saint-Étienne-de-Tinée landslide using SAR interferometry, *Tectonophysics,* 265**,** 181-190.

Gabriel, A.K. & Goldstein, R.M., 1988. Crossed orbit interferometry - theory and experimental results from SIR-B, *International Journal of Remote Sensing,* 9**,** 857-872.

Gabriel, A.K., Goldstein, R.M. & Zebker, H.A., 1989. Mapping Small Elevation Changes Over Large Areas: Differential Radar Interferometry, *JOURNAL OF GEOPHYSICAL RESEARCH,* (94)B7**,** 9183-9191.

Gambino, S. & Guglielmino, F., 2008. Ground deformation induced by geothermal processes: A model for La Fossa Crater (Vulcano Island, Italy), *J. Geophys. Res.,* 113**,** B07402.

Gao, S., Li, Y., An, F., Wang, Y. & Yan, F., 1989. *The formation and sedimentary environment of Yellow River Delta (in Chinese),* edn, Vol., pp. Pages, Science Press.

Geertsma, J., 1973. Land subsidence above compacting oil and gas reservoirs, *J. Pet. Technol.,* 25**,** 734-744.

Goldstein, R.M. & Werner, C.L., 1998. Radar interferogram filtering for geophysical applications, *Geophys. Res. Lett.,* 25**,** 4035-4038.

Goldstein, R.M., Zebker, H.A. & Werner, C.L., 1988. Satellite radar interferometry: Two-dimensional phase unwrapping, *Radio Sci.,* 23.

Gong, Y.L., Wang, L.S., Liu, S.W., Li, C., Han, Y.B., Li, H., Liu, B. & Cai, J.G., 2004. Distribution characteristics of terrestrial heat flow density in Jiyang depression of Shengli Oilfield, East China, *Sci. China Ser. D-Earth Sci.,* 47**,** 804-812.

Gordon, R.L., 1996. *Acoustic Doppler Current Profiler Principles of Opertation,* edn, Vol., pp. Pages, RD Instruments, San Diego.

Gourmelen, N., Amelung, F. & Lanari, R., 2010. Interferometric synthetic aperture radar- GPS integration: Interseismic strain accumulation across the Hunter Mountain fault in the eastern California shear zone, *J. Geophys. Res.,* 115**,** B09408.

Graham, L.C., 1974. Synthetic interferometer radar for topographic mapping, *Proceedings of the IEEE,* 62**,** 763-768.

Grasso, J.-R. & Sornette, D., 1998. Testing self-organized criticality by induced seismicity, *J. Geophys. Res.,* 103**,** 29965-29987.

Greenberg, M.D., 1971. *Applications of Green's functions in science and engineering,* edn, Vol., pp. Pages, Prentice-Hall.

Gregory, K.J. & Cullingford, R.A., 1974. Lateral variations in pebble shape in northwest Yorkshire, *Sedimentary Geology,* 12**,** 237-248.

Hackley, V.A., Lum, L.-S., Gintautas, V. & Ferraris, C.F., 2004. Particle size analysis by laser diffraction spectrometry: application to cementitious powders, *NISTIR 7097.*

Halow, J.S., 1973. Incipient rolling, sliding and suspension of particles in horizontal and inclined turbulent flow, *Chemical Engineering Science,* 28**,** 1-12.

Hanssen, R.F., 2001. *Radar Interferometry, Data Interpretation and Error Analysis,* edn, Vol. 2, pp. Pages, Kluwer Academic Publishers, New York.

Harris, R.A., 1998. Introduction to special section: Stress triggers, stress shadows, and implications for seismic hazard, *J. Geophys. Res.,* 103**,** 24347-24358.

Hart, D.J. & Wang, H.F., 1995. Laboratory measurements of a complete set of poroelastic moduli for Berea sandstone and Indiana limestone, *J. Geophys. Res.,* 100**,** 17741-17751.

Hoey, T.B. & Bluck, B.J., 1999. Identifying the controls over downstream fining of river gravels, *Journal of Sedimentary Research,* 69**,** 40-50.

Hoffmann, J., Zebker, H.A., Galloway, D.L. & Amelung, F., 2001. Seasonal subsidence and rebound in Las Vegas Valley, Nevada, observed by Synthetic Aperture Radar Interferometry, *Water Resour. Res.,* 37**,** 1551-1566.

Hooper, A., 2008. A multi-temporal InSAR method incorporating both persistent scatterer and small baseline approaches, *GEOPHYSICAL RESEARCH LETTERS,* 35.

Hooper, A., P.Segall & H.Zebker, 2007. Persistent scatterer interferometric synthetic aperture radar for crustal deformation analysis, *JOURNAL OF GEOPHYSICAL RESEARCH,* 112.

Hooper, E.C.D., 1991. Fluid migration along growth faults in compacting sediments, *Journal of Petroleum Geology,* 14**,** 161-180.

Huang, M.B., Gallichand, J., Dong, C.Y., Wang, Z.L. & Shao, M.G., 2007. Use of soil moisture data and curve number method for estimating runoff in the Loess Plateau of China, *Hydrol. Process.,* 21**,** 1471-1481.

Hyne, N.J., 1991. *Dictionary of petroleum exploration, drilling & production,* edn, Vol., pp. Pages, PennWell Publishing Company, Tulsa.

Jia, X. & Wang, H., 2011. Mineral compositions and sources of the riverbed sediment in the desert channel of Yellow River, *Environmental Monitoring and Assessment,* 173**,** 969-983.

Jolivet, R., Grandin, R., Lasserre, C., Doin, M.P. & Peltzer, G., 2011. Systematic InSAR tropospheric phase delay corrections from global meteorological reanalysis data, *Geophys. Res. Lett.,* 38**,** L17311.

Jonsson, S., Zebker, H., Segall, P. & Amelung, F., 2002. Fault slip distribution of the 1999 M-w 7.1 Hector Mine, California, earthquake, estimated from satellite radar and GPS measurements, *Bulletin of the Seismological Society of America,* 92**,** 1377-1389.

Kampes, B.M., 2006. *Radar Interferometry, Persistent Scatterer Technique,* edn, Vol. 12, pp. Pages, Springer.

Kampes, B.M., Hanssen, R.F. & Perski, Z., 2003. Radar interferometry with public domain tools. *in Third International Workshop on ERS SAR Interferometry, 'FRINGE03',* pp. 6, Frascati, Italy.

Ketelaar, V.B.H.G., 2009. *Satellite Radar Interferometry, Subsidence Monitoring Techniques,* edn, Vol., pp. Pages.

Kosloff, D., Scott, R.F. & Scranton, J., 1980a. Finite element simulation of Wilmington oil field subsidence: I. Linear modelling, *Tectonophysics,* 65**,** 339-368.

Kosloff, D., Scott, R.F. & Scranton, J., 1980b. Finite element simulation of wilmington oil field subsidence: II. Nonlinear modelling, *Tectonophysics,* 70**,** 159-183.

Kovacik, J., 2001. Correlation between shear modulus and porosity in porous materials, *Journal of Materials Science Letters,* 20**,** 1953-1955.

Kovacik, J., 2008. Correlation Between Elastic Modulus, Shear Modulus, Poisson's Ratio and Porosity in Porous Materials, *Advanced Engineering Materials,* 10**,** 250-252.

Krieger, G., Moreira, A., Fiedler, H., Hajnsek, I., Werner, M., Younis, M. & Zink, M., 2007. TanDEM-X: A Satellite Formation for High-Resolution SAR Interferometry, *Geoscience and Remote Sensing, IEEE Transactions on,* 45**,** 3317-3341.

Lewis, R.W. & Sukirman, Y., 1993. Finite element modelling of three-phase flow in deforming saturated oil reservoirs, *International Journal for Numerical and Analytical Methods in Geomechanics,* 17**,** 577-598.

Lewis, R.W. & Sukirman, Y., 1994. Finite element modelling for simulating the surface subsidence above a compacting hydrocarbon reservoir, *International Journal for Numerical and Analytical Methods in Geomechanics,* 18**,** 619-639.

Li, X.-y., Chen, S.-l., Hu, J., Chen, X.-y. & Li, W.-h., 2008. Sediment characteristic and hydrodynamics of nearshore Gudong in the Yellow River delta (in Chinese), *MARINE GEOLOGY & QUATERNARY GEOLOGY,* 28.

Li, Z., 2005. Correction of atmospheric water vapour effects on repeat-pass SAR interferometry using GPS, MODIS and MERIS data PhD, University College London, London.

Li, Z., Elliott, J.R., Feng, W., Jackson, J.A., Parsons, B.E. & Walters, R.J., 2011. The 2010 MW 6.8 Yushu (Qinghai, China) earthquake: Constraints provided by InSAR and body wave seismology, *J. Geophys. Res.,* 116**,** B10302.

Li, Z., Fielding, E.J. & Cross, P., 2009. Integration of InSAR Time-Series Analysis and Water-Vapor Correction for Mapping Postseismic Motion After the 2003 Bam (Iran) Earthquake, *Geoscience and Remote Sensing, IEEE Transactions on,* 47**,** 3220-3230.

Li, Z., Fielding, E.J., Cross, P. & Muller, J.-P., 2006a. Interferometric synthetic aperture radar atmospheric correction: GPS topography-dependent turbulence model, *J. Geophys. Res.,* 111.

Li, Z., Fielding, E.J., Cross, P. & Muller, J.-P., 2006b. Interferometric synthetic aperture radar atmospheric correction: Medium Resolution Imaging Spectrometer and Advanced Synthetic Aperture Radar integration, *Geophys. Res. Lett.,* 33.

Li, Z., Muller, J.-P., Cross, P. & Fielding, E.J., 2005. Interferometric synthetic aperture radar (InSAR) atmospheric correction: GPS, Moderate Resolution Imaging Spectroradiometer (MODIS), and InSAR integration, *J. Geophys. Res.,* 110.

Li, Z., Pasquali, P., Cantone, A., Singleton, A., Funning, G. & Forrest, D., 2012. MERIS Atmospheric Water Vapor Correction Model for Wide Swath Interferometric Synthetic Aperture Radar, *Geoscience and Remote Sensing Letters, IEEE,* 9**,** 257-261.

Lin, Q., Vesecky, J.F. & Zebker, H.A., 1992. New approaches in interferometric SAR data processing, *Geoscience and Remote Sensing, IEEE Transactions on,* 30**,** 560-567.

Lin, Y.-n.N., Simons, M., Hetland, E.A., Muse, P. & DiCaprio, C., 2010. A multiscale approach to estimating topographically correlated propagation delays in radar interferograms, *Geochem. Geophys. Geosyst.,* 11**,** Q09002.

Liu, P., Li, Z., Hoey, T., Kincal, C., Zhang, J., Zeng, Q. & Muller, J.-P., 2013. Using advanced InSAR time series techniques to monitor landslide movements in Badong of the Three Gorges region, China, *International Journal of Applied Earth Observation and Geoinformation,* 21**,** 253-264.

Lu, X., Shu, Q., Zeng, X. & Liu, T., 2005. *Geology of Gudao Oilfield (in Chinese),* edn, Vol., pp. Pages, Petroleum Industry Press.

Lu, Z. & Dzurisin, D., 2010. Ground surface deformation patterns, magma supply, and magma storage at Okmok volcano, Alaska, from InSAR analysis: 2. Coeruptive deflation, July&#8211;August 2008, *J. Geophys. Res.,* 115**,** B00B03.

Lu, Z., Dzurisin, D., Biggs, J., Wicks, C., Jr. & McNutt, S., 2010. Ground surface deformation patterns, magma supply, and magma storage at Okmok volcano, Alaska, from InSAR analysis: 1. Intereruption deformation, 1997-2008, *J. Geophys. Res.,* 115**,** B00B02.

Madsen, S.N., Martin, J.M. & Zebker, H.A., 1995. Analysis and evaluation of the NASA/JPL TOPSAR across-track interferometric SAR system, *Geoscience and Remote Sensing, IEEE Transactions on,* 33**,** 383-391.

Majer, E.L., Baria, R., Stark, M., Oates, S., Bommer, J., Smith, B. & Asanuma, H., 2007. Induced seismicity associated with Enhanced Geothermal Systems, *Geothermics,* 36**,** 185-222.

Manconi, A. & Casu, F., 2012. Joint analysis of displacement time series retrieved from SAR phase and amplitude: Impact on the estimation of volcanic source parameters, *Geophys. Res. Lett.,* 39**,** L14301.

Massonnet, D., Briole, P. & Arnaud, A., 1995. Deflation of Mount Etna monitored by spaceborne radar interferometry, *Nature,* 375**,** 567-570.

Massonnet, D., Feigl, K., Rossi, M. & Adragna, F., 1994. Radar interferometric mapping of deformation in the year after the Landers earthquake, *Nature,* 369**,** 227-230.

Massonnet, D. & Feigl, K.L., 1998. Radar interferometry and its application to changes in the Earth's surface, *REVIEWS OF GEOPHYSICS,* 36**,** 441-500.

Massonnet, D., Holzer, T. & Vadon, H.l.n., 1997. Land Subsidence Caused by the East Mesa Geothermal Field, California, Observed Using SAR Interferometry, *Geophys. Res. Lett.,* 24.

Massonnet, D., Rossi, M., Carmona, C., Adragna, F., Peltzer, G., Feigl, K. & Rabaute, T., 1993. The displacement field of the Landers earthquake mapped by radar interferometry, *Nature,* 364**,** 138-142.

Masterlark, T., Haney, M., Dickinson, H., Fournier, T. & Searcy, C., 2010. Rheologic and structural controls on the deformation of Okmok volcano, Alaska: FEMs, InSAR, and ambient noise tomography, *J. Geophys. Res.,* 115**,** B02409.

Mazzotti, S., Lambert, A., Van der Kooij, M. & Mainville, A., 2009. Impact of anthropogenic subsidence on relative sea-level rise in the Fraser River delta, *Geology,* 37**,** 771-774.

McPherson, H.J., 1971. Downstream Changes in Sediment Character in a High Energy Mountain Stream Channel, *Arctic and Alpine Research,* 3**,** 65-79.

McTigue, D.F., 1987. Elastic Stress and Deformation Near a Finite Spherical Magma Body: Resolution of the Point Source Paradox, *J. Geophys. Res.,* 92**,** 12931-12940.

Michel, R., Avouac, J., Philippe & Taboury, J., 1999. Measuring ground displacements from SAR amplitude images: Application to the Landers Earthquake, *Geophys. Res. Lett.,* 26**,** 875-878.

Milliman, J.D. & Syvitski, J.P.M., 1992. Geomorphic/Tectonic Control of Sediment Discharge to the Ocean: The Importance of Small Mountainous Rivers, *The Journal of Geology,* 100**,** 525-544.

Mindlin, R.D. & Cheng, D.H., 1950. Thermoelastic Stress in the Semi-Infinite Solid *J. Appl. Phys.,* 21.

Miranda, N., 2010. Impact of the Envisat Mission Extension on SAR data, ed Agency, E. S.

Mogi, k., 1958. Relations between the eruptions of various volcanoes and the deformation of the ground surfaces around them, *Bull. Earthquake Res. Inst. Univ. Tokyo,* 36**,** 99-134.

Monells, D., Centolanza, G., Mallorqui, J.J., Duque, S., Lopez-Dekker, P., Tomas, R., Herrera, G., Lopez-Sanchez, J.M., Vicente, F., Navarro-Sanchez, V.D., Mulas, J. & Ieee, 2010. *Application of TerraSAR-X data to the monitoring of urban subsidence in the city of Murcia,* edn, Vol., pp. Pages, Ieee, New York.

Moreira, A., Krieger, G., Hajnsek, I., Hounam, D., Werner, M., Riegger, S. & Settelmeyer, E., 2004. TanDEM-X: a TerraSAR-X add-on satellite for single-pass SAR interferometry. *in Geoscience and Remote Sensing Symposium, 2004. IGARSS '04. Proceedings. 2004 IEEE International,* pp. 1000-1003 vol.1002.

Moreira, A. & Scheiber, R., 2000. Coregistration of interferometric SAR images using spectral diversity, *Geoscience and Remote Sensing, IEEE Transactions on,* 38**,** 2179-2191.

Morton, R., Bernier, J. & Barras, J., 2006. Evidence of regional subsidence and associated interior wetland loss induced by hydrocarbon production, Gulf Coast region, USA, *Environmental Geology,* 50**,** 261-274.

Mossop, A. & Segall, P., 1997. Subsidence at The Geysers Geothermal Field, N. California from a comparison of GPS and leveling surveys, *Geophys. Res. Lett.,* 24**,** 1839-1842.

Muntendam-Bos, A., Kroon, I. & Fokker, P., 2008. Time-dependent Inversion of Surface Subsidence due to Dynamic Reservoir Compaction, *Mathematical Geosciences,* 40**,** 159-177.

Nemecz, E., Pécsi, M., Hartyáni, Z. & Horváth, T., 2000. The origin of the silt size quartz grains and minerals in loess, *Quaternary International,* 68–71**,** 199-208.

Nishimura, K. & Hunt, J.C.R., 2000. Saltation and incipient suspension above a flat particle bed below a turbulent boundary layer, *J. Fluid Mech.,* 417**,** 77-102.

Nitti, D.O., Hanssen, R.F., Refice, A., Bovenga, F. & Nutricato, R., 2011. Impact of DEM-Assisted Coregistration on High-Resolution SAR Interferometry, *Geoscience and Remote Sensing, IEEE Transactions on,* 49**,** 1127-1143.

Nur, A. & Byerlee, J.D., 1971. An Exact Effective Stress Law for Elastic Deformation of Rock with Fluids, *J. Geophys. Res.,* 76**,** 6414-6419.

Ofeigsson, B.G., Hooper, A., Sigmundsson, F., Sturkell, E. & Grapenthin, R., 2011. Deep magma storage at Hekla volcano, Iceland, revealed by InSAR time series analysis, *J. Geophys. Res.,* 116**,** B05401.

Okada, Y., 1985. Surface deformation due to shear and tensile faults in a half-space, *Bulletin of the Seismological Society of America,* 75**,** 1135-1154.

Okada, Y., 1992. Internal deformation due to shear and tensile faults in a half-space, *Bulletin of the Seismological Society of America,* 82**,** 1018-1040.

Osmanoglu, B., Dixon, T.H., Wdowinski, S., Cabral-Cano, E. & Jiang, Y., 2011. Mexico City subsidence observed with persistent scatterer InSAR, *International Journal of Applied Earth Observation and Geoinformation,* 13**,** 1-12.

Peltier, A., Bianchi, M., Kaminski, E., Komorowski, J.C., Rucci, A. & Staudacher, T., 2010. PSInSAR as a new tool to monitor pre-eruptive volcano ground deformation: Validation using GPS measurements on Piton de la Fournaise, *Geophys. Res. Lett.,* 37**,** L12301.

Peltzer, G., Rosen, P., Rogez, F. & Hudnut, K., 1998. Poroelastic rebound along the Landers 1992 earthquake surface rupture, *J. Geophys. Res.,* 103**,** 30131-30145.

Plattner, C., Wdowinski, S., Dixon, T.H. & Biggs, J., 2010. Surface subsidence induced by the Crandall Canyon Mine (Utah) collapse: InSAR observations and elasto-plastic modelling, *Geophysical Journal International,* 183**,** 1089-1096.

Pollitz, F.F., Peltzer, G. & Burgmann, R., 2000. Mobility of continental mantle: Evidence from postseismic geodetic observations following the 1992 Landers earthquake, *J. Geophys. Res.-Solid Earth,* 105**,** 8035-8054.

Powers, M.C., 1953. A new roundness scale for sedimentary particles, *Journal of Sedimentary Research,* 23**,** 117-119.

Press, W.H., Teukolsky, S.A., Vetterling, W.T. & Flannery, B.P., 1997. *Numerical Recipes in Fortran 77: The Art of Scientific Computing,* edn, Vol. 1, pp. Pages.

Pritchard, M.E., Simons, M., Rosen, P.A., Hensley, S. & Webb, F.H., 2002. Co-seismic slip from the 1995 July 30 Mw= 8.1 Antofagasta, Chile, earthquake as constrained by InSAR and GPS observations, *Geophysical Journal International,* 150**,** 362-376.

Puysségur, B., Michel, R. & Avouac, J.-P., 2007. Tropospheric phase delay in interferometric synthetic aperture radar estimated from meteorological model and multispectral imagery, *J. Geophys. Res.,* 112**,** B05419.

Qiao, S., Shi, X., Zhu, A., Liu, Y., Bi, N., Fang, X. & Yang, G., 2010. Distribution and transport of suspended sediments off the Yellow River (Huanghe) mouth and the nearby Bohai Sea, *Estuarine, Coastal and Shelf Science,* 86**,** 337-344.

Rabus, B., Eineder, M., Roth, A. & Bamler, R., 2003. The shuttle radar topography mission--a new class of digital elevation models acquired by spaceborne radar, *ISPRS Journal of Photogrammetry and Remote Sensing,* 57**,** 241-262.

Remy, D., Bonvalot, S., Briole, P. & Murakami, M., 2003. Accurate measurements of tropospheric effects in volcanic areas from SAR interferometry data: application to Sakurajima volcano (Japan), *Earth and Planetary Science Letters,* 213**,** 299-310.

Ren, J. & Xiao, L., 2002. Tectonic settings of petroliferous basins in continental China, *Episodes,* 25**,** 227-235.

Ren, M.-E. & Shi, Y.-L., 1986. Sediment discharge of the Yellow River (China) and its effect on the sedimentation of the Bohai and the Yellow Sea, *Cont. Shelf Res.,* 6**,** 785-810.

Riddick, S.N. & Schmidt, D.A., 2011. Time-dependent changes in volcanic inflation rate near Three Sisters, Oregon, revealed by InSAR, *Geochem. Geophys. Geosyst.,* 12**,** Q12005.

Rosen, P.A., Hensley, S., Joughin, I.R., Li, F.K., Madsen, S.N., Rodriguez, E. & Goldstein, R.M., 2000. Synthetic aperture radar interferometry, *Proceedings of the IEEE,* 88**,** 333-382.

Rosich, B., 2003. ASAR Image and Wide Swath Mode Optimisations and Product Quality Update. *in ENVISAT Validation Workshop (ESA SP-531).* , Frascati, Italy.

Russell, R.D., 1955. Effects of transportation on sedimentary particles. *in Recent Marine Sediments*, pp. 32-47SEPM (Society for Sedimentary Geology).

Rutledge, J.T., Phillips, W.S. & Schuessler, B.K., 1998. Reservoir characterization using oil-production-induced microseismicity, Clinton County, Kentucky, *Tectonophysics,* 289**,** 129-152.

Sagiya, T., Miyazaki, S. & Tada, T., 2000. Continuous GPS array and present-day crustal deformation of Japan, *Pure and Applied Geophysics,* 157**,** 2303-2322.

Saito, Y., Wei, H., Zhou, Y., Nishimura, A., Sato, Y. & Yokota, S., 2000. Delta progradation and chenier formation in the Huanghe (Yellow River) delta, China, *Journal of Asian Earth Sciences,* 18**,** 489-497.

Saito, Y., Yang, Z.S. & Hori, K., 2001. The Huanghe (Yellow River) and Changjiang (Yangtze River) deltas: a review on their characteristics, evolution and sediment discharge during the Holocene, *Geomorphology,* 41**,** 219-231.

Scharroo, R. & Visser, P., 1998. Precise orbit determination and gravity field improvement for the ERS satellites, *J. Geophys. Res.,* 103.

Schmidt, D.A. & Bürgmann, R., 2003. Time-dependent land uplift and subsidence in the Santa Clara valley, California, from a large interferometric synthetic aperture radar data set, *J. Geophys. Res.,* 108**,** 2416.

Scott, K.M., 1967. Downstream change in sedimentological parameters illustrated by particle distribution from a breached rockfill dam, *Int. Assoc. Sci. Hydrol. Publ.,* 75.

Segall, P., 1992. Induced stresses due to fluid extraction from axisymmetric reservoirs, *Pure and Applied Geophysics,* 139**,** 535-560.

Segall, P., Grasso, J.-R. & Mossop, A., 1994. Poroelastic stressing and induced seismicity near the Lacq gas field, southwestern France, *J. Geophys. Res.,* 99**,** 15423-15438.

Shen, Z.K., Jackson, D.D., Feng, Y.J., Cline, M., Kim, M., Fang, P. & Bock, Y., 1994. Postseismic deformation following the Landers earthquake, California, 28 June 1992, *Bulletin of the Seismological Society of America,* 84**,** 780-791.

Shi, C., 2005. Causes for continuous siltation of the lower Yellow River, *Geomorphology,* 68, 213-223.

Shi, C. & Zhang, D., 2003. Processes and mechanisms of dynamic channel adjustment to delta progradation: the case of the mouth channel of the Yellow River, China, *Earth Surface Processes and Landforms,* 28**,** 609-624.

Shi, C., Zhang, D., You, L., Li, B., Zhang, Z. & Zhang, O., 2007. Land Subsidence as a Result of Sediment Consolidation in the Yellow River Delta, *Journal of Coastal Research*, 173-181.

Shi, C., Zhang, D.D. & You, L., 2003. Sediment budget of the Yellow River delta, China: the importance of dry bulk density and implications to understanding of sediment dispersal, *Mar. Geol.,* 199**,** 13-25.

Shirzaei, M. & Bürgmann, R., 2012. Topography correlated atmospheric delay correction in radar interferometry using wavelet transforms, *Geophys. Res. Lett.,* 39**,** L01305.

Simons, M., Fialko, Y. & Rivera, L., 2002. Coseismic deformation from the 1999 M-w 7.1 Hector Mine, California, earthquake as inferred from InSAR and GPS observations, *Bulletin of the Seismological Society of America, 92*, 1390-1402.

Stanley, D.J., 1988. Subsidence in the Northeastern Nile Delta: Rapid Rates, Possible Causes, and Consequences, *Science, 240*, 497-500.

Stanley, D.J. & Hait, A.K., 2000. Deltas, radiocarbon dating, and measurements of sediment storage and subsidence, *Geology, 28*, 295-298.

Strozzi, T., Luckman, A., Murray, T., Wegmuller, U. & Werner, C.L., 2002. Glacier motion estimation using SAR offset-tracking procedures, *Geoscience and Remote Sensing, IEEE Transactions on, 40*, 2384-2391.

Sui, J., Hicks, F.E. & Menounos, B., 2006. Observations of riverbed scour under a developing hanging ice dam, *Canadian Journal of Civil Engineering, 33*, 214-218.

Sun, J., 2002a. Provenance of loess material and formation of loess deposits on the Chinese Loess Plateau, *Earth and Planetary Science Letters, 203*, 845-859.

Sun, J., 2002b. Source Regions and Formation of the Loess Sediments on the High Mountain Regions of Northwestern China, *Quaternary Research, 58*, 341-351.

Sun, X., 2005. Sutdy on the Structural Charaeteristics and Reservoir Forming Model of Neogene Guantao Formation in Jiyang Depression, Doctorate, Guangzhou.

Suo, L., 2004. River management and ecosystem conservation in China. *in Ninth International Symposium on River Sedimentation*, Yichang, China.

Syvitski, J.P.M., Kettner, A.J., Overeem, I., Hutton, E.W.H., Hannon, M.T., Brakenridge, G.R., Day, J., Vorosmarty, C., Saito, Y., Giosan, L. & Nicholls, R.J., 2009. Sinking deltas due to human activities, *Nature Geosci, 2*, 681-686.

Terzaghi, K., 1943. *Theoretical Soil Mechanic,* edn, Vol., pp. Pages, Wiley, New York.

Ting, T.C.T. & Chen, T., 2005. Poisson's ratio for anisotropic elastic materials can have no bounds, *The Quarterly Journal of Mechanics and Applied Mathematics, 58*, 73-82.

Tornqvist, T.E., Wallace, D.J., Storms, J.E.A., Wallinga, J., van Dam, R.L., Blaauw, M., Derksen, M.S., Klerks, C.J.W., Meijneken, C. & Snijders, E.M.A., 2008. Mississippi Delta subsidence primarily caused by compaction of Holocene strata, *Nature Geosci, 1*, 173-176.

Wadell, H., 1932. Volume, Shape, and Roundness of Rock Particles, *The Journal of Geology, 40*, 443-451.

Wadge, G., Webley, P.W., James, I.N., Bingley, R., Dodson, A., Waugh, S., Veneboer, T., Puglisi, G., Mattia, M., Baker, D., Edwards, S.C., Edwards, S.J. & Clarke, P.J., 2002. Atmospheric models, GPS and InSAR measurements of the tropospheric water vapour field over Mount Etna, *Geophys. Res. Lett., 29*, 1905.

Wang, G., Wu, B. & Wang, Z.-Y., 2005. Sedimentation problems and management strategies of Sanmenxia Reservoir, Yellow River, China, *Water Resour. Res., 41*, W09417.

Wang, H., Bi, N., Saito, Y., Wang, Y., Sun, X., Zhang, J. & Yang, Z., 2010. Recent changes in sediment delivery by the Huanghe (Yellow River) to the sea: Causes and environmental implications in its estuary, *Journal of Hydrology, 391*, 302-313.

Wang, H., Yang, Z., Saito, Y., Liu, J.P., Sun, X. & Wang, Y., 2007. Stepwise decreases of the Huanghe (Yellow River) sediment load (1950-2005): Impacts of climate change and human activities, *Global and Planetary Change, 57*, 331-354.

Wang, J., Gao, W., Xu, S. & Yu, L., 2012. Evaluation of the combined risk of sea level rise, land subsidence, and storm surges on the coastal areas of Shanghai, China, *Climatic Change*, 1-22.

Wang, S.J., Hassan, M.A. & Xie, X.P., 2006. Relationship between suspended sediment load, channel geometry and land area increment in the Yellow River Delta, *CATENA, 65*, 302-314.

Wang, X., Zhong, J., Xue, Z. & Jia, P., 2004. Sedimentary model of Guan ( 1+ 2) sand sets and its control over distribution of remaining oil in Gudao Oilfield (in Chinese), *Journal of the University of Petroleum, China, 28*.

Wang, Z., 2011. Oil sources in multi directions and accumulation analysis in Guantao Formation of Gudao Oilfield in Zhanhua Sag (in Chinese), *Natural gas geoscience, 22*.

Wang, Z.H. & Huang, S.G., 1988. A study of evolution of the Huanghe River delta through recent and ancient sea charts (in Chinese), *Coastal Engineering,* 7.

Webley, P.W., Bingley, R.M., Dodson, A.H., Wadge, G., Waugh, S.J. & James, I.N., 2002. Atmospheric water vapour correction to InSAR surface motion measurements on mountains: results from a dense GPS network on Mount Etna, *Physics and Chemistry of the Earth, Parts A/B/C,* 27**,** 363-370.

Wen, J., Wang, L. & Wei, Z.G., 2009. An overview of the LOess Plateau mesa region land surface process field EXperiment series (LOPEXs), *Hydrol. Earth Syst. Sci.,* 13**,** 945-951.

Wright, T.J., Parsons, B., England, P.C. & Fielding, E.J., 2004. InSAR Observations of Low Slip Rates on the Major Faults of Western Tibet, *Science,* 305**,** 236-239.

Xiong, J., 2011. The sedimentary characteristics of Guan 1+2 Sand Member in the Fault Block of B82-B19 of Gudao Oilfiled (in Chinese), Engineering Master, China University of Petroleum.

Xu, J., 2003. Growth of the Yellow River delta over the past 800 years, as influenced by human activities, *Geografiska Annaler: Series A, Physical Geography,* 85**,** 21-30.

Xu, X.G., Lin, H.P. & Fu, Z.Y., 2004. Probe into the method of regional ecological risk assessment - a case study of wetland in the Yellow River Delta in China, *J. Environ. Manage.,* 70**,** 253-262.

Xue, C., 1993. Historical changes in the Yellow River delta, China, *Mar. Geol.,* 113**,** 321-330.

Yamakawa, N., 1955. On the strain produced in a semi-infinite elastic solid by an interior source of stress, *J. Seismol. Soc. Jpn,* 8**,** 84-98.

Yang, X.-M., Davis, P.M. & Dieterich, J.H., 1988. Deformation From Inflation of a Dipping Finite Prolate Spheroid in an Elastic Half-Space as a Model for Volcanic Stressing, *J. Geophys. Res.,* 93**,** 4249-4257.

Yi, S., Saito, Y., Oshima, H., Zhou, Y. & Wei, H., 2003. Holocene environmental history inferred from pollen assemblages in the Huanghe (Yellow River) delta, China: climatic change and human impact, *Quaternary Science Reviews,* 22**,** 609-628.

Yong, Z., 2007. Studies on Hydrocarbon Accumulation Conditions and Mechanism of the Gudao Buried Hill in Jiyang Depression, Doctor of engineering, Chengdu.

Yue, T.X., Liu, J.Y., Jørgensen, S.E. & Ye, Q.H., 2003. Landscape change detection of the newly created wetland in Yellow River Delta, *Ecological Modelling,* 164**,** 21-31.

Zebker, H.A. & Goldstein, R.M., 1986. Topographic Mapping From Interferometric Synthetic Aperture Radar Observations, *Journal of Geophysical Research,* 91**,** 4993-5000.

Zebker, H.A., Rosen, P.A., Goldstein, R.M., Gabriel, A. & Werner, C.L., 1994. On the derivation of coseismic displacement fields using differential radar interferometry: The Landers earthquake, *J. Geophys. Res.,* 99.

Zebker, H.A., Rosen, P.A. & Hensley, S., 1997. Atmospheric effects in interferometric synthetic aperture radar surface deformation and topographic maps, *J. Geophys. Res.,* 102**,** 7547-7563.

Zebker, H.A. & Villasenor, J., 1992. Decorrelation in interferometric radar echoes, *Geoscience and Remote Sensing, IEEE Transactions on,* 30**,** 950-959.

Zhang, S., Wang, Y., Shi, D., Xu, H., Pang, X. & Li, M., 2004. Fault-fracture mesh petroleum plays in the Jiyang Superdepression of the Bohai Bay Basin, eastern China, *Mar. Pet. Geol.,* 21**,** 651-668.

Zhou, L., Li, G., Deng, s., Li, A., Wen, G. & Zhao, d., 2001. Change of Land Use in Modern Yellow River Delta.

Zhu, G., Zhang, S., Jin, Q., Dai, J., Zhang, L. & Li, J., 2005. Origin of the Neogene shallow gas accumulations in the Jiyang Superdepression, Bohai Bay Basin, *Organic Geochemistry,* 36**,** 1650-1663.

Zink, M., 2002. Introduction to the ASAR calibration/validation project. *in The Envisat calibration review*, Noordwijk (The Netherlands).

Zoback, M.D. & Zinke, J.C., 2002. Production-induced Normal Faulting in the Valhall and Ekofisk Oil Fields, *Pure and Applied Geophysics,* 159**,** 403-420.